An experimental investigation of the aerodynamics and vortex flowfield of a reverse delta wing

Lok Sun Ko

Department of Mechanical Engineering

McGill University

Montreal, Quebec, Canada

April 13, 2017

A thesis submitted to McGill University in partial fulfillment of requirements of the degree of Doctor of Philosophy

ACKNOWLEDGEMENTS

Firstly, I would like to express the deepest appreciation and sincere gratitude to my supervisor Professor Tim Lee for his continuous support and patience during my Ph.D. study. This endeavor would not have been possible without his guidance and persistent help.

In addition, I would like to thank the past and present colleagues of the Experimental Aerodynamics Laboratory with whom I had the pleasure to work with: Peter Gerontakos, Jennifer Pereira, Ying Yu Su, Gautam Virdi, Muneeb Dogar, Hafiz Laiq-ur Rehman, Steve Choi, Munir Nathoo, Nirmal Raju, Matt Hongzhi Mou, Yafus Siddiqui, Vincent Tremblay-Dionne, Amaan Majeed, Bilal Siddiqui, and Vikas Konduri. Many insightful discussions and long days have been made pleasurable by their presence.

A special thank goes to my family for their encouragement and support. I would not be where I am today without my parents. My brother and sister are also thanked for their help and assistance in many of my presentations and write-ups. I am also grateful to all of my friends who directly and indirectly helped me complete my dissertation.

At the end, I would like to express my appreciation to my beloved wife Christine Woo who has supported me throughout this long journey and was also always there for me when I needed help.

ABSTRACT

Reverse or inverted delta wing planforms have been employed extensively in the Lippisch-type wing-in-ground effect (WIG) craft for the past few decades. Despite their industrial applicability and popularity, the aerodynamics and the vortex flowfield generated by the reverse delta wing are, however, not available in archived publications. Extensive experimental investigations utilizing particle image velocimetry, force balances, and dye and smoke-wire flow visualizations were, therefore, conducted in this study to better understand the aerodynamic load generation and the vortex flow structure of a reverse delta wing, both slender and non-slender.

The results show that for a reverse delta wing in a free stream the wing stall was delayed and had a lowered lift and drag compared to a regular or conventional delta wing at the same angle of attack. The drag reduction of the reverse delta wing, however, underperformed the decrease in the lift, rendering an improved lift-to-drag ratio compared to the regular delta wing. More importantly, the upper surface flow of the reverse delta wing was found to be characterized by the unique multiple spanwise vortex filaments. In contrast to the leading-edge vortex breakdown-induced stalling of the regular delta wing, the stalling mechanism of the reverse delta wing was found to be triggered by the breakdown of the multiple spanwise vortex filaments. Meanwhile, the reverse-delta-wing vortices were also found to be located outboard, suggesting their irrelevance to the lift generation of the reverse delta wing. The lift of the reverse delta wing was found to be mainly generated by the pressure acting on its lower surface, while the upper surface acts like a wake generator. These two streamwise counter-rotating vortices generated by the reverse delta wing were also found to became nearly axisymmetric at 0.7 chord downstream from the leading edge of the reverse delta wing. For a non-slender reverse delta wing (i.e., with a sweep angle less than 55 deg), the above-mentioned findings were found to remain unchanged but had a much smaller magnitude compared to its slender counterpart.

Finally, in order to enhance the lift generation capability of the reverse delta wing, passive Gurney flaplike strips, of different heights and configurations, were applied to both the side

edges and the leading edges of the reverse delta wing. The addition of the side-edge strips was found to produce a leftward shift of the lift curve, resembling a conventional trailing-edge flap, and a large lift enhancement. The large lift increment overwhelmed the corresponding drag increase, thereby leading to a further improved lift-to-drag ratio compared to the clean reverse delta wing. The lift and drag coefficients were also found to increase with the strip height. The side-edge strip-equipped wing also produced a strengthened vortex compared to its baseline wing counterpart, while the leading-edge strips were found to persistently produce a greatly diffused vortex flow, which therefore suggests a promising wingtip vortex control alternative. The downward leading-edge strip was found to be capable of delivering a delayed stall and an increased maximum lift coefficient compared to the clean baseline wing.

In summary, the present first-of-its-kind experimental findings on the reverse delta wing will not only advance our understanding of the lift and drag generation and the vortex flow characteristics, but can also serve as benchmark data for CFD validation. The present study will also lay a foundation for the study of the effects of ground proximity on the reverse delta wing, and, more importantly, lead to an improved design of wing-in-ground effect craft.

ABRÉGÉ

Les ailes delta inversées sont utilisées extensivement dans les avions à effet de sol Lippisch depuis quelques décennies. Malgré leur potentiel d'application industrielle et popularité, l'aérodynamique et l'écoulement tourbillonnaire générés par le bout des ailes delta inversées sont, cependant, indisponibles dans les archives de publications. Des études expérimentales extensives par les techniques expérimentales, tel que la vélocimétrie des images de particules, balance de force, et visualisation de l'écoulement par colorant et fumée, ont été, par conséquent, réalisées pour mieux comprendre la génération de charge aérodynamique et la structure d'écoulement de tourbillon des ailes delta inversées, qu'elles soient élancées et non-élancées.

Les résultats démontrent que pour les ailes delta inversées dans l'écoulement libre, le décrochage de l'aile a été retardé ainsi qu'une réduction de la portance et de la traînée comparativement à une aile delta pour le même angle d'attaque. La réduction de la traînée de l'aile delta inversée, toutefois, sous-performait la diminution en portance, rendant une finesse améliorée comparée à l'aile delta. Plus important encore, le champs d'écoulement de la surface supérieure de l'aile delta inversée est composé de multiples uniques filaments de tourbillon d'envergure. Contrairement au décrochage causé par l'éclatement tourbillonnaire de l'aile delta, le mécanisme de décrochage de l'aile delta inversée est causé par la dégradation des filaments de tourbillon d'envergure. Entre-temps, les tourbillons de l'aile delta inversée sont localisés à l'extérieur de la surface supérieure, ce qui permet de dire qu'ils ne contribuent pas à l'augmentation de la portance. La portance de l'aile delta inversée a été trouvée d'être générée par la pression agissant sur la surface inférieure de l'aile, tandis que la surface supérieure comporte comme un générateur de sillage. Les deux tourbillons générés par l'aile delta inversée sont presque axisymétriques à 0.7c en aval du bord d'attaque de l'aile delta inversée. Pour les ailes delta inversées non-élancées (angle de balayage < 55 deg), les observations mentionnées précédemment sont valides, mais comportent des magnitudes inférieures comparées aux résultats de l'aile delta inversée élancée.

Finalement, afin d'améliorer la portance générée par l'aile delta inversée, des bandes de volets type Gurney (control passive), de différentes hauteurs et configurations, ont été ajoutées sur le bord d'attaque et aussi sur le bord de fuite de l'aile delta inversée. L'addition de bandes sur les bords de fuite a contribué à déplacer la courbe de portance à gauche, similaire aux volets de bord de fuite utilisés sur un profil conventionnel, et à augmenter la portance. Cette large augmentation de portance a surpassé l'augmentation de la traînée, par conséquent, on obtient une amélioration de la finesse comparée au cas de l'aile delta inversée sans bandes. La portance et la traînée ont augmenté avec l'augmentation de la hauteur des bandes. Les ailes équipées de bandes de bord de fuite ont produit deux tourbillons plus intensifiés comparé à celui généré par l'aile delta inversée sans bandes. Les bandes installées au bord d'attaque, par contre, produit continuellement deux tourbillons plus diffus, proposant une application de contrôle de tourbillon marginal. La bande de bord d'attaque vers le bas a été capable de retarder le décrochage et d'augmenter la portance maximale comparée à l'aile sans contrôle.

En résumé, cette étude présente une nouvelle découverte expérimentale sur les ailes delta inversées qui vont, non seulement avancer notre compréhension de la génération de portance et de la traînée ainsi que les caractéristiques du tourbillon, aussi servir de base de données pour la mécanique des fluides numérique. L'étude présente pourra servir de base pour améliorer nos connaissances sur les ailes delta inversée en effet de sol, et ainsi avancer la conception des avions à effet de sol.

TABLE OF CONTENTS

LIST OF SYMBOLS

b	geometric wing span
b'	effective span or distance between the core of two vortices
c	wing or airfoil chord
C_D	total drag coefficient
C_{Di}	lift-induced drag coefficient
C_L	total lift coefficient
$C_{L,max}$	maximum C_L
D_i	lift-induced drag
h	strip height
L/D	lift-to-drag ratio
M_∞	freestream Mach number
Re	chord Reynolds number, $= cu_\infty/\nu$
r	radius
r_c	core radius
r_o	outer radius
u	mean axial velocity
u_c	core axial vortex flow velocity
u_∞	freestream velocity
v,w	vertical and spanwise velocity
x,y,z	streamwise, vertical and spanwise direction
$(x/c)_{VBD}$	normalized vortex breakdown location
y_c	vertical vortex center position
z_c	horizontal vortex center position
v_θ	tangential velocity
$v_{\theta,peak}$	peak v_θ
α	angle of attack
α_{ss}	static-stall angle
Λ	sweep angle
ζ	streamwise vorticity

ζ_{peak}	peak ζ
Γ	circulation
Γ_c	core circulation
Γ_o	total circulation
ψ	stream function
ϕ	velocity potential
ρ	fluid density
ν	fluid kinematic viscosity

LIST OF TABLES

LIST OF FIGURES

CHAPTER 1

INTRODUCTION

Conventional fixed-wing transport aircraft fly on cruising altitude of up to 39,000 feet while boats and ships float on water. Normally, an airplane flying in a free stream produces lift because of the pressure difference between the upper and lower surfaces. The static pressure on the lower surface is higher than the upper surface. As lift is produced, drag is also generated. One component of drag called the lift-induced drag is created due to the downwash created by the wingtip vortices. One type of vehicle, however, is designed to fly close to the surface, be it ground or water. These are called ground effect (GE) vehicles or wing-in-ground effect (WIG) craft, as they generally fly at an altitude of 10% of their span. By flying close to the ground, or water surface, they are able to take advantage of the "ram" or dynamic "cushion" effect, with the pilot feeling that the aircraft is floating. The presence of the physical boundary alters the flow around the wing, causing an increase in lift and a reduction in lift-induced drag. The closer the wing is to the boundary or surface, the stronger the effect. Figure 1.1 shows the schematic of a wing flying in ground effect and the definition of ground clearance, and also the surface pressure distributions on an airfoil both in ground effect and out of ground effect.

For WIG craft flying close to the ground, the boundary alters the flow field by not allowing the flow under the wing to expand as it would in free air. The rise in static pressure causes an increase in lift. As the total pressure remains constant throughout the flow field, the total of the static and dynamic pressure must remain constant. As the flow is diverted under the wing, the dynamic pressure is decreased and the static pressure is increased. This increase in static pressure is referred to as "ram pressure". The consequential pressure flow field not only causes a change in lift, but also to other aerodynamic characteristics of the wing. In short, due to the presence of the ground, the static pressure below the wing is increased and the downwash is decreased. Thus, lift-induced drag is decreased and the lift-to-drag ratio of the WIG craft or vehicles is increased. The reduction in the lift-induced drag can be explained from the conceptual sketches of wingtip vortices

both out of ground effect and in ground effect depicted in figure 1.2. The presence of the boundary causes the tip vortices to develop a downwash smaller than without the effect of the ground. This reduction in downwash causes a reduction in downwash angle, leading to a smaller change in effective angle of attack. This change in effective angle of attack leads to a reduction of the streamwise component of the effective lift vector. The resulting increase in lift-to-drag ratio provides an increased efficiency and the reduction in drag leads to a reduction in thrust requirement during cruise flight. Detailed information of ground effect can be found in the book of Cui and Zhang (2010) and Yun et al. (2010).

In addition to causing an increase in lift-to-drag ratio, the ground effect also alters the pitching moment generated by the wing. The flow field under the ground effect changes the pressure distribution and, therefore, the aerodynamic center of the wing is changed along with the pitching moment. Conventional rectangular wings normally create a small nose down pitching moment in cruise flight. Ground effect accentuates this pitching moment, requiring a large tail to stabilize the vehicle. Furthermore, the pitching moment also changes with height above the boundary. In freestream flight, the aerodynamic center is usually located at the quarter-chord. For a ground effect vehicle, this can shift up to the half-chord location, depending on the distance between the trailing edge and the boundary. This undesirable movement of the aerodynamic center requires design considerations that can cause drag, structural and weight penalties.

It is noteworthy that in nature, birds such as ducks, pelicans, or sandpiper can also be observed to fly just over water. Ground effect comes into play when the bird flies within its full wingspan above the surface of water or ground. Brown pelicans, for example, are large birds having a wingspan of over seven feet and weighing 10 lb_f. By soaring over the waves in ground effect, these birds can save energy, thus requiring less food and less feeding time. One of the first aircraft experiencing ground effect was actually the Wright brothers' 1903 Flyer. Because the Flyer was flying close to the ground, it experienced a lift increase and a reduction of the lift-induced drag.

Similarly, when an aircraft flies within the length of its wingspan, ground effect can affect its aerodynamic performance. The ground effectively reduces the downwash of the aircraft by hindering the formation of the tip vortices due to the obstruction of the ground. Therefore, lift-induced drag is reduced. Furthermore, the ground also creates a higher pressure zone on the pressure side of the wing, thus increasing lift. Combined, these factors improve the lift-to-drag ratio of the aircraft while flying in ground effect. Consequentially, the aircraft will require a less powerful engine, and can save fuel and fly longer.

While research on rectangular wings is abundant, the research on reverse delta wings is rather limited. The regular delta wing, however, has been studied extensively by researchers elsewhere. While the main topic of this study is the reverse delta wing, the delta wing was also studied to serve as a comparison. Note that since delta wings can be categorized as slender (with a sweep angle $\Lambda > 55°$) and non-slender (with a sweep angle $\Lambda < 55°$), the flow phenomena on either case are therefore greatly different. The effect of slenderness will also be explored in this study, for both delta wing and reverse delta wing. Finally, a passive flow control device employing Gurney flaplike strips, of different heights and configurations, are also applied to the trailing edges (or side edges) and also the leading edge of the reverse delta wing to increase the lift generation and the lift-to-drag ratio of the reverse delta wing. In the following section, the design and development of ground effect vehicles is reviewed, followed by the motivation of this study. The reviews on regular delta wing and reverse delta wing-related work will be given in Chapter 2. It should be noted that due to the scarcity or almost nonexistence of archived information on reverse delta wing even in free stream, to the author's best knowledge, the present experimental investigation of the aerodynamics and vortex flow structure generated by a reverse delta wing, both slender and non-slender, will not only improve our understanding of the reverse delta wing but also advance the development and design of Lippisch-type WIG craft.

1.1 Wing-in-ground effect (WIG) craft

In this section, the design and development of the two main categories of WIG craft: the Russian-built Ekranoplans, where the craft have a low aspect ratio rectangular wing combined with a large horizontal tail stabilizer, and the Lippisch-type WIG craft, which is designed by Dr. A. Lippisch, or German-built ground effect vehicle employing reverse delta wing with anhedral as wing planform are discussed.

1.1.1 Russian Ekranoplans

The world's first Ekranoplan was designed and constructed by R. Alexeyev, who is a Russian designer of high-speed shipbuilding. In contrast with the rest of the world, there are many hydrofoils operating commercially in Russia due to the many bodies of water present. There are 150,000 rivers and 250,000 lakes in Russia; hence Alexeyev began his work in hydrofoil design. During and after the World War II, he built a prototype hydrofoil called the Raketa-1. On its maiden voyage, on August 25 1957, it was able to ferry 30 passengers from Nizhny Novgorod to Kazan (a 420 km distance) in seven hours. The Raketa was in serial production between 1957 and 1976, with 389 units built, 26 to 32 of them for export (see, for example, Caspian Sea Monster (n.d.) and Tarantola (2013) for details).

To improve the efficiency of the hydrofoils, Alexeyev began building a new type of high-speed ground effect vehicle called Ekranoplan in the 1960s. The most impressive vehicle he designed was the KM (Korabl Maket, "prototype ship" in Russian). It was designed in 1964-1965 and was a 544-ton vehicle. In 1966, the KM was tested in the Caspian Sea near Kaspiysk. When the first spy photograph from American satellites showed up with a strange vehicle with the writing "KM" on its fuselage, the CIA thought it meant "Caspian Monster", hence its nickname, the Caspian Sea Monster (see Figure 1.3). The Ekranoplan had a wingspan of 37.6 m, a height of 21.4 m, and a length of 92 m. Its maximum take-off weight was 544 tons. It was the largest airplane, with a wing area of 662.5 m^2, in the world until the Antonov An-225 Mriya cargo plane. It was designed to fly at an altitude of 5-10 meters to make use of the ground effect phenomenon. It use include military and rescue

applications. The optimum (fuel efficient) cruising speed was 430 km/h (267 mph) and had a maximum operational speed of 500 km/h (311 mph). Maximum speeds up to 740 km/h (460 mph) have been reported. It was powered by eight Dobrynin VD-7 turbojets on the front of the fuselage, and two on the tail for extra thrust during takeoff. Despite its ground effect advantages, the KM, however, suffered some drawbacks for military applications. For instance, the plane had a very low maneuverability and if a wingtip touched the water, it could cartwheel. Furthermore, it always had to take off into the wind when ground effect was not available. The Caspian Sea Monster was tested at the Caspian Sea until 1980 when a pilot error caused an unrecoverable crash without human casualties. After the fall of the Soviet Union, Alexeyev's work became public and he is now generally considered as the father of ground effect vehicle designs.

In general, the Russian-type Ekranoplans overcame the large undesired nose-down pitching moment by fitting tail planes approximately 50% of the area of the main wing with a span similar to the wing. The tail planes, with a stabilizer span of 37 m, were also mounted out of ground effect (mounted high) so that their aerodynamic characteristics would not be affected by the height above the aircraft. This design, however, came with substantial efficiency penalties due the size and mounting position. The addition of large tail planes also introduced drag and a structural weight penalty.

1.1.2 Lippisch-type WIG craft

The first proof of concept Lippisch-type wing-in-ground effect (WIG) craft was the aerofoil boat or Collins/Lippisch X-112. It had a reverse delta wing planform and was designed and developed by Dr. Alexander Lippisch in 1963. The X-112 (see Figure 1.4) was an experimental two-seat ground effect vehicle featuring the use of reverse delta wing with a strong anhedral (Arndt n.d.). This configuration would later be known as the Lippisch-type ground effect vehicle. Testing began in 1963, with the Collins X-112 rising clear of the water surface from ground effect at speeds of around 58 km/h (36 mph). Free flights with one or two occupants up to 124 km/h (77 mph) were also performed. The Collins X-112 provided satisfactory stability and, especially, longitudinal control characteristics and was considered a success.

The X-112 was succeeded by the RFB X-114 (see Figure 1.5). The RFB X-114 is a 12 m long seven-seater with a 6.7 m wing span. Once again, the RFB X-114 was equipped with a reverse delta wing with an anhedral angle estimated to be 19°. It was able to fly above the water at 144 km/hr (90 mph), and saving fuel by ground effect. The RFB X-114 can also fly over ground effect obstacles such as trees, peninsulas or waterfalls. Furthermore, to fly over a ship, all the pilot has to do is to pull back on the craft's control wheel. The craft is also equipped with an unusual item: an extremely sensitive radar altimeter that can measure altitude over average wave heights within two inches.

It is also of interest to note that Hanno Fischer, a designer and test pilot for Rhein-Flugzeugbau GMBH who helped build and has flown the RFB-X114 provided many insights in a Popular Science article by Ben Kocivr (1977). Fischer said that in free flight, the RFB X-114's lift-to-drag (L/D) ratio was 8, and could reach up to 20-25 in ground effect. This translated to being able to fly a 3000-pound aircraft at 113 km/h in ground effect with simply a 70 hp engine. In comparison, a conventional plane such as the 2000-pound Grumman American two-seater Traveler required a 150 hp engine to fly at 225 km/h in free flight. The difference in power and fuel savings was substantial. Furthermore, he revealed several advantages using the reverse delta wing with anhedral angle planform: (1) the reverse delta wing provided longitudinal stability: on conventional wings, the center of pressure shifted forward from 45% of the wing chord while in ground effect to 25% of the wing chord at a higher altitude; (2) when the reverse-delta-wing craft was in water, only the small leading-edge tip of the wing was immersed. This reduces the hydrodynamic lift versus a regular delta wing plane where the majority of the trailing edge would be in the water; (3) the anhedral provided an immediate "air tunnel" under the wing for the ground effect to start as soon as the plane was in forward motion during takeoff; (4) the compact delta wing shape offered structural advantages. Conventionally, good lift-to-drag ratios were obtained by long slender wings, similar to those of high performance gliders. However, the reverse delta wing was able to generate 35% of its total lift by ground effect, without inducing induced drag. Hence, the aerofoil could be relatively narrow, compact, stronger, lighter and fly with less power; and (5) the reverse delta wing

was absolutely stable. Fischer describes as once the desired altitude is reached, the airplane holds the altitude automatically, even when piloting hands off. To land, the pilot only has to reduce power and the plane comes down and levels off automatically.

The RFB X-114 later evolved into WSH-500 (see figure 1.6) by Wing Ship Technology Corp. (Wing Ship Technology n.d.) in South Korea. WSH-500 is a 50-seater WIG craft with an overall length of 28.5 m, a wing span of 27 m, and a take-off weight of 17.1 tons. It cruises at 180 km/h and at an altitude of 1 to 5 m.

In summary, while the Ekranoplan have a low aspect-ratio rectangular wing, the Lippisch-type craft employs a reverse delta wing. Because the reverse delta wing can fly in ground effect for up to 50% of its span as opposed to the 10% of the wing chord of the Ekranoplan, the study of the reverse delta wing might be very rewarding. Surprisingly, no archived information on the aerodynamics and vortex flow field of the reverse delta wing, even in a free stream, is readily available.

1.2 Motivation

It is evident that the Lippisch-type wing-in-ground effect craft, which employ reverse delta wing planforms, have been rigorously constructed and undergone sea trials in countries like South Korea, Singapore, Australia, Japan, Taiwan, and the U.S. The practical and commercial applications of the Lippisch-type wing-in-ground effect craft are evident. However, in spite of the great commercial endeavors, the development of the WIG craft is still somewhat experimental, and published information on the aerodynamics and vortex flowfield generated by a reverse delta wing, both slender and non-slender, are very scarce or none (to the author's best knowledge). To better understand how a reverse delta wing behave, both aerodynamically and fluid dynamically, so as to advance the design and performance of Lippisch-type WIG craft, extensive vortical flowfield and aerodynamic force measurements by using particle image velocimetry, flow visualization, and force balances were therefore acquired. Furthermore, due to the potential applications of the half reverse delta wing for wingtip vortex control, the full reverse delta wing need to be studied first.

This present research work was, however, focused on a reverse delta wing in a free stream or out of ground effect. It is believed that the present out-of-ground effect investigations will lay the foundation for the understanding and improvement of the aerodynamics and vortex flow produced by the reverse delta wing planform employed in the Lippisch-type WIG craft. To better understand the flow around a reverse delta wing, the leading-edge vortices and the aerodynamics of a regular or conventional delta wing are reviewed first in the next chapter, followed by the discussions of the limited reverse delta wing-related research work. The review on the regular delta wing, which has been investigated extensively by researchers elsewhere, was particularly included to help understand the discrepancies between a regular delta wing and a reverse delta wing.

(a)

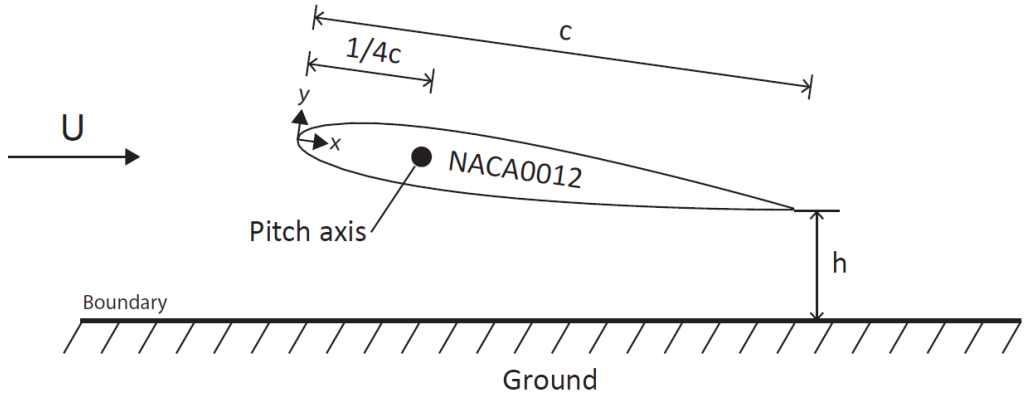

(b)

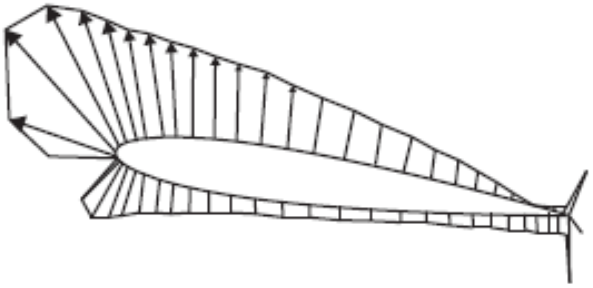

(c)

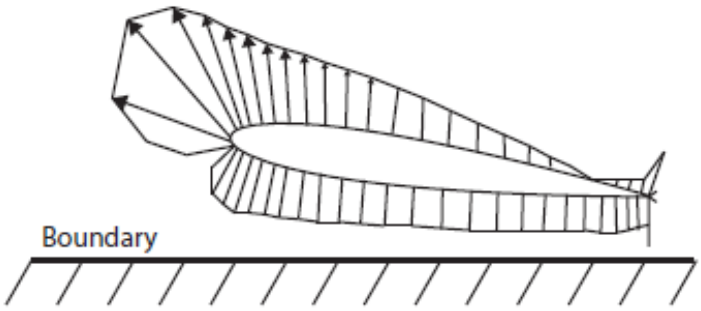

Figure 1.1 (a) Schematic of a wing flying in ground effect and the definition of ground clearance h, and surface pressure distributions along an airfoil (b) out of ground effect and (c) in ground effect.

(a)

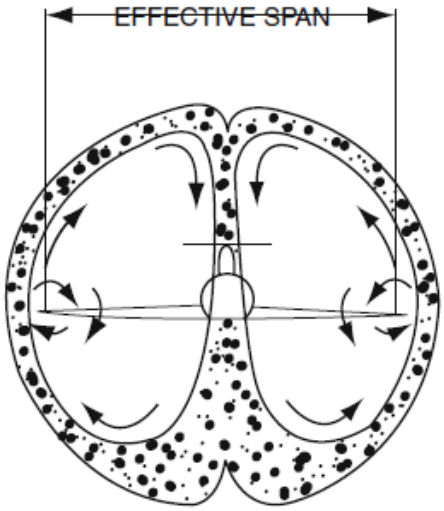

(b)

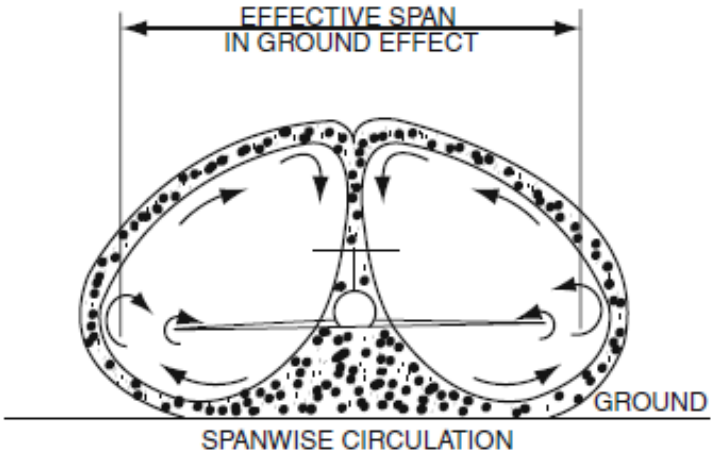

Figure 1.2 Conceptual sketches of wing tip vortex. (a) Out of ground effect and (b) in ground effect (Yun et al. 2010).

Figure 1.3 Photo of the Caspian Sea Monster (Caspian Sea Monster n.d.).

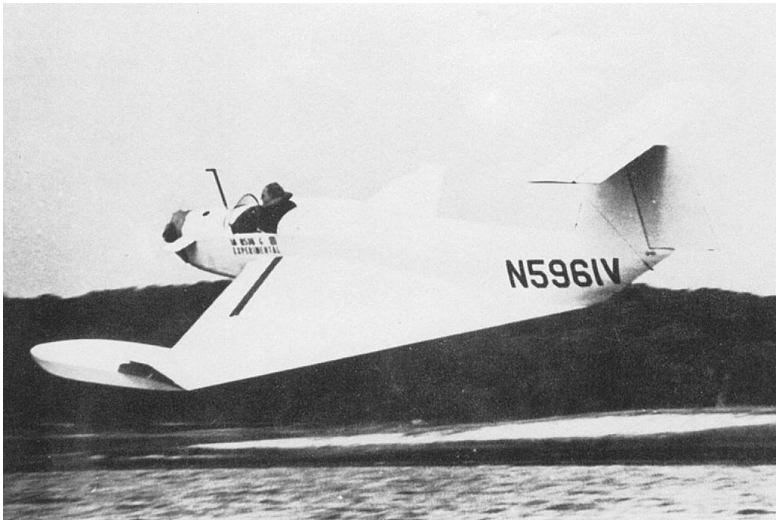

Figure 1.4 Collins/Lippisch X-112 WIG craft with a length of 7.62 m, a wing span of 4.27 m, a wing area of 10 m^2, a take-off weight of 332 kg, and a maximum speed of 124 km/h (Alexander Lippisch n.d.).

(a)

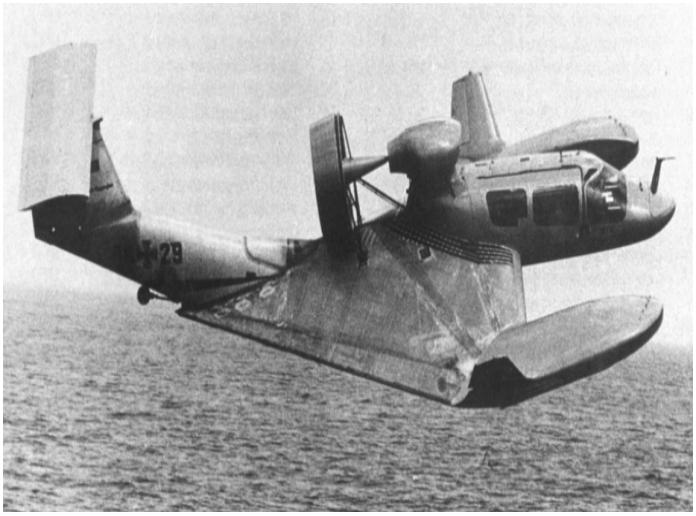

(b)

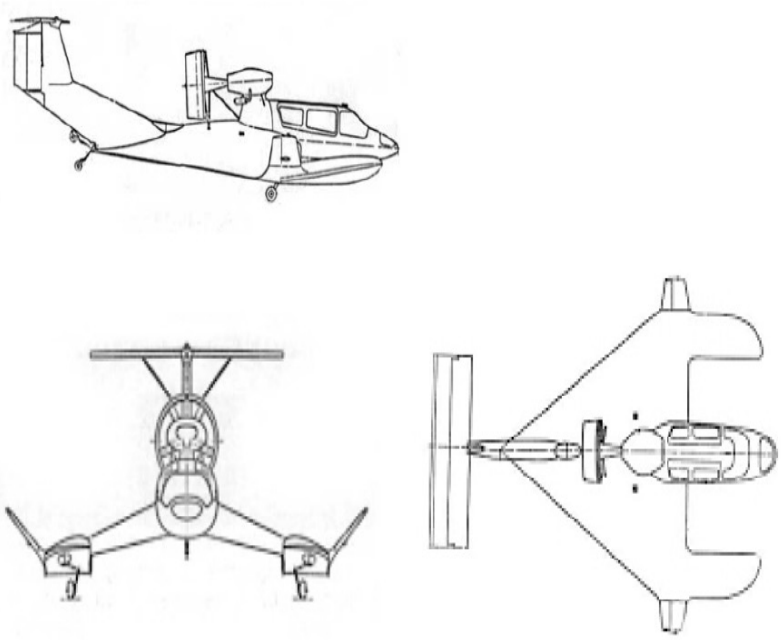

Figure 1.5 (a) Photo of a RFB X-114 in flight, and (b) schematics of the RFB X-114 (Alexander Lippisch n.d.).

(a)

(b)

Figure 1.6 (a) Photo and (b) schematics of WingShip-500 (Wing Ship Technology n.d.).

CHAPTER 2

LITERATURE SURVEY

To better understand the aerodynamics and vortex flow characteristics of a reverse delta wing, the typical aerodynamics and flowfield generated by a regular or conventional delta wing were reviewed first. Special attention was focused on the formation and growth of the leading-edge vortices and their breakdown over the delta wing. The review of the regular delta wing will be followed by the discussions of the reverse delta wings-related publications.

2.1 Regular delta wing

Delta wings have been employed in high-speed flight. As the angle of attack increases, the aerodynamics is dominated by the presence of two energetic counter-rotating streamwise leading-edge vortices, which energizes the flow and provides nonlinear vortex lift, rendering a very high stall angle. At high angles of attack, the leading-edge vortical flow may breakdown, resulting in a decreased lift force and an increased drag force. Leading-edge vortex is sensitive to the nature of the vortex structure and also to the flow field (i.e., the pressure gradient and streamwise vorticity) in which the vortex is embedded. The vortex breakdown can also affect the stability of the aircraft and cause buffeting and wing rock, as well as a detrimental pitch-up moment increase. Delta wings are, however, low aspect ratio wings which result in a lower lift-to-drag ratio and also a smaller lift-curve slope compared to the rectangular wing planforms. However, due to the high demand of super maneuverability, delta wings have been employed extensively in high-speed military aircraft. Extensive experimental, theoretical and numerical investigations on delta wings, especially on the growth and development of the leading-edge vortices and their subsequent breakdown, have been conducted by researchers elsewhere. Massive data have therefore been archived for regular delta wings. The majority of the published work is, however, dedicated to slender delta wings (i.e., with a sweep angle $\Lambda > 55°$) rather than

non-slender wings (with $\Lambda < 55°$). This literature survey is therefore concentrated on slender delta wings.

2.1.1 Leading-edge vortex flow characteristics

Figure 2.1 depicts the detailed leading-edge vortex flow structure over a sharp-edged slender delta wing at high angle of attack (Benmeddour et al. 2009). The boundary layer separation is often fixed at the apex by the sharp leading edge which results in the formation of the three-dimensional shear layers. These shear layers ultimately roll up to form a stable coherent pair of nearly axisymmetric leading-edge vortices of high vorticity concentration. These vortices inherit various forms of instabilities as a consequence of their developing mechanism which then induce unsteadiness and nurtures vortical substructures which progress along the primary vortex. The detailed flow structure of primary vortex, or leading-edge vortex, can be divided into three different regions (Earnshaw 1961): (1) the shear layer, formed by flow separation at the leading-edge which subsequently rolls up to form the vortex structure and feeds vorticity, (2) rotational core, whose diameter is about 30% of the local semi-span and circumferential velocities are isolated from the effect of the vortex sheet, and (3) viscous sub-core, extended to about 5% of the local semi-span, where the gradients of flow parameters, i.e., pressure and velocities, are very high and, in the case of slender wings, the tangential and axial velocity can reach 2 to 3 times the free stream velocity (Visser and Nelson 1993, and Payne et al. 1986).

The rolling up of the shear layer touches the wing surface which creates an attachment line. This attachment can be traced along the chord in the streamwise direction. The location and extent of this reattachment is a flow dependent phenomenon and varies with the angle of attack. As a consequence, an attached flow is created just beneath the primary vortex and shear layer is then redirected towards the low pressure region near the leading-edge region. This spanwise progression of the attached shear layer is then hindered by an adverse pressure gradient near the leading edge and thereby caused the secondary flow separation. Eventually, the adverse gradient rolls up this separated shear layer in an opposite sense of the primary vortex to form the secondary vortex. Moreover, the jet-like

axial convection of high radial gradients aggravates the interaction among the vortical and boundary layer flow which supplements the formation of the secondary vortex. Figure 2.2 shows the photos of dye and smoke flow visualized leading-edge vortices. This region of opposite sign vorticity spurs the relocation of the primary vortex towards the centerline and away from the wing surface (Payne et al. 1988). In the turbulent regime, the vigorous momentum exchange increases the ability of flow to withstand the adverse pressure gradient and therefore prolongs the primary attachment which results in a smaller secondary vortex compared to the laminar regime. The velocity field across these vortices is also of interest and will be discussed later. A more in-depth review on the leading-edge vortex formation, growth and development can be found in the thesis work of Pereira (2011) and Dogar (2012).

Since the axial velocity profiles across the core are informative in determining the evolution of the leading-edge vortex along the span and pre- and post-breakdown behavior. Both intrusive (see, for example, Visser and Nelson 1993, Payne et al. 1986, and Honkan and Andreopoulos 1997) and non-intrusive measurement methods (see, for example, Ol and Gharib 2003) have been employed to acquire the axial velocity flowfield of the leading-edge vortices. It is known that the leading-edge vortex usually exhibits a strong jet-like flow with a value as high as 3.5 times the free stream velocity (Mitchell and Molton 2002). This strong axial convection is a consequence of the radial equilibrium required for the conservation of momentum augmented by the vortex sheet spiraling around the vortex axis (Earnshaw 1964). The vortex also increases in strength through continuous feeding of vorticity by free shear layer separated from the leading edge, as it travels downstream. The resulting chordwise increase in swirl velocity induces a favorable pressure gradient along the vortex axis.

Visser and Nelson (1993) used a X-wire probe to acquire the velocity distributions for 75°-sweep delta wing at $\alpha = 20°$. They found that the horizontal spread of axial velocity was a good Gaussian fit prior to its breakdown. As the angle of attack increased to 27°, the jet core diffused to an extent of 50% of local semi-span. Their high-frequency time resolved measurements also revealed the unsteadiness of vortical flow even at locations well

upstream of breakdown where it was accompanied by large amplitude velocity fluctuations. The maximum root-mean-square (*rms)* circumferential velocity often exceeded the free stream velocity depending on the angle of attack. These large fluctuations were later found to be a consequence of vortex meandering (Devenport et al. 1996), and Menke and Gursul 1997) rather than the instabilities associated with the separated shear layer (Mitchell et al. 2006). Devenport et al. (1996) further suggested that this phenomenon of vortex meandering or vortex wandering has a connection with freestream turbulence and found its origin in tunnel unsteadiness.

The distribution of vorticity across the vortex is also of prime interest along with the core value and radial derivatives. Numerous investigators hypothesized theories for vortex stability and breakdown based on vorticity distribution and circulation confined within the primary vortex. To date, distinct techniques have been used to study the effect of vorticity on vortex structure which includes references (Nelson and Pelletier 2003, Visser and Nelson 1993, Kegelman and Roos 1990, and Gursul 2004). It is also vital in the determination of vortex strength because the maximum vortex strength, given by maximum swirl ratio, is strongly dependent on local freestream pressure gradient and therefore restraining the ability of flow to move downstream. Vorticity is also important for an existence of stable vortices since it can be considered as a balance between streamwise convection of vorticity and the vorticity generation from the boundary layer, imperious for an existence of stable leading-edge vortex. Conversely, the vortex breakdown can also be seen as a disturbance of vorticity balance due to a reduction in axial convection of vorticity (Green 1995). The ratio between the circumferential and axial velocity, or swirl angle, is an indication of this balance. The preceding discussion underlines the significance of vorticity in detailing the flow structure and acts as a definitive tool to locate or predict vortex breakdown.

A reflective work on vorticity and circulation on a 75°-sweep delta wing has been done by Nelson and Visser (1991) and Visser and Nelson (1993). There was a substantial difference in the value of axial vorticity even for identical geometries and flow conditions, for which a close analysis revealed the sensitivity of vorticity field on the grid spacing. The highest

derived value was reported for the finest grid resolution and vice versa. They also reported that by scaling the radial circulation distribution and vorticity field by local semi-span resulted a self-similar distribution in vorticity in the chordwise direction before the vortex breakdown. Additionally, the distribution of vorticity across this secondary vortex showed similar behavior but it is sensitive to Reynolds number due to its presence in the boundary layer. Finally, in the case of vorticity, likewise, core location can be determined based on peak of axial vorticity or by locating the peak in axial velocity. Note that in theory the core does not necessarily mean the viscous portion of the leading-edge vortex but a relatively small cylindrical region.

Mitchell and Molton (2002) reported the vorticity contours around the leading-edge vortex breakdown location for a 70°-sweep delta at $\alpha = 27°$ for a chord Reynolds number Re = 1.56×10^6 (see Figure 2.3). The data was collected for eleven different chordwise stations within a length of 0.3c and vorticity field is presented for each location by using laser Doppler velocimetry. c is the chord of the delta wing. Prior to the breakdown location (i.e., $(x/c)_{VBD} = 0.65$) the vorticity contours are organized with concentration in the center and had a peak non-dimensional value larger than 200, which subsequently dropped to 140-150 after breakdown ($x/c = 0.74$). They further deduced that the dissipation of vorticity in the breakdown process has no implication on the stationary substructures and pointed towards the existence of convective instabilities near the leading edge. It is noteworthy that the benefit of laser-Doppler-velocimetry measurements made by Mitchell and Molton (2002) in detecting the reverse flow revealed that the abrupt deceleration of core flow to a stagnation point is followed by a zone of recirculation with a considerable increase in vortex size. The expected presence of a wake-like core is witnessed in post breakdown region.

The circulation confined by the primary vortex is imperious for vortex strength correlation and in the calculation of aerodynamic lift force. Circulation is calculated either by computing the line integral of tangential velocity along a closed contour centered about the designated vortex core or by integrating the vorticity over the area under investigation, also known as Stoke's theorem, therefore it can also be seen as vorticity flux. Johari and

Durgin (1998) employed an ultrasonic technique to compute the circulation for a 60°-sweep and a 70°-sweep delta wing at a chord Reynolds number of 1.9×10^5. They found that circulation was measured to grow non-linearly in the chordwise direction for which the breakdown occurs aft of the trailing edge. Conversely, an approximately linear growth is witnessed until the breakdown reached the vicinity of wing apex.

The strength of the primary vortex increases with increase in angle of attack until a sudden disorganization terminates this progression. The post breakdown flow can be characterized by massive dilatation of vortex structure, a profound alteration of velocity field along with large scale fluctuations (Delery 1994). In this process the primary vortex loses its coherence and rapid exchange of momentum results in large scale turbulence. Moreover, the detrimental phenomenon of vortex breakdown is typically characterized by an increase in vortex diameter whereas the non-linear vortex lift is a strong function of vortex size and strength. Note that the leading-edge vortex breakdown is an outcome of cascade of events which are still unanswerable and different theories were formulated. Delery (1994) further suggested that the leading-edge vortex breakdown process is highly dependent on swirl ratio and breakdown occurs when swirl ratio reaches a critical value. The circumstances of breakdown are practically insensitive to Reynolds number and the local turbulent properties but these factors have profound influence on vortex evolution. The onset of vortex breakdown plays an important role in limiting the high lift, high angle of attack performance of the delta wing.

Since the observance of the leading-edge vortex, a substantial amount of research effort has been devoted to thoroughly study the phenomena and mechanisms responsible for the deleterious effect of vortex breakdown on lift generation. Literature survey reveals that the vortex bursting is not solely responsible for the lift deterioration but also incites the detrimental aero elastic effects. In addition, high frequency fluctuations at the breakdown location results in asymmetry flow over a wing and may induce undesirable roll moments. The unsteadiness associated with breakdown is well documented and even involves an out-of-phase oscillation of breakdown points along the vortex axis which results in periodic roll motion, or wing rock (Delery 1994, and Nelson and Pelletier 2003). This self-induced

oscillation adversely affects the maneuvering envelope of combat fighter jets and approach angle of attacks of high speed commercial aircrafts.

In summary, there are many factors which influence the vortex breakdown in relation to wing geometry. Firstly, leading and trailing-edge beveling, it was found that beveling delays the vortex breakdown at the given angle of attack (Jobe 2004). This can also be looked as the leading-edge bluntness, which was widely studied. Moreover the upstream progression of the vortex breakdown is delayed for the round edge leading edge compared to sharp edge wing. Luckring (2004) conducted surface pressure measurements on a 65°-sweep delta wing and revealed that unlike the sharp leading edge, where separation is fixed at apex, blunt edge delayed the shear layer separation to about 30% of the chord. Another geometric factor which influences the vortex breakdown is the thickness-to-chord ratio of the wing model. Observations have been made that wings with higher thickness-to-chord ratio tends to stall earlier than the thinner wings (Lowson and Riley 1995).

It is well known that the flow over slender delta wings is insensitive to Reynolds number as long as the wing leading-edge remains sharp, so does the vortex breakdown. Figure 2.4 summarizes the typical leading-edge vortex breakdown location obtained via flow visualization by researchers elsewhere. As can be seen there was a substantial scatter in vortex breakdown locations over a same sweep delta wing but under different tunnel and flow conditions. These discrepancies may be attributed to wind tunnel factors, i.e. wall effects and buoyancy, or different flow visualization techniques, support interference, model deformation (built-in yaw and roll), and the unsteady nature of breakdown location (Wentz and Kohlman 1971). A data collection presented by Jobe (2004) on a 65°-sweep delta wing summarizes the sensitivity of breakdown locations to different parameters. It was evident that the thickness-to-chord (t/c) ratio of the wing model, and the visualization techniques have profound effect on vortex breakdown location. The unsteady nature of vortex characteristics was validated by Gursul (2005). The data has been acquired for a range of sweep angles (Λ = 60° to 80°) for Re = 2.5×10^4 to 1×10^5. The acquired data showed large amplitude velocity fluctuations, along with variations in breakdown

locations. A fluctuation of about 10% of chord length was reported in the case of slender delta wings.

Note that Lowson and Riley (1995) also examined the reasons for this variation in vortex breakdown location from different investigations on delta wings of equivalent sweep, by reproducing the similar model and flow condition. It was evident from the recorded data that vortex breakdown was also influenced by support interference, wind tunnel factors, differing flow visualization methods and Reynolds numbers. Additionally, effects due to geometry variation were found to far outweigh the interference induced by aforementioned factors. Therefore, neither there is an agreed location of vortex breakdown nor any evitable dependence on wing sweep or angle of attack.

2.1.2 Aerodynamic characteristics

Research into aerodynamic characteristics of delta wings is also quite extensive. This includes experimental, theoretical and numerical investigations. Unlike the classical potential lift, vortex lift is a non-linear phenomenon and often accompanied by high frequency of unsteadiness. After the vortex breakdown, this non-linear vortex lift diminishes and leads to wing stall conditions. Soltani and Bragg (1990) inferred that non-linear vortex lift and the movement of the burst point on the wing, due to the flow unsteadiness (Menke et al. 1999), are related to changes in measured lift-curve slope. Likewise, increasing the sweep angle decreases the lift curve slope because for the given angle of attack the circulation decreases with increasing sweep angle (Nelson and Pelletier 2003).

Figure 2.5 presents the lift curve for various delta wings of different sweep angles. It was observable that at low angle of attack, that, regardless of sweep angle, the lift curves are linear whereas on increasing the angle of attack, the contribution of the non-linear vortex-lift increases and so do the non-linearity in the lift curve. The presence of breakdown on the wing led to a reduction in lift curve slope but the lift continued to increase until the maximum lift coefficient is achieved and the wing stalls. It is to be noted that this phenomenon is limited to wings with low and moderate sweep angle ($\Lambda < 70°$). Also, at a

given angle of attack the strength of leading-edge vortices increases with decreasing sweep angle. Consequently, higher normal force coefficient is witnessed for the higher aspect ratio delta wings.

It should be noted that before 1970, theoretical lift prediction theories are entirely based on attached flow assumption which subsequently fails for delta wing planform. Polhamus (1971) estimated the vortex-lift based on leading-edge suction analogy and calculated total lift by augmenting the potential and vortex lift components. The correlation only applies to thin wing sections with no camber and twist. Moreover, there would be no leading-edge suction or the leading edge should be sufficiently sharp to fix the shear layer separation point. Given these assumptions, the total lift can approximated as:

$$C_L = K_P \sin\alpha \cos^2\alpha + K_V \sin^2\alpha \cos\alpha \tag{2.1}$$

where the value of K_P and K_V depends on wing geometry. K_p and K_v are the potential-flow lift constant and vortex-lift constant, respectively. Considering the incompressible flow (M < 0.3), with increasing aspect ratio (decreasing sweep angle), a slight increase in value of K_V asymptotically levels at π. On the other hand, K_P increases rapidly with wing aspect ratio because it is the lift-curve slope at zero lift. Polhamus theoretical approximations were in total agreement with experimental results only before the breakdown reaches the trailing-edge. Since the analogy is based on potential flow leading-edge suction analogy which expects flow re-attachment inboard of the vortex, therefore the deviance from experimental values was observed for higher angle of attacks. Polhamus also cautioned that the lift prediction method has tendency to over-predict the vortex lift for moderate and low sweep wings because the vortices over such wings cannot provide full suction courtesy of their orientation with respect to the trailing-edge. On the other hand, the Polhamus theory is in full agreement with experimental results acquired for high sweep delta wings because lesser area is required for full vortex lift. Figure 2.6 shows the vortex lift and potential-flow lift components of a 75°-sweep delta wing.

2.2 Reverse delta wing

As mentioned in the introduction, aircraft flying close to the ground can experience additional lift and less lift-induced drag. Under the ground effects, the dividing streamline and the stagnation point generally move down for positive angle of attack, causing a reduction in velocity and an increase in pressure under the airfoil. For very small clearances, the air tends to stagnate under the airfoil, which gives the highest possible pressure called ram pressure. The WIG (wing-in-ground effect) craft are especially designed to take advantage of the benefit of ground effect; that is, a considerably increased lift-to-drag ratio or aerodynamic efficiency compared to the craft flying out of the ground effect. Moreover, the WIG craft utilizes the dynamic air cushion, created by the forward flight speed of the WIG craft, as opposed to the hovercraft's static air cushion. Two representative types of WIG craft have been designed and constructed: the Russian Ekranoplans, which have a straight wing with a low aspect ratio (generally between 2 and 3), and the Lippisch-type WIG craft, which employ a reverse delta wing planform with strong anhedral. The Ekranoplans, however, suffer poor longitudinal stability and are sensitive to the water surface conditions which limit their use in rough seas. Excellent reviews on the WIG craft, especially the Ekranoplan-type WIG craft, are given by Ollila (1980), Halloran and O'Meara (1999), and Rozhdestvensky (2006). Extensive investigations have been conducted to characterize the aerodynamics of rectanguler NACA wings in ground effect (see, for example, Tomaru and Kohama 1990, Moore et al. 2002, and Ahmed et al. 2005 and 2007). The ground effects on the F1 race car front wing (i.e., an inverted wing in ground effect) have also been investigated vigorously by Zerihan and Zhang (2000 and 2001), Zhang and Zerihan (2003a and 2003b), and Roberts et al. (2016). It is noteworthy that the WIG craft concept has also been applied to the development of the so-called aero-levitation electric vehicles (AVEs) for ground transportation by Cho et al. (2001) and Han et al. (2005).

Ahmed et al. (2005 and 2007) investigated the aerodynamics and surface pressure distribution along a NACA 4412 airfoil for ground clearance from 5% of chord to 100% chord at a chord Reynolds number $Re = 3 \times 10^5$. A loss of upper surface suction was

recorded as the airfoil approached the ground for all the angles of attack α. They also found that for $\alpha \leq 4°$, the lift decreased with reducing ground clearance, whereas for higher α, the lift increased due to a higher pressure on the lower surface. Meanwhile, the drag was higher close to the ground for all α tested mainly due to the modification of the lower surface pressure distribution. The lift force was also found to decrease at low α as the ground clearance decreased below 10% of the chord, as a result of the existence of a converging-diverging flow passage between the airfoil's bottom surface and the ground plane, which culminates in a suction effect. They further observed that the pressure drag decreased with reducing ground clearance if there was a higher contribution of the modified upper surface suction in the direction opposite to that of drag; otherwise the pressure drag was higher at low ground clearances due to the higher contribution to the pressure drag mainly from the lower surface.

Zerihan and Zhang (2000 and 2001) and Zhang and Zerihan (2003a and 2003b) reported that for a F1 race car front wing (i.e., an inverted wing) positioned at large heights, the downforce increases asymmetrically with a reduction in height. The maximum downforce is dictated by gains in downforce from lower surface suction increases and losses in downforce caused by upper pressure and lower pressure surface suction losses, with a reduction in height. For the high flap angle there is a sharp reduction just beyond the maximum, mainly because of the boundary layer separating, and a resultant loss of circulation on the main element. Roberts et al. (2016) further investigated the influence of Reynolds number on the aerodynamic characteristics of F1 racing car front wings of varying complexity through wind-tunnel experimentation. The single-element wing showed significant Reynolds-number dependency, with up to 320% and 35% difference in downforce and drag, respectively, for $Re = 0.81 \times 10^5$. Across the same test range the multi-element configuration of the same wing and the F1 wing displayed less than 6% difference in downforce and drag. Surface-flow visualization conducted at various Reynolds numbers and ground clearance showed that the separation bubble that forms on the suction surface of the wing changes in both size and location. As the Reynolds number decreased the bubble moved upstream and increased in size, whilst reducing ground clearance caused the bubble to move upstream and decrease in size.

On the other hand, the reverse, or inverted, delta wing planform with strong anhedral, employed by Dr. Alexander Lippisch in 1963 in the Collins X-112 (which later evolved into RFB X-114 and, most recently, WSH-500), has proved to produce stable and safe flight in ground effect. The Lippisch-type WIG craft have therefore become very popular lately. The employment of the reverse delta wing platform also renders the small trailing tip of the wing immerses when the craft is in the water, which gives a much less drag than a conventional delta wing platform in which the whole trailing edge of the wing would be in the water. Meanwhile, the anhedral creates makes an immediate "air tunnel" under the wing that gives lift as soon a forward motion begins during takeoff (Kocivar 1977). It is, however, noteworthy that despite the extensive employment of the reverse delta wing in the Lippisch-type WIG craft, the aerodynamic and vortex flowfield characteristics of the reverse delta wing, with and without ground effects, are scarce. It is the purpose of this study to investigate the effect of the anhedral on the aerodynamic and vortex flow of a reverse delta wing. A brief review of the aerodynamics and vortices produced by a reverse delta wing, both in and out of ground effect is given below. Note also that, surprisingly enough, the impact of the ground effect on the aerodynamics and vortex structure of regular delta wings with ground proximity are also limited (see, for example, Que et al. 2015).

Que et al. (2015) numerically investigated the influence of the ground effect on the aerodynamics of a 65°-sweep delta wing at $\alpha = 20°$. The chord Reynolds number Re was fixed at 1.2×10^7. The flight height was varied from high altitude to the ground. The lift, drag, and nose-down pitching moment of the slender delta wing were found to increase with decreasing flight height, mainly as a result of flowfield variation in the windward side of the wing. They also concluded that in ground effect the pressure under the delta wing increases due to the "ramping" effect, and that the strength of the leading-edge vortex enhances before breakdown. The vortex breakdown is, however, promoted due to the increased adverse pressure gradient. Investigations, including the aerodynamic loading information, covering a wide range of angle of attack are still needed.

Gerhardt (1996) claimed that a reverse delta wing, which also resembles forward-swept-wing aircraft, can produce some certain favorable aerodynamic characteristics. The reverse delta wing design was found to generate additional lift at low speeds, reducing power requirements and therefore noise, during environmentally crucial takeoff and landing phases. Also, in contrast to the strong pressure gradients occur near the leading edges of the regular delta wing where they cause unfavorable conditions for boundary layer stability, the strong pressure gradients are confined to the trailing edge regions of the reverse delta wing where they do not interfere with boundary development. Spanwise pressure gradients which cause boundary layer crossflow are likewise concentrated near the leading edge of the delta wing and near the receding trailing edge of the reverse delta wing. As a result, crossflow and attachment line instabilities (the primary modes of transition on swept wings) are thus absent on the reverse delta wing. More importantly, the absence of pressure gradients near the leading edge and the favorable gradients downstream provide the reverse delta wing with ideal conditions for achieving natural laminar flow, which extends generally spanwise across the wing and located at a fraction of the chord of the wing from the leading edge. The achievement of laminar boundary layers poses a significant step in reducing aerodynamic drag and thereby increasing the cruise performance of commercial and military aircraft. Various natural laminar flow control techniques have also been proposed by Gerhardt.

Musaj and Prince (2008) conducted the ground-effect analysis (both numerically and experimentally) of a W-shaped leading edge, reversed delta planform wing (i.e., the AVCEN Jetpot air-taxi wing; see figure 2.7), having a NACA 2412 section throughout at $Re = 3 \times 10^5$. The ground effect was found to increase slightly the magnitude of the leading-edge suction region on the upper surface of the wing. They also found that there was an increase in the lift and hence the lift-to-drag ratio with decreasing ground clearance. A lift-to-drag ratio of 30 were observed for $h/b = 0.09$ (where h is the ground clearance and b is wing span), which doubled the values of those with no ground effect or in free flight condition. No major difference in the drag coefficient was noticed as the ground was approached. Additionally, the vortical flow emanating from the wing was found to increase in strength in the presence of the ground. Flow separation was, however, more pronounced with

decreasing ground clearance. They also reported that outward tip vortex movements (as opposed to the inward movement of the RDW in free flight) were observed with the decreasing ground height, demonstrating an increasing effective wing aspect ratio. No other archived publications on reverse delta wings with ground effect, to the authors' best knowledge, were available. In short, regardless of the improved performance such as increased lift-to-drag (L/D) ratio, improved stall capability, and enhanced short take-off and landing (STOL) potential, the vortex formation and aerodynamics of the reverse delta wing with no ground effects are still not clear.

Recently, Altaf et al. (2011) investigated the vortex structure and characteristics of a 75°-sweep reverse delta wing in a free stream by using particle image velocimetry and force balance measurements for angles of attack α = 5°, 10°, 15° and 20° at two fixed streamwise positions (with x/c = 1.359 and 3.418, where c is the chord) for Re = 3.82×10^5. Computational fluid dynamics (CFD) simulation of the streamlines (see figure 2.8), velocity vectors, and surface pressure contours was also carried out. They reported that the reverse delta wing exhibited a lower magnitude of tangential velocity, circulation, and vorticity than the regular delta wing counterpart, and that the reverse delta wing also had a lower lift and drag coefficient than the delta wing while an improved lift-to-drag ratio than the delta wing was observed. Despite the interesting findings reported by Altaf et al., detailed streamwise reverse-delta-wing vortex flow measurements and the physical mechanisms responsible for the observed reverse-delta-wing vortex structure and aerodynamic characteristics were not reported.

Most recently, the reverse delta wings, of different slendernesses Λ, root chords c_r and deflections δ, were employed in the control of the wingtip vortex generated by a rectangular NACA 0012 wing at Re = 3.45×10^5 by Lee and Su (2012) and Lee and Choi (2015). Figure 2.9 depicts the wing models with tip-mounted reverse half-delta wings (HDWs) employed by Lee and Su (2012) and Lee and Choi (2015). These investigators found that, regardless of its root chord and sweep angle, the tip-mounted reverse half-delta wings always caused a rapid diffusion and breakdown of the wingtip vortex. The degree of diffusion was, however, found to increase with decreasing Λ and c_r. A unique double-

vortex pattern also exhibited downstream of the $c_r \leq 50\%c$ HDW wings. The vortex produced by the small-chord half-delta wing interacted with the vortex from the rectangular NACA 0012 wing, causing both vortices to break down, which gave the benefit of a reduced lift-induced drag. The interaction and merging of the double vortex was expedited by upward HDW deflection. They also found that the full-chord reverse delta wing generated a lower lift and drag in comparison to the regular full delta wing. The leading-edge vortices were, however, found to be more concentrated and had a higher circulation and peak tangential velocity than the RDW vortex. In short, in addition to the practical WIG craft application of the reverse delta wing, the reverse delta wing can also serve as a wingtip vortex control scheme. The reverse delta wing can also have potential application in micro aerial vehicles (MAVs). In summary, the current understanding of the reverse delta wing, which is largely based on assumption and limited experiments, therefore demands further study.

It is, however, noteworthy that the control of the tip vortex generated by a rectangular NACA 0012 wing via tip-mounted half-delta wings (HDWs) was first investigated experimentally at $Re = 2.45 \times 10^5$ by Lee and Pereira (2013). Their results show that the addition of the tip mounted regular HDW consistently led to a diffused tip vortex. The degree of diffusion was, however, found to increase with decreasing sweep angle and root chord of the reverse half-delta wing. The tip vortex generated behind a rectangular NACA 0012 wing was greatly diffused and enlarged by a tip-mounted 65°-sweep half-delta wing (HDW), as a result of the breakdown of the HDW vortex developed on the upper surface of the half-delta wing. The HDW tip vortex control concept was inspired by the pioneering work of Nikolic (2005) in which the half delta wing was attempted to improve the wing lift generating capability. The lift increment and also the lift-curve slope can be further enhanced by increasing the deflection the half delta wing, relative to the main wing chord line. Lee and Pereira further noticed that, in addition to the observed changes in the size and strength of the HDW-wing tip vortex, the lowered vorticity level also led to a much reduced lift-induced drag coefficient C_{Di} ($= D_i/\frac{1}{2}\rho_\infty u_\infty^2 S$ where S is the wing surface area). The lift-induced drag D_i was computed by using the Maskell wake integral model (Maskell 1976, Kusunose 1997, Birch and Lee 2004).

$$D_i = \tfrac{1}{2}\rho_\infty \iint_{S_\xi} \psi\zeta \, dy\, dz - \tfrac{1}{2}\rho_\infty \iint_{S_1} \varphi\sigma \, dy\, dz - \tfrac{1}{2}\rho_\infty \iint (1 - M_\infty^2)(\Delta u)^2 \, dy\, dz \qquad (2.2)$$

where ζ (= $\partial v/\partial x - \partial u/\partial y$) is obtained from *vw*-crossflow measurements, $\psi(y,z)$ and $\phi(y,z)$ are stream function and velocity potential, and $\sigma = \partial v/\partial y + \partial w/\partial z$. The reduced lift-induced drag coefficient also translates into a smaller drag, especially at high lift force range, compared to the baseline wing at the same lift condition. Together with the HDW-induced lift increment, the zero-deflection slender full-chord HDW was therefore capable of producing the best lift-to-drag ratio improvement, compared to the baseline wing, among all the deflections tested (for $-10° \le \delta \le +15°$). This HDW tip vortex control concept is, however, shadowed by the undesired HDW-induced increase in wing weight and bending moment. A 13.4% and 41.8% increase in the total wing surface area and aspect ratio compared to the baseline wing, respectively, for the 65°-sweep HDW wing were produced. Figure 2.10(a)-(d) show the typical wingtip vortex development along the tip and in the near wake behind a NACA 0012 wing equipped with tip-mounted half delta wings (HDWs), of different root chords (i.e., full-size and small-size). The effectiveness of the passive control of the wingtip vortex through the use of tip-mounted reverse half-delta wings can be clearly seen. A comparison between the HDW and rake wingtips currently used can be made. The rake wingtips currently installed on certain Boeing planes have a sweeping angle $\Lambda = 57°$ according to the Boeing patent while the sweeping angle used in the above mentioned HDW studies were $\Lambda = 50°$ and 65°. Furthermore, the rake wingtips are blended to the main wing while the HDW are just flat plates. The main goal of both devices, however, are similar.

In summary, these investigators found that, regardless of the size of its root chord and sweep angle, the tip-mounted reverse half-delta wings always caused a rapid diffusion and the breakdown of the wingtip vortex, suggesting a potential alternative for wingtip vortex wake alleviation. The vortex produced by the small half-delta wing interacted with the vortex from the regular NACA 0012 wing, causing both vortices to break down, which gave the benefit of reduced lift-induced drag. They also found that the full reverse delta wing, however, generated a lower lift and drag in comparison to the conventional full delta wing. The leading-edge vortices of a regular delta wing were, however, found to be more

concentrated and had a higher circulation and peak tangential velocity than the reverse-delta-wing vortex. It should be noted that despite the observed drag reduction, the potential application of the reverse delta wing was overshadowed by its inferior lift generation capability. Physical mechanisms responsible for the aerodynamic behavior and the vortex flow characteristics of the reverse delta wing remained unclear.

2.3 Objectives

The objectives of this thesis work were to investigate the aerodynamic characteristics, such as the lift and drag coefficient behaviors, and the vortex flow structure, such as the vorticity and circulation behaviors, along x/c = 0.1 to 1.5 at different angles of attack generated by a reverse delta wing in a free stream in both wind and water tunnels. To the author's best knowledge, there are no research work, at least from the archived publication point of view, conducted by researchers elsewhere. Both slender (i.e., with a sweep angle $\Lambda > 55°$) and non-slender (i.e., with a sweep angle $\Lambda < 55°$) reverse delta wings were investigated. The results were also compared to a regular delta wing of the sweep angle. Special emphasis were placed on the measurement and characterization of the aerodynamic loadings of the reverse delta wing through the use of a two-component force balance in the *J. A. Bombardier* wind tunnel in the Aerodynamics Laboratory in the Department of Mechanical Engineering at McGill University, and also the vortex flow structure by using particle image velocimetry in conjunction with dye-injection and smoke-wire flow visualizations. Passive control technique employing Gurney flaplike stripes was also used to enhance the lift generation of the reverse delta wing. The main objective of this research work is divided into the following three parts. It should be noted that the present out-of-ground effect aerodynamics and vortex flowfield measurements should serve as benchmark data to the future study of the reverse delta wing in ground effect.

2.3.1 Aerodynamic and vortex flow characteristics of a slender reverse delta wing

The objective of this part of study was to investigate the streamwise structure and characteristics of the vortex generated by a 65°-sweep reverse delta wing in a water tunnel by using particle image velocimetry (PIV) for $0.1 \leq x/c \leq 1.5$ at $\alpha = 4°$ to 30° with Re =

11,000. The aerodynamic characteristics of the reverse delta wing were investigated first by using a two-component force balance in the *J. A. Bombardier* wind tunnel and were used as an experimental guideline for the vortex flow measurements. The reverse delta wing results were also compared to the regular delta wing data. Smoke-wire and dye-injection flow visualizations were also performed to supplement the particle-image-velocimetry measurements. The leading-edge vortex breakdown location occurred on the regular delta wing was also acquired. The variation of the critical leading-edge vortex flow parameters with the streamwise distance x/c was also discussed. The PIV *vw*-crossflow measurements were also used to compute the total lift coefficient via the Kutta-Joukowski theorem. Physical mechanisms responsible for the observed RDW vortex flow behavior and aerodynamic characteristics were also discussed.

2.3.2 Vortex flow and lift generation of a non-slender reverse delta wing

The objective of this part of study was to extend the previous 65°-sweep slender reverse-delta-wing investigation in Section 2.3.1 to a non-slender reverse delta wing with a sweep angle of 50° in the water tunnel at McGill University by using particle image velocimetry in conjunction with a one-axis force balance and flow visualizations. Special emphasis was placed on the characterization of the streamwise development of the vortex for $0.1 \leq x/c \leq 1.5$ at $\alpha = 4°$ to 18°. The vortex flow of the non-slender regular delta wing was also investigated to serve as a comparison. Physical mechanisms responsible for the observed reverse-delta-wing vortex flow behavior and lift generation of the non-slender reverse delta wing were then discussed.

2.3.3 Passive control of lift and vortex flow of a reverse delta wing via Gurney flaplike strips

In order to enhance the lift generation of the reverse delta wing, Gurney flaplike strips, of different heights and configurations, were considered. The Gurney flaplike strips were placed in three positions: 1) leading-edge upper surface, 2) leading-edge lower surface, and 3) along both trailing edges' lower surfaces. The objective of this part was to investigate the

impact of Gurney flaplike side-edge strips and leading-edge strips, of different heights and configurations, on the aerodynamic loads of a reverse delta wing through wind-tunnel force-balance measurements. The corresponding vortical flowfield generated by the reverse delta wing with Gurney flaplike strips was also examined by using particle image velocimetry. Special emphasis was placed on the impact of these strips on the streamwise growth and development of the RDW vortex at different angles of attack. Physical mechanisms responsible for the experimental observations were also discussed.

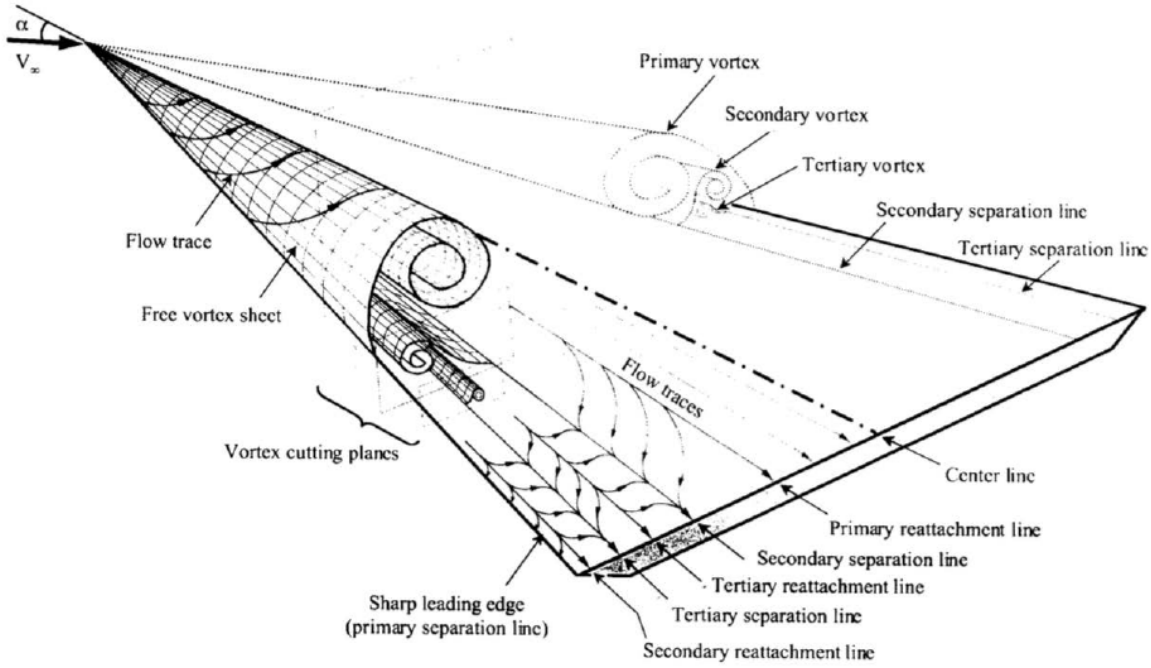

Figure 2.1 Detailed leading-edge vortex flow structure over a sharp-edged delta wing at high angle of attack (Benmeddour et al. 2009).

(a)

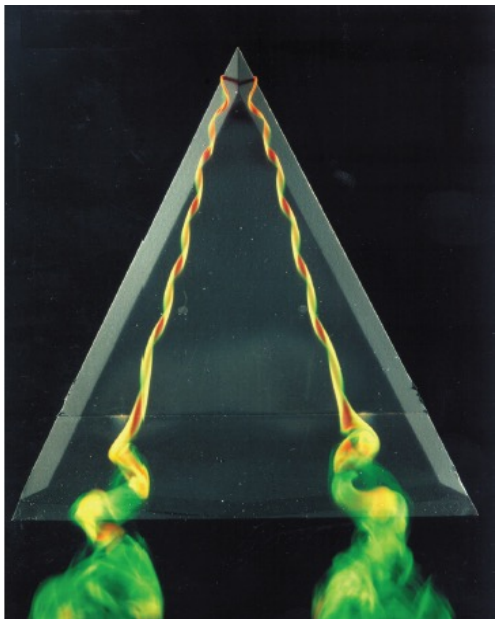

(b)

Figure 2.2 Photos of dye-flow and smoke-flow visualized leading-edge vortices and their breakdown over a delta wing (Delery 1994).

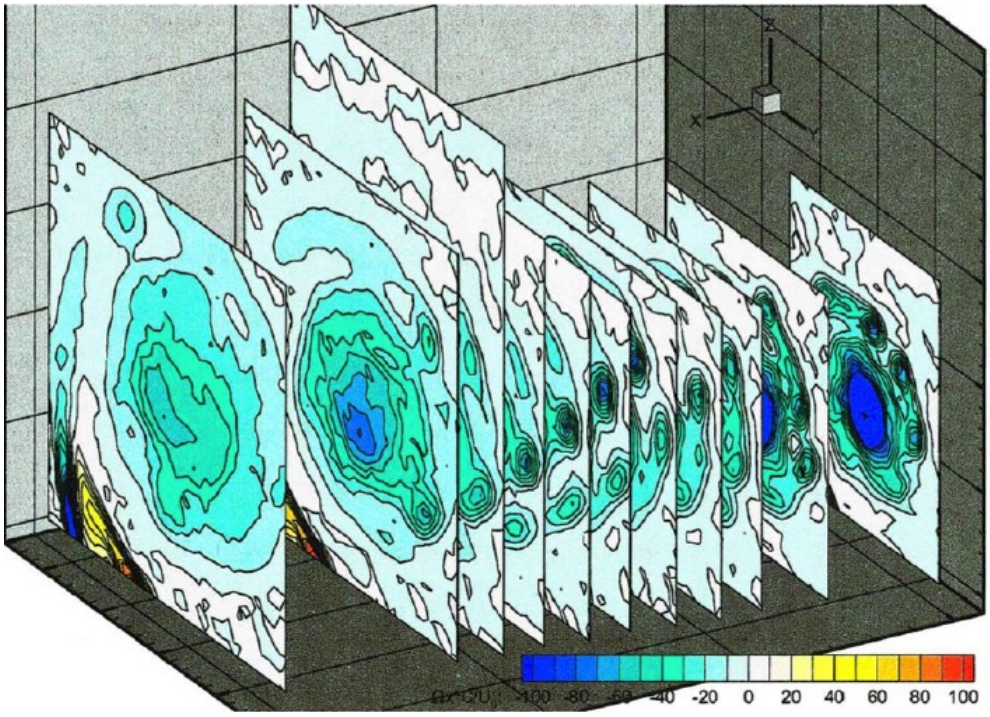

Figure 2.3 Streamwise vorticity distribution of a 70°-sweep delta wing at α = 27° (Mitchell and Molton 2002).

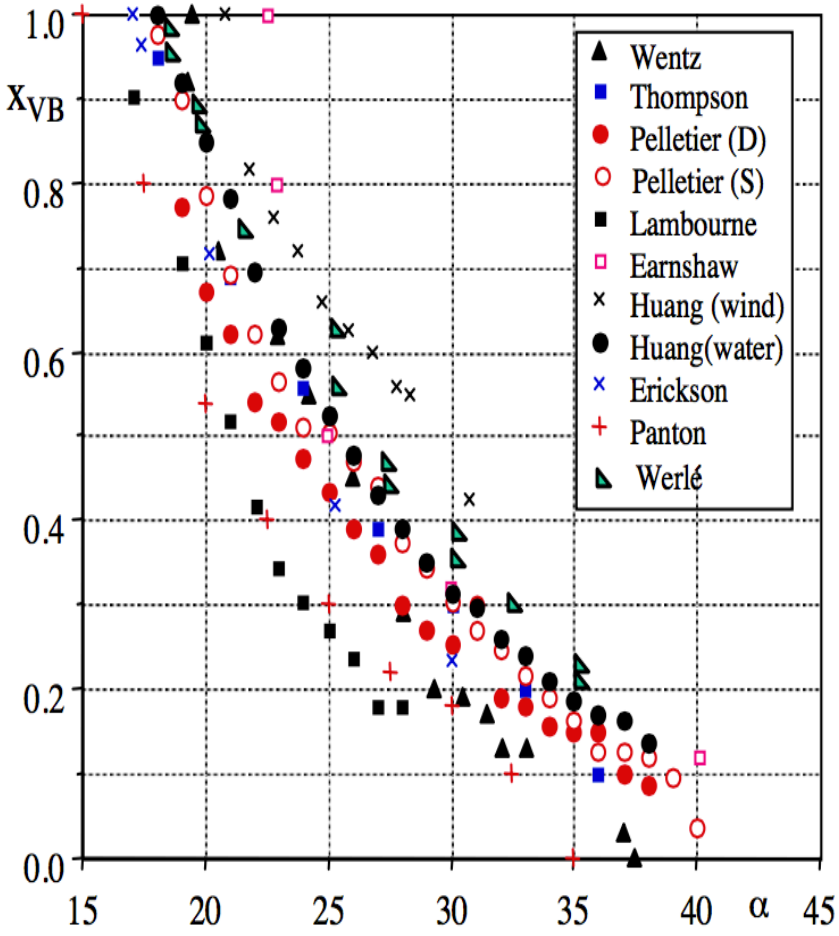

Figure 2.4 Leading-edge vortex breakdown locations over slender delta wings (Jobe 2004).

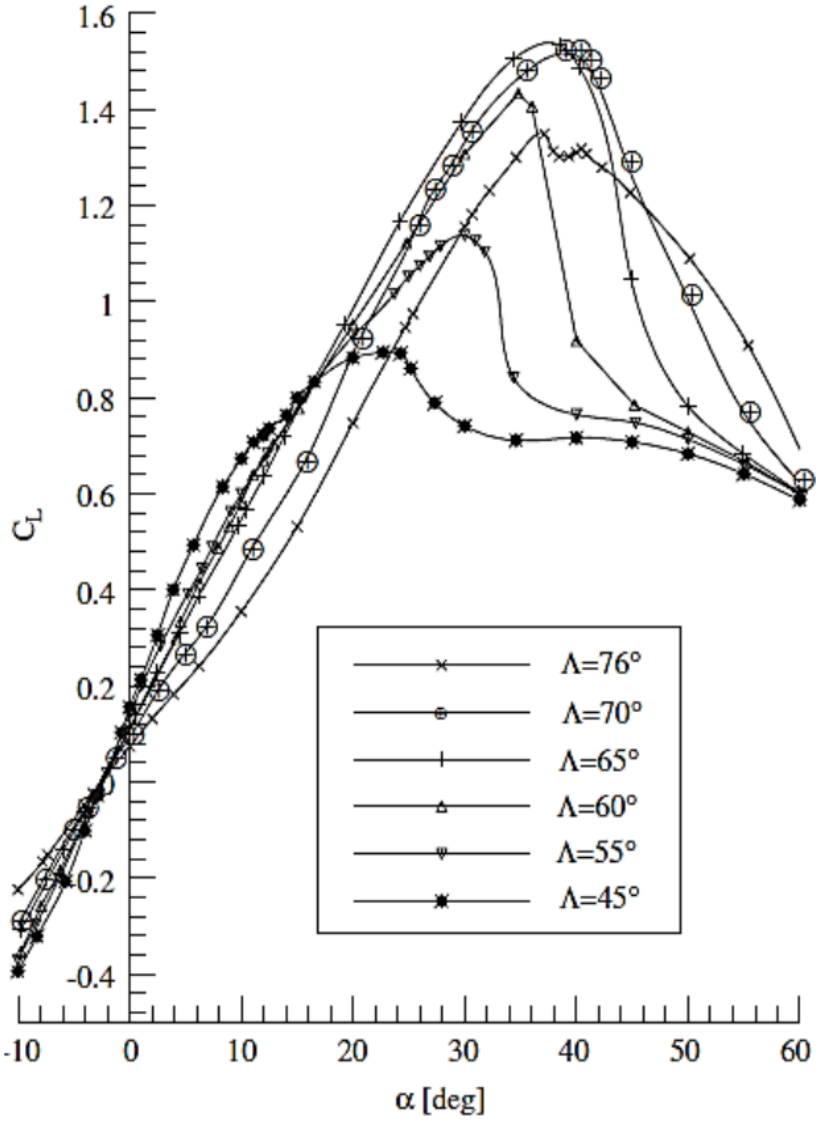

Figure 2.5 Lift characteristics of delta wings of various sweep angles (Soltani and Bragg 1990).

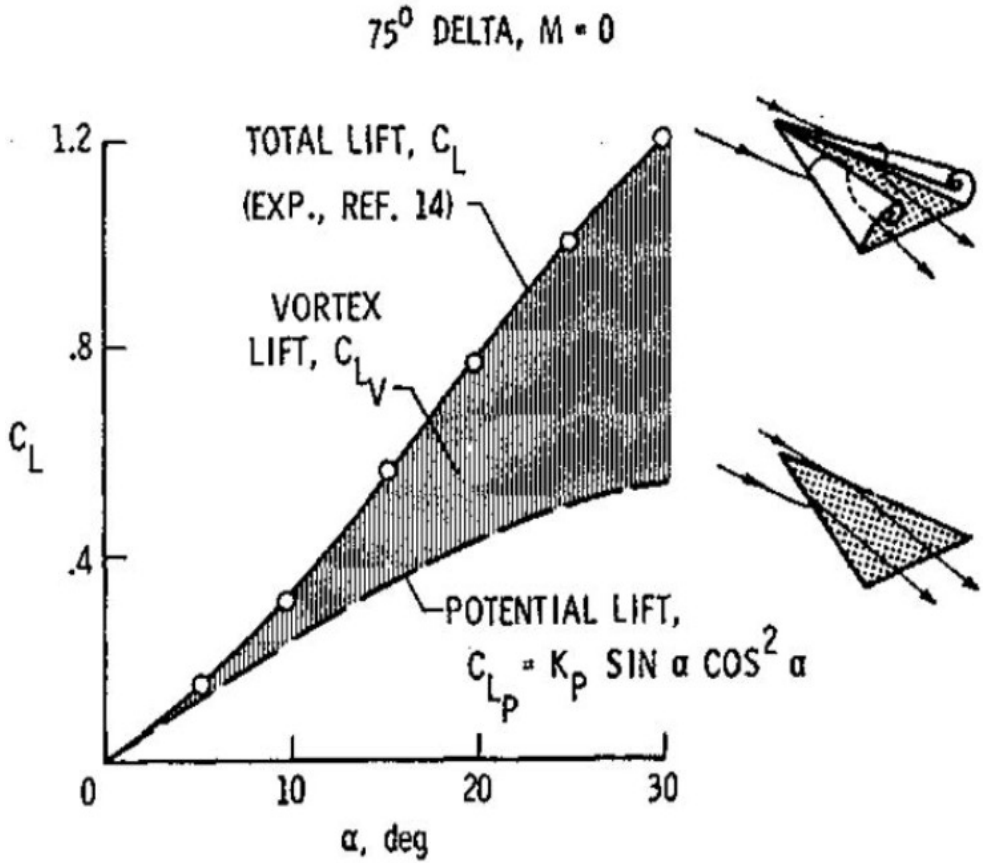

Figure 2.6 C_L components of a 75°-sweep delta wing.

(a)

(b)

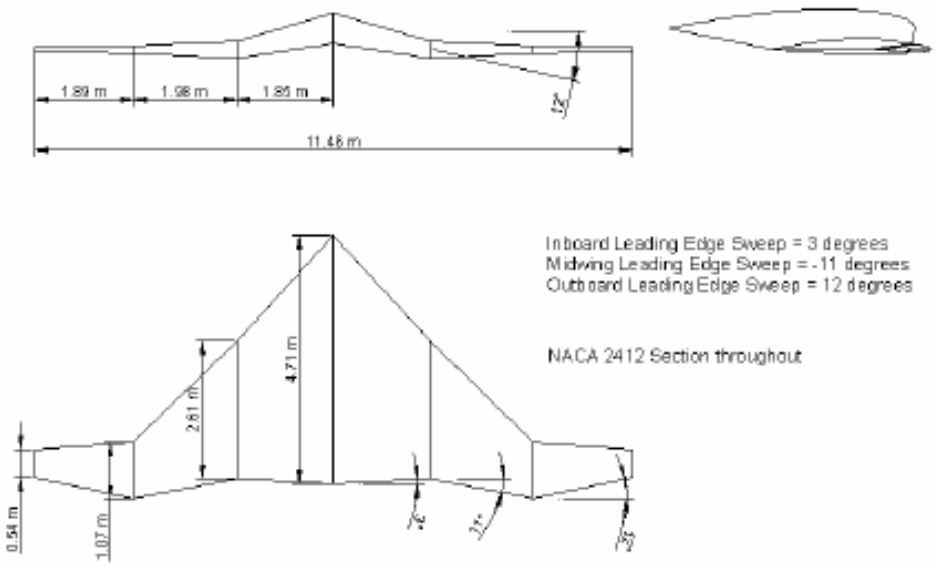

Figure 2.7 (a) Photo of Avcen Jetpot air taxi and (b) schematics of the wing model (Musaj and Prince 2008).

(a)

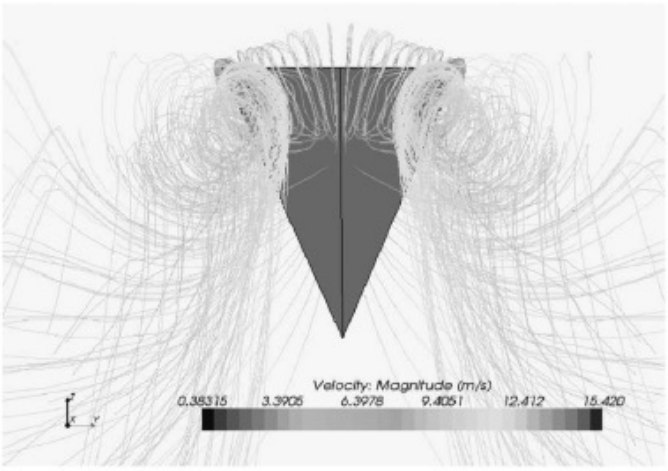

(b)

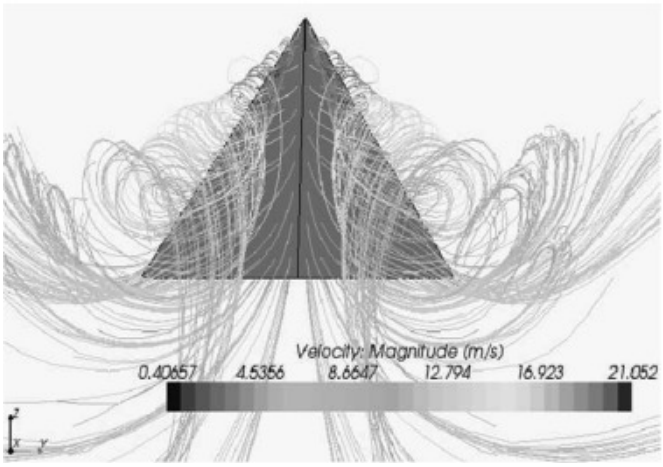

Figure 2.8 CFD simulation of the streamlines over 75°-sweep (a) reverse delta wing and (b) delta wing at $\alpha = 30°$ for $Re = 3.82 \times 10^5$ (Altaf et al. 2010).

(a)

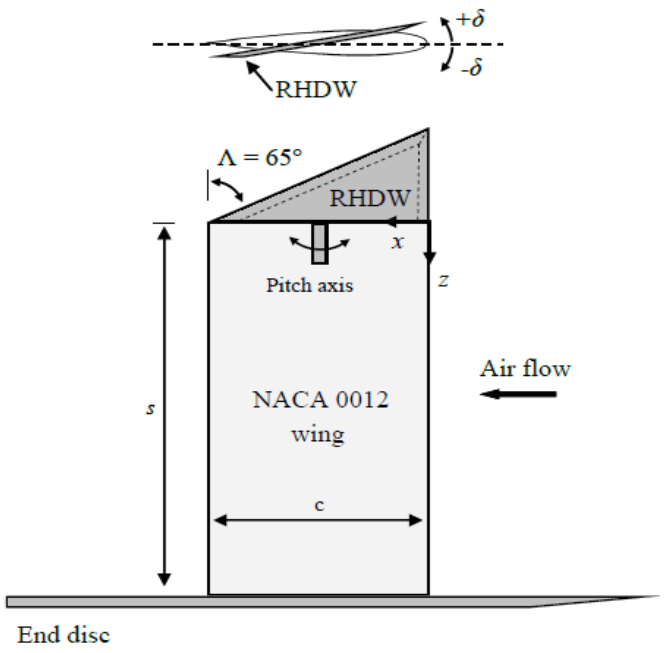

(b)

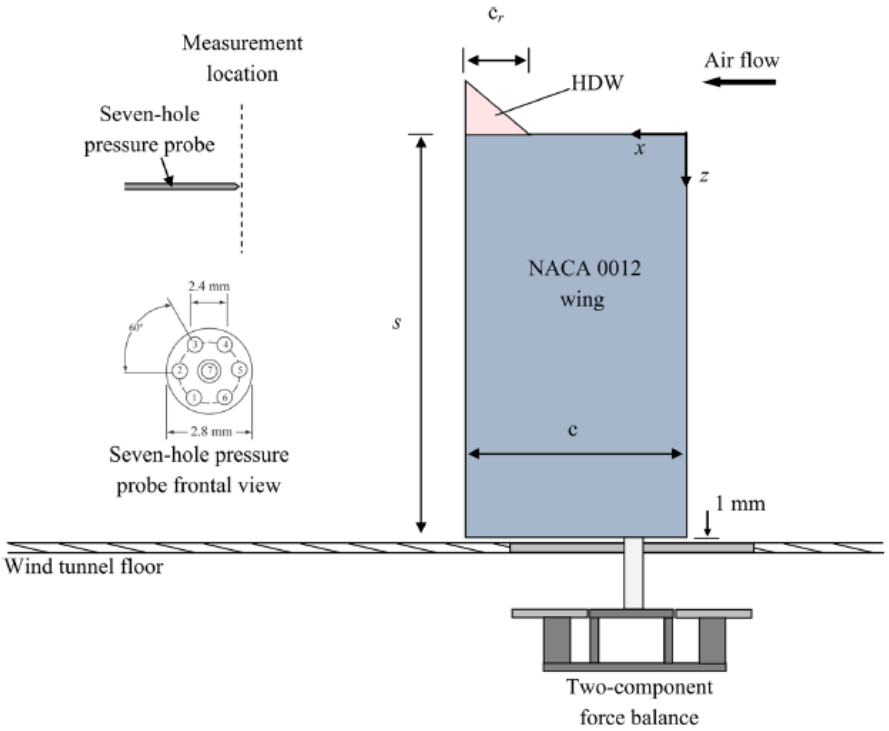

Figure 2.9 Schematic diagrams of the deflected half delta wing test setup. (a) Lee and Su (2012), and (b) Lee and Choi (2015).

(a)

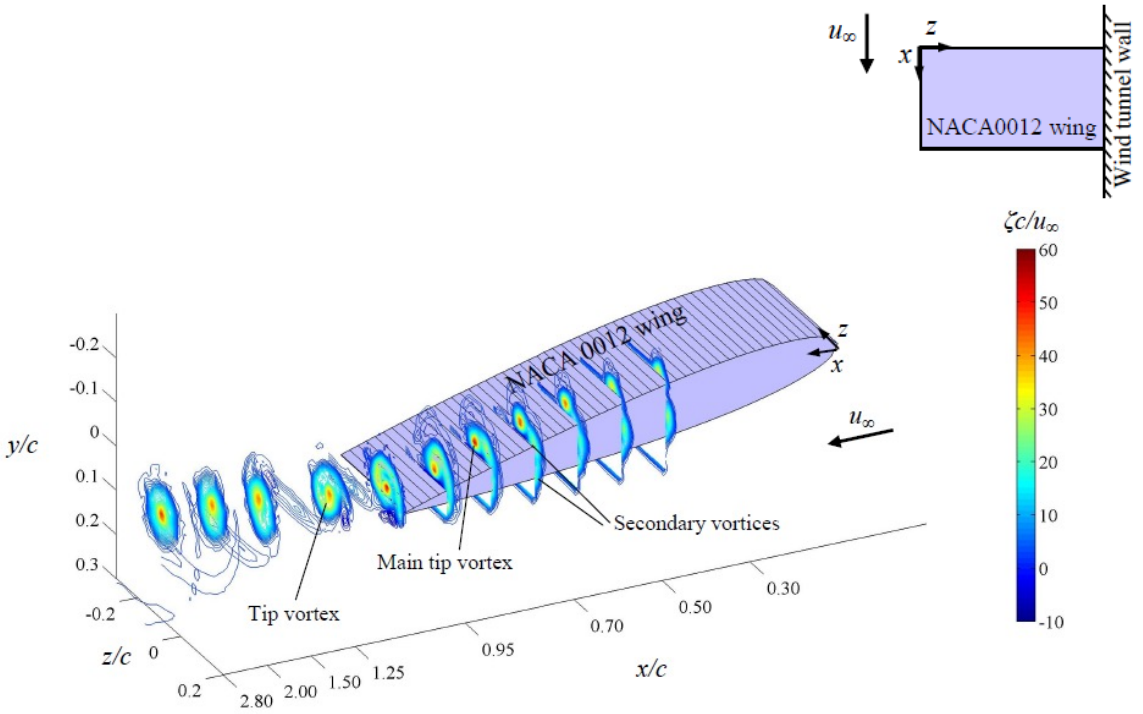

(b)

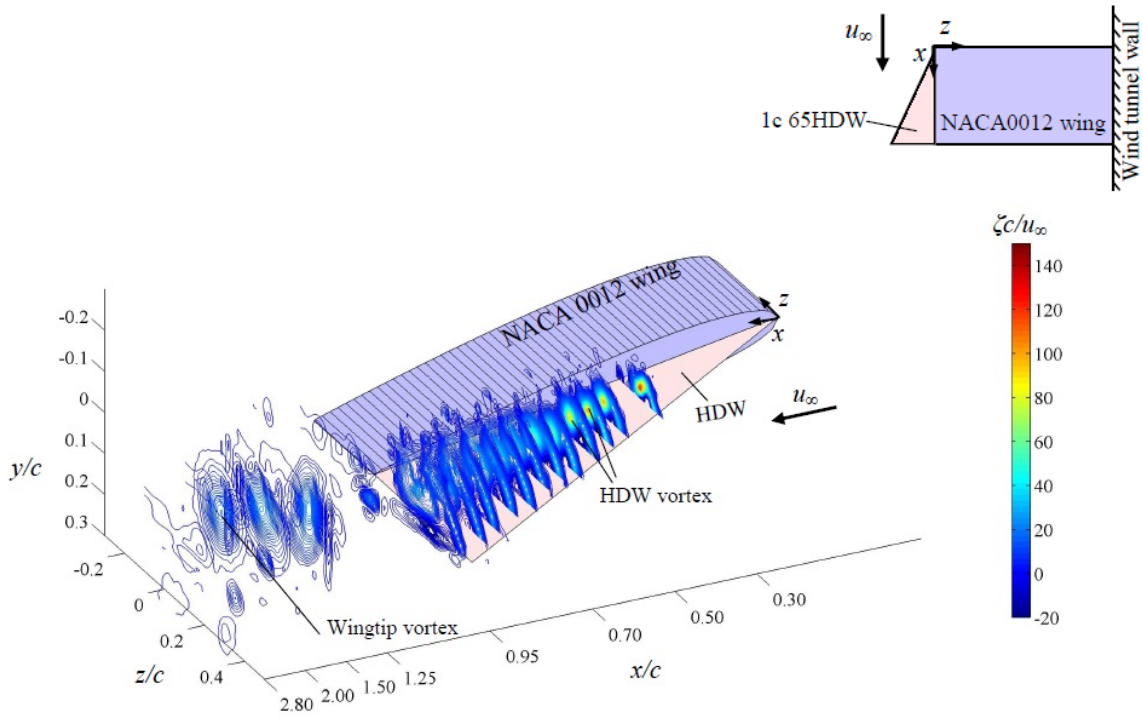

Figure 2.10 Typical wingtip vortex development along the tip and in the near wake behind the NACA 0012 wing with tip-mounted full-size and small-size half-delta wings.

(c)

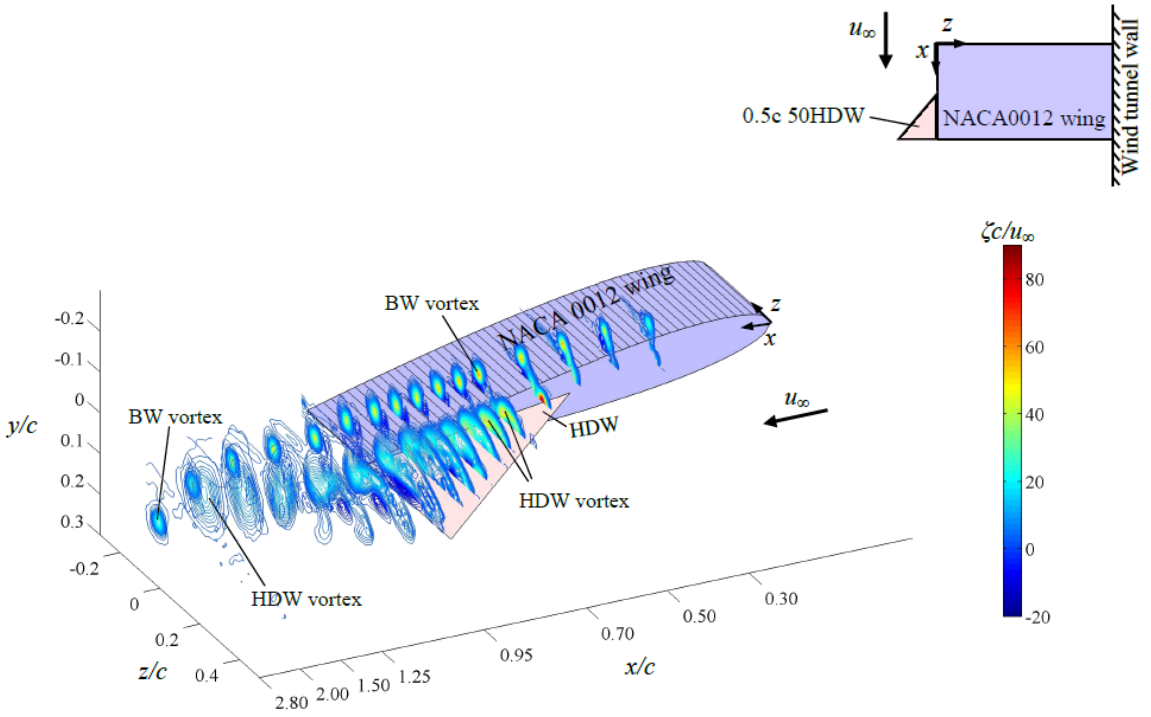

(d)

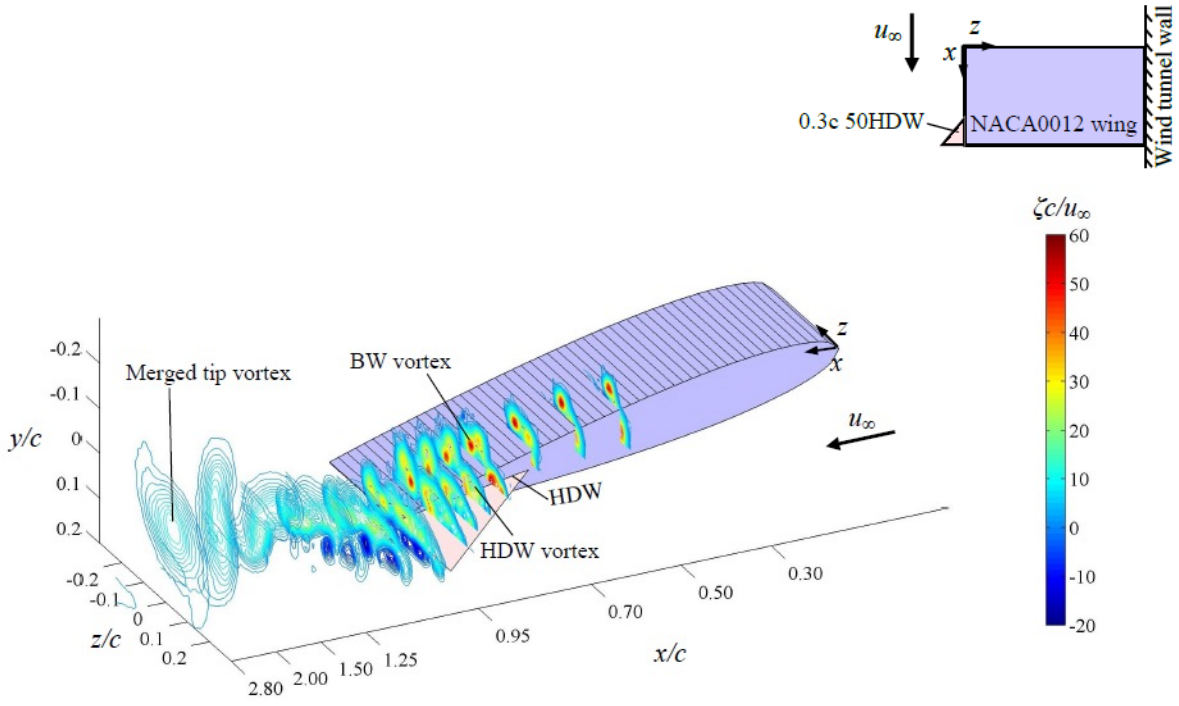

Figure 2.10 Typical wingtip vortex development along the tip and in the near wake behind the NACA 0012 wing with tip-mounted full-size and small-size half-delta wings.

CHAPTER 3

EXPERIMENTAL METHODS AND APPARATUSES

In this chapter, the flow facilities and experimental techniques and apparatus employed in this research work are presented. This chapter is divided into four sections. In Section 3.1, the wind tunnels and water tunnel utilized in the lift and drag force measurements are discussed. In Section 3.2, the experimental techniques and apparatuses such as the particle image velocimetry, the seven-hole pressure probe, the two-component wind-tunnel force balance, the one-axis Rolling Hill Research Corp. (RHRC) force balance, and the smoke-wire and dye-injection flow visualizations, are described. In Section 3.3, the test wing models employed in both wind tunnel and water tunnel are presented. Finally, the experimental uncertainty is discussed in Section 3.4.

3.1 Flow Facilities

3.1.1 Joseph Armand Bombardier wind tunnel

The *Joseph Armand Bombardier* wind tunnel is a low-turbulence, suction-type wind tunnel located in the Aerodynamics Laboratory in the Department of Mechanical Engineering at McGill University. This wing tunnel has a 0.9 m × 1.2 m × 2.7 m test section and is powered by a 16 blades, 2.5 m diameter fan rated at 125 hp. The end of the tunnel is fitted with a specially designed acoustic silencer right downstream of the fan to attenuate high tone noises. This wind tunnel has a total length of 19 m, consisting of a 3.3 m contraction leading into a 2.7 m test section followed by a 9.1 m 2-stage diffuser. The inlet has a contraction ratio of 10:1 and has a combination of 10-mm honeycomb and three 2 mm anti-turbulence screens providing inlet flow conditioning. The turbulence intensity of the wind tunnel is 0.05% at a free stream velocity of 35 m/s. Figure 3.1 shows the schematic diagram of the wind tunnel. Figure 3.2 shows the photos of the *J. A. Bombardier* wind tunnel.

The *J. A. Bombardier* wind tunnel is also equipped with an in-house designed and constructed two-degree-of-freedom traverse mechanism (see Figure 3.3). Both axes are controlled remotely by National Instruments step motor drive controller and are controlled by an in-house LabView program. This traverse is used to hold and traverse a subminiature seven-hole pressure probe for pointwise three-component (u, v, w) flowfield measurement.

3.1.2 Smoke-wire flow visualization wind tunnel

The smoke-wire flow visualization was performed in a smaller open-loop wind tunnel designed similarly to the *J. A. Bombardier* wind tunnel. At the inlet, this wind tunnel consists of a section of honeycomb followed by two anti-turbulence screens for flow quality control purposes. The wind tunnel has a contraction ratio of 13:1 and a test section of 0.2 m × 0.2 m × 0.56 m. The test section is made from 9.5 mm thick clear Plexiglas (acrylic) on all four sides to allow for optical or photographing access. The turbulence intensity is 0.9% at 10 m/s. The test section is followed by a diffuser measuring 28% of the entire length of the wind tunnel. Figure 3.4 shows that schematic diagram of the wind tunnel.

This wind tunnel is also equipped with a specially designed four-bar mechanism that can be used to pitch the wing model for dynamic-stall flow study. Furthermore, a pneumatic cylinder setup can also be used to heave the wing model for airfoil heaving experiments. The test section can be accessed by two optical windows: one on the top and one on the side. Holes were drilled in the ceiling and floor of the test section upstream of the test models to allow the passing of a smoke flow visualization wire. The particle-image-velocimetry tunnel room is also equipped with a small ThorLabs optical table on which sits a two-axis computer controlled Velmex traverse. The PIV camera is mounted on it for fine positioning purposes.

3.1.3 Water tunnel

The Model 0710 water tunnel built by Rolling Hills Research Corporation (RHRC) was also used in the present work. This water tunnel has a contraction ratio of 6 to 1 and a test

section of 28 cm × 20 cm × 56 cm. An AMT 1.1 kW (1.5 hp) pump and an AC Tech controller allow the tunnel to achieve a top speed of 12.7 cm/s. A set of flow conditioners consisting of a porous plate, three screens and a honeycomb is located in the settling chamber upstream of the contracting section of the water tunnel to reduce turbulence in the flow and ensure flow uniformity. The test section can be visualized by three optical windows made of tempered glass; two windows located on each side of the test section and one window located at the end of the tunnel to allow dye-injection flow visualization and particle image velocimetry experiments to be conducted. Furthermore, a force balance can also be mounted in the test section in order to obtain aerodynamic characteristics. Figure 3.5 shows the photo of the test section of the water tunnel.

The water tunnel test section also came predrilled with mounting holes for a sting mount model support in the shape of a C-structure. This model support allows one to mount delta or reverse delta wings with minimal disturbance for force balance and dye-injection flow visualization. This sting mount support is machined from aluminum and anodized to protect it from corrosion. The entire assembly is bolted down by two bolts in pre-existing holes on the tunnel near the end of the test section. The model's sting slides into the hole of the force balance and is secured by four setscrews. With the help of a tubular bubble level, the wing is set to be at zero pitch. In order to change the angle of attack, the force balance and the test model is mounted on a rotatable C-structure. The position of the C-structure at the angle of attack of zero is then noted. The C-structure itself has built-in indices every 5° from 0° to 50°. By rotating a small knob attached to a gear that meshes with a rack on the C-structure, the angle of attack can be changed and repeated with relative ease. After setting the desired angle of attack, two locking thumbscrews are used to lock the angle. In addition, the assembly also allows for yaw angle adjustments. The yaw of the model can be adjusted by loosening the thumbscrews on the top of the mount and rotating the platform to the desired yaw angle.

3.2 Experimental techniques and apparatuses

In this section, the particle image velocimetry (employed in the *vw*-flowfield measurement in the water tunnel), the seven-hole-pressure probe (used in the axial flowfield measurement in the *J. A. Bombardier* wind tunnel), the two-component force balance (for lift and drag forces measurement in the *J. A. Bombardier* wind tunnel), the RHRC one-component force balance (for the force measurement at low Reynolds number in the RHRC water tunnel), and the smoke-wire and dye-injection flow visualization techniques are presented.

3.2.1 Particle image velocimetry (PIV)

Particle-image-velocimetry crossflow measurements were conducted in the 28 cm × 20 cm × 56 cm water tunnel at McGill University. Figure 3.6 depicts the schematic diagram of the PIV experimental setup. The water tunnel was seeded with Dantec PSP-20 polyamid seeding particles (Dantec 80A4011) with a mean diameter of 20 μm and a density of approximately 1.03 g/cm^3, which is near neutral buoyancy. These particles are produced by polymerization processes and have a round but not perfectly spherical shape. The particles are made from polyamid 12 and have a melting point of 175°C with a refractive index of 1.5. At the beginning, approximately 2 g of particles are dissolved in two liters of water by mixing the container with mechanical vibrations. The mixture then introduced upstream of the flow conditioners and were allowed 10 minutes to recirculate in the flow before conducting the day's experiments. The process is repeated until the desired density of particles is achieved. Furthermore, due to particles settling down overnight when the water tunnel is off, new particles need to be added at the beginning of the day of the experiments. The seeding particles are approximately 3-5 pixels in diameter in the PIV pictures.

A dual-head Continuum Nd:YAG laser was used to generate two overlapping laser pulse lights sheets. The laser was emitted at a wavelength of 532 nm with consecutive 5 – 7 ns 300 mJ pulses at a rate of 5 Hz. The laser beam was guided towards the water tunnel test section by a series of redirecting mirrors and was expanded into a light sheet by a

cylindrical lens. Before reaching the test section, the light sheet went through a slit, turning it 0.158 m (6.25") high and an 1143 μm (0.045") thick. The laser pulse delay was determined by assuming the seeding particles should only travel one quarter of the light sheet thickness at freestream velocity during that period of time and was set at Δt = 2381 μs. A TSI LaserPulse synchronizer model 610035 was used in order to synchronize the different components (the Nd:YAG laser, CCD camera, and the frame grabber) to interact together. The acquisition and post-processing of the PIV images was performed with the TSI Insight 3G version 9.1.0.0 software package.

A TSI 4 megapixels PowerView Plus CCD camera (Model 360059, 2048 x 2048, 7.4 μm/pixel, 12 bit dynamic range and 16 Hz maximum frame rate) was coupled with a 105 mm focal lens at f/5.6. It was calibrated by taking a picture of a ruler in the field of view. The PIV calibration was determined to be 45.15 μm/pixel, yielding a magnification ratio of 6.10. The distance between the measurement plane and camera lens was 0.81 m (32"). The field of view varied between x/c locations and was between 7.5 cm × 3.5 cm and 3 cm × 1.2 cm. The PIV images were captured by a 64-bit Coreco Imaging X64-CL frame grabber installed in a HP xw9400 workstation. This setup allowed one delta-wing or reverse-delta-wing vortex to be captured on one side of the wing. Figure 3.6 shows the schematic diagram of the PIV setup.

Processing the PIV pictures require many steps: pre-processing, a two-frame cross-correlation analysis processing, and post-processing. A processing mask consisting of the port side of the wing model, directly on the wing surface to 0.8 y/s high, and from the centerline to 0.5 z/s beyond the leading edge of the measurement plane, is defined for each case of x/c along the wing. s is the semi wing span. y and z are vertical and spanwise distances from the origin of the axes. x and c are the streamwise distance and the wing chord, respectively. For cases downstream of the trailing edge of the delta wing, a bigger processing mask, 1673 × 781 pixels, is used in order to catch the entire vortex structure. Before analysis, each frame is normalized using the minimum and maximum intensity in order to improve image quality.

A multi pass 2-frame cross-correlation technique was chosen to improve the signal-to-noise ratio and removes directional ambiguity. A multi pass "DeformationGrid" grid engine was then used to break the input images up into smaller spots for processing and performs image deformation before each pass by using the local flow found in the previous pass. This process effectively reduces peak locking error. The starting spot dimension is 64 × 64 pixels and the final spot 32 × 32 pixels, with 50% overlapping of interrogation windows, yielding a final vector spacing of 16 × 16 pixels, corresponding to a $y/c = z/c = 0.01$ for non-slender delta wing models (c = 0.07 m = 2.74") and $y/c = z/c = 0.007$ for the slender wing case (c = 0.11 m = 4.25"). Three initial passes (for starting spot size) and 2 final passes (for final spot size) were chosen for a total of 5 passes. The maximum displacement as a fraction of spot size was set at $dx = dy = 0.25$. A "DeformationMask" spot mask engine designed for the "DeformationGrid" was used to condition the spots. The correlation engine was the "HartCorrelator". This direct correlation method processes only the most significant pixels to improve processing speed. The peak engine selected was the "BilinearPeak"; it locates the correlation peak with subpixel accuracy by fitting a set of linear functions to the highest pixel and its four nearest neighbors. Overall, the algorithms selected results in the slowest processing time but should have the highest accuracy.

Finally, post-processing is used to validate the raw vectors. A global vector validation is used to remove vectors that are clearly out of valid velocity range. This is followed by a local vector validation which uses the median test with neighborhood size of 3 × 3 to replace bad vectors by the local median. A recursive filling algorithm is used to fill holes with a neighborhood size of 3 × 3 using the local mean. The holes could be caused by, for example, failed signal-to-noise ratio during the PIV processing (unable to compute vector), or failed vector validation in previous validation steps (vector is out of range and removed). At the end, the entire flow field is smoothed by a 5 × 5 Gaussian smoothing filter (low-pass filter) with $\sigma = 0.8$. The particle image velocimetry setup followed those of Raffel et al. (1998) and Gerontakos and Lee (2008). A more detailed discussion on the PIV flow measurement system is given in Appendix A.

3.2.2 Seven-hole pressure probe

The seven-hole pressure probe used in the present study to obtain the two-dimensional plane along or behind the wing model for the three-component velocity at each grid point along the wing model is shown in figures 3.7(a)-(b). The probe was mounted on the computer-controlled traverse mechanism presented in figure 3.3. The probe tip was made from brass and machined to a 30° cone angle. The tip of the probe had a diameter of 2.7 mm and seven 0.5 mm diameter holes drilled parallel to the sting axis, six of which were arranged on a 2.4 mm diameter circle. The probe had a 130 mm long shaft, and the shaft was fixed to a 12 mm diameter, 400 mm aluminum probe sting. A set of 1.6 mm diameter, 550 mm long Tygon tubing was used to connect the pressure taps and the pressure transducer array box. The Tygon tubing was passed through the probe sting. The pressure transducer array box was fixed on the arm of the traverse and it contained seven Honeywell DC002NDR5 differential pressure transducers with a maximum head of 50 mm water. The reference pressure for all transducers was the ambient atmospheric pressure measured from inside a fiberglass covered damping unit. The output of the transducer array was connected to a custom-built signal conditioner. The signal conditioner consisted of a seven-channel analog signal differential amplifier with a gain of 5:1 and an external DC offset. The resolution of the pressure transducers was on average 61 pascal/volt and their response was linear to 2%. The probe was calibrated in-situ, using the calibration procedures described in Wenger and Devenport (1999).

A 16-channel, 16-bit National Instruments-6259 A/D board was used to acquire data. This A/D board was powered by a Dell Dimension E100PC, which was used to collect and store data. A NI BNC-2110 connector box was used to connect A/D board and sensor output. Output voltages were sampled at 500 Hz for nine seconds (including a two seconds traverse mechanism motion settling time) in order to obtain a reliable average for recording. Other sampling frequencies and longer sampling times were also tested to ensure convergence, but the differences were less than 0.1 mV. Figure 3.7(c) shows the block diagram of the data acquisition and processing of the seven-hole pressure probe flow measurement system.

3.2.3 Two-component wind tunnel force balance

Figure 3.8 shows the photos of the two-component force balance in the Aerodynamics Laboratory at McGill University. The force balance is mounted with the top side flush with the floor in the center of the test section of the *J. A. Bombardier* wind tunnel. It is a two-axis force balance based on linear variable differential transformers (Sanborn 7DCDT-100 LVDT) and was mounted in the center of the *J. A. Bombardier* wind tunnel. The top plate of the force balance is circular in shape to allow for change of angle of attack and a rectangular sensing plate is located in the center. This sensor plate can only move in two perpendicular axes aligned to the axial and normal forces acting of the wing model and was mounted in the center of the *J. A. Bombardier* wind tunnel. The sensing elements of the force balance are protruded outside the test section floor. The design of the force balance is such that the axial load and normal load are decoupled by two flexural platforms. Each of the two axes are held in place by four flexures that are 0.889 mm (0.035") thick.

To obtain the lift and drag forces measurements, the wing is first mounted onto the sensing plate. Special adapters are made for each of the different wing model geometries. The desired angle of attack α, hence the wing model's angle of attack will change at the same time. The sensing axes, however, rotate with the wing model and in order to obtain the real lift and drag forces, a simple mathematical relationship can be used:

$$L = N\cos(\alpha) - A\sin(\alpha) \tag{3.1}$$

$$D = N\sin(\alpha) + A\cos(\alpha) \tag{3.2}$$

3.2.4 One-component water tunnel force balance

The one-component strain gage balance is built by the Rolling Hill Research Corporation and is composed of a set of flexures and strain gages bonded to the upper and lower surfaces of a flexure. A flexure is simply an element designed to be more flexible in the direction of its measurement than any other direction. Figure 3.9(a) shows that photo of the flexures of the RHRC force balance before installing the strain gages and waterproofing silicone can be seen in the photo. A Wheatstone bridge (see figure 3.9(b)) is used to measure the tiny change in resistance transformed into voltage. The electric signal is

normally amplified before reaching the data acquisition system. The RHRC one-component balance is made of semi-conductor strain gages and they are extremely sensitive. As the strain gages are deformed under the aerodynamic forces, their resistance values will change. The Wheatstone bridge will measure this small resistance change and give a proportional linear voltage output that will be converted into aerodynamic coefficient through the calibration curve. The calibration slope obtained for the current investigation is 4.8 mg/mV.

The RHRC one-component force balance software is based on National Instruments LabView. To run the software, a Windows compatible computer, preferably running Microsoft Windows XP, is required. Furthermore, only the LabView Run Time Engine (RTE) is required to run the RHRC software. The RHRC one-component force balance is equipped with a data acquisition module to record the balance output and bridge excitation voltages. The unit is a National Instruments USB-6009 14-bit multi-function data acquisition and analog output module. The input voltages are acquired between +/- 10 V in differential mode. The balance signal has been programmed for a gain of 200.

3.2.5 Smoke-wire and dye-injection flow visualization

Smoke-wire flow visualization is performed in the 20 cm × 20 cm × 180 cm wind tunnel in the Aerodynamics Laboratory to visualize the spanwise flow field around the reverse delta wing. The smoke generated usually last for approximately one to two seconds. In this short period of time, a Casio EX-FH25 digital high-speed camera is set up to record the flow pattern in a high-speed snap shot or video modes. A 5-μm nichrome wire, coated with 5W40 motor oil beads, is used to generate the smoke streaklines. Each end of the wire is connected to the + and – ends of a variable output power supply. A high-speed camera on a tripod is located next to the wind tunnel test section, focused on the wing model. Figure 3.10 shows the schematic diagram of the smoke-wire flow visualization setup.

Dye-injection flow visualization was performed in the RHRC water tunnel by injecting colored dye from a point source injector upstream of the test model. The injector was made out of a hypothermic needle with an inner diameter of 0.81 mm (0.032”), bent 90°

two inches downstream of the injecting tip. Special care was taken to minimize the needle's vortex shedding by adding a flow guide composed of two flat plates glued together in the shape of an airfoil. The flow visualization system is composed of a panel of three valves (for each color), dye containers, and a polyethylene pressure tank (bleach sprayer container). All the components are connected by a series of Tygon tubing.

3.3 Wing models

In this section, the reverse delta wing and the regular delta wing, both slender and non-slender, employed in the *J. A. Bombardier* wind tunnel and the RHRC water tunnel are discussed.

3.3.1 J. A. Bombardier wind tunnel wing model

Figure 3.11 shows the schematics of the delta wing model used in the 0.9 m × 1.2 m × 2.7 m test section of the *J. A. Bombardier* wind tunnel. The wing model was built by a CNC milling in the machine tool lab of the Department of Mechanical Engineering at McGill University. It features a chord measuring 0.42 m (16.5") with a sweeping angle $\Lambda = 65°$. The three sides of the delta or reverse delta wing, depending on its orientation, were beveled at 25° on the bottom side. This wing has a thickness of 0.635 cm (0.25"), rendering a thickness-to-chord ratio t/c = 1.52%. The sharp leading edges and trailing edge allowed the fixation of the flow separation location. Five countersunk holes are added in the middle of the wing for mounting purposes. This wing is used for force balance measurements at high Reynolds numbers and also for seven-hole pressure probe measurements.

3.3.2 RHRC water tunnel wing models

Figure 3.12 shows the schematic diagram for both slender and non-slender wing models. The wing models were made of 0.040" (1.016 mm) thick aluminum sheet. The chord is 4.25" (107.95 mm) and the sweeping angle Λ was set at 65°, which rendered a semi-span of 50.3 mm (1.98") at the trailing edge of the model. For non-slender reverse delta wing models, the sweeping angle Λ was set at 50°, with a chord of 69.6 mm (2.74") and a trailing edge semi-span of 5.03 cm (1.98"). To make the models, a 0.61 m × 0.61 m (2' x 2')

aluminum sheet metal was first sheared into a strip with the height of the chord length. One leading edge of the reverse delta wing was traced onto with a sharp hobby knife using a square head protractor's adjustable arm as reference. The line is then sheared using a 16 gauge foot shear. The second leading edge was traced again and sheared to produce the delta wing. Many models were made using this method and the accuracy of the sweeping angle is approximately +/- 0.5°. The models were spray painted in a flat black color for PIV investigation purposes to minimize reflection of the Nd:YAG laser. They were spray painted white for dye-injection flow visualization experiments.

3.4 Experimental uncertainty

In this section, experimental uncertainties for the different wing models and experimental procedures, following the suggestions of Moffat (1988), are presented. The uncertainties arise due to several reasons: machining tolerance, instrumentation resolution, mechanical hardware experimental procedure, and uncontrolled changes due to environment. The experimental uncertainties in this investigation are presented in the following tables.

Table 3.1 Experimental uncertainty regarding flow properties and wing models

Parameter	**Uncertainty**	**Operating Range**
J. A. Bombardier wind tunnel free stream	±0.2 m/s	10 m/s
PIV wind tunnel free stream	±0.05 m/s	1 m/s
Water tunnel free stream	±0.01 m/s	0.12 m/s
Bigger reverse delta wing chord	±0.001 m	0.42 m (16.5”)
Smaller reverse delta wing chord	±0.001 m	0.11 m (4.25”)
Reverse delta wing sweeping angle	±1°	50°, 65°
Wing model roll angle	±1°	0°
Wing model yaw angle	±1°	0°
Wing model angle of attack	±0.5°	0° – 350°
Low Reynolds number	±100	11,000
High Reynolds number	±0.05 x 10^5	3.4 x 10^5

Table 3.2 Experimental uncertainty regarding data acquisition board

Parameter	**Uncertainty**	**Operating Range**
Measurement accuracy	±0.15 mV	0 – 10 V

Table 3.3 Experimental uncertainty regarding two-axis force balance measurements

Parameter	**Uncertainty**	**Operating Range**
Axial resolution	±0.05 N	0 – 17 N
Normal resolution	±0.09 N	0 – 15 N
Wing model angle of attack	±0.25°	0° – 50°
Axial LVDT calibration linearity	0.70%	0.04 N/mV
Normal LVDT calibration linearity	0.10%	0.09 N/mV
Axial LVDT uncertainty	±0.06 N	0 – 17 N
Normal LVDT uncertainty	±0.12 N	0 – 15 N
Maximum C_L uncertainty	±0.06	0 – 1.6
Maximum C_D uncertainty	±0.03	0 – 1.3

Table 3.4 Experimental uncertainty regarding RHCH force balance measurements

Parameter	**Uncertainty**	**Operating Range**
Resolution	±0.001 N	0 – 0.05 N
Wing model angle of attack	±0.50°	0° – 40°
Strain gage calibration linearity	0.70%	2.42 N/V
Uncertainty	±0.002 N	0 – 0.05 N
Maximum C_N uncertainty	±0.04	0 – 1.6

Table 3.5 Experimental uncertainty regarding particle image velocimetry measurements

Parameter	**Uncertainty**	**Operating Range**
Magnification ratio	±0.3%	6.10
Particle size	±15 μm	20 μm
Time delay, Δt	±1 ns	2381 μs
Light sheet thickness	±3%	1 mm
Wing model streamwise location	±0.25 cm	0 – 16 m
Spanwise velocity	±1%	-0.15 – 0.15 m/s
Vertical velocity	±1%	-0.15 – 0.15 m/s
Spanwise vorticity, $\zeta c/u_\infty$	±5%	-30 – 50

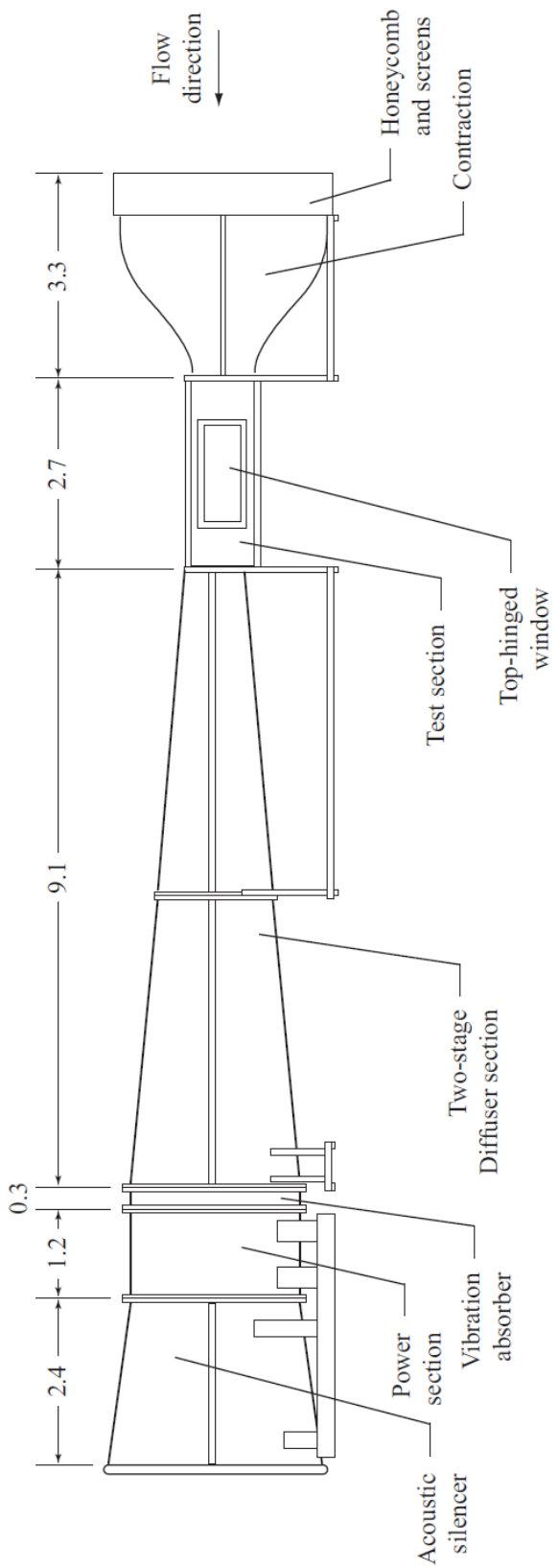

Figure 3.1 Schematic diagram of the *Joseph Armand Bombardier* wind tunnel.

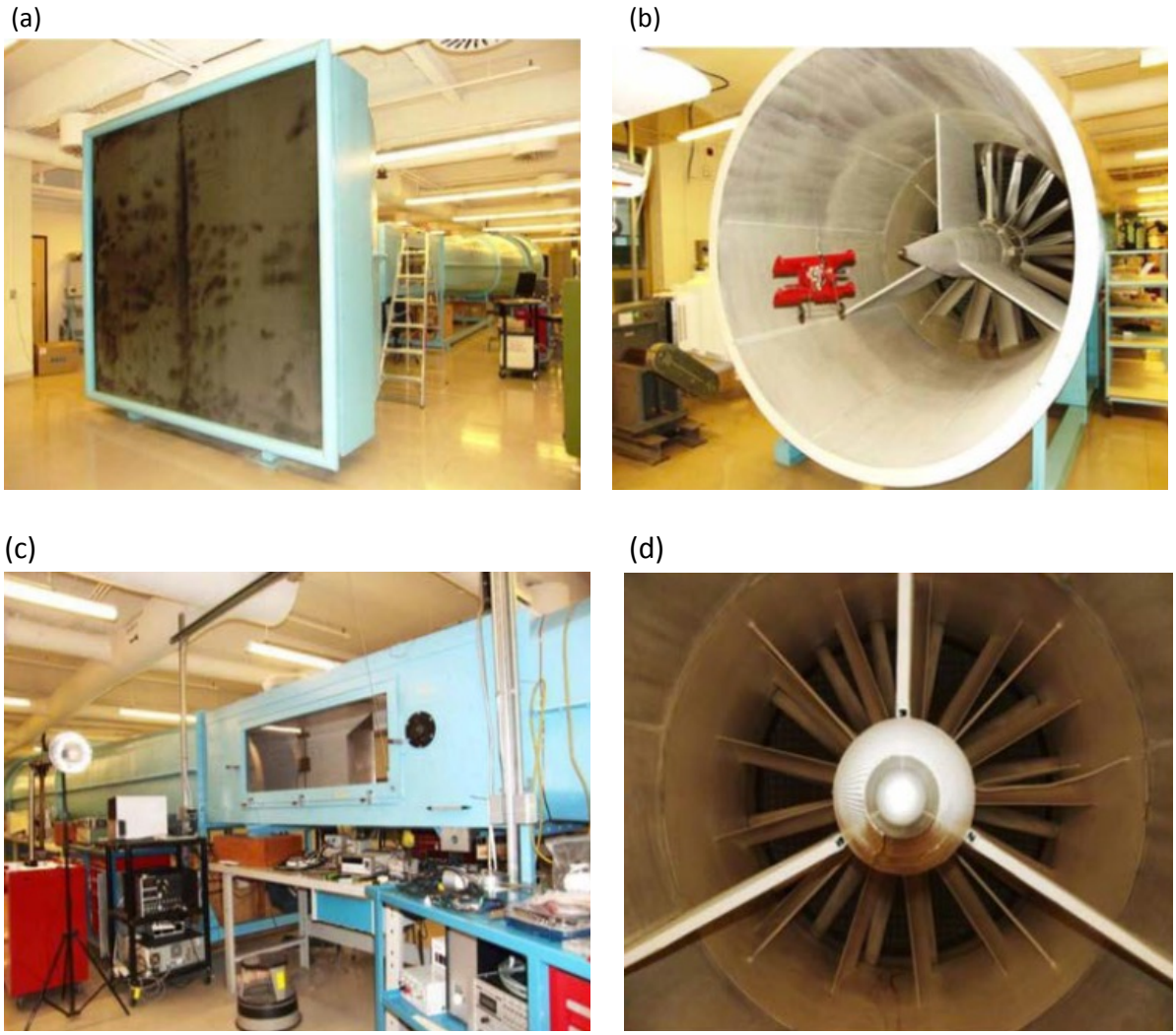

Figure 3.2 Photos of the *Joseph Armand Bombardier* wind tunnel. (a) The inlet with the honeycomb structure clearly shown in black, (b) the exit of the wind tunnel with both the fans and the acoustic silencer being visible, (c) the outside of the test section with one side window clearly visible, and (d) the detailed view into the exit of the tunnel.

(a)

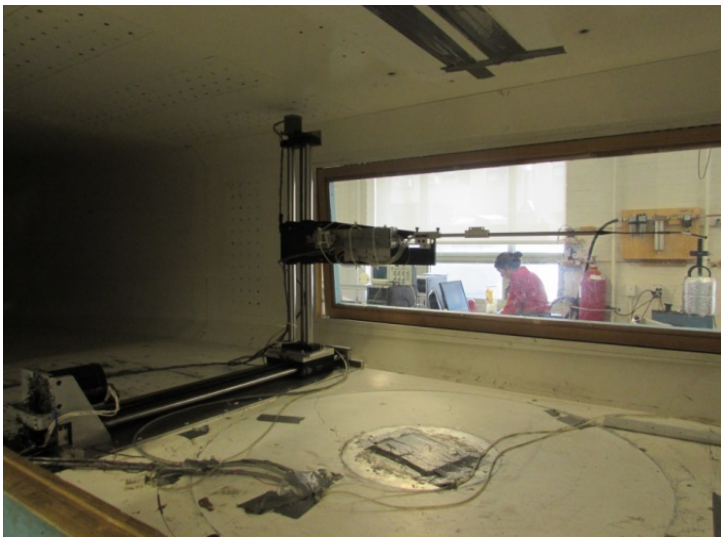

(b)

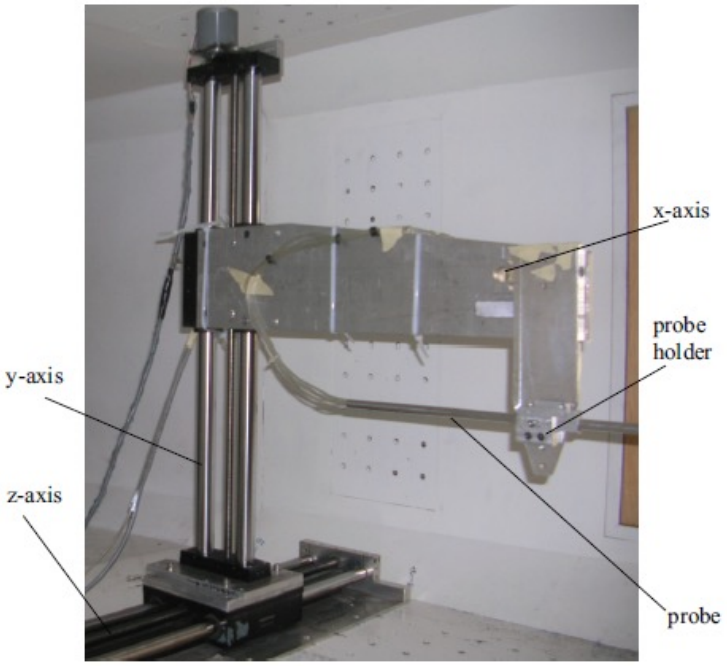

Figure 3.3 Photos of the two-axis seven-hole pressure probe traverse mechanism. (a) Whole view, and (b) close-up view.

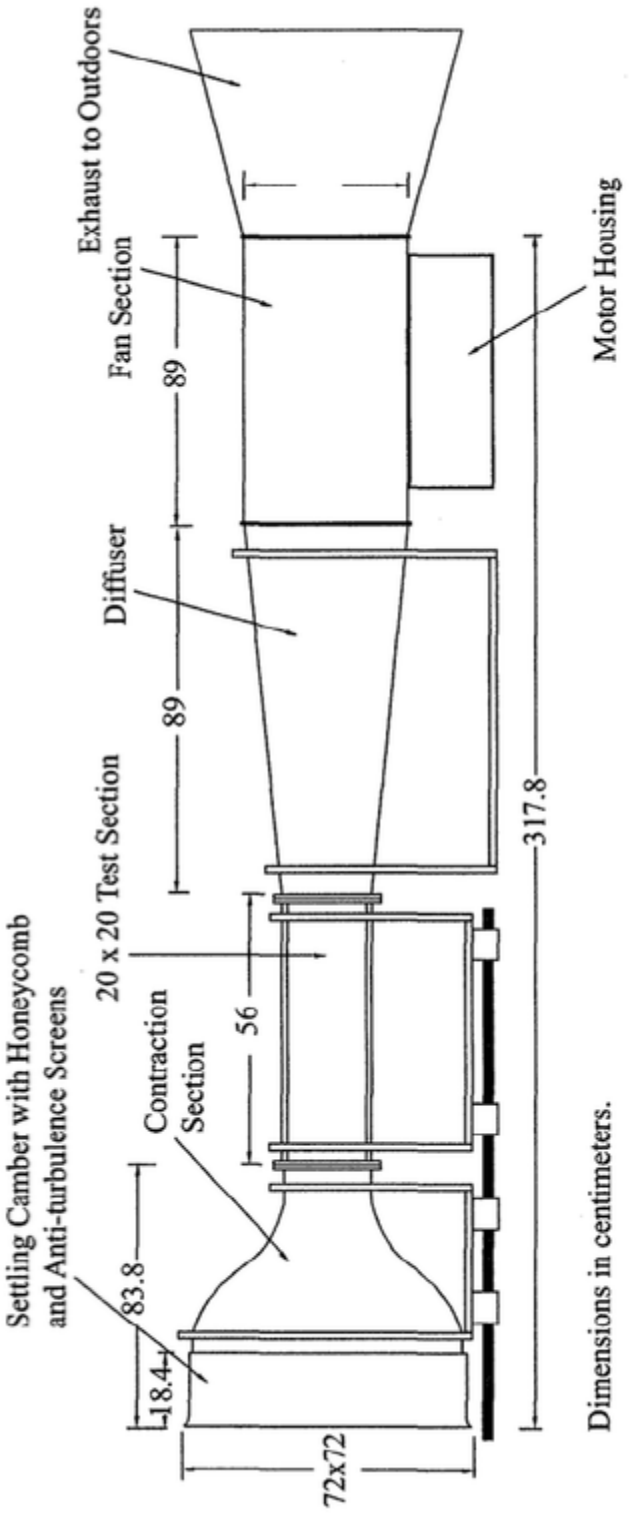

Figure 3.4 Schematic diagram of the smoke-wire flow visualization wind tunnel.

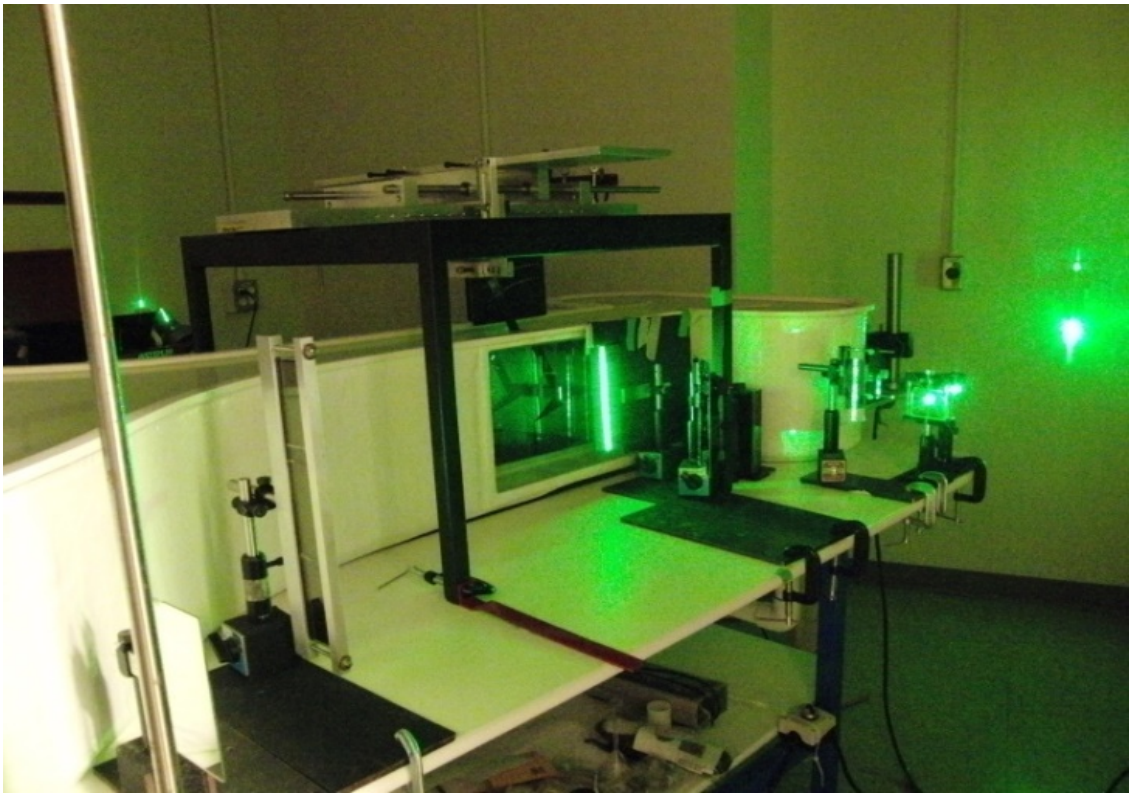

Figure 3.5 Photo of the water tunnel test section in which the test model and green 532 nm Nd:YAG laser are both visible. The particle-image-velocimetry system of mirrors and optics can also be seen.

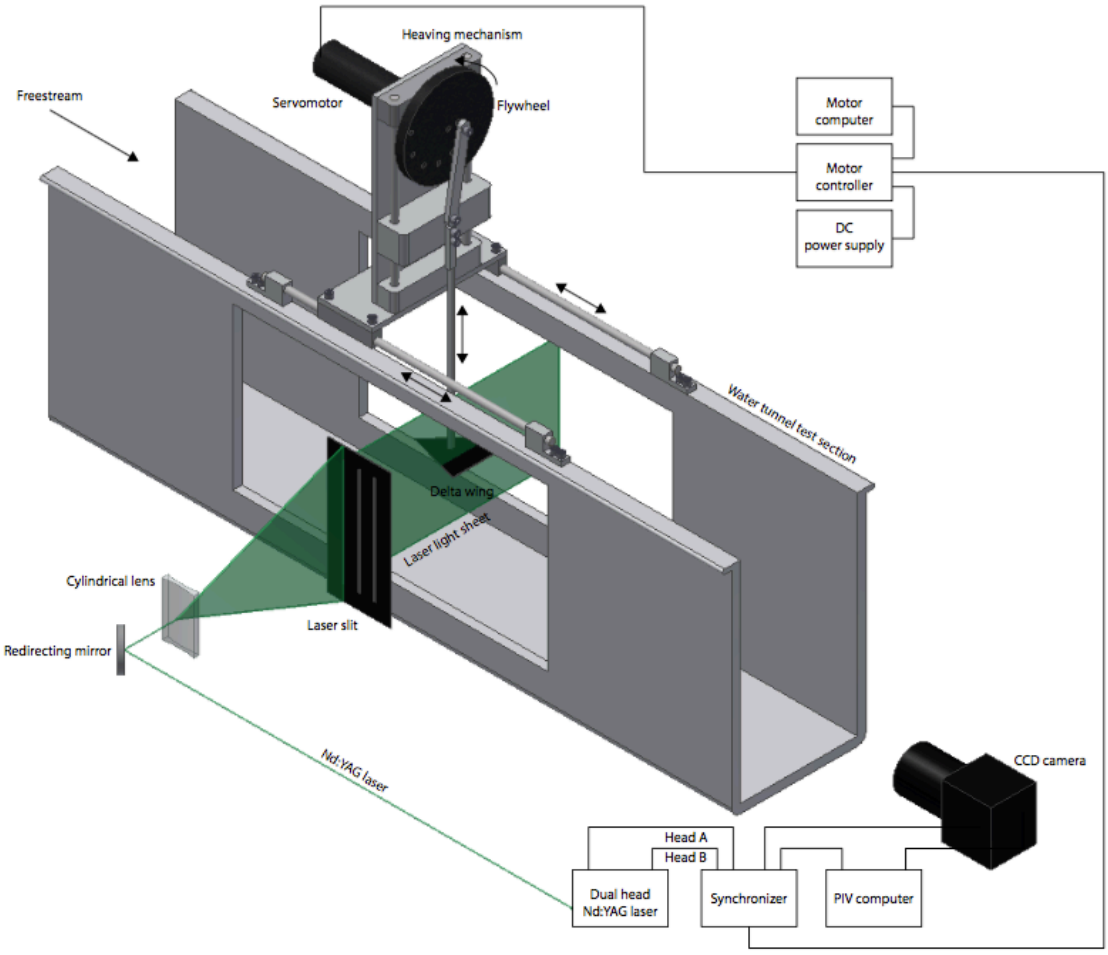

Figure 3.6 Schematic diagram of the PIV experimental setup.

(a)

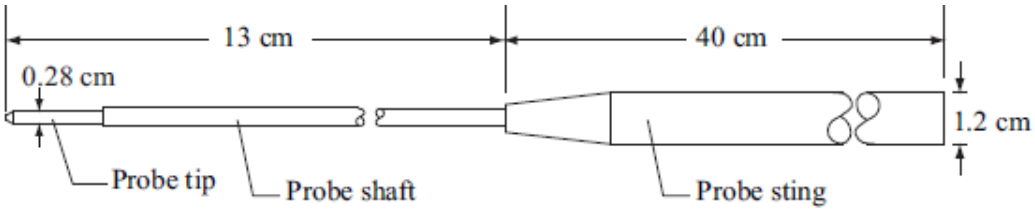

(b)

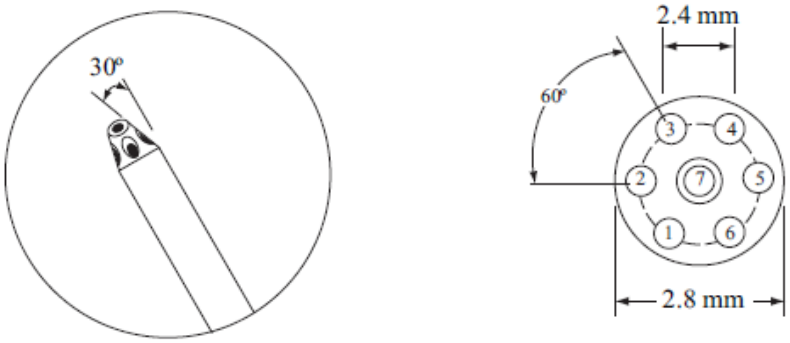

(c)

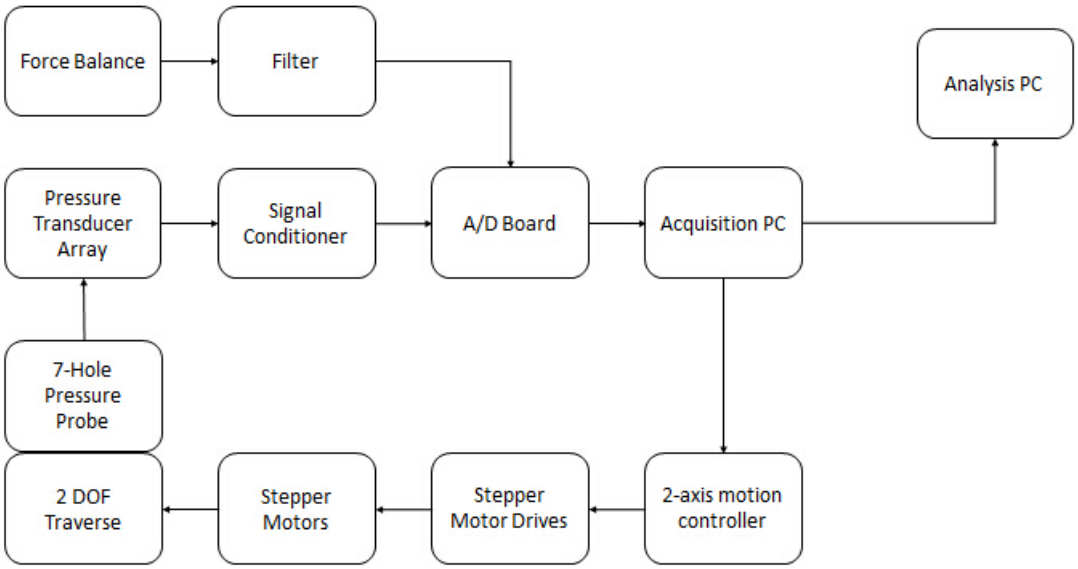

Figure 3.7 (a)-(b) Schematic diagrams of the seven-hole pressure probe, and (c) data acquisition and processing block diagram.

(a)

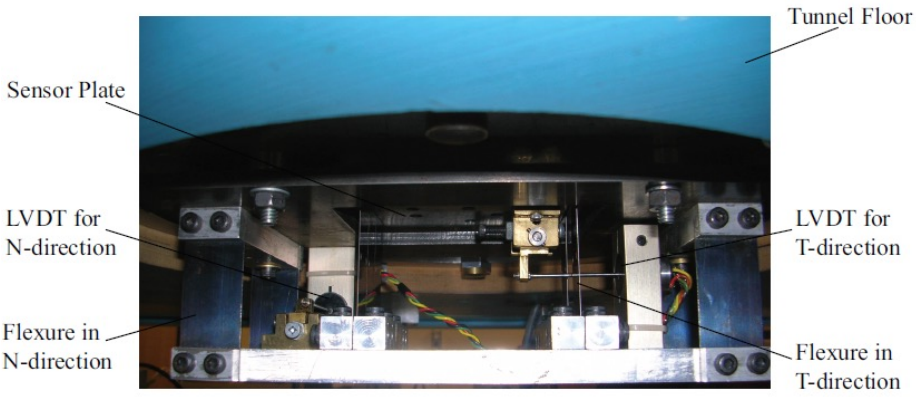

(b)

(c)

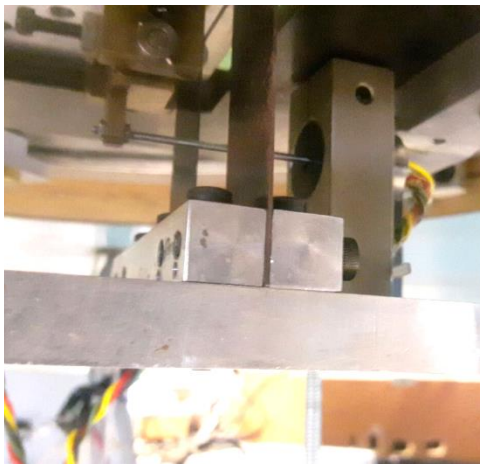

Figure 3.8 Photos of the two-component force balance in the Aerodynamics Laboratory. (a) Photo of force balance based on eight flexures and two LVDT viewed from underneath of the test section, (b) top view of the force balance from inside the test section, and (c) close-up look of one of the two LVDTs of the force balance.

(a)

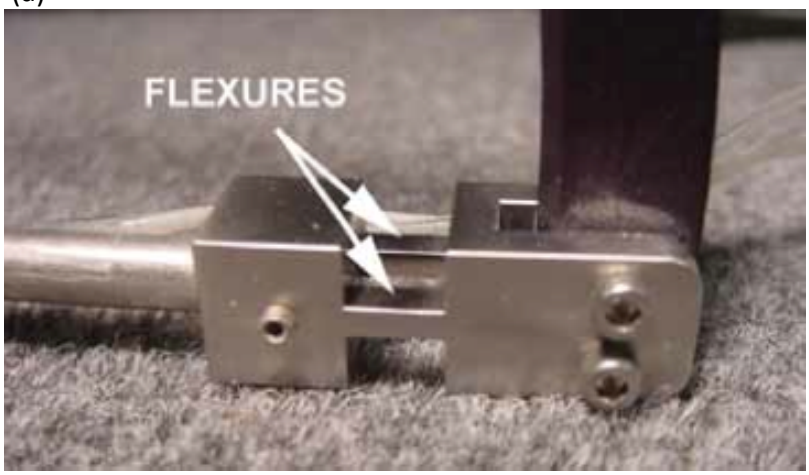

(b)

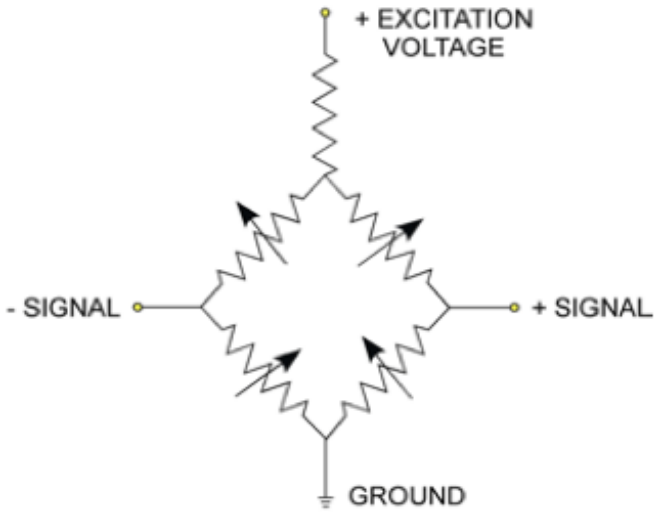

Figure 3.9 RHRC one-axis force balance. (a) Photo of the flexures of the RHRC force balance before strain gage installation, and (b) Wheatstone bridge used for force balance.

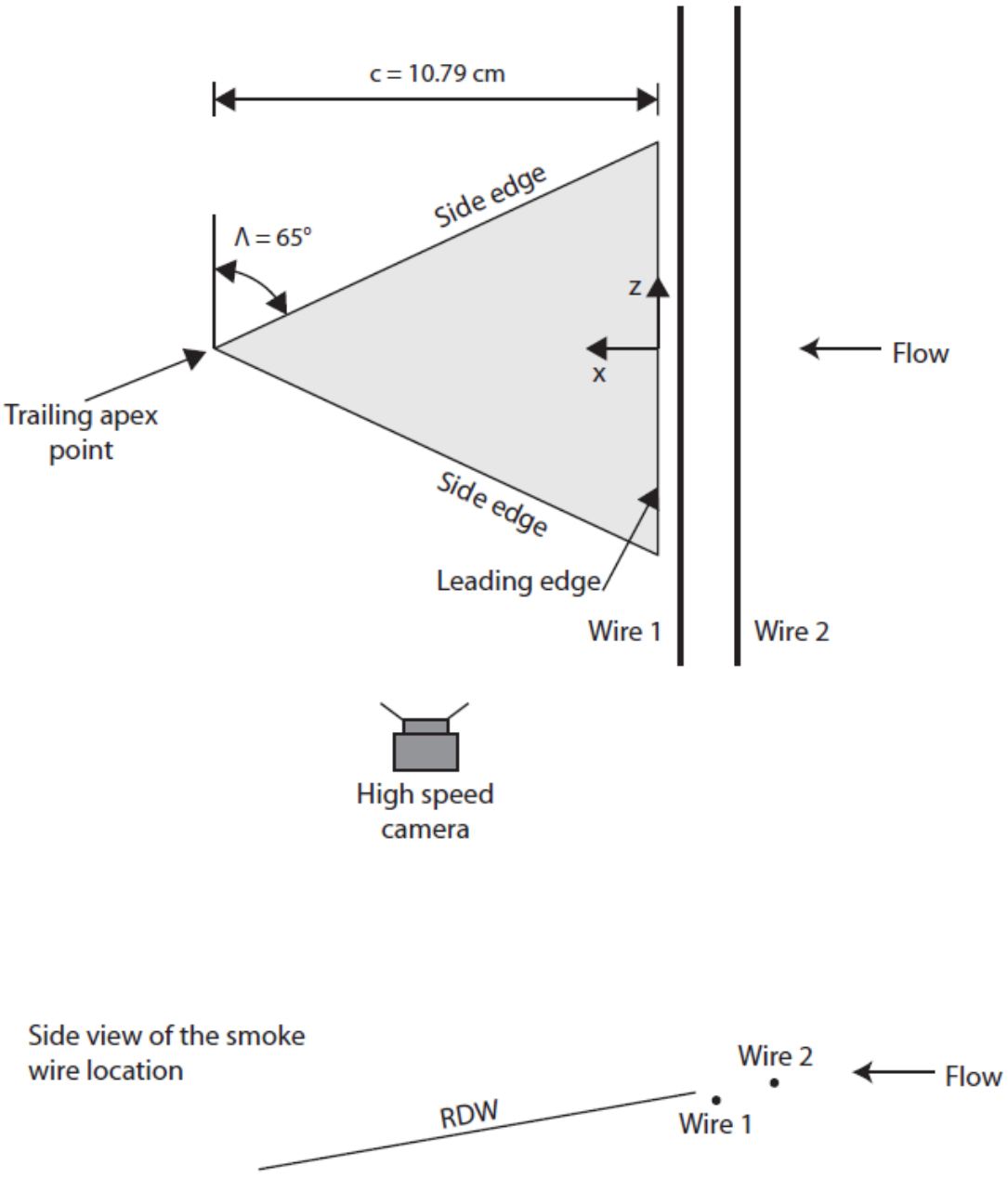

Figure 3.10 Schematics of smoke-wire flow visualization setup.

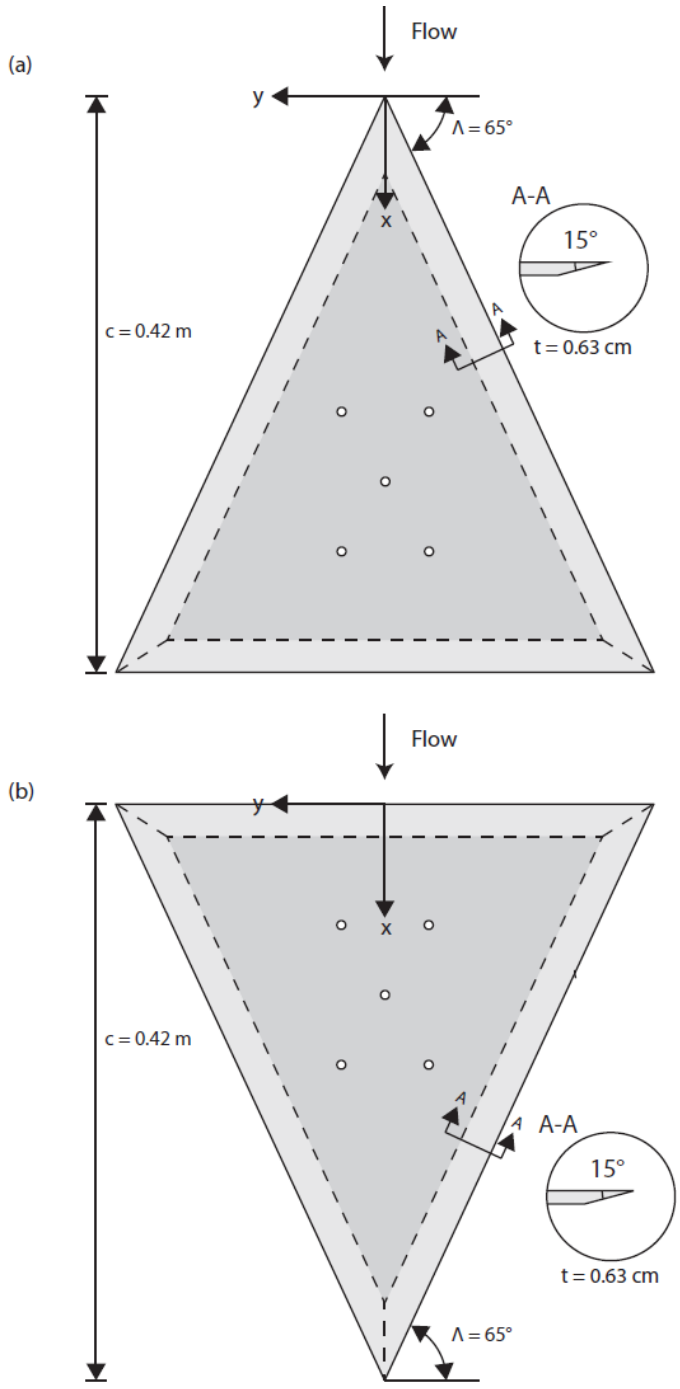

Figure 3.11 Schematic diagram of the delta and reverse delta wing used in the *J. A. Bombardier* wind tunnel.

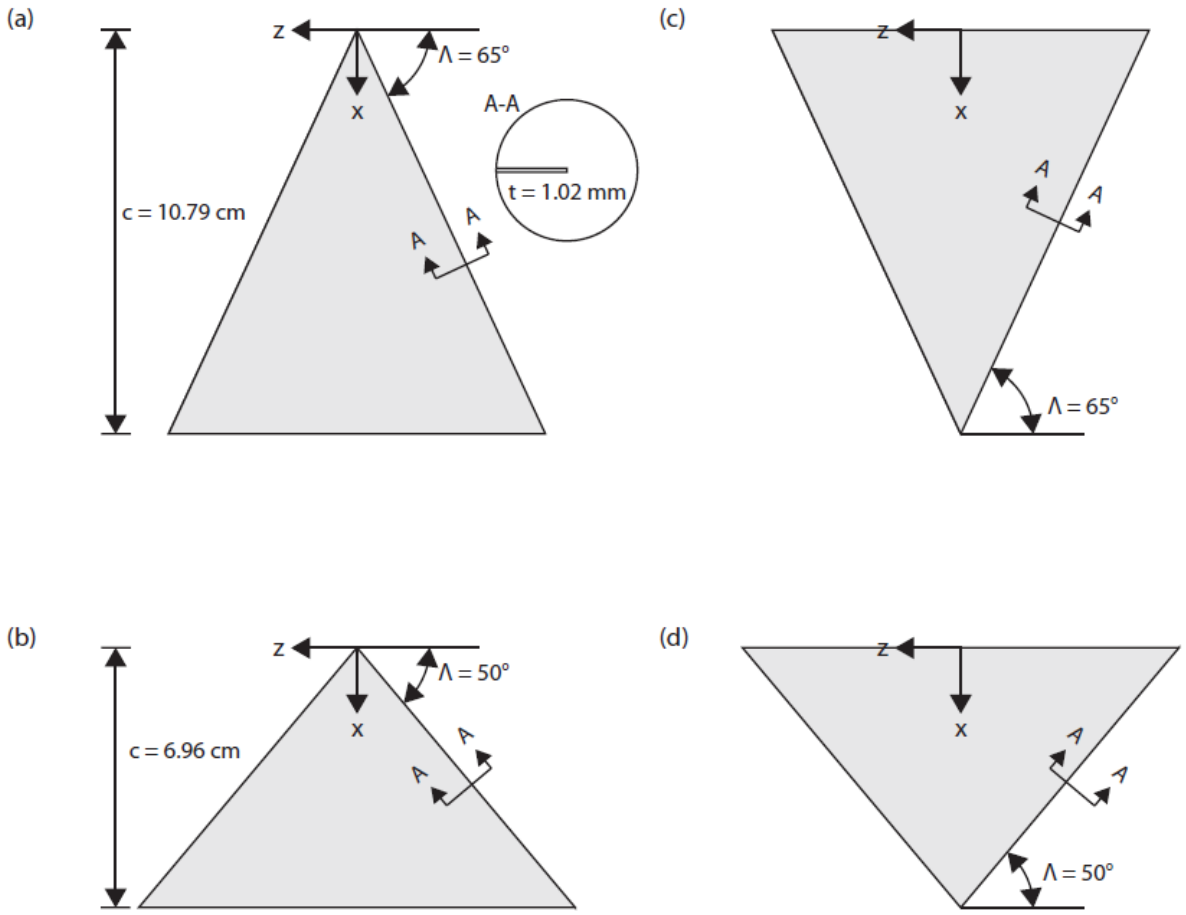

Figure 3.12 Schematic diagram of the water-tunnel test wing models. (a) Slender regular delta, (b) slender reverse delta wing, (c) non-slender regular delta wing, (d) non-slender reverse delta wing.

CHAPTER 4

RESULTS AND DISCUSSIONS

The aerodynamics and vortex flowfield of the reverse delta wing, both slender and non-slender (with Λ = 65° and 50°), are discussed in this chapter. The results of the regular delta wings, of the same sweep angle, are also included to serve as a comparison. This chapter is divided into three sections. Section 4.1 will be devoted to the investigation of the aerodynamic and vortex flow characteristics of a 65°-sweep slender reverse delta wing. Section 4.2 will be focused on the characterization of the aerodynamics and vortex flowfield generated by a 50°-sweep non-slender reverse delta wing. Finally, the Gurney flaplike strips, of various configurations and heights, were employed to passively increase the lift generation capability of the reverse delta wing. The objectives of the above-mentioned experimental works were aimed to better understand the lift generation and the vortex flow structure, with and without passive control, of a reverse delta wing, and lay the foundation for the future investigation of the reverse delta wing in ground proximity.

4.1 Aerodynamic and vortex flow characteristics of a 65°-sweep slender reverse delta wing

In this section, the aerodynamic characteristics of the reverse delta wing were investigated first and served as an experimental guideline for the vortex flow measurements. The reverse delta wing results were also compared to the regular delta wing data. The particle-image-velocimetry measurements were then used to compute the total lift coefficient. Special attention was also given to the behavior of the leading-edge vortex and its bursting over the slender regular delta wing.

4.1.1 Aerodynamic characteristics of the slender regular delta wing

To better understand the lift generation and the stalling mechanism of the 65°-sweep slender reverse delta wing, the behavior of the leading-edge vortices and their breakdown process and location of a 65°-sweep regular delta wing was investigated first.

Figures 4.1 illustrate the variation of the leading-edge vortex breakdown location $(x/c)_{VBD}$, obtained via dye-injection flow visualization, on a 65°-sweep regular delta wing at selected angles of attack α for a chord Reynolds number Re = 12,000. The flow visualization results of $(x/c)_{VBD}$ of the 65°-sweep delta wing published by researchers elsewhere are also plotted in figure 4.2 for a direct comparison. The leading-edge vortex of the present delta wing was found to break down at $x/c = 1.0$ at $\alpha = 17.5^{o}$ (see • symbols) in comparison to $\alpha = 20°$ at Re = 9×10^5 (Lowson and Riley 1995). The discrepancy could be due to the Reynolds number effect since they are different by almost a factor of 10. Figure 4.2 also indicates that there exhibited a large disparity in the published $(x/c)_{VBD}$ data (see also Jobe 2004), due to the strong dependence of the leading-edge vortex breakdown on the Reynolds number, sweep angle, bevel angle, and flow facility. It is noteworthy that the bursting behavior of the leading-edge vortex is, however, only slightly sensitive to the Reynolds number. Nevertheless, the present $(x/c)_{VBD}$ data were found to be in good agreement with those of Skow and Erikson (1982) and Huang et al. (1997) at Re = 15,000. The details of the wing model and the Reynolds number of the published data are listed in Table 4.1.

Table 4.1 Test conditions of the references in figure 4.2

	Reference	Case	Upper surface	Lower surface	t/c (%)	Re
6	Lambourne & Bryer (1961)	A	flat	16° chamfer	2.21	10,000
10	Skow & Erickson (1982)	A	n/a	n/a	n/a	30,000
10	Skow & Erickson (1982)	B	n/a	n/a	n/a	30,000
11	Thompson (1975)	--	15° chamfer	15° chamfer	1.2	9,800
14	Huang et al. (1997)	1	10° bevel	10° bevel	7.2	15,000
14	Huang et al. (1997)	4	flat	45° bevel	1.6	15,000
14	Huang et al. (1997)	5	45° bevel	flat	1.6	15,000
14	Huang et al. (1997)	7	10° bevel	flat	1.6	15,000
14	Huang et al. (1997)	8	10° bevel	flat	1.6	15,000
14	Huang et al. (1997)	10	10° bevel	flat	1.6	15,000

To pinpoint the leading-edge vortex breakdown location and to elucidate the bursting behavior, extensive particle-image-velocimetry measurements (with a small increment of $\Delta(x/c) = 0.85\%$; see figure 4.3) in the vicinity of $(x/c)_{VBD}$, obtained qualitatively from the dye flow visualization, were obtained. It is noteworthy that the particle image velocimetry technique not only provides the best resolution in the study of low-Reynolds-number vortex flow, but also eliminates the interference of the mechanical probes with the vortex flow (Payne et al. 1989), which can affect the location of vortex burst.

Figure 4.4(a)-(e) show the representative samples of particle image, velocity vector plot, and iso-vorticity contour overlapped with the velocity vector plot. Figures 4.5(a)-(c) show the effect of the number of images on ensemble average for $\alpha = 18°$ at $x/c = 0.8$. An ensemble-averaged result consists of 60 images was employed in the present study. This number was chosen by testing different numbers of images up to 120; it was noted that after 60 the changes in vorticity values were insignificant. Performing PIV processing on 60 images took approximately one hour.

Figure 4.6 presents the PIV measurements coupled with the photos of the visualized leading-edge vortices and their breakdown at $\alpha = 25°$. To save space, only the normalized iso-vorticity ($\zeta c/u$) contours immediately before and after the $(x/c)_{VBD}$ location are presented here. The iso-$\zeta c/u_\infty$ contours were ensemble-averaged over 60 PIV images at each measurement position. The streamwise vorticity ζ ($= \partial w/\partial y - \partial v/\partial z$) was calculated from the ensemble-averaged cross-flow (vw) velocity components by using a central differencing scheme to evaluate the derivatives. The PIV measurements indicate that, at $\alpha = 25°$, the $(x/c)_{VBD}$ appeared at 0.54 on the BW (figure 4.6). The leading-edge vortex breakdown was identified based on the large drop in the normalized peak vorticity ζ_{peak} value together with the loss of coherence or regularity of the iso-$\zeta c/u_\infty$ contour of the vortex. To further elucidate the leading-edge vortex breakdown process, the spatial evolution of the iso-$\zeta c/u_\infty$ contours of the leading-edge vortex and the associated critical vortex flow parameters, such as the vortex trajectory (y_c and z_c), ζ_{peak}, peak tangential velocity $v_{\theta,peak}$, core radius r_c, and core circulation Γ_c, are discussed in figure 4.7.

Figures 4.7(a)-(f) summarize the variation of the normalized critical leading-edge vortex flow parameters with x/c for $0.3 \leq x/c < 0.9$ at $\alpha = 25°$. The leading-edge vortices was found to continuously move away from the wing upper surface (figure 4.7(a)) and centerline (figure 4.7(b)), up to their breakdown location at $(x/c)_{VBD} = 0.54$. The vortex center was identified by the location of maximum vorticity. At $(x/c)_{VBD}$, there was a sudden movement of the vortex toward the wing surface and centerline. Downstream of $(x/c)_{VBD}$, the vortex trajectory became indiscernible. Figures 4.7(c)-(d) show that the change in the normalized peak vorticity and tangential velocity (indicatives of the vorticity level and strength of the leading-edge vortex) along the delta wing. As can be seen, both the peak vorticity and tangential velocity of the slender delta wing were found to increase with the streamwise distance x/c, reaching a local maximum at $x/c \approx 0.43$, and began to drop rapidly for $0.43 < x/c < 0.6$. The observed drop in the peak vorticity and tangential velocity between $x/c = 0.43$ and 0.6, together with the loss of regularity (as shown earlier in figures 4.3 and 4.6), allowed the determination of $(x/c)_{VBD}$ location at 0.54 of the regular delta wing. For $x/c > (x/c)_{VBD}$, the peak tangential velocity value became indiscernible and no circumferentially averaged peak tangential velocity was therefore reported here.

Finally, the change in the normalized core radius r_c/c and core circulation Γ_c/cu_∞ of the leading-edge vortex generated by the 65°-sweep slender delta wing at $\alpha = 25°$ is also summarized in figures 4.7(e)-(f). The core circulation was determined via the Stokes theorem. The grid size is interpolated from the raw data to be $\Delta y/c = \Delta z/c = 0.005$. The core radius of the leading-edge vortex was found to increase with x/c for $x/c < (x/c)_{VBD}$ for the regular delta wing (figure 4.7(e)). The smaller core radius in conjunction with a higher peak vorticity and tangential velocity also led to a concentrated and well-defined leading-edge vortex before its breakdown for $x/c \leq 0.54$; That is, the core circulation of the leading-edge vortex was found to increase continuously with x/c up to its breakdown location, followed by a drop for $x/c > (x/c)_{VBD}$ (see figure 4.7(f)). The identification of the peak tangential velocity and the core radius of the vortex will be discussed in the next section.

4.1.2 Aerodynamic characteristics of the slender reverse delta wing

Now the aerodynamics and vortex flow generated by the slender reverse delta wing are discussed. The results of the reverse delta wing were also compared to those of the regular delta wing of the same sweep angle. Figure 4.8(a) shows that the 65°-sweep regular delta wing (designated by DW65) had a better lift generation capability compared to its reverse delta wing (RDW) counterpart, especially for the high-angle of attack range, regardless of the magnitude of the Reynolds number. No lift force difference, however, exhibited between these two delta wing models for angle of attack smaller than 15°. The delta wing had a static-stall angle α_{ss} = 33° (or 35°) and a maximum total lift coefficient $C_{L,max}$ = 1.17 (or 1.15) for Re = 3.4×10^5 (or 1.1×10^4). For the reverse delta wing (RDW65), the stalling was found to occur at α_{ss} = 38° and 40° with a maximum lift coefficient of 0.93 and 0.963 for Re = 3.4×10^5 and 1.1×10^4, respectively.

In contrast to the leading-edge vortex (LEV) breakdown-induced stalling of the regular delta wing (see, for example, figures 4.9(a)-(b)), the stalling of the reverse delta wing was, however, induced by the breakdown of the multiple spanwise vortex filaments (SVFs) developed over the upper surface of the reverse delta wing (figure 4.9(c)-(d)). The SVFs originated from the spanwise leading-edge vortex as a result of the roll-up of the lower wall-shear layer along the leading edge of the reverse delta wing. At α = 14°, for example, the spanwise vortex filaments can be clearly identified and the reverse-delta-wing vortex remained concentrated (figures 4.9(c) and (e)). At α = 20°, SVF3 was, however, disrupted, as a consequence of the instability of the SVF and its interaction with the boundary-layer flow, rendering a diffused RDW vortex at $x/c \approx 0.8$ (figures 4.9(d) and 4.9(f)). With a further increase in the angle of attack (to the vicinity of the static-stall angle), all the SFVs were disrupted by the three-dimensional flow originating along the side edges of the reverse delta wing, creating a massively separated flow on the wing upper surface and the stalling of the reverse delta wing, suggesting that the real mechanism of lift the flow is on the lower side of the reverse delta wing while the upper side acted as a wake generator, especially at high angle of attack. That is to say, the reverse-delta-wing vortices have little relevance to lift generation of the wing. For a delta wing, it is known that the total lift can

be separated into potential and vortex lift components. The potential lift comes from the attached flow while the vortex lift comes from the presence leading-edge vortices. Hence, the leading-edge vortices are mainly responsible for lift at moderate to high angles of attack. However, because of the change in geometry, the leading edge of the reverse delta wing is longer than the delta wing leading edge. Hence, the lift force generated by the stagnation pressure on the bottom of the surface of the reverse delta wing is higher than the delta wing's. At high angle of attack, while vortex breakdown is present on the upper surface of the delta wing, the lift generation capability of the delta wing is lowered, while for the reverse delta wing, the lower surface still experiences a lift component from the stagnation pressure. The stagnation pressure is experienced on a smaller area for the delta wing due to a smaller span. Note that due to the location of the smoke wire, the spanwise leading-edge vortex filament was not visualized. The presence of the leading edge vortex filament can be found from the computational fluid dynamics (CFD) simulation of Altaf et al. (2011). Figures 4.9(a)-(d) further show that the reverse-delta-wing vortex was located outside the reverse delta wing while the leading-edge vortices lay above the regular delta wing. The vortex trajectory and the characteristics of the reverse-delta-wing vortex will be discussed in the next section via the PIV measurements.

To validate the present lift force measurements, the lift coefficient–α curves from Lowson & Riley (1995) for a 65°-sweep regular delta wing (i.e., DW65) at a chord Reynolds number $Re = 9 \times 10^5$ and Altaf et al. (2011) for both DW75 and RDW75 (i.e., 75°-sweep delta wing and 75°-sweep reverse delta wing) at $Re = 3.82 \times 10^5$ are also included in figure 4.8(a). The present measurements agreed well with published results. More interestingly, the RDW65 (i.e., the 65°-sweep reverse delta wing) was also found to have a reduced drag coefficient C_D compared to the DW65 at the same angle of attack (figure 4.8(b)). The higher drag coefficient associated with the DW65 can be attributed to the large profile drag caused by the presence of the leading-edge vortices. The subsequent leading-edge vortex breakdown led to a further increase in the drag coefficient of the 65°-sweep delta wing. On the other hand, due to the fact that the RDW vortices were found to be located outside the reverse delta wing upper surface and that the multiple spanwise vortex filaments remained attached to the wing upper surface up to a high-α regime, a lower-than-the-DW drag

coefficient was therefore observed. Figure 4.8(c) further demonstrates that at same lift condition the reverse delta wing produced a smaller drag coefficient than the delta wing. The lower lift generation of the 65°-sweep reverse delta wing together with the drag reduction led to a lift-to-drag ratio comparable to its delta wing counterpart (figure 4.8(d)). For both reverse delta wing and regular delta wing, the maximum lift-to-drag (C_L/C_D) value ($\approx$ 2.5) was attained at α = 10°. The variation in the lift-to-drag ratio at the same lift condition was also plotted in figure 4.8(e). As can be seen, the reverse delta wing also produced a lift-to-drag ratio improvement over the regular delta wing at the same lift condition.

The impact of the non-slenderness of the RDW50 (i.e., with a sweep angle Λ = 50°) on the aerodynamic characteristics was also explored at Re = 3.3×10^5 (denoted by ■ symbols in figure 4.8). The DW50 was found to stall at α_{ss} = 20° (with a $C_{L,max}$ of 0.83), as a result of the close vicinity of the DW50 vortex to the wing upper surface and its detrimental interaction with the boundary-layer flow, which led to an earlier leading-edge vortex breakdown and stalling than their slender regular delta wing counterpart. Surprisingly, the RDW50 was able to generate more lift than its delta wing counterpart for $\alpha \leq 10°$ (figure 4.8(a)). Due to the RDW50's increase in span with the decreased sweeping angle, the area over which the lower surface stagnation pressure acts is larger than other wing planforms, leading to a higher lift coefficient. The total lift coefficient, however, seemed to plateau for $\alpha > 10°$. The lift coefficient continued to increase gradually for $10° < \alpha \leq \alpha_{ss} = 24°$ (with a maximum lift coefficient $C_{L,max}$ = 0.6), followed by a minor decrease for $\alpha > 24°$. Meanwhile, the drag coefficient was found to increase monotonically with the angle of attack and had a lower value than its slender delta wing counterpart for $\alpha > 24°$ (figure 4.8(b)). The behavior of C_L–α and C_D–α curves of the RDW50 requires further investigations. Nevertheless, the lift-to-drag value of the non-slender reverse delta wing and regular delta wing are also included in figure 4.8 for reference.

In the next section, the streamwise structure and characteristics of the vortices developed along the 65°-sweep reverse delta wing for $0.1 \leq x/c \leq 1.5$ at α = 10° (which corresponds to angle of attack with the maximum C_L/C_D, i.e., $(C_L/C_D)_{max}$, value) were investigated by using

particle image velocimetry at Re = 11,000. It is noteworthy that the PIV technique not only provides the best resolution in the study of low-Reynolds-number vortex flow, but also eliminates the interference of the mechanical probes with the vortex flow (Payne et al. 1989). The *vw*-crossflow measurements were also used to compute the lift coefficient via Kutta-Joukowski theorem.

4.1.3 Reverse delta wing vortex flow structure and characteristics at $\alpha = 10°$

Figures 4.10(a)-(d) present the streamwise development of the normalized iso-vorticity ($\zeta c/u_\infty$) contours of the RDW vortex (or the reverse-delta-wing vortex) for $\alpha = 10°$ at selected x/c positions. The RDW vortex flow is characterized by an unique "arm-and-fist" RDW vortex pattern, which is a combination of the roll-up of the shear layer, originating from the pressure-side surface of the reverse delta wing, and the RDW vortex (initiated by the spanwise leading-edge vortex filament). The size of the RDW vortex and extent of the "arm" grew in length with increasing x/c. For $x/c \geq 0.7$, the strength of the shear layer became insignificant (as shown in figures 4.10(b)-(c)), suggesting a small shear-layer vorticity addition to the RDW vortex and, consequently, a near completion of the RDW vortex. At $x/c = 1.5$, a single RDW vortex existed. The streamwise vorticity ζ ($= \partial w/\partial y - \partial v/\partial z$) was calculated from the ensemble-averaged cross-flow (*vw*) velocity components by using a central differencing scheme to evaluate the derivatives. The PIV results shown here are ensemble-averaged over 60 particle-image-velocimetry images. No noticeable discrepancy was observed between ensemble averages of 40 and 80 PIV images in the present study. The iso-$\zeta c/u_\infty$ contours of the leading-edge vortex, or DW vortex, developed on the regular delta wing at the same angle of attack are also included in figures 4.10(e)-(h) for a direct comparison. For the DW vortex, the feeding sheet and the secondary vortex with vorticity of opposite sign are clearly visible at $x/c = 0.5$ (figure 4.10(e)). At $x/c \geq 1.5$, the feeding sheet and secondary vortex disappeared, leaving behind a single vortex structure similar to a wingtip vortex (figure 4.10(h)). Note that the leading-edge vortices always remained intact at $\alpha = 10°$.

The particle-image-velocimetry measurements also indicate that both the peak vorticity ζ_{peak} and peak tangential velocity $v_{\theta,peak}$ of the RDW vortex increased with x/c, reaching a local maximum at around $x/c = 0.2$ (suggesting a spanwise leading-edge vortex filament of a diameter of around 0.3c), and began to drop for $0.3 < x/c \leq 1.5$ (figures 4.11(a)-(b)). Meanwhile, the RDW vortex was found to locate outside the reverse delta wing but moved inboard and further above the wing with increasing x/c (figures 4.11(c)-(d)). The vortex center was identified by the position of the maximum vorticity ζ_{peak}. The peak tangential velocity was obtained from the tangential velocity distribution across the vortex center (figure 4.12(a)). Note that for $x/c > 0.7$ the RDW vortex center (identified by the peak vorticity ζ_{peak} value) coincides with the tangential velocity $v_\theta = 0$ position, suggesting a near completion of the RDW vortex rolling up and the existence of a nearly axisymmetric vortex with $v_{\theta,max} \approx |v_{\theta,min}|$. For $x/c < 0.7$, circumferential averaged $v_{\theta,peak}$ value was employed. The near axisymmetry (indicative of the attainment of full development) can also be demonstrated quantitatively from the radial circulation $\Gamma(r)$ distribution, normalized by the core circulation Γ_c, presented in figure 4.12(b). Figure 4.12(b) indicates that the RDW vortex at $x/c = 1.5$ followed an $\Gamma(r) \sim r^2$ profile for $r/r_c < 0.4$ and varied logarithmically for $0.5 < r/r_c < 1.4$, regardless of x/c; a phenomenon similar to that of a tip vortex generated by a rectangular NACA 0012 wing at $x/c = 2.5$ (Birch and Lee 2004). $\Gamma(r)$ is the radial circulation and r_c is the core radius. The empirical curve-fit relationships that describe the inner-core region and the region where the $\Gamma(r)$ distribution is logarithmic, according to Hoffman and Joubert (1963) and Phillips (1981), are $\Gamma(r)/\Gamma_c = a_1(r/r_c)^2$ for $r/r_c < 0.4$ and $\Gamma(r)/\Gamma_c = a_2\log(r/r_c) + a_3$ for $0.5 < r/r_c < 1.4$. The curve-fit constants are listed in figure 4.12(b), which are in good agreement to each other.

Figure 4.11(e) indicates that, at $\alpha = 10°$, the total circulation Γ_o (a direct indicative of the total lift force or the lift coefficient C_L) of the RDW vortex increased with x/c up to about $x/c = 0.7$ and attained a rather constant value (with $\Gamma_o \approx 0.1cu_\infty$) for $0.7 < x/c \leq 1.5$. The total circulation was determined via the Stokes theorem. The grid size is interpolated from the raw data to be $\Delta y/c = \Delta z/c = 0.005$. Also shown in figure 4.11(e) is the normalized total circulation versus x/c of the regular delta wing (DW) at $\alpha = 10°$. By contrast, the total

circulation of the DW vortex continued to increase up to the trailing edge of the wing, reaching a virtually constant (with $\Gamma_o \approx 0.145cu_\infty$) for $x/c \geq 1.0$. The inner flow of the DW vortex only attained near axisymmetry for $x/c \geq 1.5$. The axisymmetric and non-axisymmetric behavior of the DW vortex can be demonstrated from the v_θ distributions plotted in figure 4.12(a). For $x/c < 1.5$, the $v_{\theta,max} \neq |v_{\theta,min}|$ condition persisted for the DW vortex. At $x/c = 1.5$, the DW vortex became axisymmetric (with $v_{\theta,max} = |v_{\theta,min}| = v_{\theta,peak}$), satisfying Hoffman & Joubert's model (see figure 4.12(b)). Note that the DW vortex also exhibited a higher peak vorticity and peak tangential velocity than the RDW vortex at the same x/c (figures 4.11(a)-(b)), suggesting a more concentrated DW vortex than the RDW vortex at the same α and x/c. For the DW vortex, both ζ_{peak} and $v_{\theta,peak}$, however, exhibited a local maximum at around $x/c = 0.6 - 0.7$. Furthermore, in contrast to the inboard movement of the RDW vortex, the DW vortex was found to be displaced outboard and closer to the wing upper surface compared to the reverse delta wing counterpart (figures 4.11(c)-(d)). More importantly, the total circulation Γ_o value was also used to compute the lift coefficient C_L via Kutta-Joukowski theorem ($L = \rho u_\infty \Gamma_o b'$, where L is the lift force, and b′ is the effective span which is twice the distance between the observable core of the DW or RDW vortex and the wing center plane). Figure 4.11(f)) shows that the PIV-derived lift coefficient had a value of about 0.35 for the delta wing for $x/c > 1.25$ and the reverse delta wing for $x/c > 0.7$, respectively, which is in good agreement with the force balance measurement of $C_L = 0.36$ at $\alpha = 10°$. The PIV-derived lift coefficient and the RDW vortex flow characteristics at different angles of attack are now discussed.

4.1.4 PIV-derived total lift coefficient C_L and reverse-delta-wing vortex at various angles of attack

Figure 4.8(a) shows the PIV-derived C_L value (denoted by ♦ symbol), based on the total circulation Γ_o and effective span b′ at a streamwise position $x = 1.01c$, as a function of angle of attack for the reverse delta wing. The b′-based C_L computation was slightly lower than the corresponding force-balance data. The PIV-derived lift coefficient computation was limited to $\alpha = 23°$ which was based on the fact that the RDW vortex remained concentrated

and axisymmetric for $\alpha \leq 16°$ (figures 4.13(a)-(b)) and became diffused for $16° < \alpha \leq 23°$ (figures 4.13(c)-(e)). For $\alpha > 23°$, the RDW vortex resembled a weak circulation-like flow with small patches of vorticity (figure 4.13(f)). Kaplan and Altman (2007) attempted to use a similar PIV-based C_L calculation for a delta wing with an aspect ratio of two and tried to scale by both b and b'. Comparison with force balance results revealed that b' underestimates while b overestimates the lift coefficient. The mechanisms responsible for the above-mentioned various states of the RDW vortex in different angle of attack regimes can be explained by the behavior of the unique multiple spanwise vortex filaments developed on the upper wing surface, as discussed previously in figures 4.9(c)-(d). Figure 4.9(c) shows the formation of three distinct spanwise vortex filament at $\alpha = 14°$. The well concentric and circular RDW vortex can also seen from the two tips of the leading edge. This represents the concentric and axisymmetric state of the RDW vortex. As the angle of attack is increased to $\alpha = 20°$ (figure 4.9(d)), the SVF3 is seen to be disrupted and diffused, and all three SVFs have also moved upstream. The wake-like flow downstream of SVF3 can be seen to diffuse outside of the upper surface of the RDW and interact with the RDW vortex. This leads to a diffused RDW vortex, with a bigger diameter vortex shown in Figure 4.9(c). As the angle of attack is increased furthermore, the SVFs are all completely disrupted and the upper surface of the reverse delta wing acts as a wake generator. The RDW vortices generated at this state are thus circulation-like with small patches of vorticity.

The lift coefficients, calculated based on the total vortex strength Γ_o and the wing span b, are also included in figure 4.8 (denoted by $\Diamond$ symbol). The b-based C_L had a much higher magnitude than the force-balance data, especially at higher α range. It therefore suggests that the effective span b′ seems to be the more relevant length scale and that the Kutta-Joukowski theorem is also applicable to the reverse delta wing. It is of interest to note that the b′-based PIV-derived C_L values of 0.341 and 0.421 at $\alpha = 10°$ and 12° of the regular delta wing in comparison to 0.362 and 0.441 from the force balance measurements were also obtained in the present study. The PIV-derived C_L determination had also been employed by Kaplan et al. (2007) of a regular 63.5°-sweep delta wing at Re = 24,000.

The variation of the normalized total and core circulation (Γ_o and Γ_c), peak vorticity ζ_{peak} and peak tangential velocity $v_{\theta,peak}$, and the vortex trajectory (y_c and z_c) with the angle of attack of the RDW vortex is also summarized in figure 4.14. For $\alpha > 16°$, circumferentially averaged $v_{\theta,peak}$ values are used. As expected, the vortex strength increased monotonically with the angle of attack (figure 4.14(a)), which is in agreement with the force balance measurements. The concentrated RDW vortex also produced a continuous increase in both ζ_{peak} and $v_{\theta,peak}$ for $\alpha \leq 16°$, and started to decrease for $\alpha > 16°$ (figure 4.14(b)). Meanwhile, the vortex center was found to move further inboard and above the wing upper surface with increasing α for $\alpha \leq 22°$ (figure 4.14(c)). The large inboard movement of the RDW vortex at high angles of attack further expedited the interaction of the RDW vortex with the separated flow, leading to the observed messy circulation-like flow presented in figure 4.13(f).

The concentration and diffusion of the RDW vortex can be further illustrated by the streamwise evolution of the iso-vorticity contours at $\alpha = 14°$ and 20° presented in figure 4.15(a). To be concise, the results of $\alpha = 14°$ and 20° are plotted three-dimensionally and jointly in figure 4.15(a). At $\alpha = 20°$ (plotted on the right-hand side in figure 4.15(a)), the vortex remained concentrated until $x/c \approx 0.8$ and became diffused further downstream, as a result of the disruption of the spanwise vortex filament SVF3 (as shown previously in figure 4.9(d)). At $\alpha = 14°$, the spanwise vortex filaments, however, stayed basically intact, leading to a concentrated and axisymmetric RDW vortex throughout the x/c studied. To aid the illustration, enlarged insets at selected $x/c = 0.6$ and 0.9 are also included in figure 4.15(a), which clearly illustrated the status of the RDW vortex at these two representative angles of attack. The evolution of the DW vortex, or the leading-edge vortices, along the regular delta wing at $\alpha = 14°$ and 24° are also plotted jointly in figure 4.15(b) for a direct comparison. The DW vortex remained intact for $\alpha = 14°$. At $\alpha = 24°$, the DW vortex breakdown occurred at $x/c = 0.53$, identified by the large diffusion and broadening of the DW vortex (see the enlarged insets between $x/c = 0.51$ and 0.54 in figure 4.15(b)).

At last, the streamwise variation of the vortex flow parameters of the RDW vortex with α (= 8°, 10°, 14°, 16°, and 20°) is also summarized in figure 4.16. The RDW vortex was found to displace consistently further inboard and upward as the angle of attack was increased (figures 4.16(a)-(b)). The total circulation increased with the angle of attack, becoming rather insensitive to x/c for $x/c > 0.7$, regardless of α (figure 4.16(c)). Meanwhile, the peak vorticity and tangential velocity were always found to increase with x/c and the angle of attack, reaching a local maximum in the vicinity of $x/c = 0.2$, and began to decrease as the RDW vortex progressed further downstream (figures 4.16(d)-(f)). The diffusion of the RDW vortex at $\alpha = 20°$ gave rise to a reduced peak vorticity and tangential velocity.

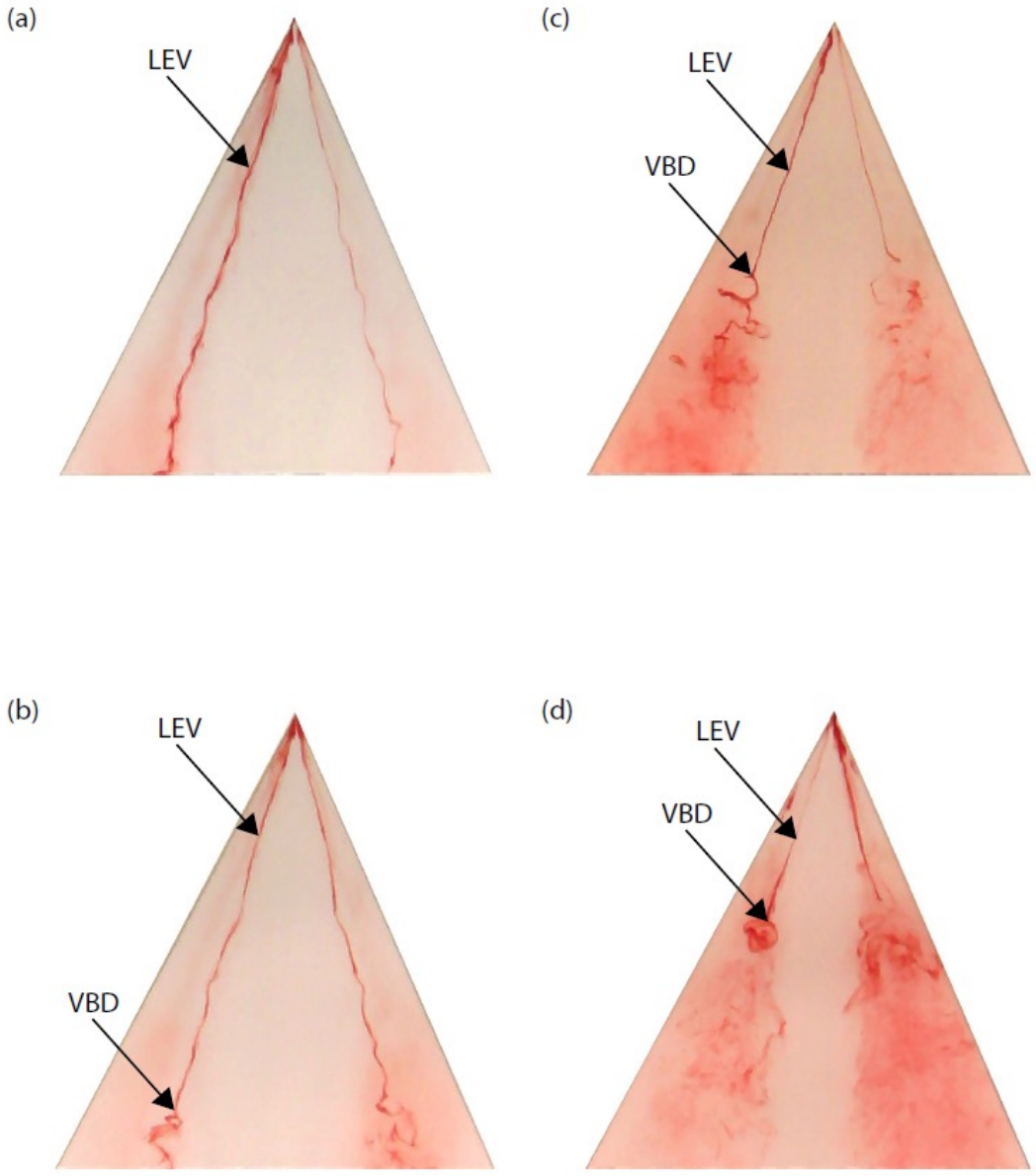

Figure 4.1 Dye-injection flow visualization showing the growth and development of the leading-edge vortices over the 65°-sweep delta wing at selected angles of attack. (a) α = 17° and $(x/c)_{VBD}$ = 1.0; (b) α = 19.5° and $(x/c)_{VBD}$ = 0.87; (c) α = 24.5° and $(x/c)_{VBD}$ = 0.56; (d) α = 27° and $(x/c)_{VBD}$ = 0.45; (e) α = 29.5° and $(x/c)_{VBD}$ = 0.35; (f) α = 32° and $(x/c)_{VBD}$ = 030; and (g) α = 34.5° and $(x/c)_{VBD}$ = 0.27. LEV denotes leading-edge vortex. (x/c)VBD denotes vortex breakdown location.

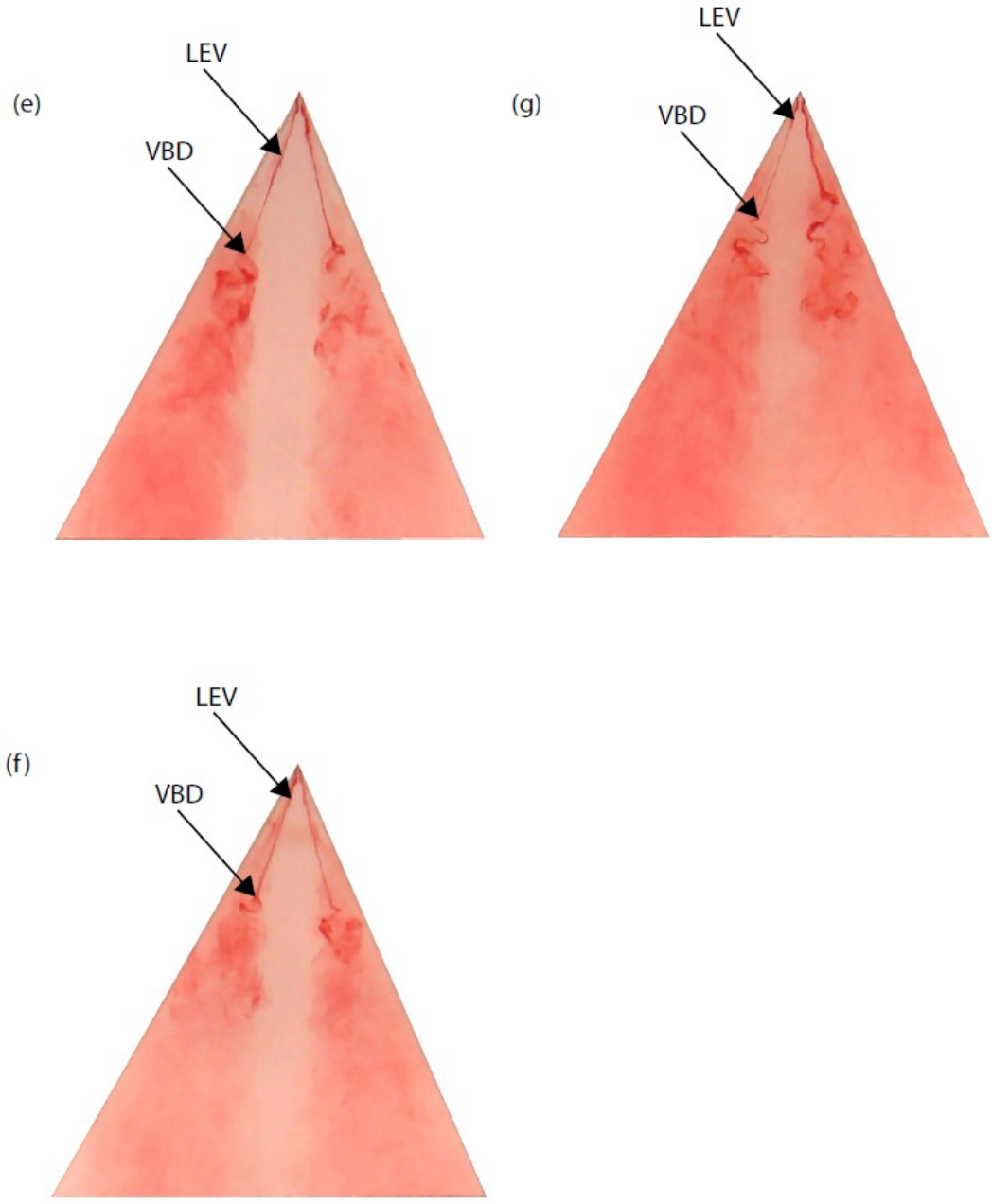

Figure 4.1 Dye-injection flow visualization showing the growth and development of the leading-edge vortices over the 65°-sweep delta wing at selected angles of attack. (a) α = 17° and $(x/c)_{VBD}$ = 1.0; (b) α = 19.5° and $(x/c)_{VBD}$ = 0.87; (c) α = 24.5° and $(x/c)_{VBD}$ = 0.56; (d) α = 27° and $(x/c)_{VBD}$ = 0.45; (e) α = 29.5° and $(x/c)_{VBD}$ = 0.35; (f) α = 32° and $(x/c)_{VBD}$ = 030; and (g) α = 34.5° and $(x/c)_{VBD}$ = 0.27. LEV denotes leading-edge vortex. (x/c)VBD denotes vortex breakdown location.

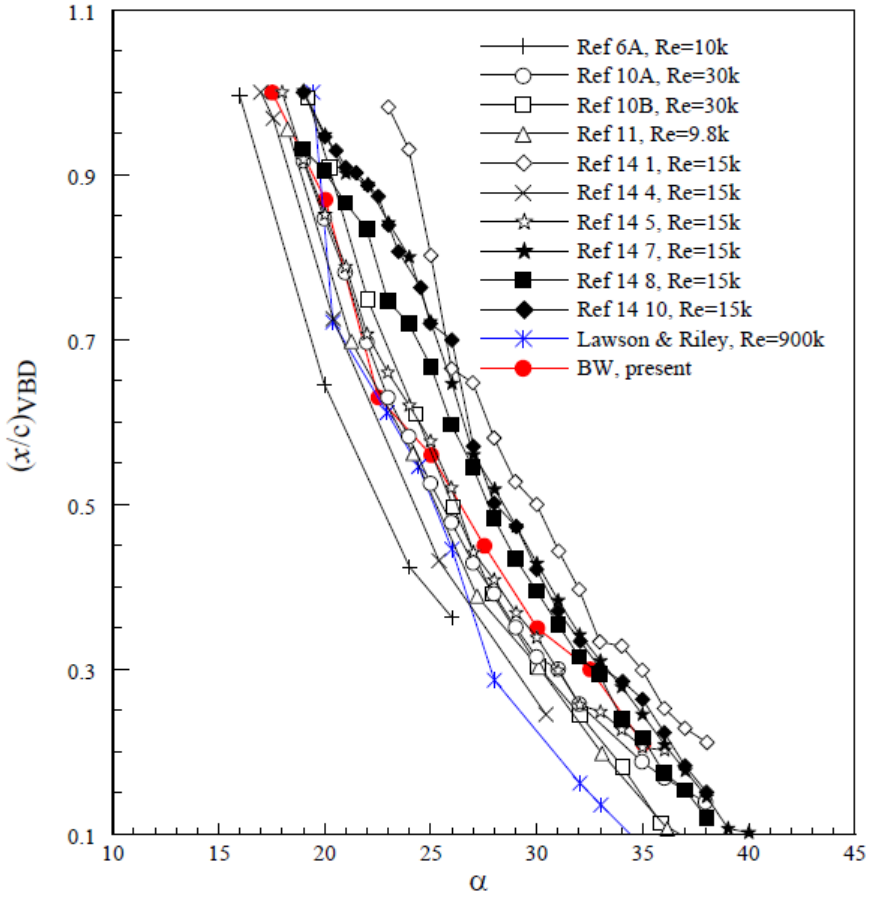

Figure 4.2 Leading-edge vortex breakdown locations as a function of angle of attack.

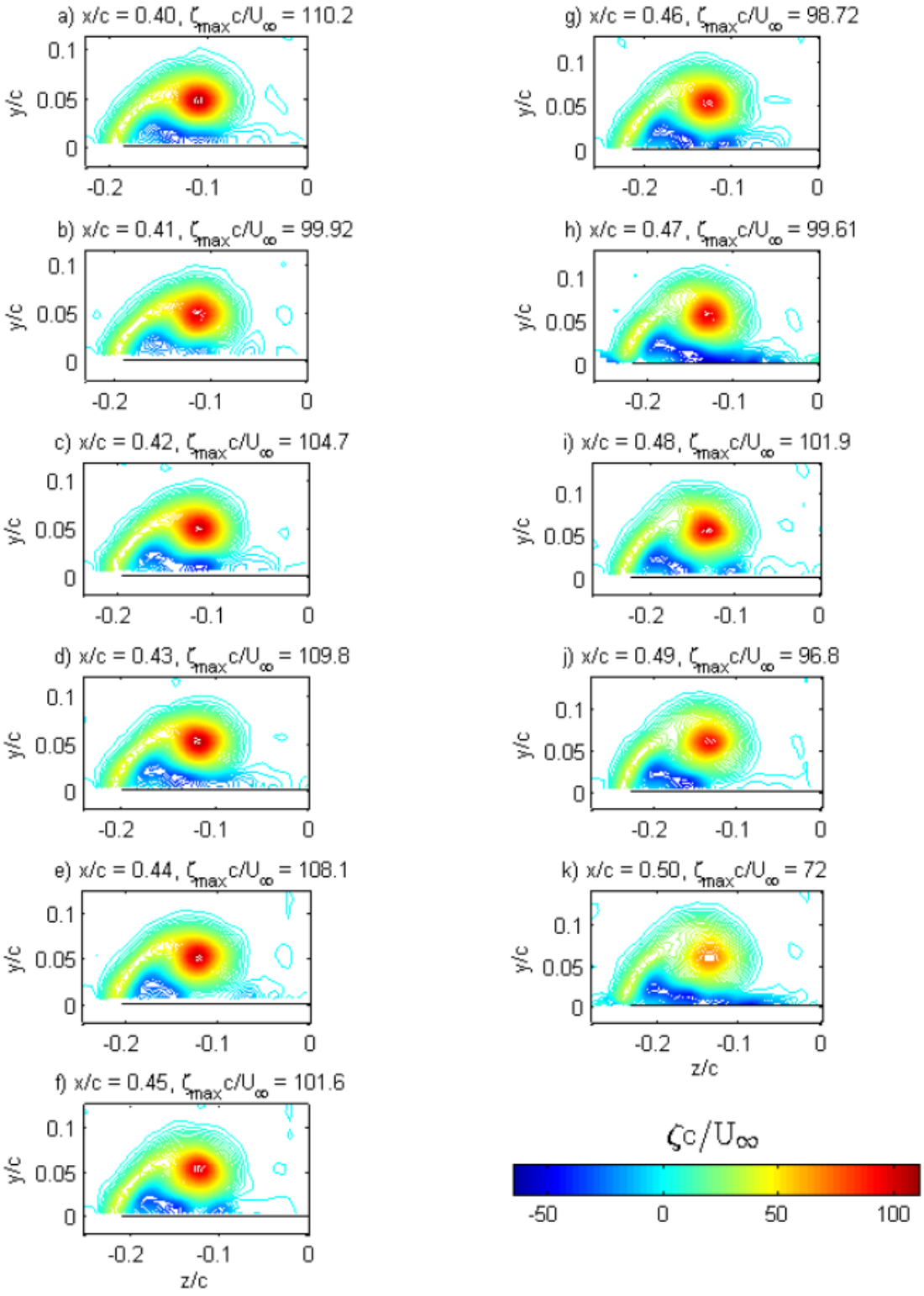

Figure 4.3 Particle-image-velocimetry sliced images in the vicinity of leading-edge vortex breakdown location with an $\Delta x/c = 0.01$ increment at $\alpha = 24°$.

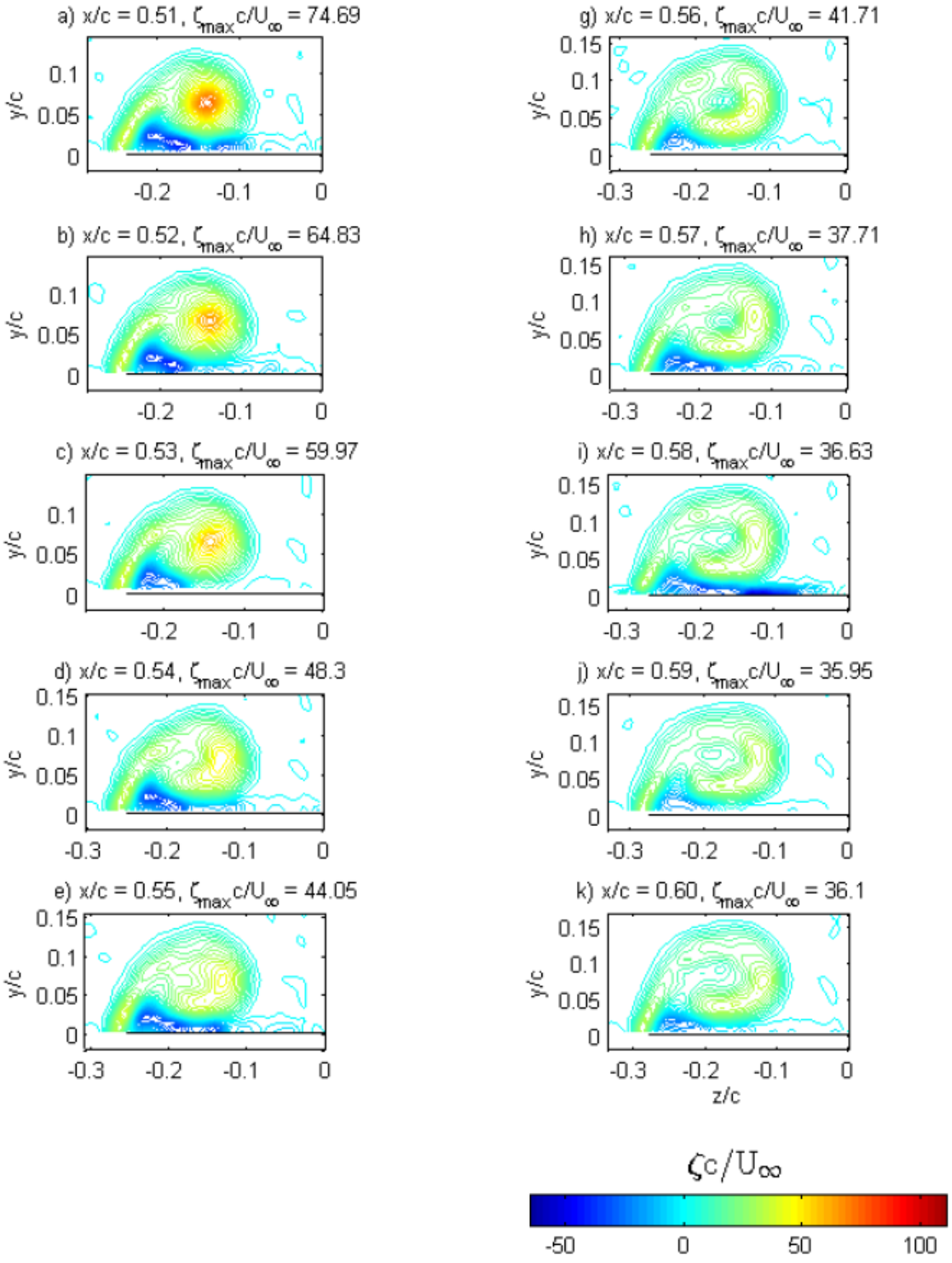

Figure 4.3 Particle-image-velocimetry sliced images in the vicinity of leading-edge vortex breakdown location with an $\Delta x/c = 0.01$ increment at $\alpha = 24°$.

(a)

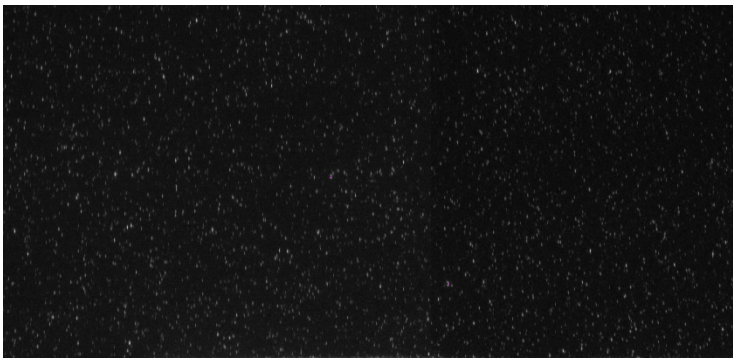

(b)

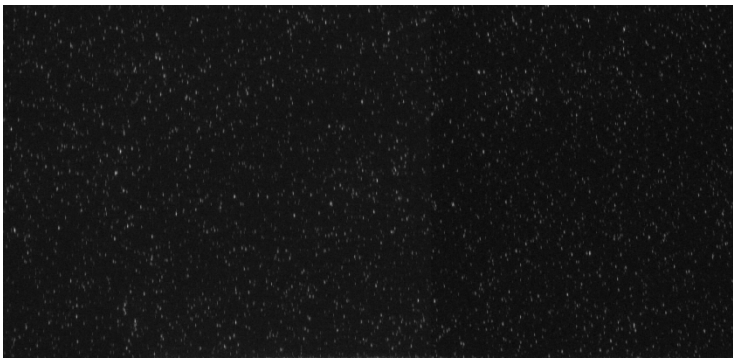

(c)

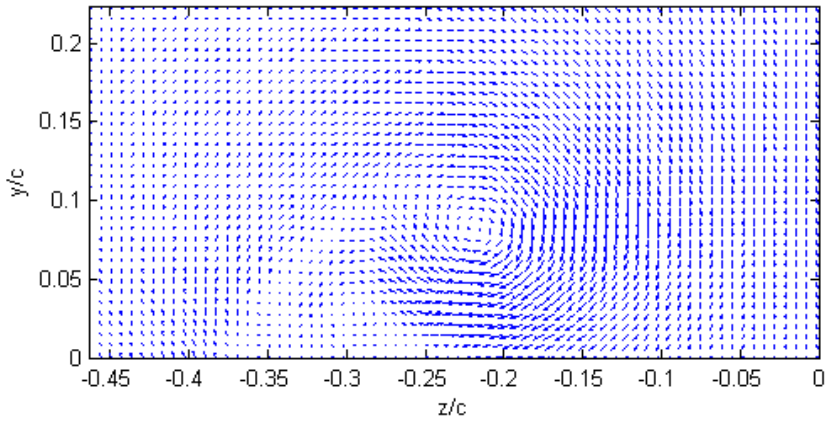

Figure 4.4 Typical particle images for a field of view is 13 cm in length and 7 cm in height at x/c = 0.8 and α = 18° of the delta wing. (a) Raw image I, (b) raw image II, (c) velocity vector over ensemble-averaging of 60 images, and (d) iso-vorticity contour, and (e) iso-vorticity contour overlapped with velocity vector.

(d)

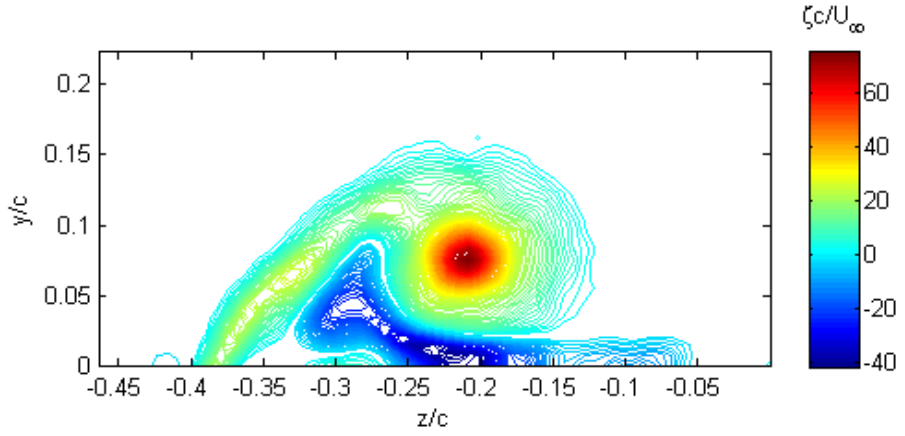

(e)

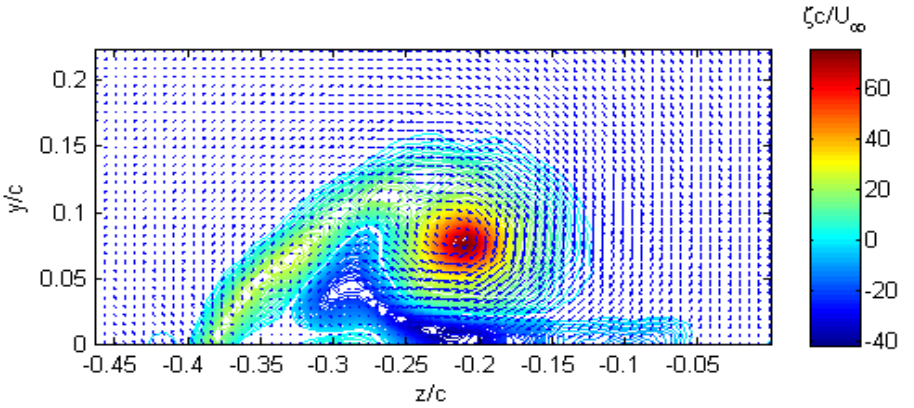

Figure 4.4 Typical particle images for a field of view is 13 cm in length and 7 cm in height at $x/c = 0.8$ and $\alpha = 18°$ of the delta wing. (a) Raw image I, (b) raw image II, (c) velocity vector over ensemble-averaging of 60 images, (d) iso-vorticity contour, and (e) iso-vorticity contour overlapped with velocity vector.

(a)

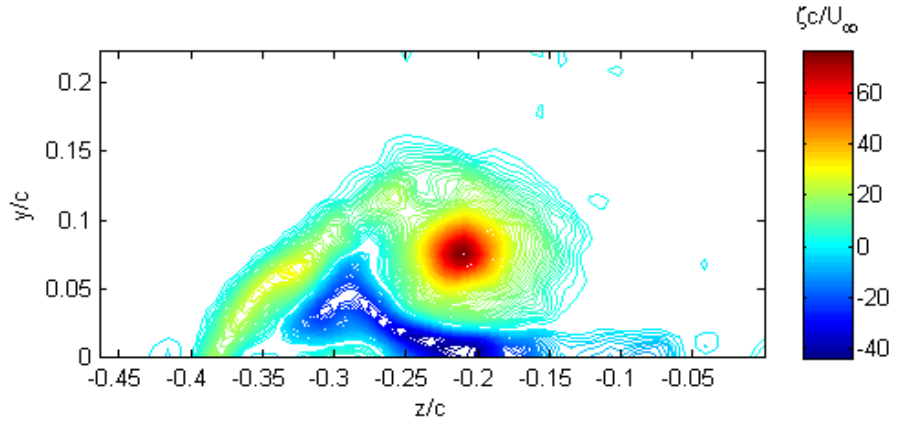

(b)

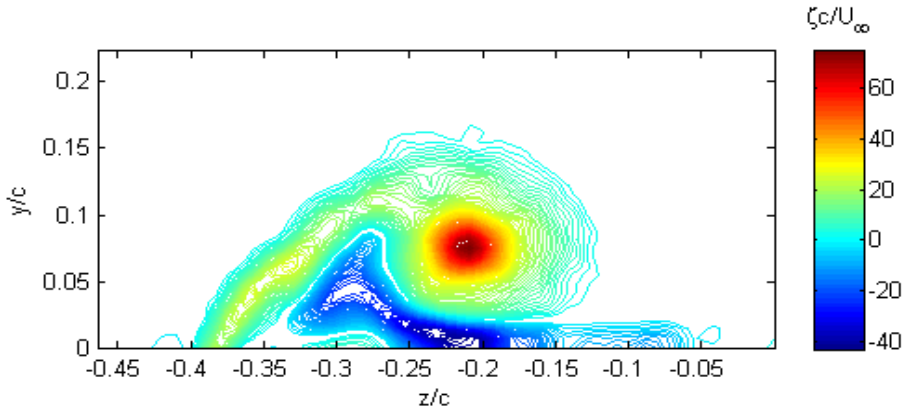

(c)

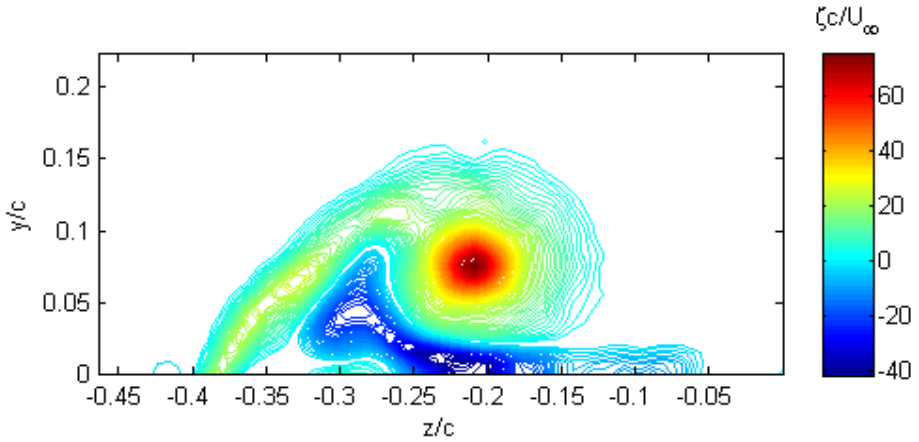

Figure 4.5 Effect of number of PIV images on ensemble average iso-vorticity for $\alpha = 18°$ at $x/c = 0.8$. (a) Ensemble average over 20 images, (b) ensemble average over 40 images, and (c) ensemble average over 60 images.

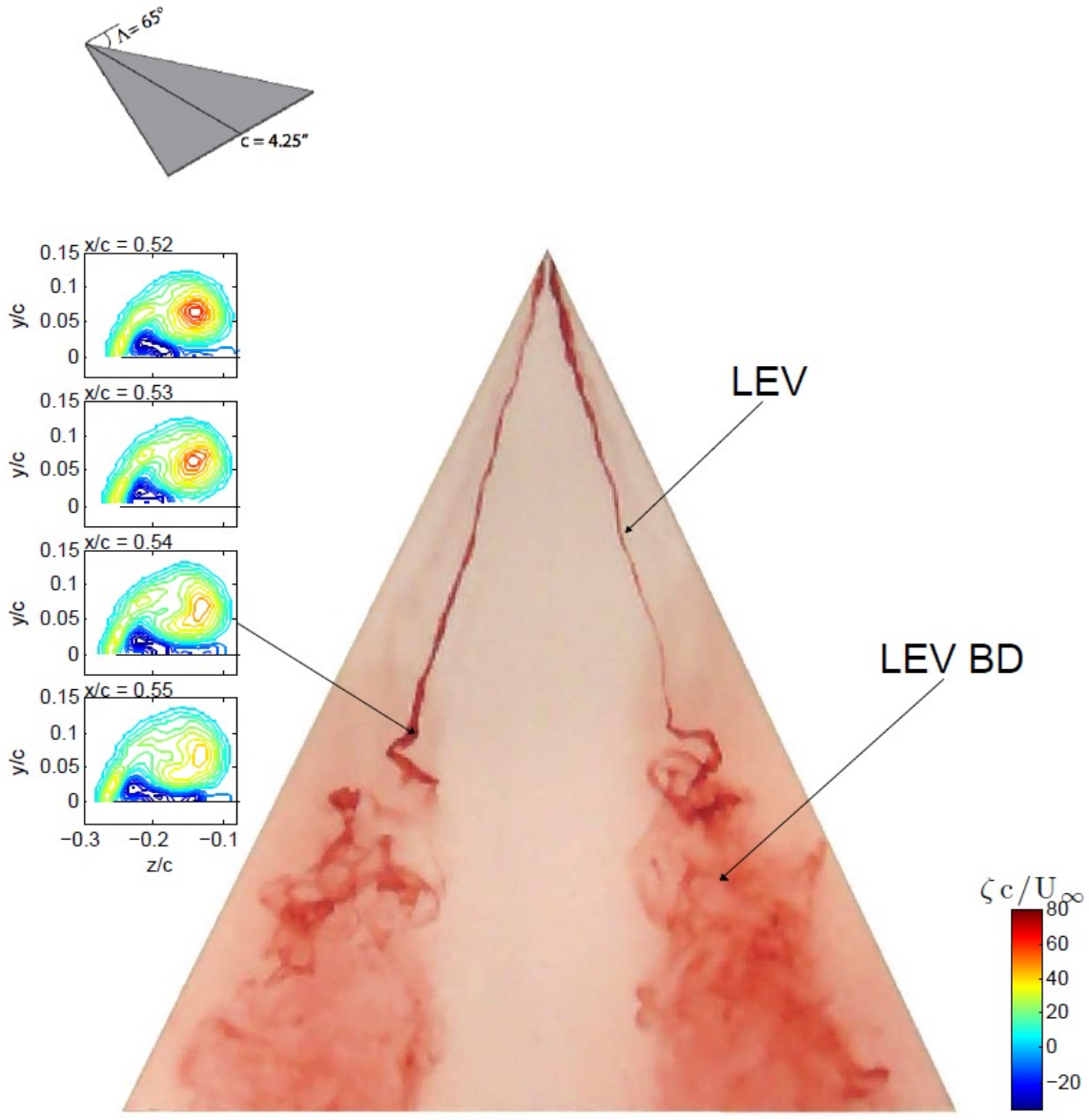

Figure 4.6 Joint dye flow visualization and particle-image-velocimetry results showing the leading-edge vortex breakdown location at $\alpha = 24°$.

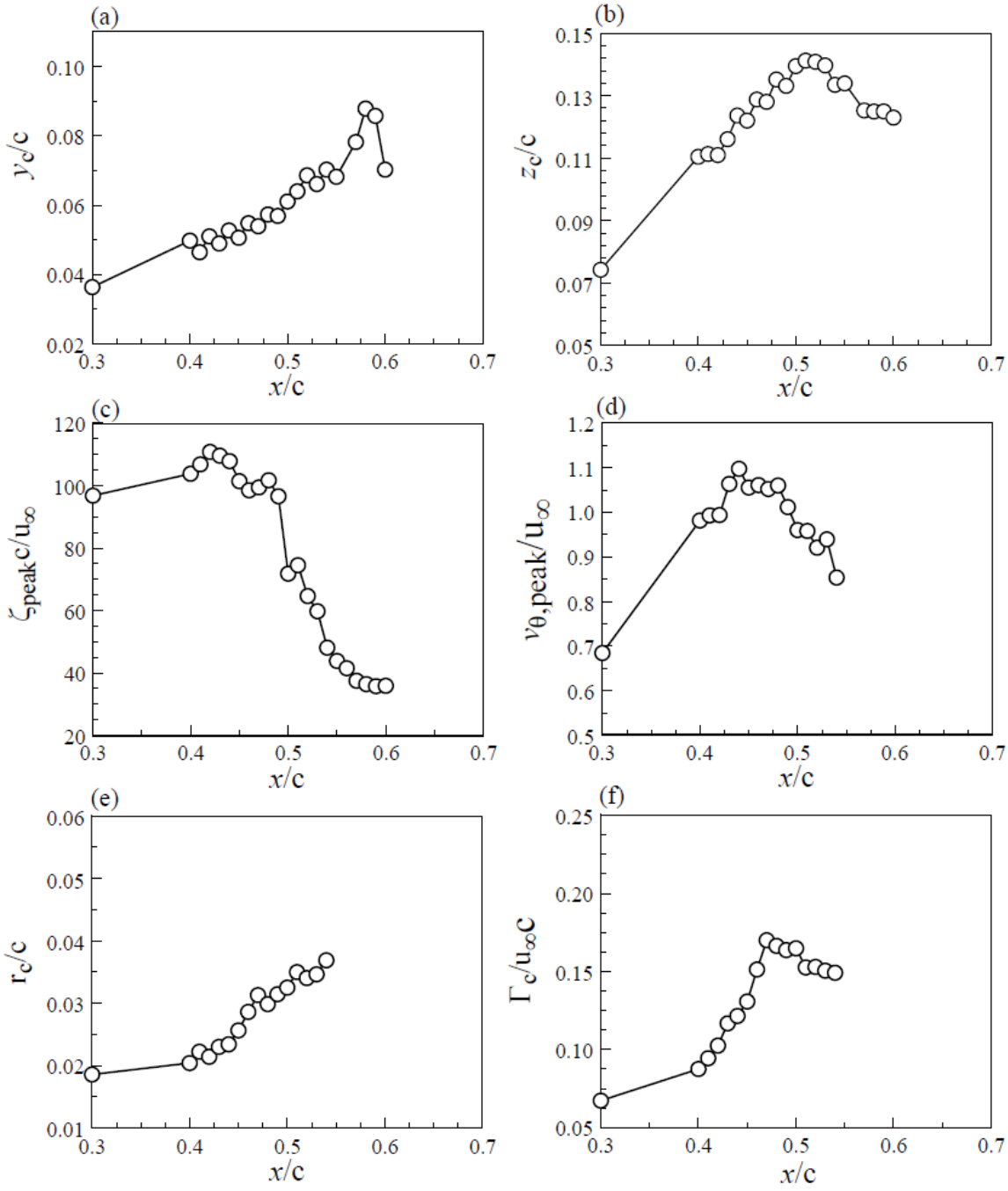

Figure 4.7 Variation of normalized leading-edge vortex flow parameters of the 65°-sweep delta wing with the streamwise distance x/c at $\alpha = 25°$.

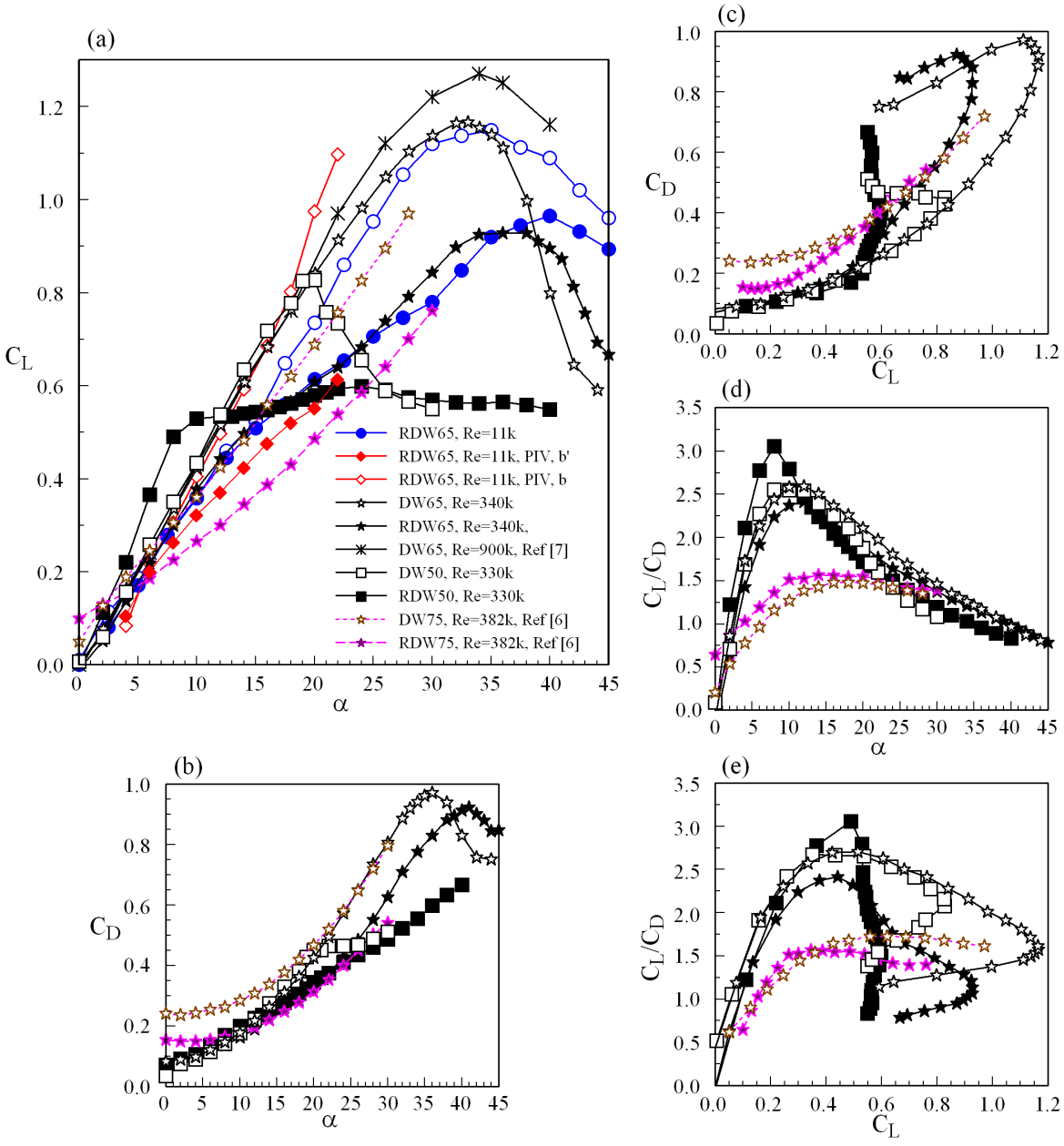

Figure 4.8 Aerodynamic characteristics of DW and RDW at different Re. DW and RDW denote regular delta wing and reverse delta wing, respectively.

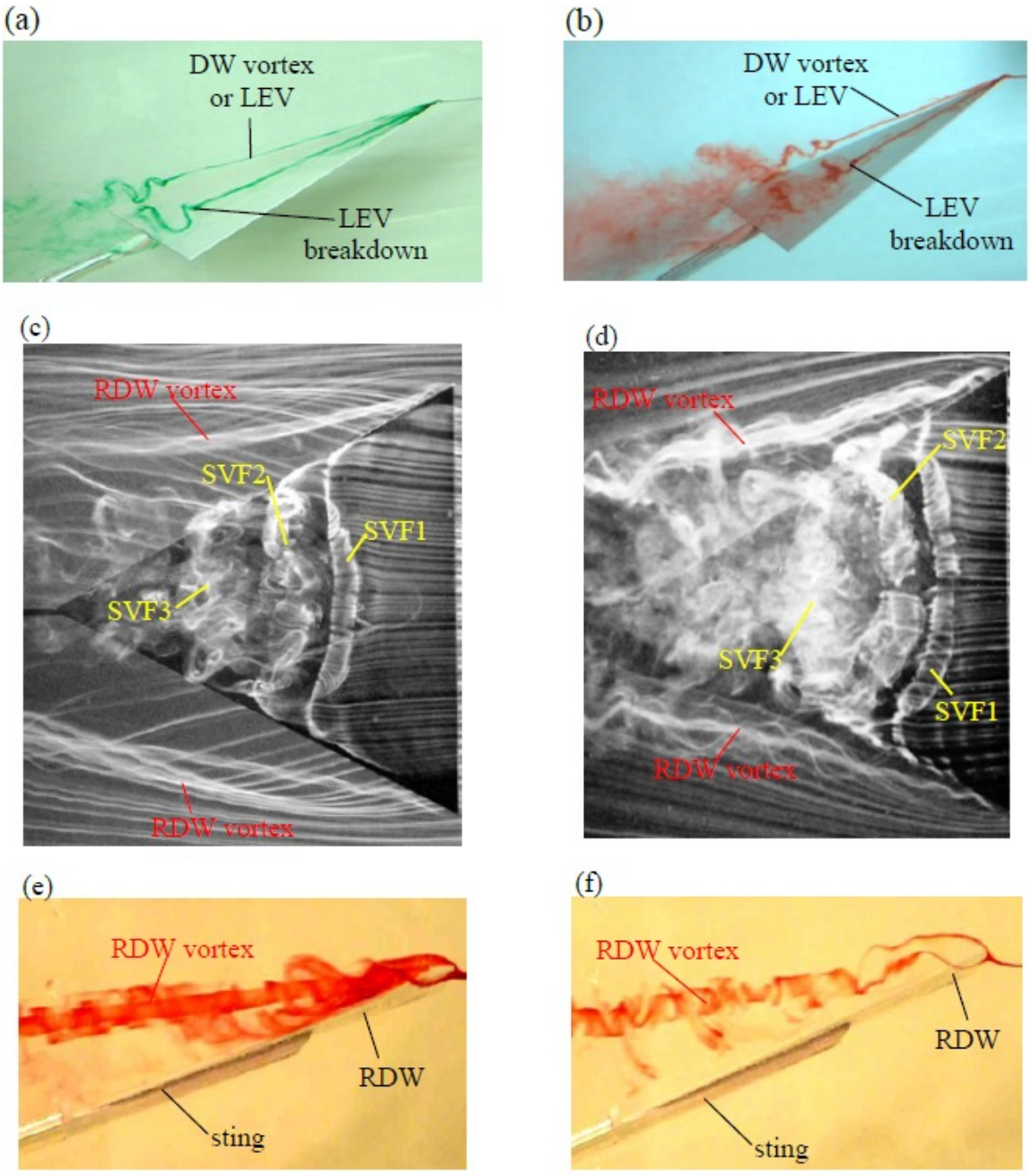

Figure 4.9 Photos of flow visualization. The flow is from right to left. DW: (a) α = 19° and (b) α = 27.5°. RDW: (c) and (e) α = 14°; (d) and (f) α = 20°. (g) Sketch of the boundary layer flow on RDW upper surface. SVF denotes spanwise vortex filament. DW and RDW denote delta wing and reverse delta wing, respectively.

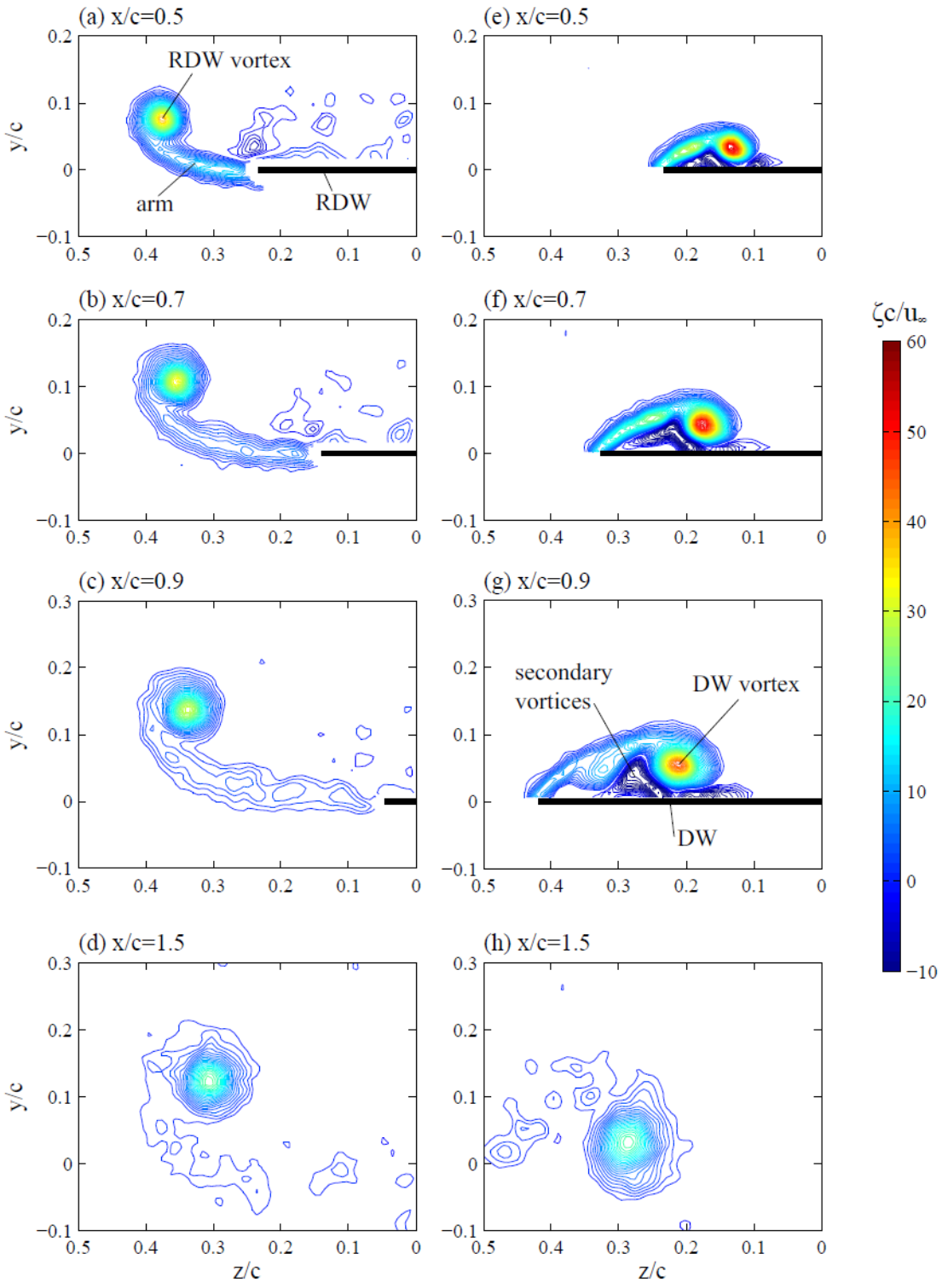

Figure 4.10 Representative normalized iso-vorticity contours of RDW vortex and DW vortex at selected x/c for $\alpha = 10°$. DW and RDW denote delta wing and reverse delta wing, respectively.

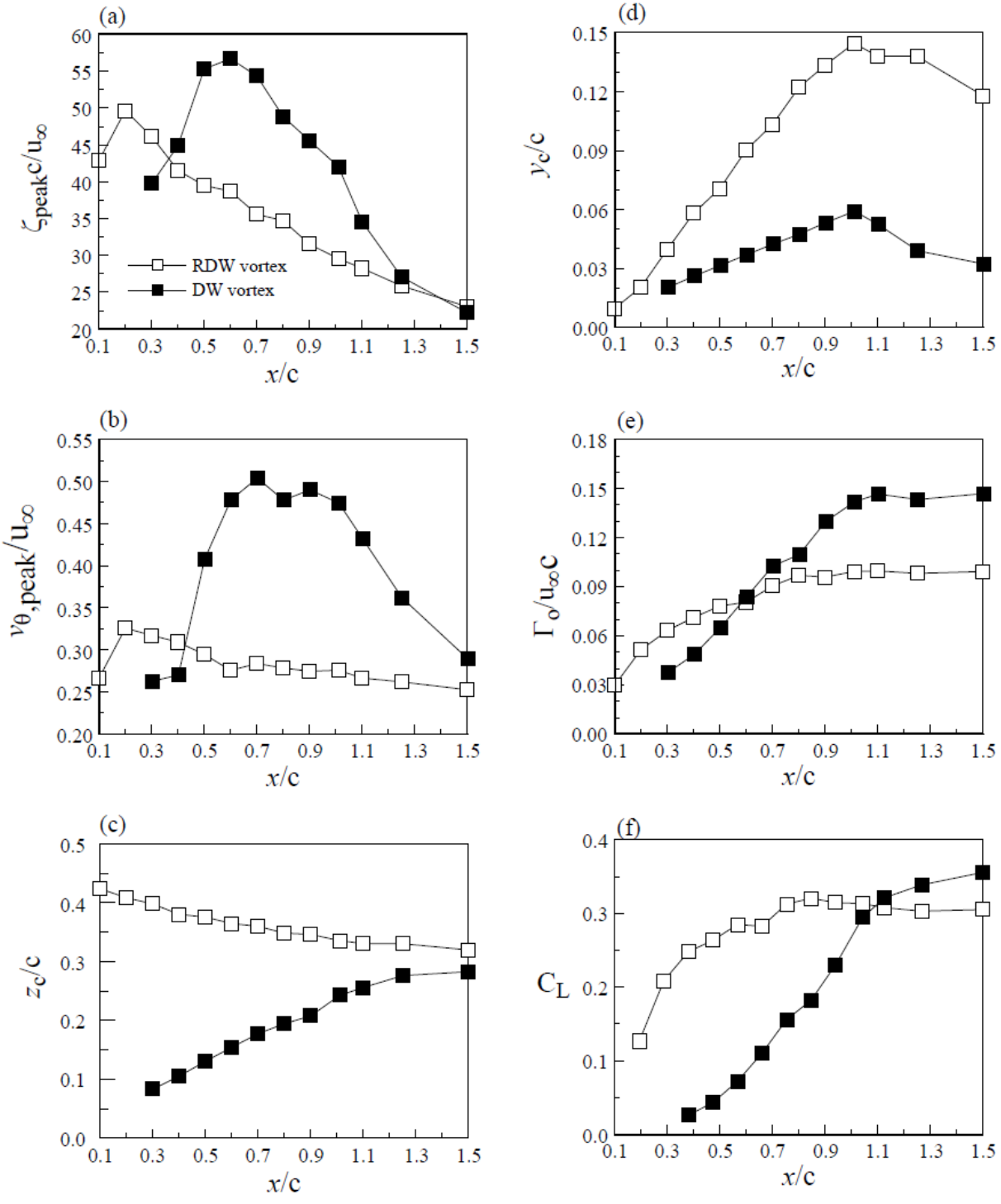

Figure 4.11 Variation of RDW vortex and DW vortex flow parameters and PIV-derived C_L with x/c at $\alpha = 10°$. PIV denotes particle image velocimetry. C_L denotes total lift coefficient.

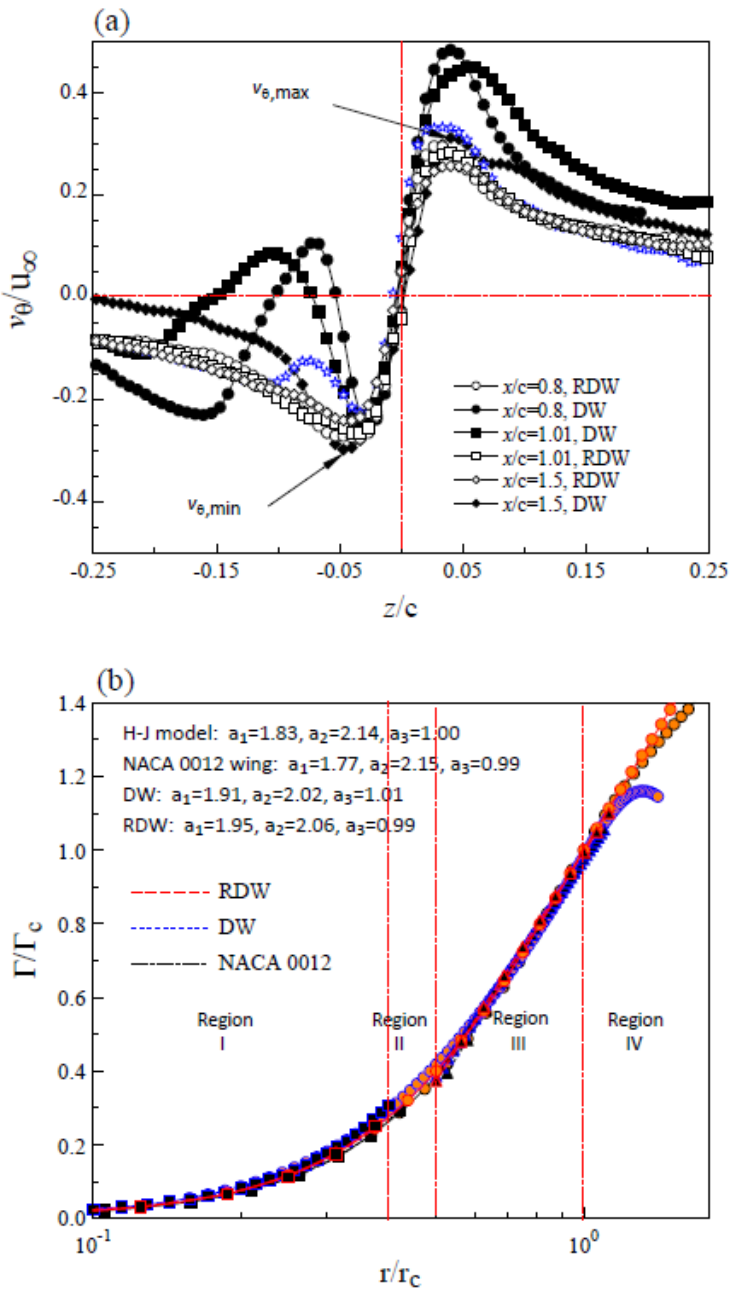

Figure 4.12 Normalized (a) tangential velocity distributions across vortex center and (b) circulation behavior at α = 10°. I: linear region; II: buffer region; III: logarithmic region; and IV: wake region. H-J model denotes Hoffman and Joubert model (1963). RDW: x/c = 1.01 and α = 10°. DW: x/c = 1.5 and α = 10°. NACA 0012 wing: x/c = 2.5 and α = 9°. RDW and DW denote reverse delta wing and regular delta wing, respectively.

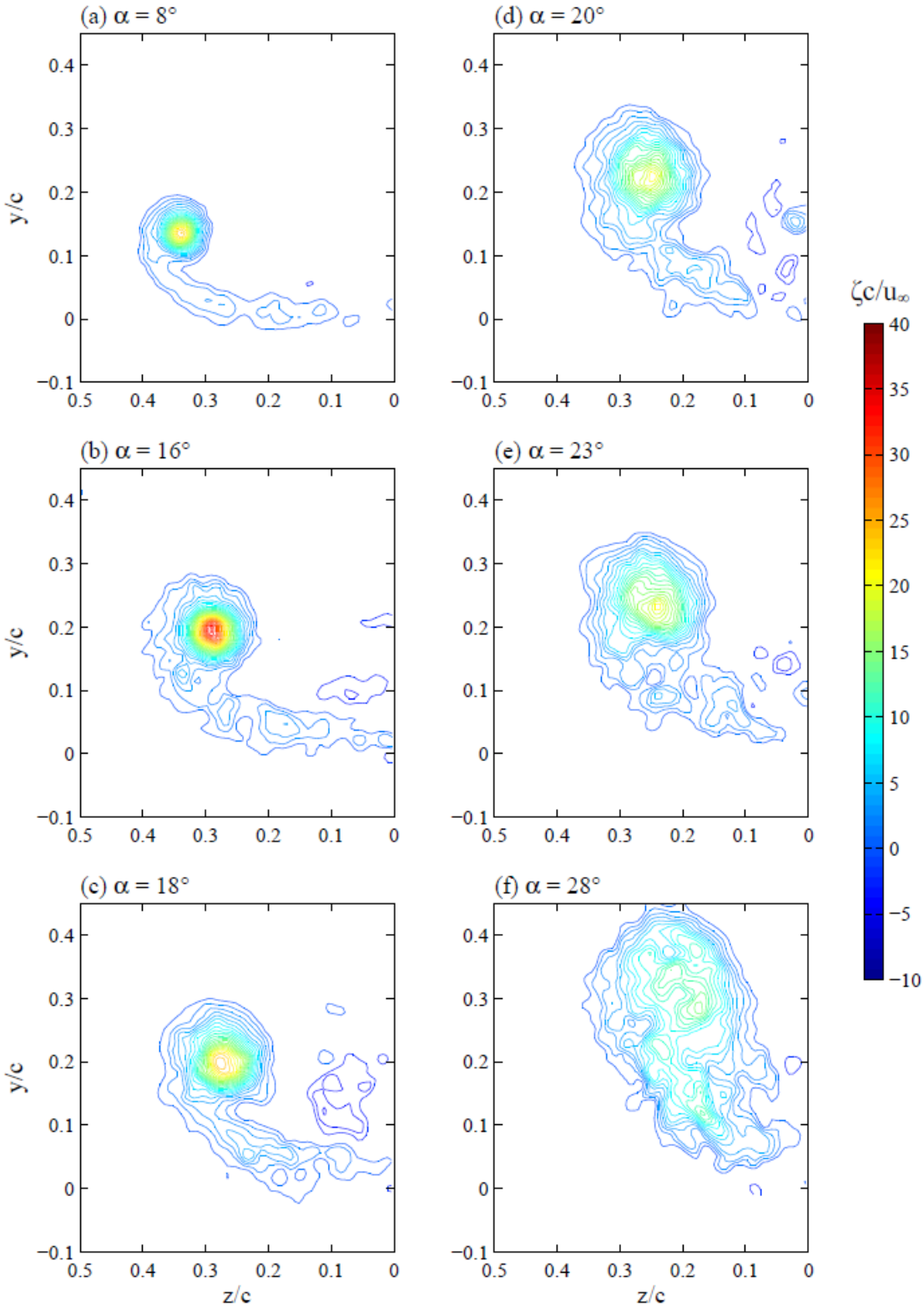

Figure 4.13 Representative normalized iso-vorticity contours of the RDW vortex at x/c = 1.01 for selected angles of attack.

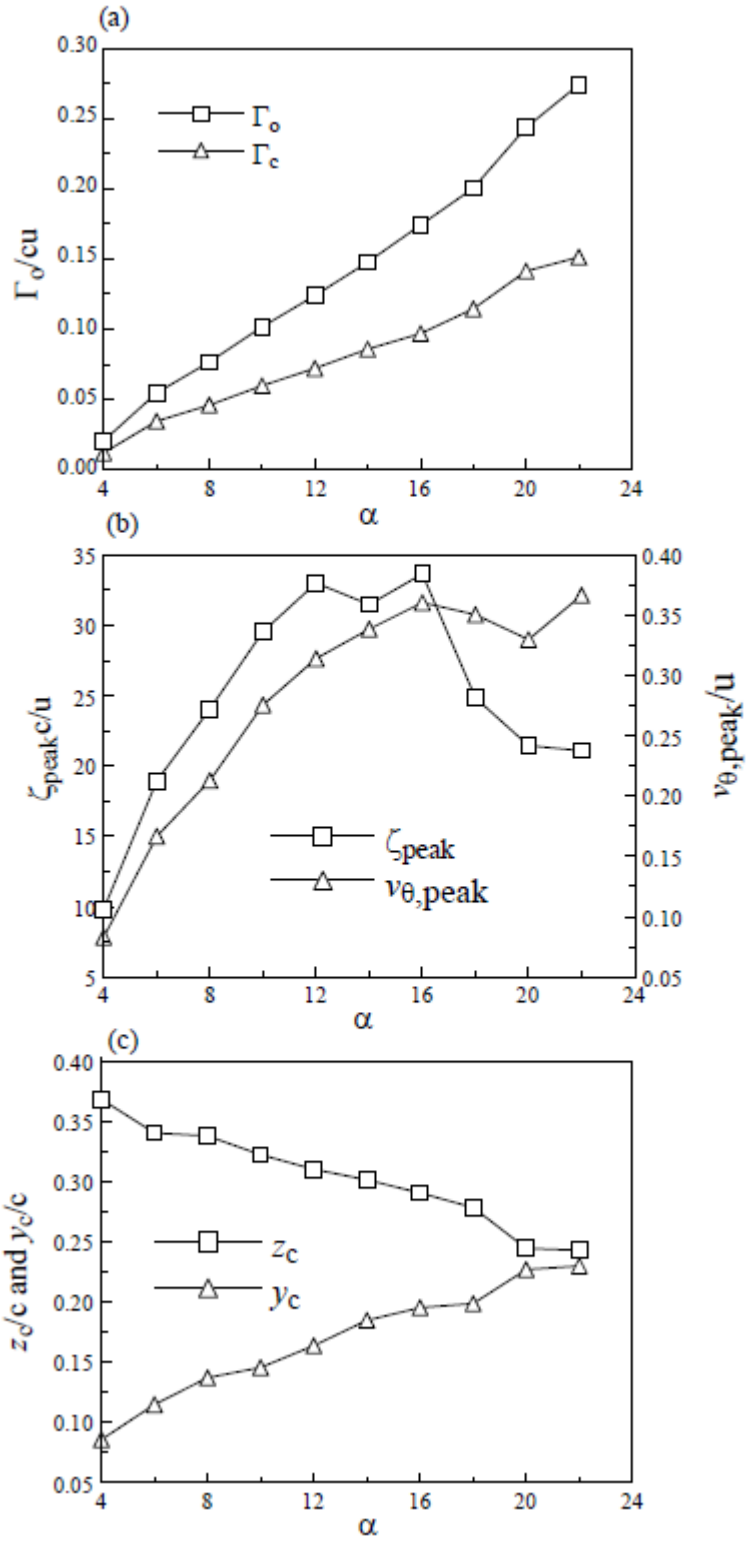

Figure 4.14 Variation of normalized reverse-delta-wing (RDW) vortex flow parameters with α at x/c = 1.01.

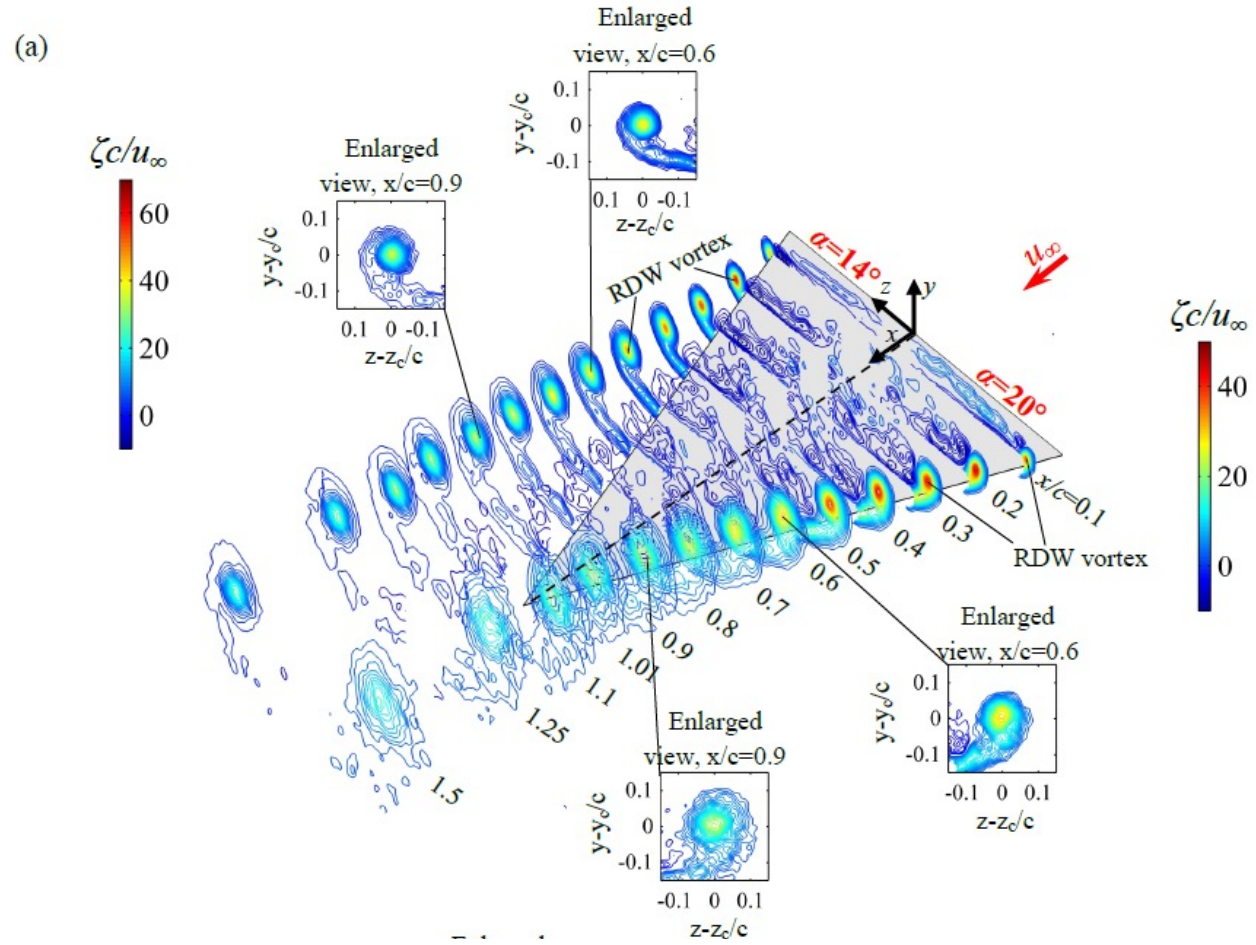

Figure 4.15 Joint three-dimensional representation of iso-ζc/u∞ contours. (a) Reverse delta wing (RDW) at α = 14° and 20°; (b) delta wing (DW) at α = 14° and 24°.

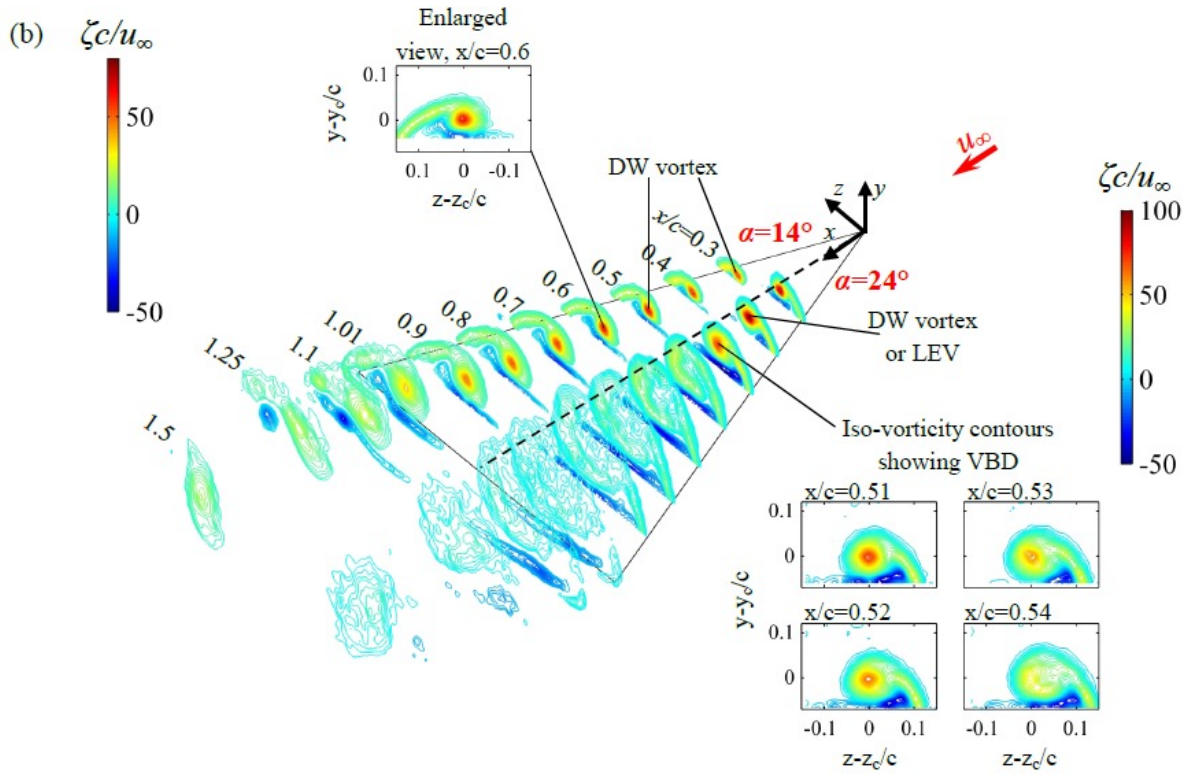

Figure 4.15 Joint three-dimensional representation of iso-ζc/u∞ contours. (a) Reverse delta wing (RDW) at α = 14° and 20°; (b) delta wing (DW) at α = 14° and 24°.

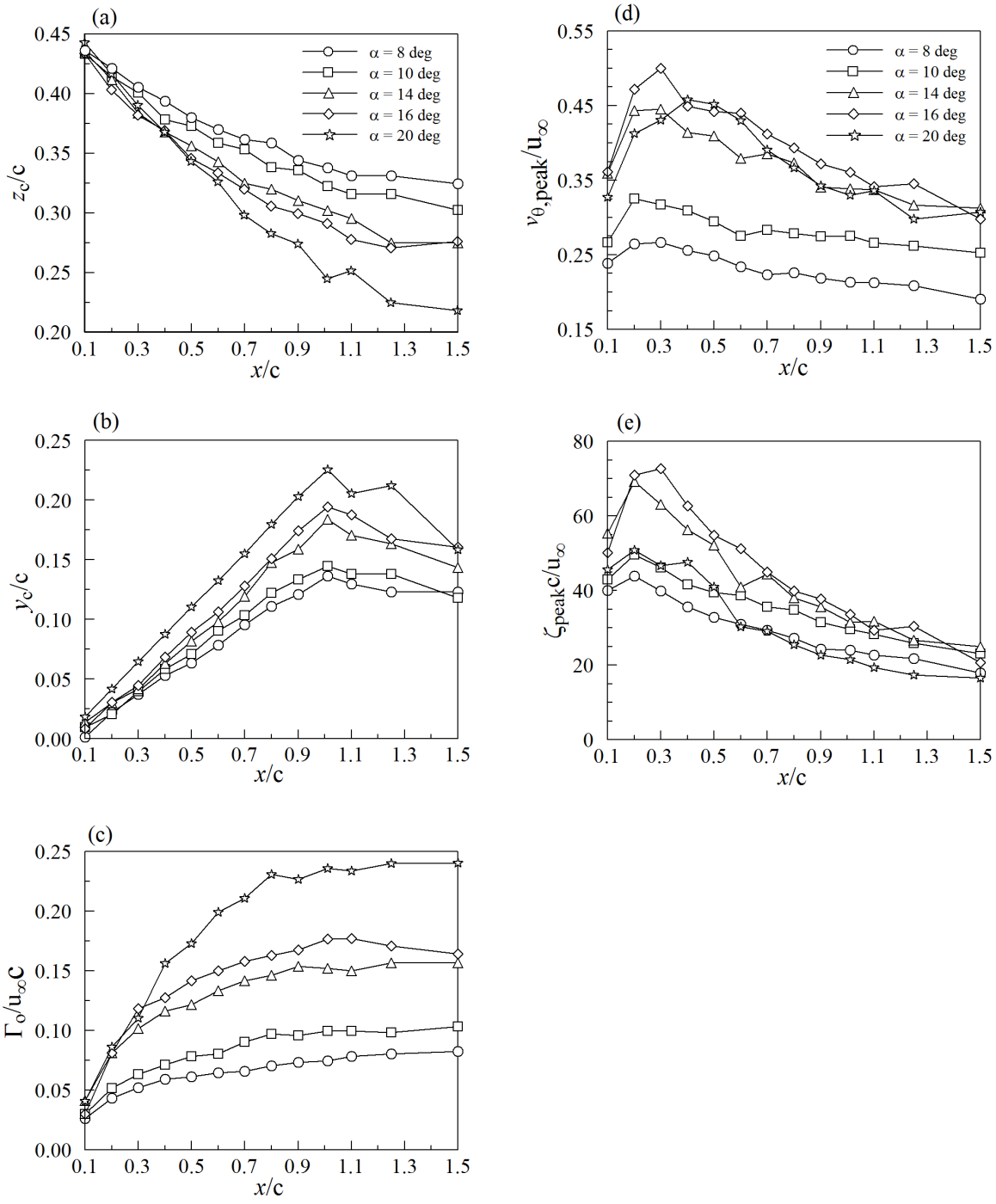

Figure 4.16 Variation of normalized RDW vortex flow parameters with x/c at selected angles of attack. RDW denotes reverse delta wing.

4.2 Vortex flow and lift generation of a 50°-sweep non-slender reverse delta wing (RDW50)

In this section, the lift force generated by the 50°-sweep non-slender reverse delta wing (designated by RDW50) was obtained first followed by the PIV vortex flow measurements. The results were also compared to their regular delta wing (i.e., DW50) counterpart.

4.2.1 Lift coefficient of reverse delta wing and regular delta wing

Figure 4.17 shows that the 65°-sweep slender delta wing (designated by DW65) produced a greater lift than the non-slender 50°-sweep delta wing (designated by DW50) at Re = 11,000. The aerodynamic load coefficients at a higher Reynolds number Re = 3.3×10^5 can be found in figure 4.8(a). The overall lift coefficient C_L–α behavior remained insensitive to the Reynolds number. The DW65 wing had a static-stall angle α_{ss} of 35° with a maximum lift coefficient $C_{L,max}$ of 1.15 in comparison with α_{ss} = 20° and $C_{L,max}$ = 0.592 of the non-slender delta wing. The earlier stalling of the DW50 can be attributed to the strong interaction of the leading-edge vortices with the boundary-layer flow developed on the upper surface of the non-slender delta wing. The breakdown of the leading-edge vortices, over both slender and non-slender delta wings, can be illustrated from the joint PIV measurements and dye flow visualization presented in figures 4.18(a)-(b). In figure 4.18 extensive PIV measurements along x/c (with a small $\Delta(x/c)$ increment of 0.0085) were conducted in the vicinity of the leading-edge vortex breakdown location identified qualitatively from the dye flow visualization. Figure 4.18(b) reveals that for the DW65 at α = 25°, the leading-edge vortex breakdown (identified by the sudden reduction in the peak vorticity value or by the sudden expansion of the iso-vorticity contours) was found to occur at x/c = 0.54. For the DW50 at α = 14° (figure 4.18(a)), the leading-edge vortex breakdown, however, happened at x/c = 0.585. It should be noted that for the DW50 wing, the leading-edge vortex breakdown was less straightforward compared to its slender counterpart, and was identified by the loss of regularity or coherence of the iso-vorticity pattern (between x/c = 0.5699 and 0.585).

Figure 4.17 further shows that, regardless of the sweep angle or slenderness, the reverse delta wing always generated less lift but a delayed stall compared to its regular wing counterpart. The larger the sweep angle the lower the lift generation was produced. At moderate to high angle of attack, the RDW65 generated less lift than the DW65 because it does not benefit from vortex lift generated by the DW65 leading-edge vortices. The RDW65 stall is delayed because the upper surface flow remains attached compared to DW65 vortex breakdown propagating upstream with increasing angle of attack. The RDW65 was found to stall at 40^{o} with $C_{L,max} = 0.962$. Note that all the wing configurations (i.e., DW50, DW65, RDW50 and RDW65) were tested at Re = 11,000 in the present study. Surprisingly enough, for the RDW50 the stalling appeared to be very gradual and was found to first occur at around $\alpha \approx 22.5°$ with a $C_{L,max}$ of 0.445, which remained unchanged with a further increase in α. Also, in contrast to the leading-edge vortex breakdown-induced stalling of the regular delta wing (as elucidated in figure 4.18), the stalling of the reverse delta wing was originated from the loss of the coherence of the unique multiple spanwise vortex filaments (SVFs) developed over the upper surface of the reverse delta wing (see figures 4.19(a)-(b)). As can be seen, the spanwise vortex filaments became disorganized or incoherent as the angle of attack was increased.

The spanwise vortex filament was originated from the spanwise leading-edge vortex as a result of the roll-up of the lower wall-shear layer along the leading edge of the reverse delta wing. The disruption or loss of coherence of the spanwise vortex filaments, caused by the separated flow arising from the trailing apex region of the reverse delta wing, also led to a large separated flow over the upper wing surface. The formation of the large flow separation suggests that the upper side of the reverse delta wing acts as a wake generator. The formation and growth of the RDW vortex of the non-slender reverse delta wing can also be understood qualitatively from the dye flow visualizations presented in figures 4.19(c)-(e) at $\alpha = 14°$, 18° and 21°. Figures 4.19(c)-(e) clearly show that as α was increased the RDW vortex became less concentrated as it progressed downstream, and that the RDW vortices were always located outside the reverse delta wing. The outboard location of the RDW vortices also implies that the lift was mainly generated by the flow on the lower side of the reverse delta wing which, in turn, also helps explain the inferior lift generation of the

reverse delta wing compared to the regular delta wing. Nevertheless, the stalling mechanism and the behavior of the spanwise vortex filaments of the non-slender reverse delta wing were, however, found to be similar to their slender counterpart (Lee and Ko 2016). For the RDW50, the SVFs, however, became disorganized at a lower α compared to the RDW65 wing. In the following section, the streamwise development of the vortex generated by the regular DW50 wing was investigated first, followed by the discussion of its reverse counterpart.

4.2.2 Streamwise evolution of iso-vorticity contours of non-slender regular delta wing

Figures 4.20(a)-(e) display the normalized iso-vorticity ($\zeta c/u_\infty$) of the DW50 vortex at selected x/c for $\alpha = 10°$. The iso-$\zeta c/u_\infty$ contours of the 65°-sweep slender delta wing (i.e., DW65) at $x/c = 0.9$, 1.01, and 1.5 are also included in figures 4.20(f)-(h) for a direct comparison. The results show that at $\alpha = 10°$, the leading-edge vortex breakdown already happened in the trailing-edge region of the 50°-sweep non-slender delta wing (DW50). By contrast, the leading-edge vortex remained intact over the entire DW65 upper wing surface at the same angle of attack. The leading-edge vortices of the non-slender wing also appeared to be less concentrated and more stretched in the spanwise direction compared to the slender wing at the same x/c and angle of attack. In addition to the lowered vorticity level and tangential velocity, the leading-edge vortices of the 50°-sweep delta wing also found to be located closer to its upper wing surface compared to its slender counterpart. The streamwise evolution of the normalized trajectory (y_c/c and z_c/c), peak vorticity $\zeta_{peak}c/u_\infty$, peak tangential velocity $v_{\theta,peak}/u_\infty$, core radius r_c/c, and core circulation Γ_c/cu_∞, of the LEV at $\alpha = 10°$ is summarized in figures 4.21(a)-(f) (denoted by the Δ symbols).

Figures 4.21(a)-(b) show that for the 50°-sweep delta wing, the leading-edge vortices were displaced further above (or away) the wing upper surface (or centerline) as it progressed downstream. The vortex center was identified by the position of the maximum vorticity ζ_{peak}. At $\alpha = 10°$, the peak vorticity of the leading-edge vortex of the non-slender delta wing was found to first to grow with x/c, reaching a local peak at around $x/c = 0.5$ and began to

decrease with x/c (figure 4.21(c)). The normalized peak tangential velocity and core circulation values were, however, found to increase continuously with x/c (figures 4.21(d)-(e)). The core circulation was computed via Stokes theorem. The grid size is interpolated from the raw data to be $\Delta y/c = \Delta z/c = 0.005$. The change of the normalized peak vorticity $\zeta_{peak}c/u_\infty$, peak tangential velocity $v_{\theta,peak}/u_\infty$, core radius r_c/c, and core circulation Γ_c/cu_∞ of the 65°-sweep slender regular delta wing at $\alpha = 10°$ are also included in figures 4.21(c)-(f) (denoted by solid ▲ symbols). The core radius r_c is the half distance between maximum and minimum tangential velocities (i.e., $v_{\theta,max}$ and $v_{\theta,min}$) of the vortex. The leading-edge vortices of the slender delta wing clearly have a smaller size but a higher vorticity level and rotational velocity compared to the non-slender delta wing.

To further investigate the growth and development of the leading-edge vortex flow, the PIV measurements were also extended to $\alpha = 4°$, 6°, 8°, and 14°. To save space, the iso-$\zeta c/u_\infty$ contours of the non-slender delta wing at $\alpha = 8°$ and 10°, and $\alpha = 14°$ and 16° are plotted jointly in figure 4.22. As can be seen, no leading-edge vortex breakdown was noticed for $\alpha = 8°$ while the leading-edge vortex breakdown was observed between $x/c = 0.8$ and 0.9 for $\alpha = 10°$. The change in the critical vortex flow parameters of the non-slender delta wing with x/c at different α is also summarized in figure 4.21. The overall behavior of the leading-edge vortices was found to be similar to that associated with $\alpha = 10°$ up to the breakdown location. The core circulation and peak tangential velocity grew with the angle of attack (see figures 4.21(d)-(e)). The vortex center was displaced further above and away from the wing upper surface as α was increased (figures 4.21(a)-(b)). The increase-decrease trend of $\zeta_{peak}c/u_\infty$ with x/c persisted, regardless of angle of attack (figure 4.21(c)). The location of the local maximum of the peak vorticity was, however, found to move closer to the apex as α was increased.

4.2.3 Vortex flow characteristic of non-slender reverse delta wing

Now, the spatial progression of the iso-$\zeta c/u_\infty$ contours of the vortex generated by the non-slender 50°-sweep reverse delta wing (RDW50) for $x/c \leq 1.5$ at $\alpha = 10°$ is discussed (figures 4.23(a)-(f)). The results are also compared to their slender counterparts at $x/c =$

0.9 and 1.5 (figures 4.23(g)-(h)). Figure 4.23 shows that, regardless of the slenderness, the reverse-delta-wing vortex flowfield is persistently characterized by an "arm-and-fist" flow pattern. In contrast to the dominant appearance of the RDW vortex of the slender reverse delta wing, the vortex flowfield of the non-slender reverse delta wing is dominated by the formation of the RDW vortex in conjunction with multiple shear-layer vortices for $x/c \leq 1.5$ tested in the present study. Note that the RDW vortex of the slender delta wing became singular and attained axisymmetry at $x/c = 1.5$ (see figure 4.23(f)), which is similar to the wingtip vortex developed in the near field behind a NACA 0012 wing (Lee and Choi 2015). The variation of the critical RDW50 vortex flow parameters with x/c at $\alpha = 10°$ is summarized in figures 4.24(a)-(e) (denoted by the ◊ symbols).

Figures 4.24(a)-(b) indicate that, similar to the RDW65 vortex, the non-slender reverse-delta-wing vortex was also located outside and above the wing upper surface. The RDW50 vortex was however located further above and outboard the wing upper surface compared to the RDW65 vortex (denoted by ♦symbols). For clarity, the normalized spanwise vortex center location z_c/c of the RDW65 vortex is plotted separately in figure 4.24(f). The magnitude of $\zeta_{peak}c/u_\infty$ and $v_{\theta,peak}/u_\infty$ of the RDW50 vortex were also found to first increase with x/c, reaching a local maximum at around $x/c = 0.3$, and began to drop for $x/c \geq 0.3$ (figures 4.24(c)-(d)). The peak vorticity and tangential velocity, however, had a lower value than their slender counterparts. The total circulation Γ_o of the vortex generated by the 50°-sweep non-slender reverse delta wing was found to remain insensitive to x/c (figure 4.24(e)). By contrast, the total circulation of the vortex created by the slender reverse delta wing increased with x/c up to $x/c = 0.7$ and attained a rather constant value for $x/c > 0.7$.

Finally, the streamwise growth and development of the vorticity flowfield of the RDW50 vortex at $\alpha = 4°$, 6°, 8°, 14°, 16° and 18° were also obtained. To save space, the iso-vorticity contours of $\alpha = 10°$ and 14°, and 16° and 18° along x/c are plotted jointly in figures 4.25(a)-(b), respectively. The change in the critical vortex flow parameters with x/c at different angles of attack is also given in figure 4.24. Regardless of the angle of attack, the RDW50 vortex was always located outboard and above the non-slender reverse delta wing (figures

4.24(a)-(b)), which also suggests that the strength of the RDW vortex is not a direct indication of the lift generation of the non-slender reverse delta wing. The extent of z_c/c and y_c/c was however found to increase with the angle of attack. The results further reveal that the change in $\zeta_{peak}c/u_\infty$, $v_{\theta,peak}/u_\infty$ and Γ_o/cu_∞ with x/c at different angles of attack also followed the trend observed for $\alpha = 10°$ except for the $\alpha = 18°$ case (figures 4.24(c)-(e)). That is to say, the non-slender RDW-generated vortex remained concentrated and axisymmetric for $\alpha \leq 14°$ (see figures 4.26(a)-(e)) and became diffused or disorganized at $\alpha = 16°$ (figure 4.26(f)). For $\alpha > 18°$, the RDW50 vortex resembled a weak circulation-like flow with small patches of vorticity (figure 4.26(g)). By contrast, the weak circulation-like flow only observed for $\alpha > 24°$ of a slender reverse delta wing (Lee and Ko 2016). Nevertheless, the observed disruption or disorganization of the RDW vortex further suggests their irrelevant role in the stalling of the reverse delta wing because they do not contribute to lift.

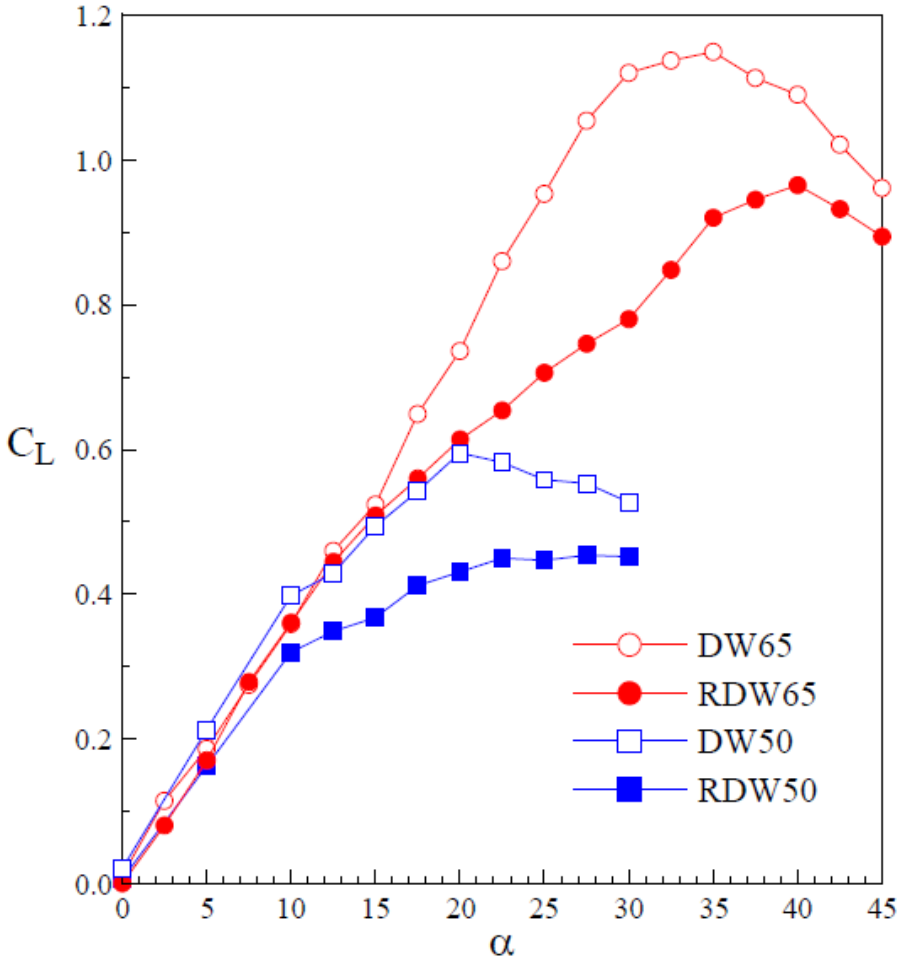

Figure 4.17 Lift coefficient of slender and non-slender reverse and regular delta wings at Re = 11,000. DW50 and DW65 denote 50°-sweep and 65°-sweep regular delta wings, respectively. RDW50 and RDW65 denote 50°-sweep and 65°-sweep reverse delta wings, respectively.

(a)

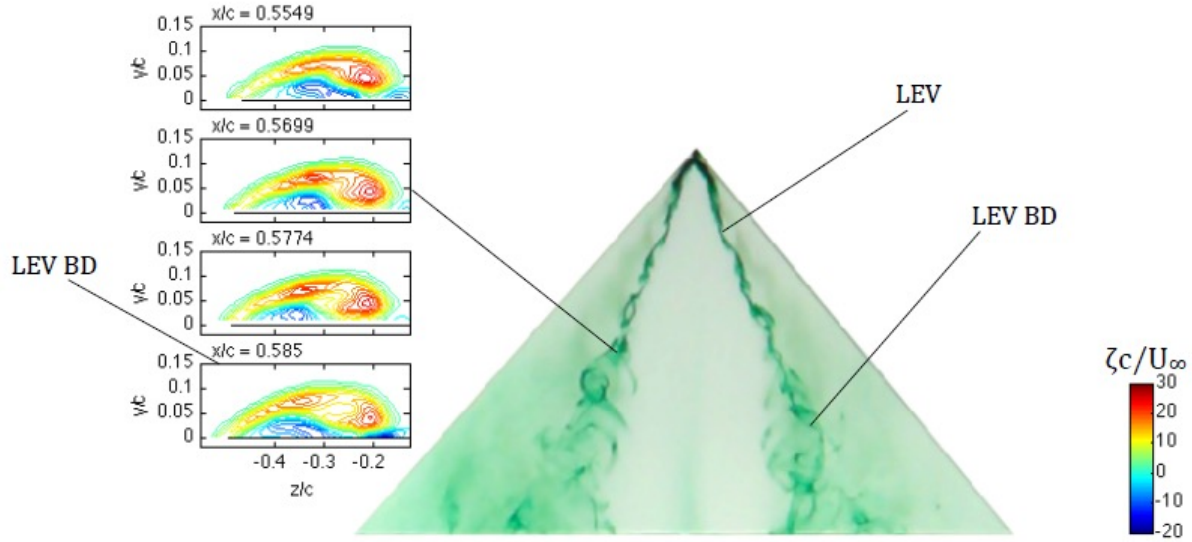

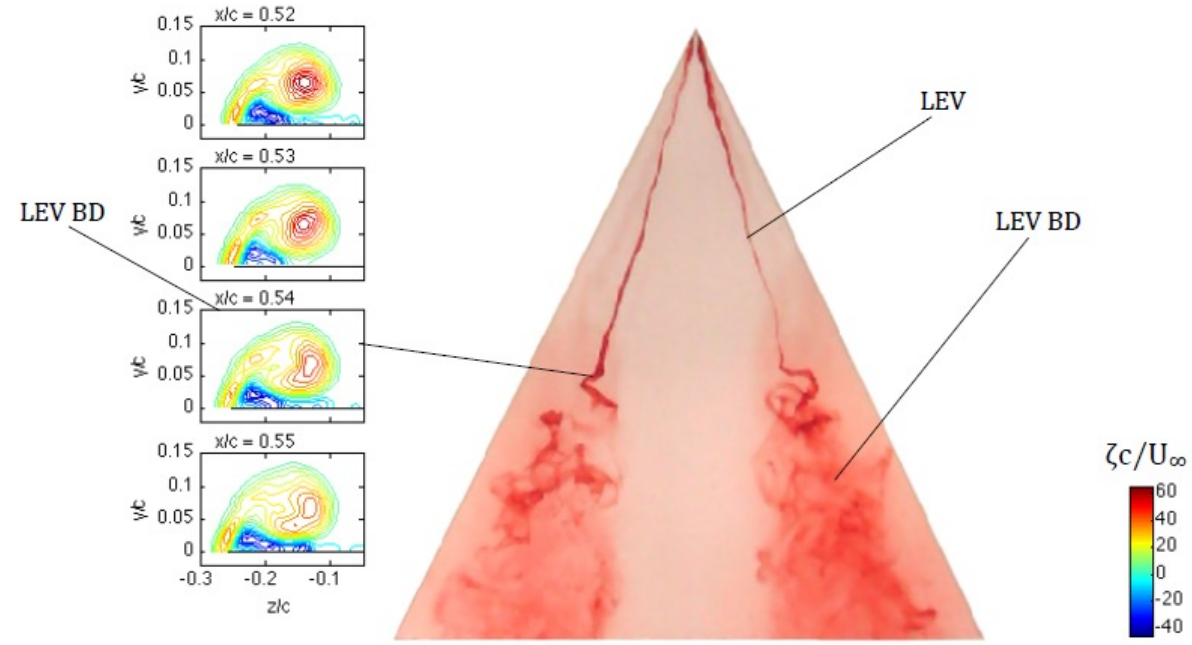

(b)

Figure 4.18 Joint PIV measurements and photos of dye flow visualization. (a) DW50 at α = 14° and (b) DW65 at α = 25°. Flow is from top to bottom. DW50 and DW65 denote delta wing with 50°-sweep and 65°-sweep, respectively.

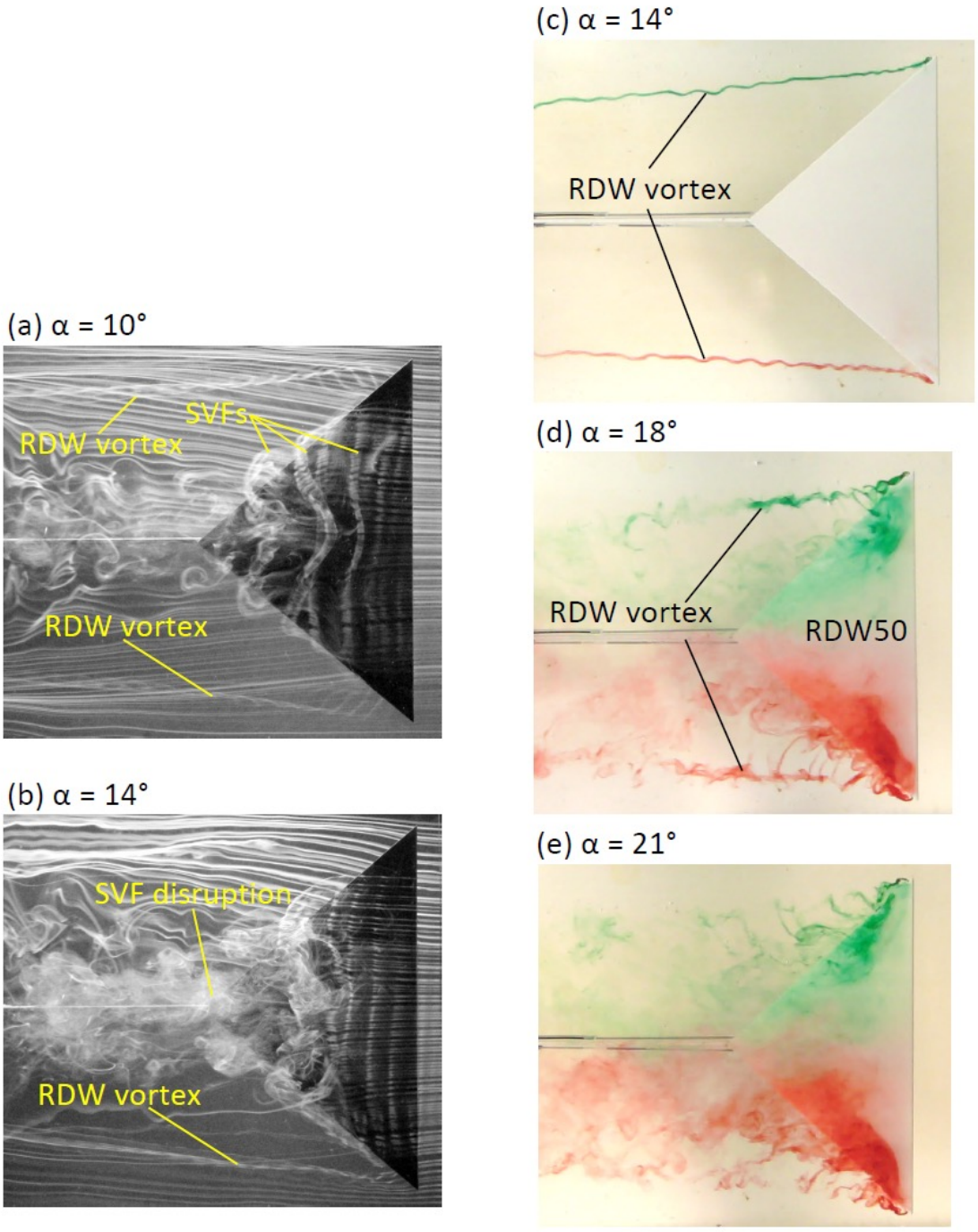

Figure 4.19 Photos of visualized flow pattern of non-slender reverse delta wing. (a)-(b): Smoke-wire flow visualization, and (c)-(d): dye flow visualization. The flow is from right to left. SVF denotes spanwise vortex filament.

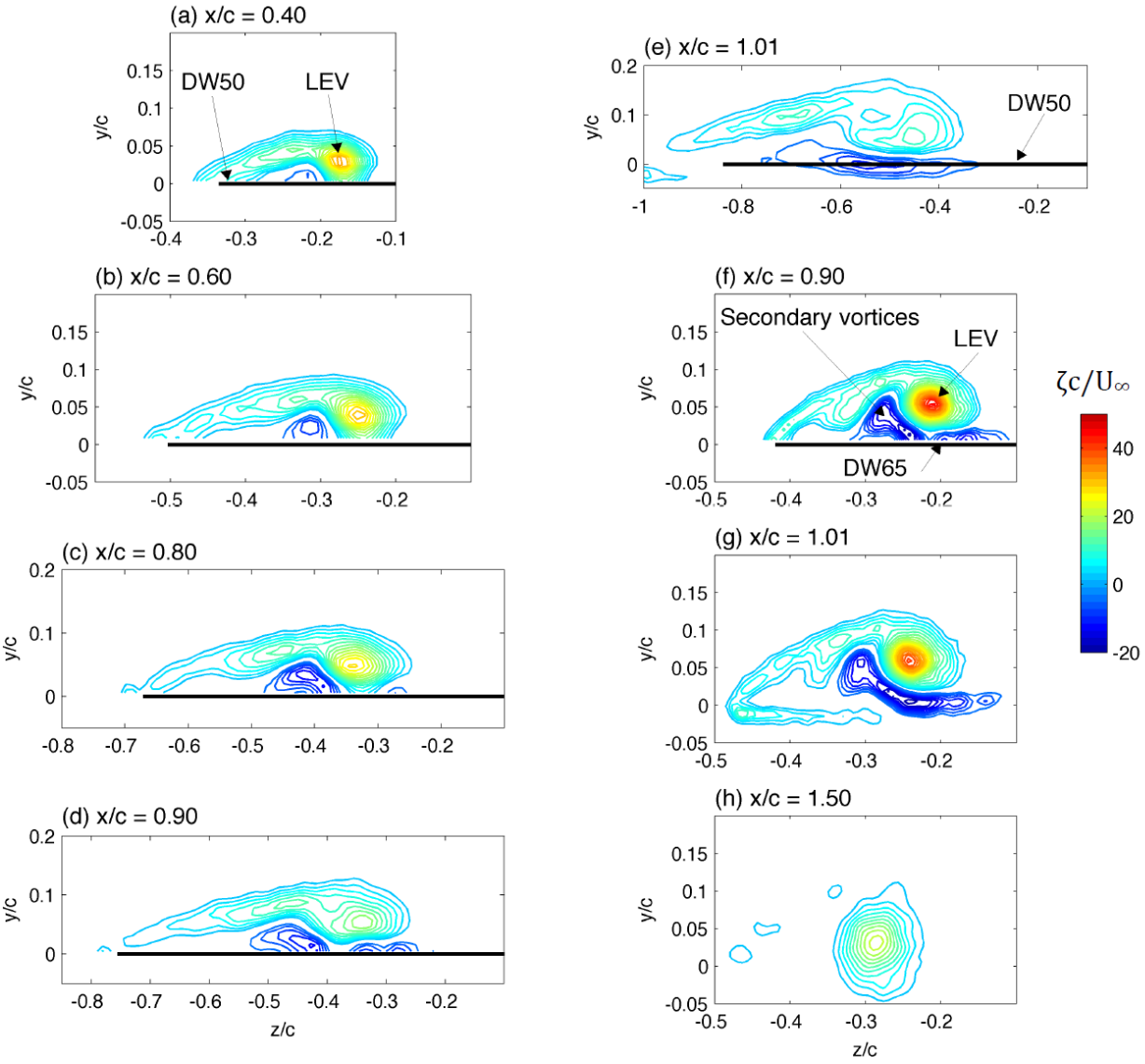

Figure 4.20 Representative normalized iso-vorticity contours of regular delta wing at α = 10°. (a)-(e): DW50 and (f)-(h): DW65. DW50 and DW65 denote delta wing with a sweep of 50° and 65°, respectively.

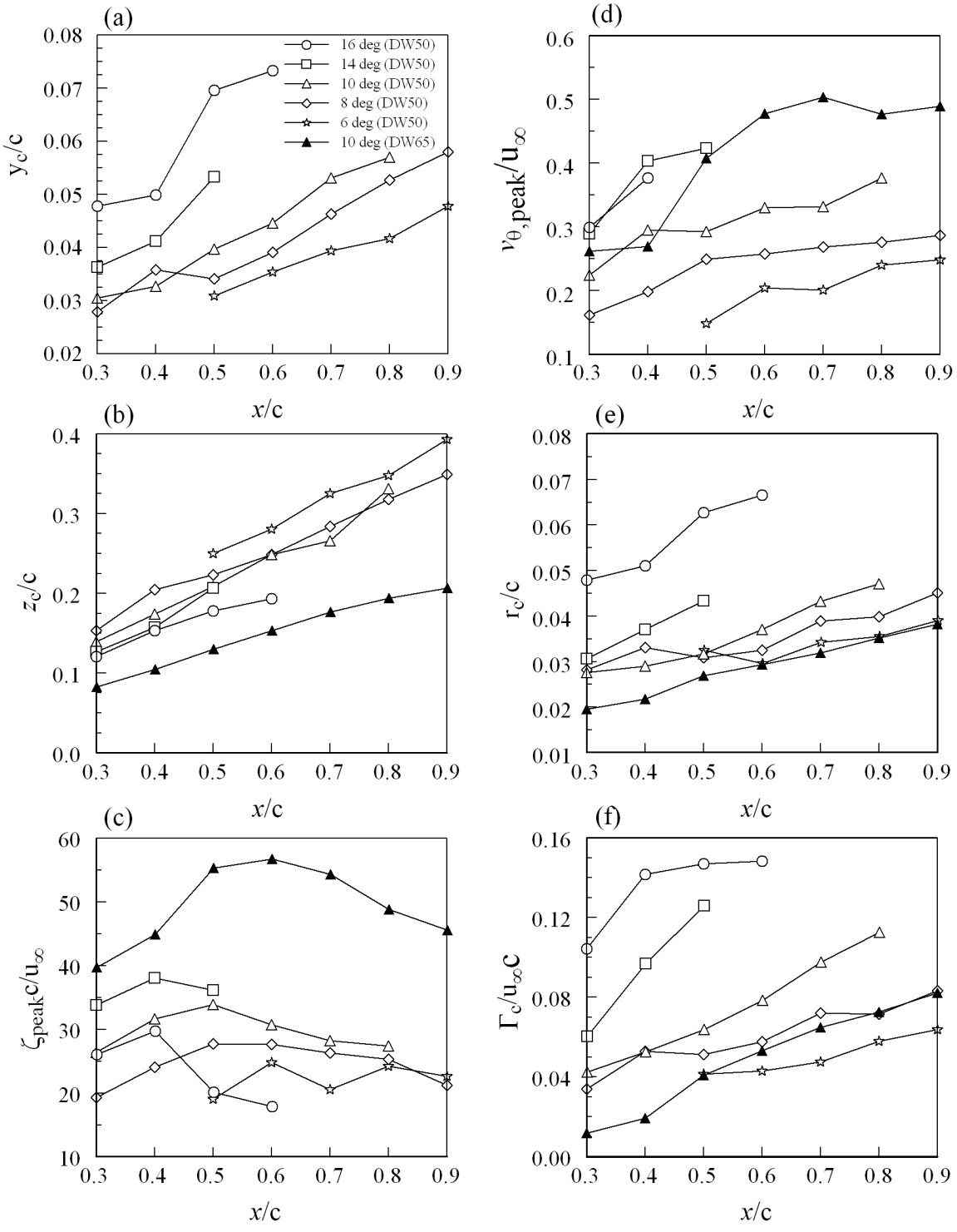

Figure 4.21 Variation of normalized leading-edge vortex flow parameters of non-slender delta wing with x/c.

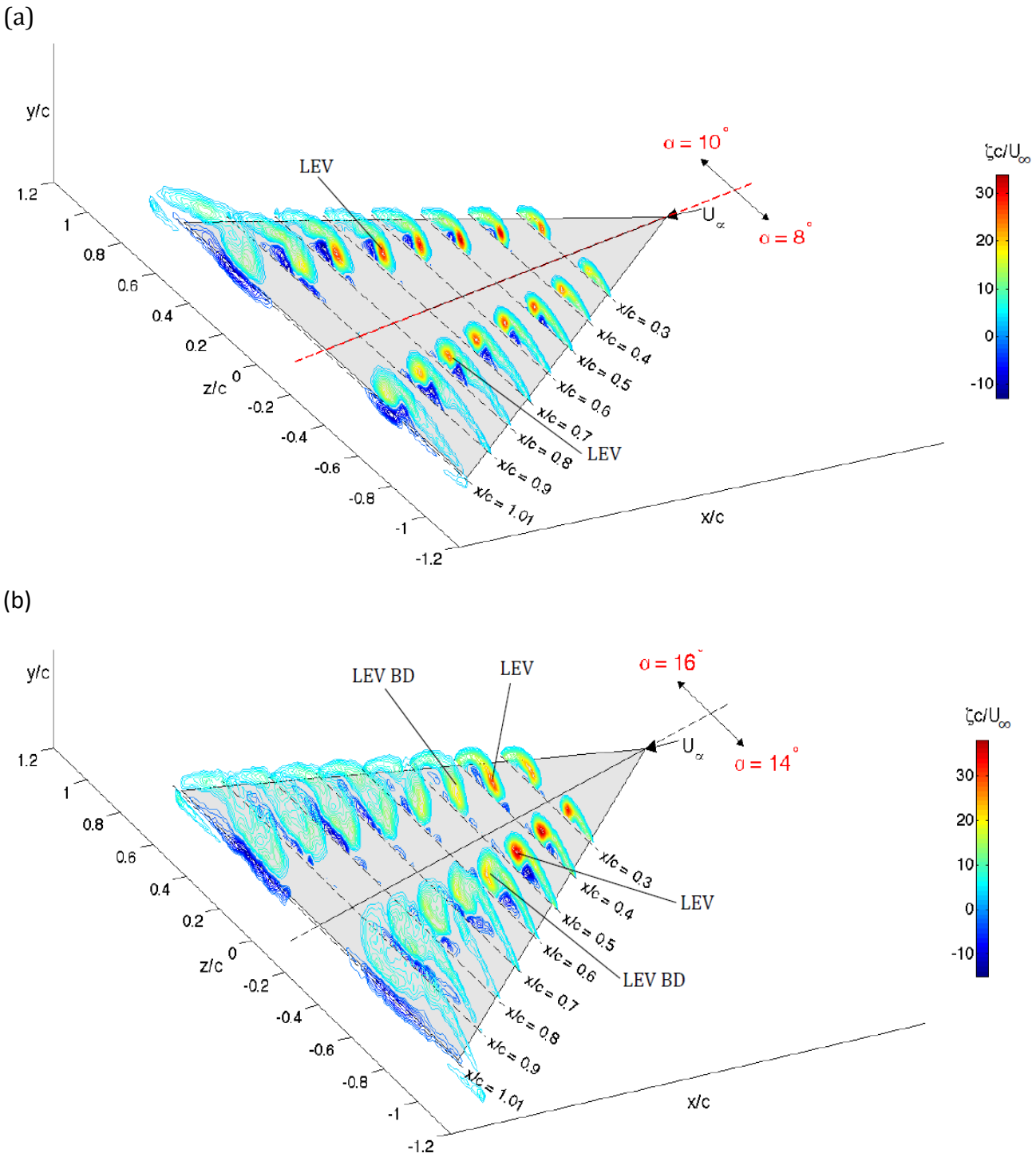

Figure 4.22 Combined spatial progression of iso-vorticity contours of the DW50 vortex. (a) α = 8° and 10°, and (b) α = 14° and 16°. DW50 denotes delta wing with a sweep of 50°.

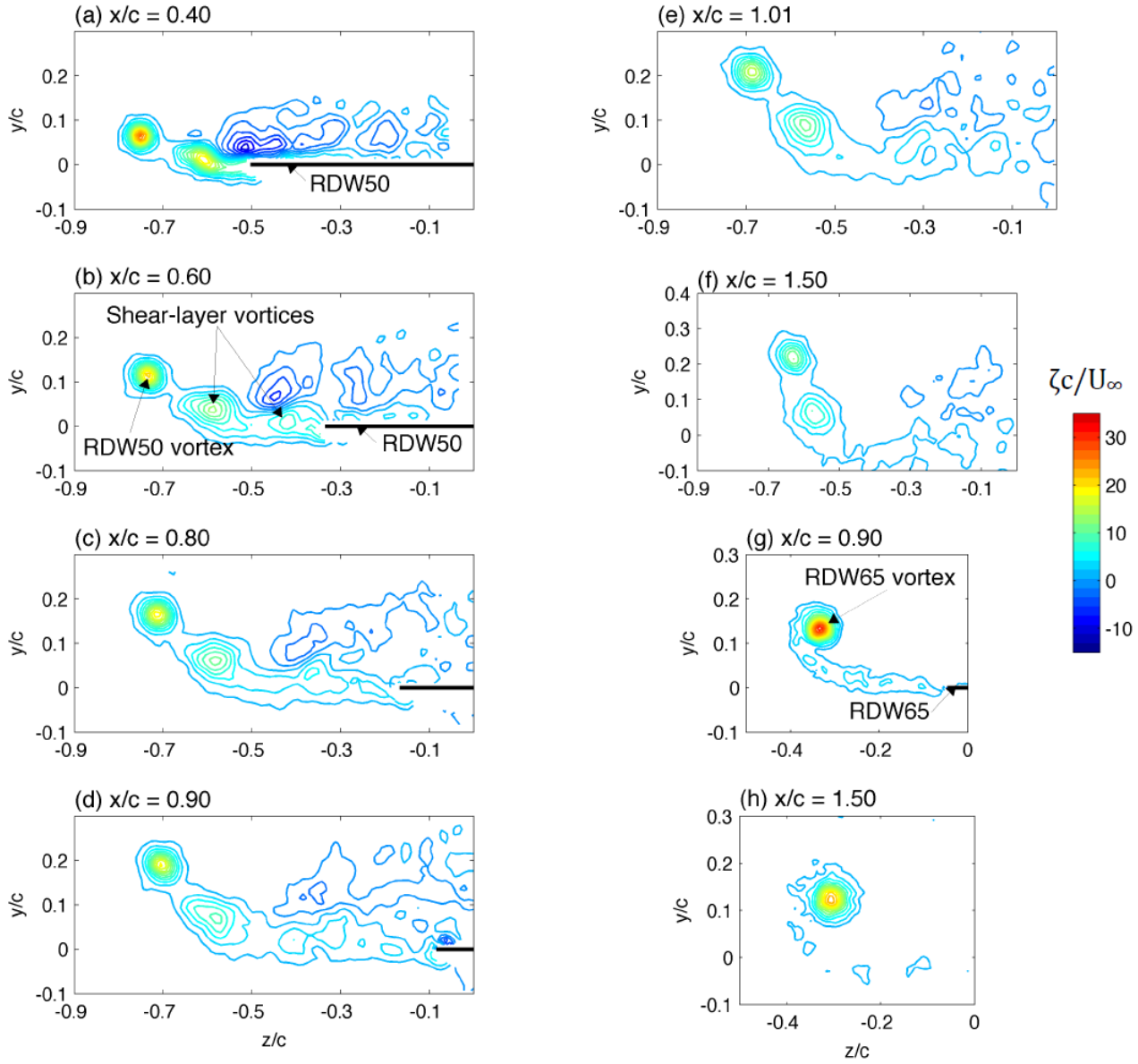

Figure 4.23 Representative iso-ζc/u$_\infty$ contours of the RDW vortex at selected x/c for α = 10°. (a)-(f): RDW50 and (g)-(h): RDW65. RDW50 and RDW65 denote reverse delta wing with a sweep of 50° and 65°, respectively.

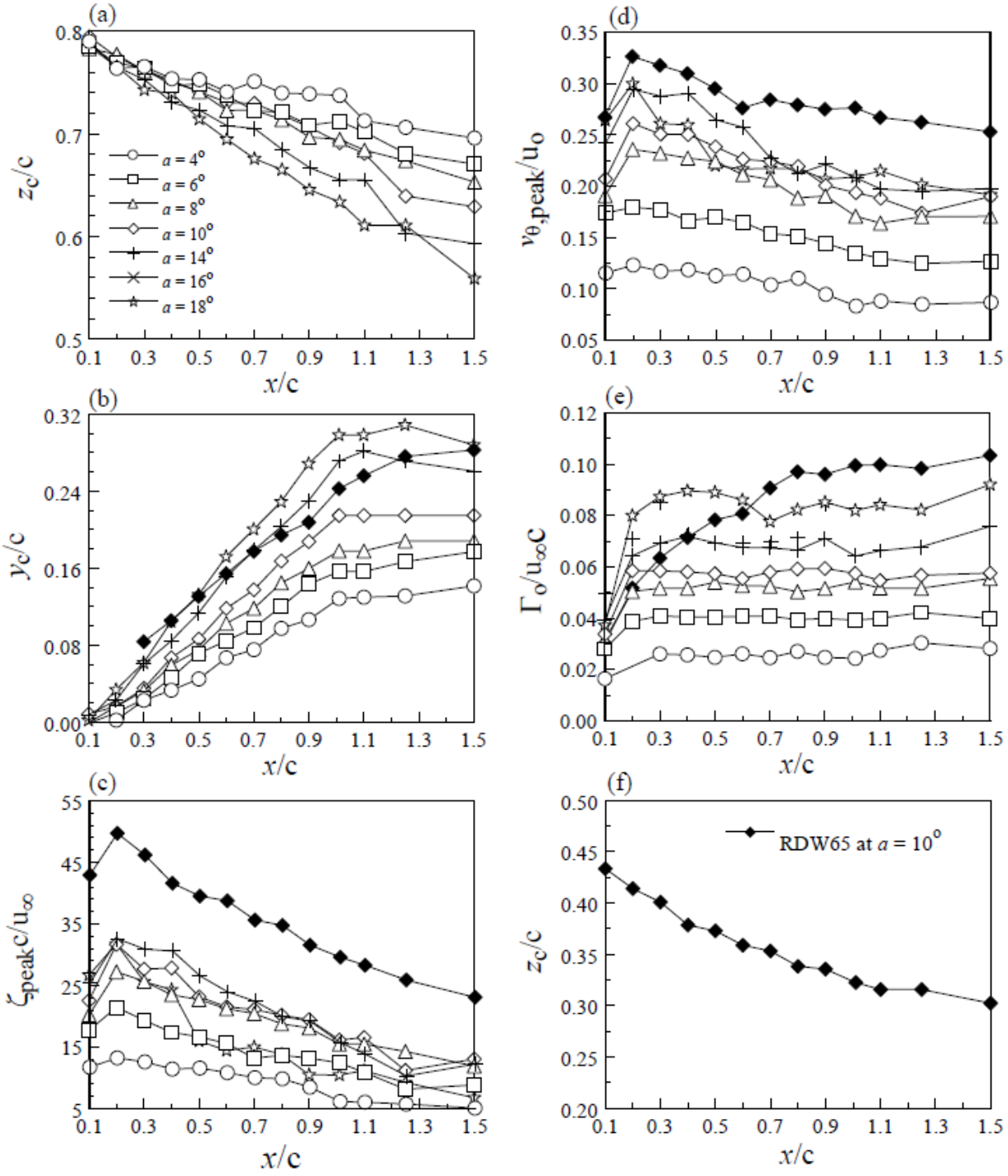

Figure 4.24 Variation of RDW50 vortex flow parameters with x/c for α = 4° to 18°. Solid rhombus denotes RDW65 vortex at α = 10°. RDW50 and RDW65 denote reverse delta wing with a sweep of 50° and 65°, respectively.

(a)

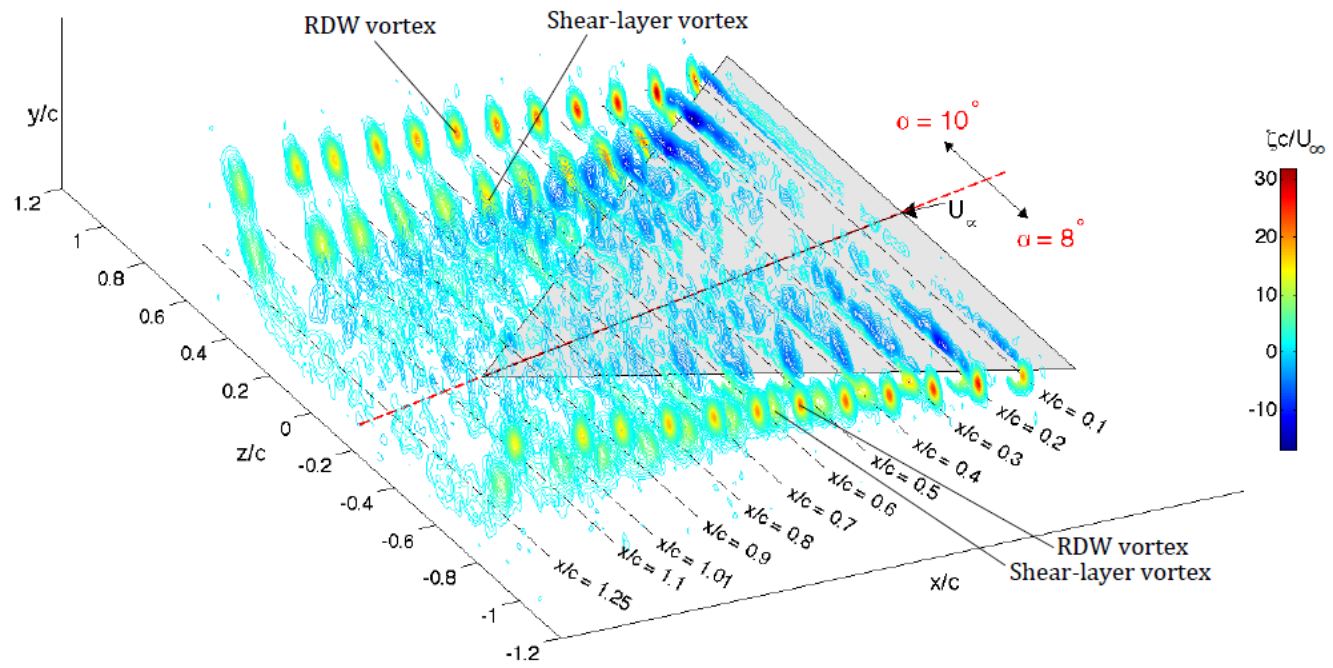

Figure 4.25 Joint 3-D plot of the normalized iso-vorticity contours of the RDW50 vortex. (a) α = 6° and 10° and (b) α = 14° and 18°.

(b)

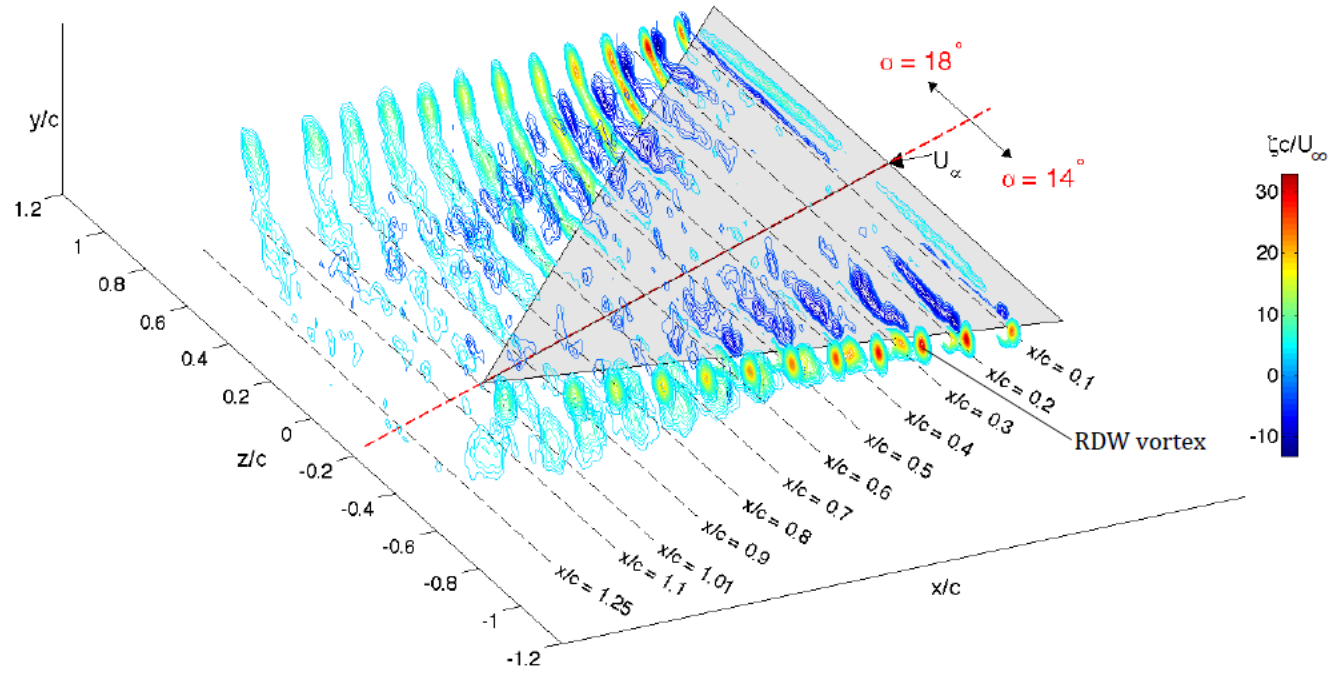

Figure 4.25 Joint 3-D plot of the normalized iso-vorticity contours of the RDW50 vortex. (a) $\alpha = 6°$ and $10°$ and (b) $\alpha = 14°$ and $18°$.

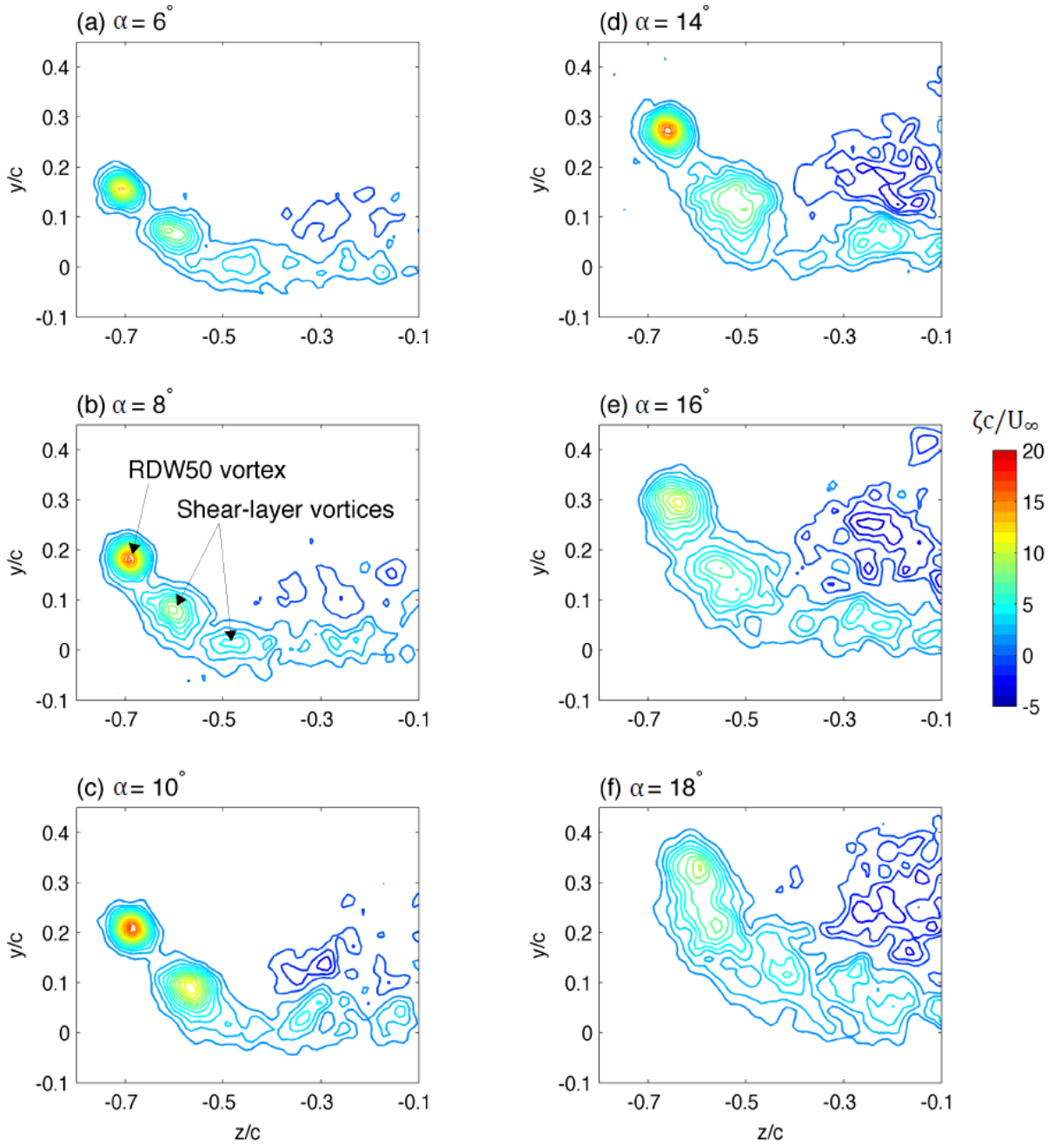

Figure 4.26 Normalized iso-vorticity contours of the RDW50 vortex at x/c = 1.01 for α = 6° to 18°.

4.3 Passive control of lift and vortex flow of a reverse delta wing via Gurney flaplike strips

In this section the passive control of the lift generation and the vortex flowfield of a reverse delta wing via the use of Gurney flaplike strips, of various configurations and heights (see figure 4.27), was investigated. The objective was to increase the lift generation capability of the reverse delta wing. The aerodynamic loading coefficients were measured with a wind-tunnel force balance. The force-balance data were then used as an experimental guideline for the particle-image-velocimetry measurements of the corresponding vorticity flowfield.

4.3.1 Aerodynamic characteristics of baseline reverse delta wing

Figure 4.28 illustrates the aerodynamic characteristics of the baseline RDW and their comparison with the regular delta wing at $Re = 4.06 \times 10^5$. The results of Altaf et al. (2011) of a $\Lambda = 75°$ delta wing and RDW at $Re = 3.8 \times 10^5$ are also included in figure 4.28 for a direct comparison. As can be seen, the delta wing had a better lift generation capability compared to the reverse delta wing for $\alpha \geq 11°$ (figure 4.28(a)). A 28.2% reduction in the lift coefficient of the reverse delta wing at, for example, $\alpha = 24°$ compared to the delta wing was observed. For $\alpha < 11°$, the delta wing, however, had a slightly lower-than-RDW lift coefficient, which can be attributed to the fact that at low angle of attack the leading-edge vortices were absent and the lift was mainly produced by the potential or attached-flow developed on the delta wing. At higher angle of attack, the large leading-edge vortex-induced vortex lift overwhelmed the lift production of the reverse delta wing. The lower lift coefficient of the reverse delta wing can be attributed to the outboard location of the RDW vortices, which suggests that the RDW vortices did not contribute to the RDW lift generation. Figure 4.28(a) further indicates that the delta wing had a maximum lift coefficient $C_{L,max}$ of 1.285 at $\alpha_{ss} = 35°$ in comparison to 1.03 and 35° of the reverse delta wing. α_{ss} is the static-stall angle. Also, in contrast to the leading-edge vortex breakdown-induced stalling of the delta wing, the stalling of the reverse delta wing was triggered by

the breakdown of the multiple spanwise vortex filaments (SVFs), or the loss of SVFs coherence, developed over the upper surface of the reverse delta wing (figure 4.29).

The overall behavior of the SVFs and the RDW vortices can be illustrated from the smoke-wire and dye-injection flow visualizations at α = 14° and 24°, respectively. At α = 14° (figures 4.29(a) and 4.29(c)), the RDW vortices, originating from the spanwise leading-edge vortex as a result of the roll-up of the lower-wall shear layers along the leading edge of the reverse delta wing, were concentrated and stable compared to those at α = 24° (figures 4.29(b) and 4.29(d)). Due to the location of the smoke wire the spanwise leading-edge vortex filament was not visualized, the presence of the leading edge vortex filament can be found from the CFD simulation of Altaf et al. (2011). Figure 4.29(a) further indicates that at α = 16° the surface flow structure was characterized by three clearly defined multiple SVFs (i.e., SVF_1, SVF_2 and SVF_3). The appearance of these well-defined SVFs is due to the fact that at low α the strong pressure gradients were confined to the trailing apex region of the reverse delta wing where they did not interfere with the laminar boundary layer development, which, in turn, allowed the spanwise vortex filaments to be unaffected, and led to a better lift generation than the delta wing. The laminar boundary layer development can be seen Figure 4.9c where the streaklines over approximately one third of the leading edge of the reverse delta wing are straight. On the other hand, Figure 4.9d shows that the SVF moves upstream and the laminar flow region is reduced. The flow over the trailing apex of the reverse delta wing can also be seen to be separated. The spanwise vortex filaments, however, became diffused as α was increased. At α = 24° (see figure 4.29(b)), the SVFs were disrupted by the separated cross-flow originating in the trailing apex region of the reverse delta wing. In the vicinity of α = 35° (not shown here), the massive breakdown of the spanwise vortex filaments gave rise to a largely separated flow over the surface of the reverse delta wing, leading to the stalling of the reverse delta wing.

The force-balance measurements also reveal that the presence of the leading-edge vortices and its subsequent breakdown on the delta wing produced a higher profile drag and subsequently a higher drag coefficient compared to the reverse delta wing for α > 14° (figure 4.28(b)). By contrast, the presence of the SVFs on the upper surface of the reverse

delta wing led to a higher profile drag for $\alpha < 14°$ instead. Note that at the same lift condition the reverse delta wing was, however, found to produce a higher drag coefficient than the delta wing (figure 4.28(c)), leading to a lower lift-to-drag (C_L/C_D) value (figure 4.28(d)).

4.3.2 Aerodynamic characteristics of the reverse delta wing with side-edge strip (SES) and leading-edge strip (LES)

Figure 4.28(a) shows that the addition of h = 3%c side-edge strips (SES) caused a leftward shift of the C_L–α curve, resembling the employment of a conventional trailing-edge flap, thereby giving a greater $C_{L,max}$ (= 1.25) and also a small stall delay (with α_{ss} = 37.5°) compared to the baseline RDW. h is the height of the strip. The observed lift force increase can be attributed to the SES-induced spanwise camber effects and the alleviation of the cross-flow leakage at the side edges, which thereby rendered an increased bottom-surface pressure and consequently an increased lift coefficient compared to the baseline wing. The pressure on the bottom surface increased similar to the mechanism for airfoils. The presence of the Gurney flaplike device causes an increased pressure ahead of the flap, leading to higher pressure on the lower surface. The smaller the h the lesser extent of the leftward C_L–α shifting became. A 43% and 28.4% increase in lift at, for example, $\alpha = 24°$ was obtained by the SES wing with h = 3%c and 1.5%c, respectively. The maximum lift coefficient and the static-stall angle were, however, found to be insensitive to the strip height h. Figure 4.28(a) further indicates that the h = 3%c SES wing produced a lift higher than the delta wing for both pre-stall (up to $\alpha = 26°$) and post-stall α regimes.

Undesirably, the employment of side-edge strips also produced a higher drag compared to the baseline RDW at the same α (see figure 4.28(b)). The increase in the drag coefficient can also be understood from the normalized iso-u/u_∞ contours, obtained by a seven-hole pressure probe, at $\alpha = 16°$ (figure 4.30). The separated wake behind the h = 3%c SES wing had a lesser extent but a larger wake, or momentum, deficit in comparison to the baseline RDW (figures 4.30(a)-(b)), as a consequence of the SES-caused interruption of the higher momentum fluid transfer from the bottom surface to the upper surface. Special attention

should also be given to the wake-like core axial flow of the SES-wing vortex (with a core axial velocity $u_c = 0.52u_\infty$) compared to the jet-like core flow of the baseline RDW vortex (with $u_c = 1.09u_\infty$). The entrainment of the turbulent shear layer flow, separating from the bottom surface of the SES wing, by the RDW vortex as it progressed downstream, however, led to a wake-like core flow. Surprisingly enough, the increase in the lift coefficient outperformed the corresponding increase in the drag coefficient (figure 4.28(c)), rendering an improved lift-to-drag (C_L/C_D) ratio compared to the baseline reverse delta wing and the delta wing as well (figure 4.28(d)). Similar change in C_L, C_D and C_L/C_D was also noticed for the h = 1.5%c case, but to a lesser extent, in comparison with the h = 3%c case.

The influence of upward and downward leading-edge strips (designated as LES_u and LES_d, respectively) on the aerodynamic load coefficients is also discussed. The presence of LES always gave a lower lift coefficient for the pre-stall angle of attack regime while a higher lift coefficient for the post-stall angle regime (figure 4.28(a)). The larger the strip height h is, the smaller (or larger) the lift coefficient for the pre-stall (or post-stall) α regime became. The addition of LES_d also led to a delayed stall and an increased maximum lift coefficient compared to the baseline reverse delta wing. The larger the strip height is, the higher the stall angle and maximum lift coefficient became. The LES_d wing gave a small drag reduction (figure 4.28(b)), as a result of the smaller extent and deficit of the separated wake flow behind the LES_d wing compared to the baseline reverse delta wing (see figure 4.30(c)). The reduction in drag of the LES_d wing was not able to outperform the corresponding lift reduction (see figure 4.28(c)), resulting in a lowered lift-to-drag ratio compared to the baseline RDW (figure 4.28(d)). The difference in lift and drag coefficients for the LES_d and LES_u cases should be able to be explained by performing PIV experiments along the center chord line of the RDW in order to study the leading-edge spanwise vortex filament and spanwise vortex filament. It can be hypothesized that the leading-edge strips also introduce a chordwise camber effect. For the LES_d, the leading-edge spanwise vortex filament is strengthened and the SVF disruptions are delayed, leading to a delayed stalling angle. However, since the lift generation is not from the upper surface, the C_L values are similar to the baseline case. The drag is also decreased slightly due to the improved upper surface SVF disruption being delayed. For the LES_u, although the laminar flow on the

bottom surface is improved, the earlier disruption of the SVFs on the upper surface lead to a similar C_L and C_D values compared to baseline.

4.3.3 Reverse delta wing vortex flow characteristics

Now, the impact of side-edge strip and leading-edge strip on the RDW vortex was investigated by using PIV at Re = 1.1×10^4. The strip height was set at h = 3%c. Figures 4.31(a)-(c) depict the joint plots of the spatial progression of the normalized iso-vorticity ($\zeta c/u_\infty$) contours of the RDW vortex, with and without strips, for $x/c \leq 1.5$ at $\alpha = 16°$. The corresponding vortex flow parameters are summarized in figure 4.32. To save space, the baseline reverse delta wing results are plotted on the right-hand side in figures 4.31(a)-(c) and the controlled cases are plotted on the left-hand side. The streamwise vorticity ζ (= $\partial w/\partial y - \partial v/\partial z$) was calculated from the ensemble-averaged cross-flow (vw) velocity components by using a central differencing scheme to evaluate the derivatives. The PIV results shown here are ensemble-averaged over 60 PIV images.

Figures 4.31(a)-(c) show that the RDW vortices are characterized by an ″arm-and-fist″ vortex flow pattern and that the extent of the "arm" grew as the RDW vortex progressed downstream. For the baseline reverse delta wing, a single and axisymmetric vortex exhibited at $x/c = 1.5$ (see figure 4.31(a)). The RDW vortex was also located outboard the reverse delta wing (see also figures 4.32(a)-(b)), which helps explain the inferior lift generation of the baseline reverse delta wing compared to the regular delta wing and also the fact that the RDW vortex breakdown is not a direct contributor to the stalling of the reverse delta wing. The peak vorticity ζ_{peak} and tangential velocity $v_{\theta,peak}$ (indicative of the strength of the vortex) of the baseline RDW vortex were found to increase with x/c, reaching a local maximum at around $x/c = 0.3$ (suggesting a spanwise leading-edge vortex with a diameter of around 0.3c), and began to drop for $x/c \geq 0.3$ (figures 4.32(c)-(d)). The $v_{\theta,peak}$ was obtained from the tangential velocity v_θ distribution across the RDW vortex center (see, for example, at $x/c = 1.5$ in figure 4.33). Note that for an asymmetric vortex (with $v_{\theta,peak} \neq v_{\theta,max} \neq |v_{\theta,min}|$), a circumferentially averaged value was used. The present measurements also indicate that the total circulation Γ_o of the baseline RDW vortex,

computed via Stokes theorem, increased with x/c up to 0.7 and attained a rather constant value for $x/c \geq 0.7$ (figure 4.32(e)), suggesting a near completion of the RDW vortex roll-up.

For the SES wing vortex, the iso-$\zeta c/u_\infty$ contours (presented on the left-hand side in figure 4.31(a)) remained concentrated and well-defined. The change in the peak vorticity and tangential velocity with x/c of the SES-wing vortex followed the trend of the baseline RDW vortex but had a higher magnitude (figures 4.32(c)-(d)). A more direct comparison of the SES-wing vortex and the baseline RDW vortex can be reflected from the enlarged views at x/c = 0.6 and 0.9, which manifests the higher vorticity level of the SES wing vortex compared to the baseline wing vortex at the same x/c and angle of attack. The SES-wing vortex center was also found to be located further inboard and closer to the wing upper surface (figures 4.32(a)-(b)). More importantly, the total circulation Γ_o of the SES-wing vortex also became invariant with x/c for $x/c > 0.7$ with $\Gamma_o \approx 0.246cu_\infty$, which translates into a 42% increase compared to its baseline reverse delta wing (with $\Gamma_o \approx 0.173cu_\infty$). The 42% increase in the total circulation is in agreement with the observed 39% increase in the lift coefficient of the SES wing in comparison to the baseline reverse delta wing at $\alpha = 16°$ for $Re = 1.1 \times 10^4$ (see figure 4.34). Note that the variation in the lift coefficient with α at $Re = 1.1 \times 10^4$ followed that at $Re = 4.06 \times 10^5$ but had a smaller magnitude. Also shown in figure 4.34 are the C_L data of the regular delta wing and the reverse delta wing with leading-edge strips at $Re = 1.1 \times 10^4$.

The PIV measurements also indicate that the presence of LES_d produced a diffused vortex (see figure 4.31(b)) with a smaller peak vorticity and tangential velocity and Γ_o compared to the baseline wing (figures 4.32(c)-(e)). Enlarged iso-$\zeta c/u_\infty$ contours at x/c = 0.6 and 0.9 were also plotted in figures 4.31(b)-(c) for a better comparison. The RDW vortex was also found to move further inboard and closer to the LES_d wing surface with increasing x/c (figures 4.32(a)-(b)). The extent of diffusion and irregularity of the RDW vortex was further elevated for the LES_u wing (figure 4.31(c)). Typical tangential velocity distributions across the center of the RDW vortex illustrating the axisymmetry and asymmetry of the RDW vortex are given in figure 4.33. Due the irregularity of the vortex, only the vortex

trajectory, peak vorticity and total circulation of the LES_u-wing vortex are summarized in figure 4.32.

Finally, the vortex flow parameters as a function of α (= 4° to 30°) was also investigated at x/c = 1.10. Figure 4.35(a) shows that the total circulation of the RDW vortex persistently increased with α and was accompanied by a further inboard movement of the vortex (figure 4.35(b)). The baseline RDW vortex was found to remain concentrated and axisymmetric for $\alpha \leq 16°$ but became diffused for $16° < \alpha \leq 23°$ (see figures 4.36(a1)-(a3)). For $\alpha > 23°$, the RDW vortex was circulation-like flow with patches of small vorticity (figures 4.36(a4)-(a6)). The peak vorticity and tangential velocity of the baseline RDW vortex were also found to increase with the angle of attack, reaching a local maximum at α = 16°, and started to drop for $\alpha > 16°$ (figures 4.35(c)-(d)). The measured Γ_o and b' (the distance between the RDW vortices) of the baseline RDW vortex were also used to compute the PIV-derived C_L value via the Kutta-Joukowski theorem ($L = \rho u_\infty \Gamma_o b'$, where L is the lift force). The PIV-derived C_L value (denoted by ♦ symbols in figure 4.34) is in good agreement with the force-balance data. The PIV-derived C_L technique had also been employed by Kaplan et al. (2007) to a 63.5°-sweep delta wing at $Re = 8 \times 10^3$ and 2.4×10^4.

Figures 4.36(b1)-(b6) show that the SES-wing vortex remained concentrated up to α = 24°. The vortex was also strengthened and moved closer the wing centerline with α compared to the baseline reverse delta wing (see also figures 4.35(a)-(b)). The higher vortex strength also translates into a more rigorous vortex rotation and peak vorticity level (figures 4.35(c)-(d)). No PIV-derived C_L values were obtained for the SES or LES-equipped wings. The employment of LES_d and LES_u, however, persistently gave rise to a greatly diffused and sometimes ill-defined RDW vortex throughout the α range tested (figures 4.36(c1)-(d6)). The LES_u-wing vortex, however, exhibited a higher (or lower) peak vorticity compared to its LES_d counterpart for $\alpha < 13.5°$ (or $\alpha > 13.5°$). The LES_u wing also had a total circulation comparable to its BW counterpart. Due to the asymmetry of the LES_u-wing vortex, no circumferentially averaged peak tangential velocity value is reported here.

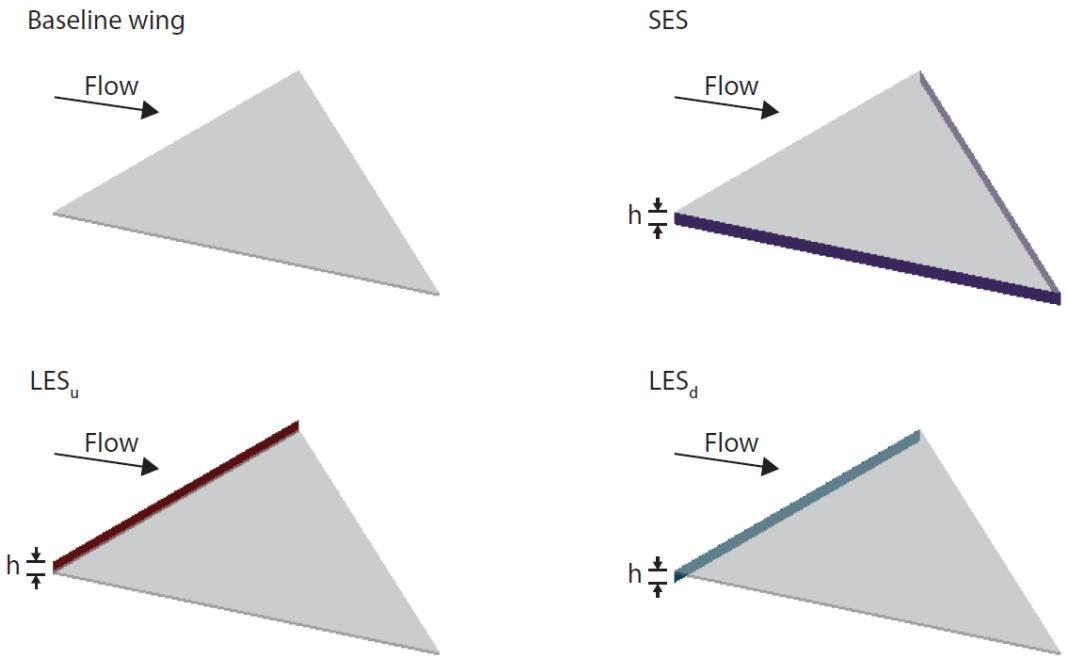

Figure 4.27 Schematics of reverse delta wing test models with Gurney flaplike strips.

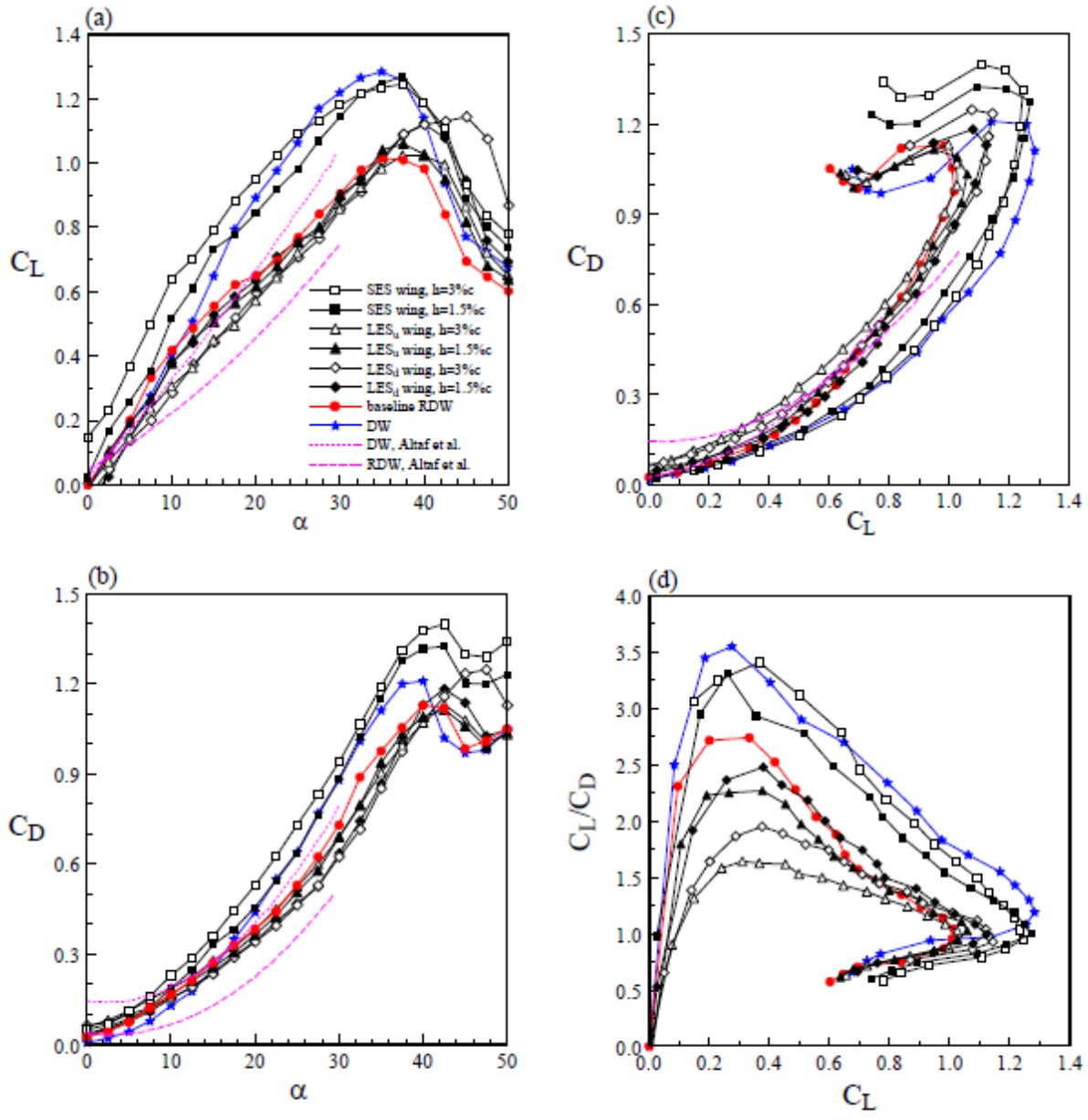

Figure 4.28 Impact of side-edge strip (SES) and leading-edge strip (LES) on RDW aerodynamic characteristics at Re = 4.06 × 10^5. RDW and DW denote reverse delta wing and regular delta wing, respectively.

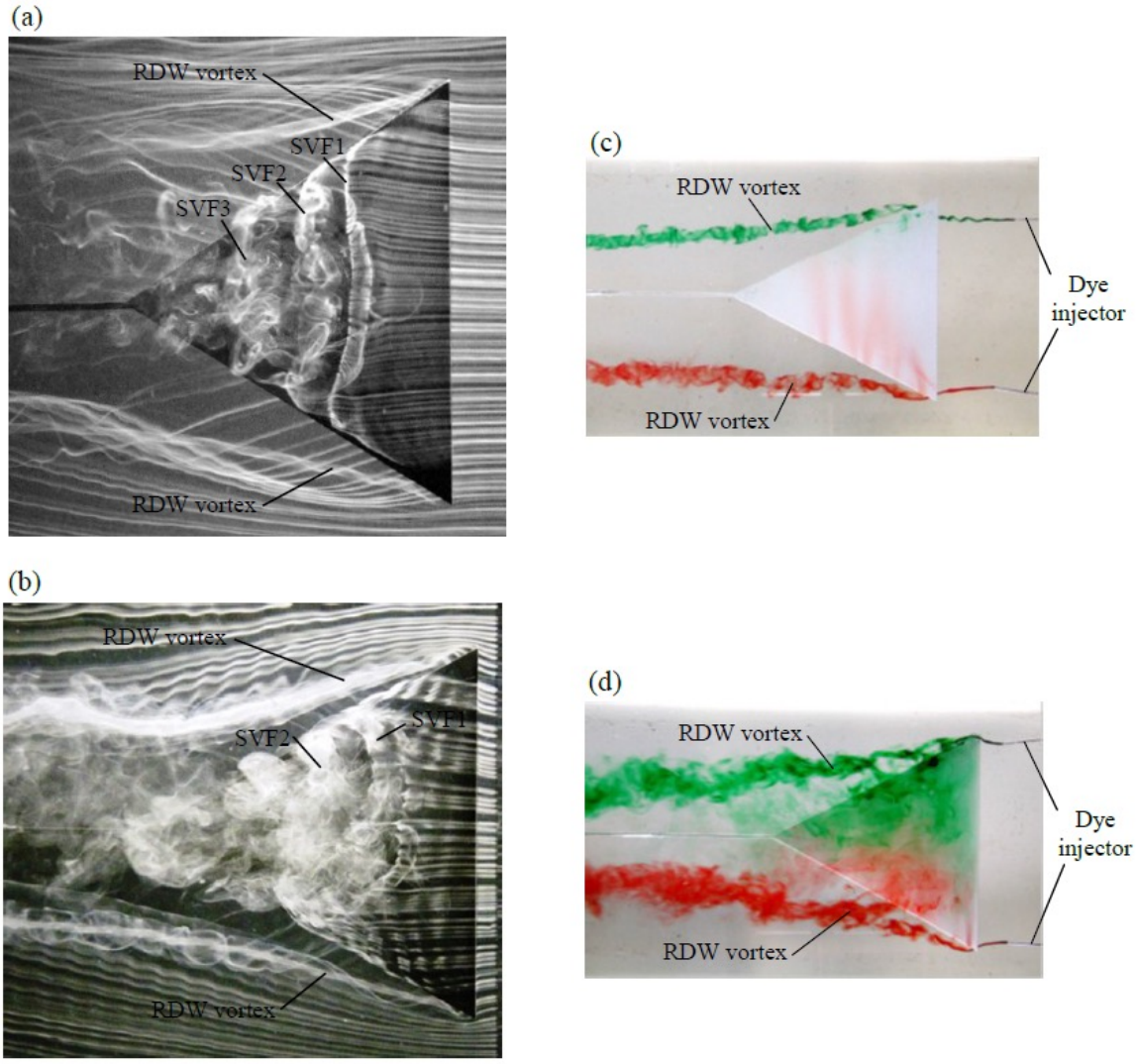

Figure 4.29 Photos of visualized baseline RDW flow patterns at $\alpha = 14°$ and 24°. The flow is from right to left. Smoke-wire flow visualization: (a) $\alpha = 14°$ and (b) $\alpha = 24°$. Dye-injection flow visualization: (c) $\alpha = 14°$ and (d) $\alpha = 24°$. SVF denotes spanwise vortex filament.

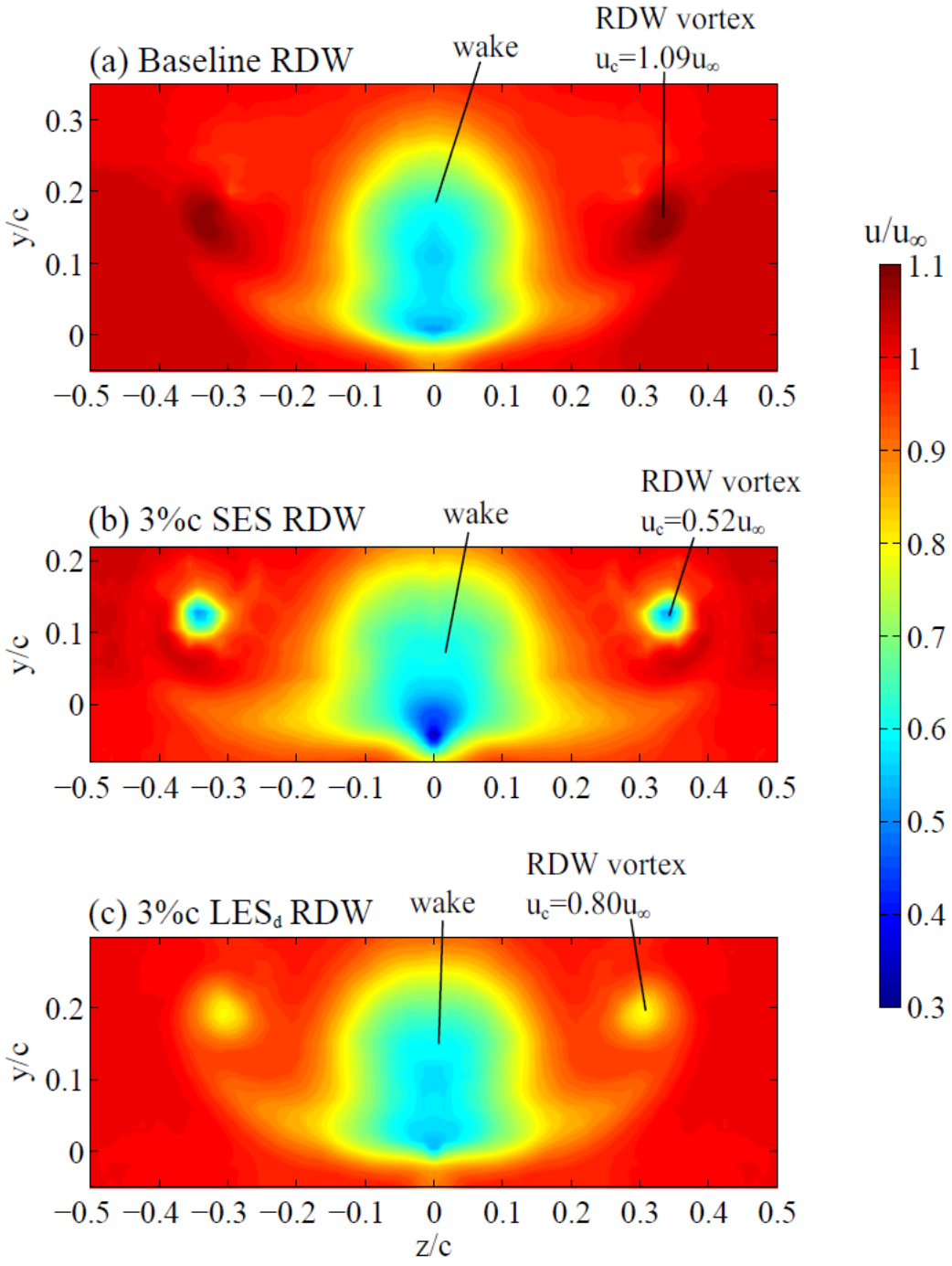

Figure 4.30 Normalized iso-axial velocity contours at x/c = 1.01 for α = 16°.

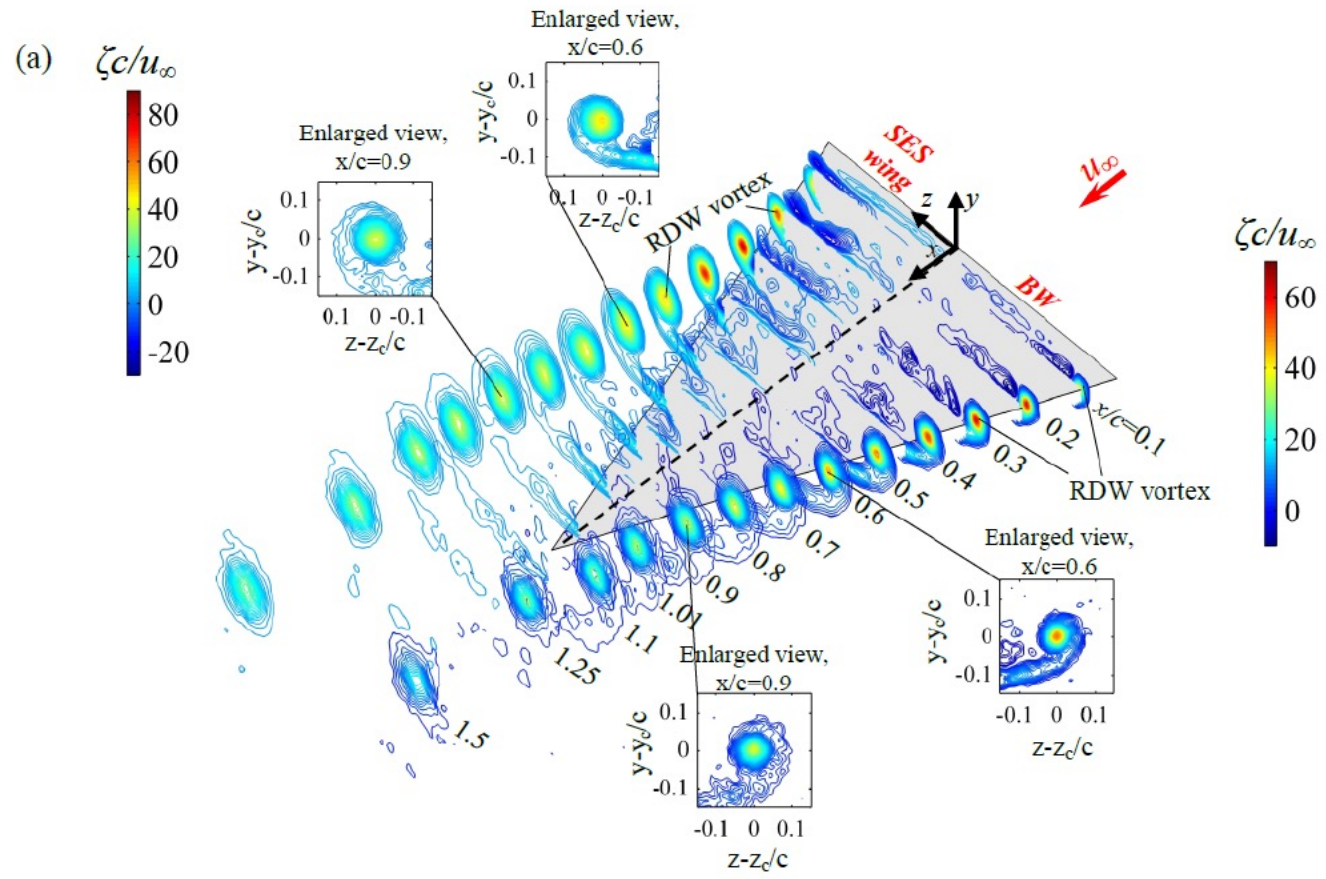

Figure 4.31 Combined spatial progression of normalized iso-vorticity contours at α = 16°. (a) BW and SES wing, (b) BW and LES_d wing, and (c) BW and LES_u wing. BW denotes baseline RDW. BW denotes baseline wing. SES denotes side-edge strip. LES_d and LES_u denote downward and upward leading-edge strips, respectively.

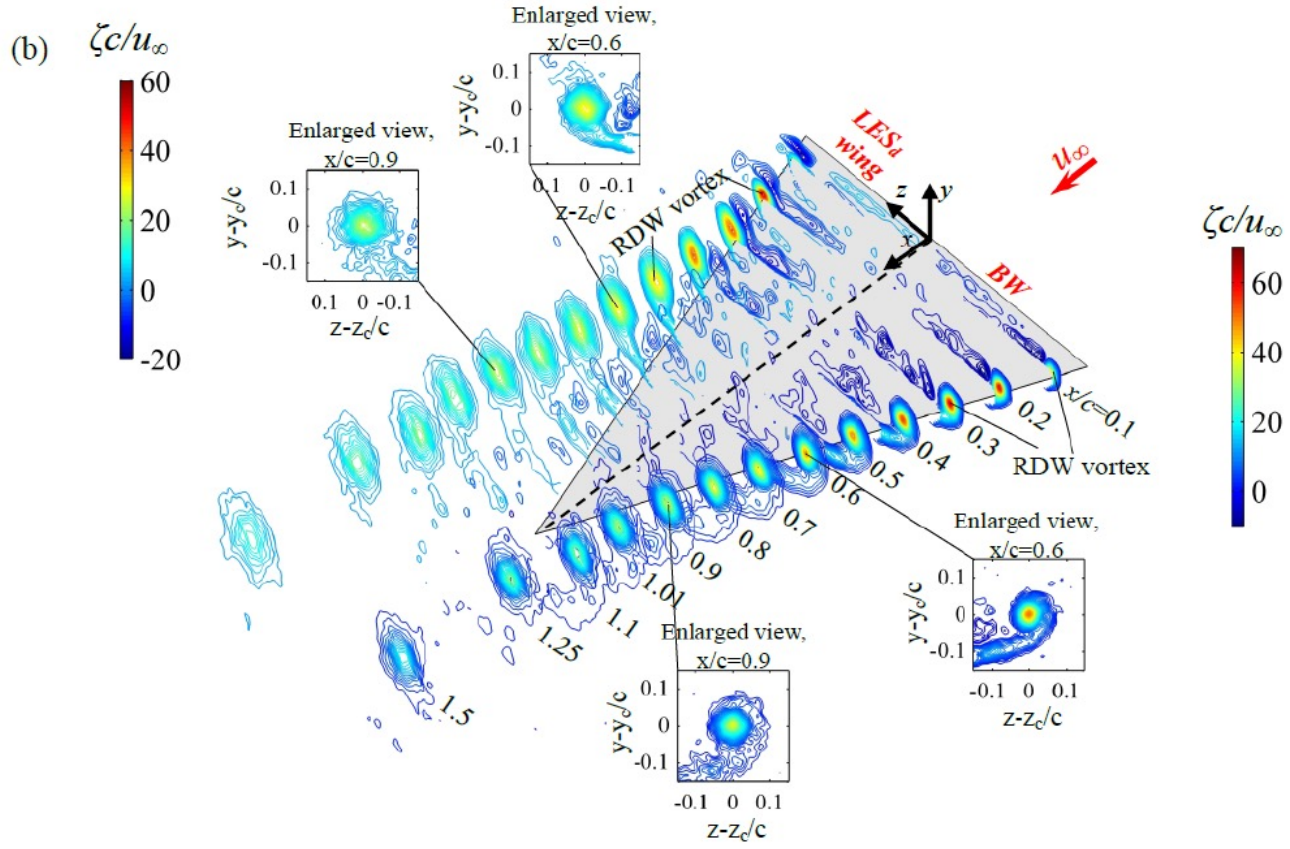

Figure 4.31 Combined spatial progression of normalized iso-vorticity contours at α = 16°. (a) BW and SES wing, (b) BW and LES_d wing, and (c) BW and LES_u wing. BW denotes baseline RDW. BW denotes baseline wing. SES denotes side-edge strip. LES_d and LES_u denote downward and upward leading-edge strips, respectively.

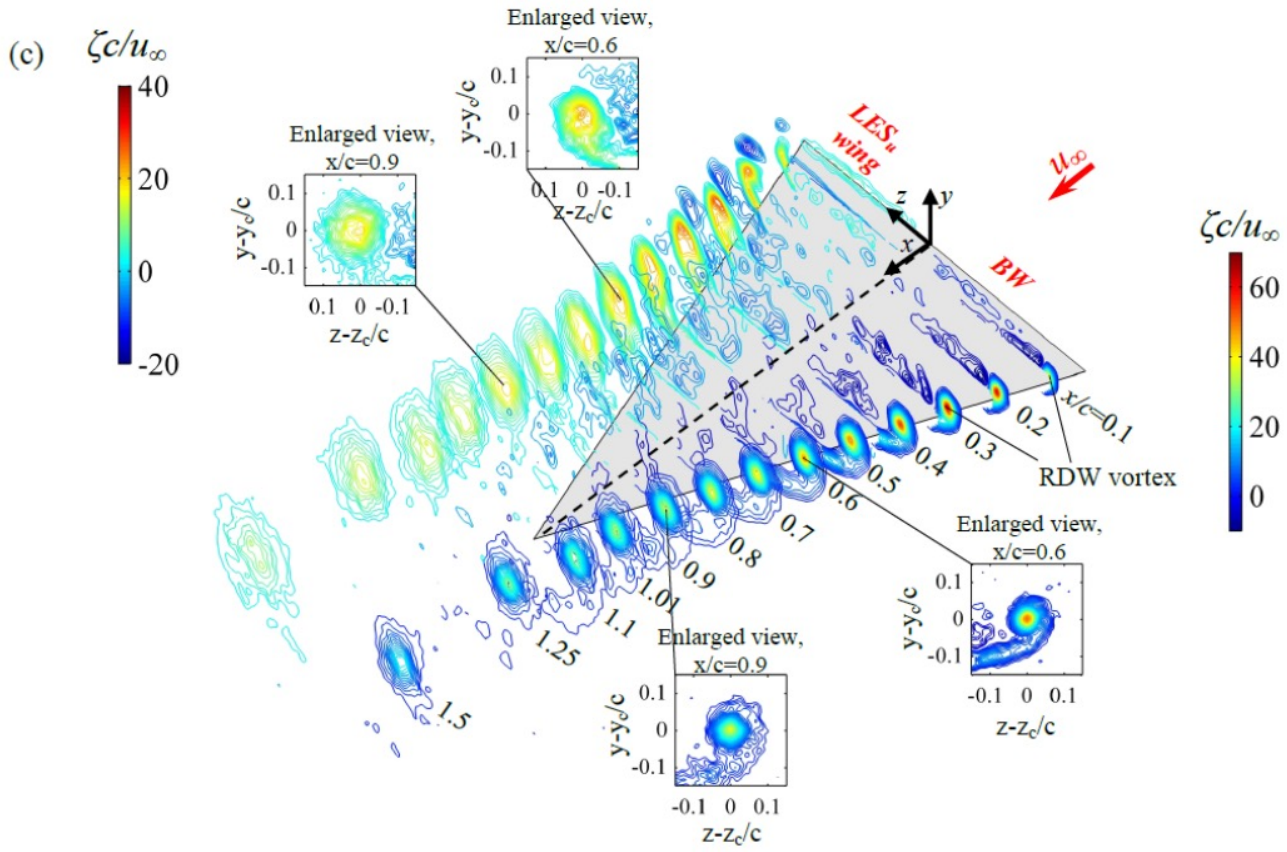

Figure 4.31 Combined spatial progression of normalized iso-vorticity contours at α = 16°. (a) BW and SES wing, (b) BW and LES_d wing, and (c) BW and LES_u wing. BW denotes baseline RDW. BW denotes baseline wing. SES denotes side-edge strip. LES_d and LES_u denote downward and upward leading-edge strips, respectively.

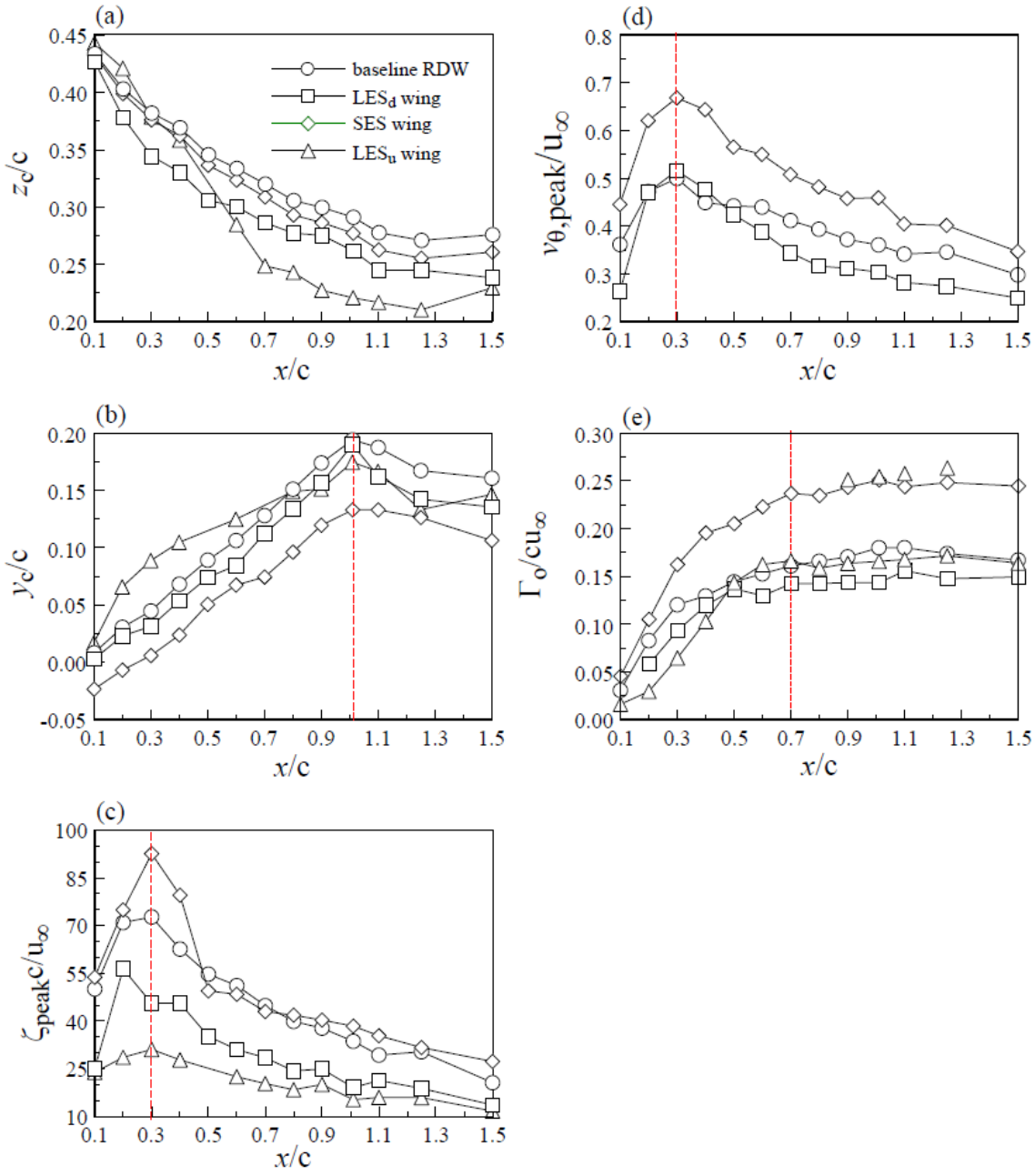

Figure 4.32 Variation of normalized vortex flow parameters with x/c at $\alpha = 16°$.

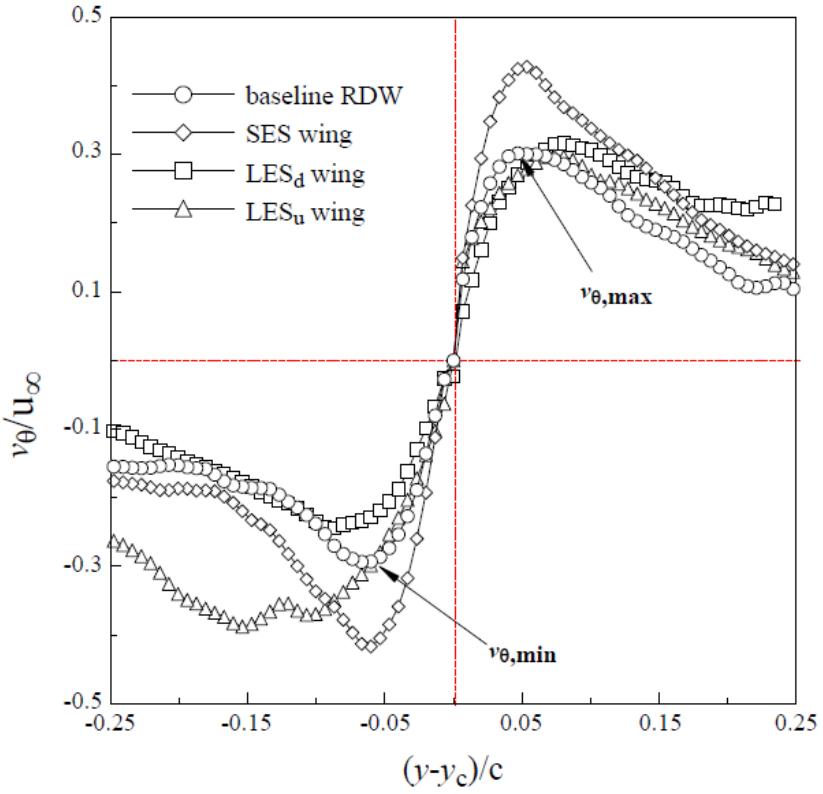

Figure 4.33 Normalized tangential velocity across the vortex center at $x/c = 1.5$ for $\alpha = 16°$.

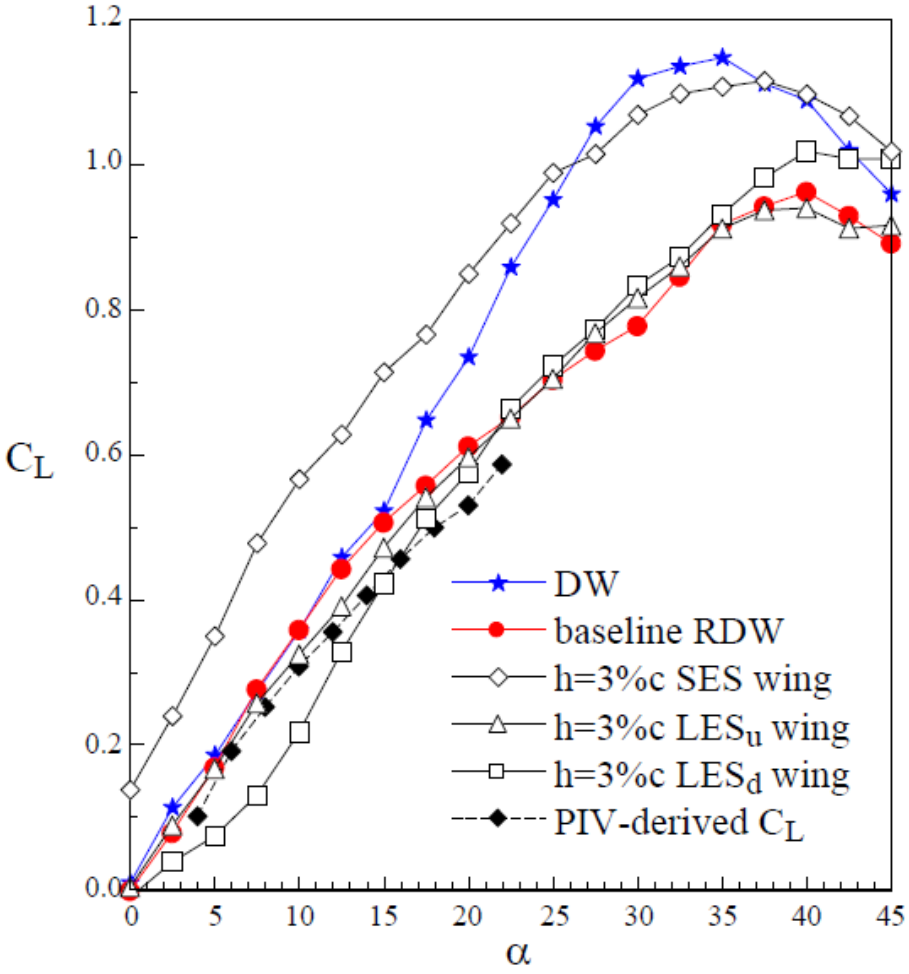

Figure 4.34 C_L-α curves at Re = 1.1×10^4. DW denotes regular delta wing. RDW denotes reverse delta wing.

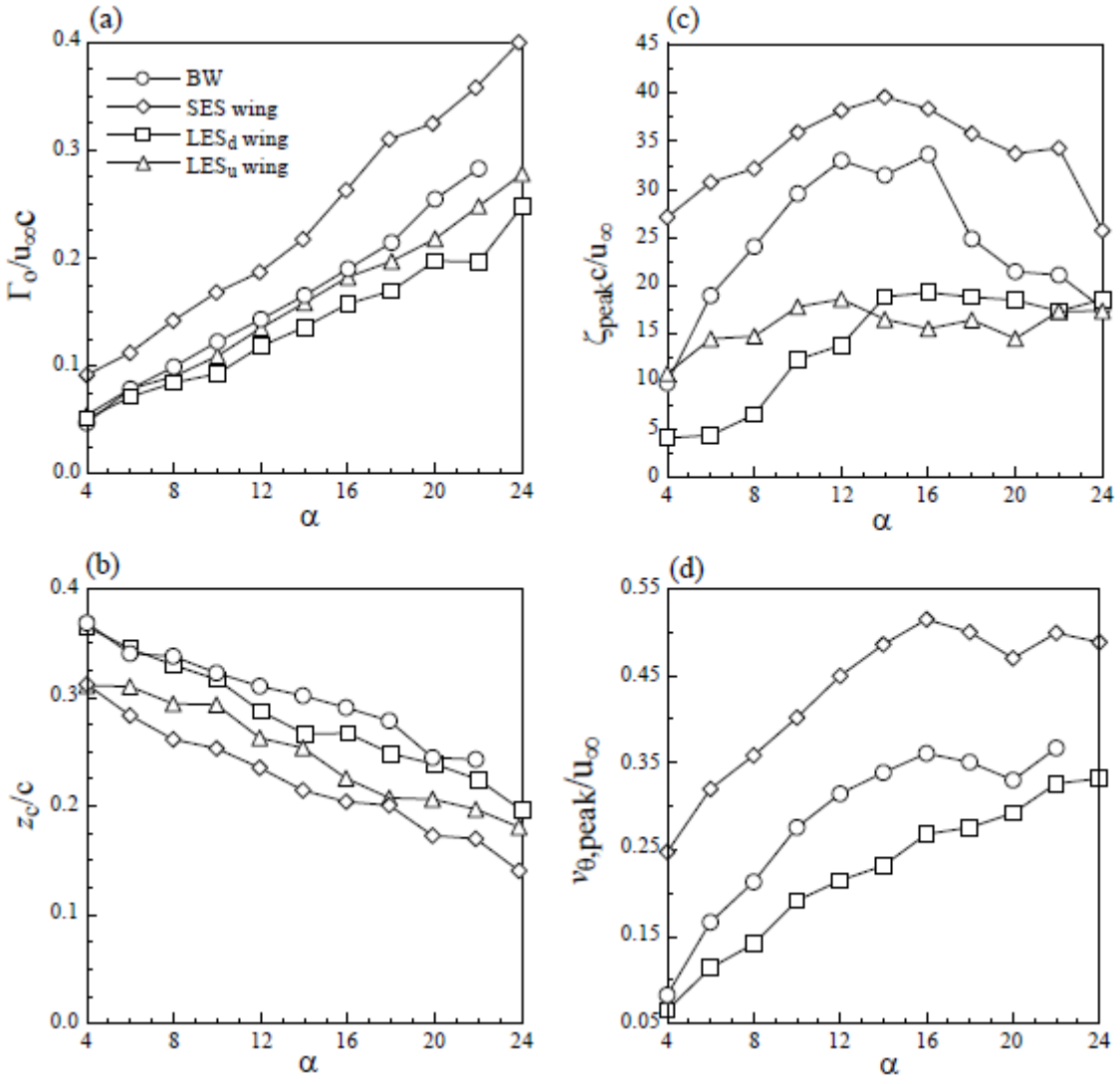

Figure 4.35 Variation of normalized vortex flow parameters with the angle of attack at $x/c = 1.01$.

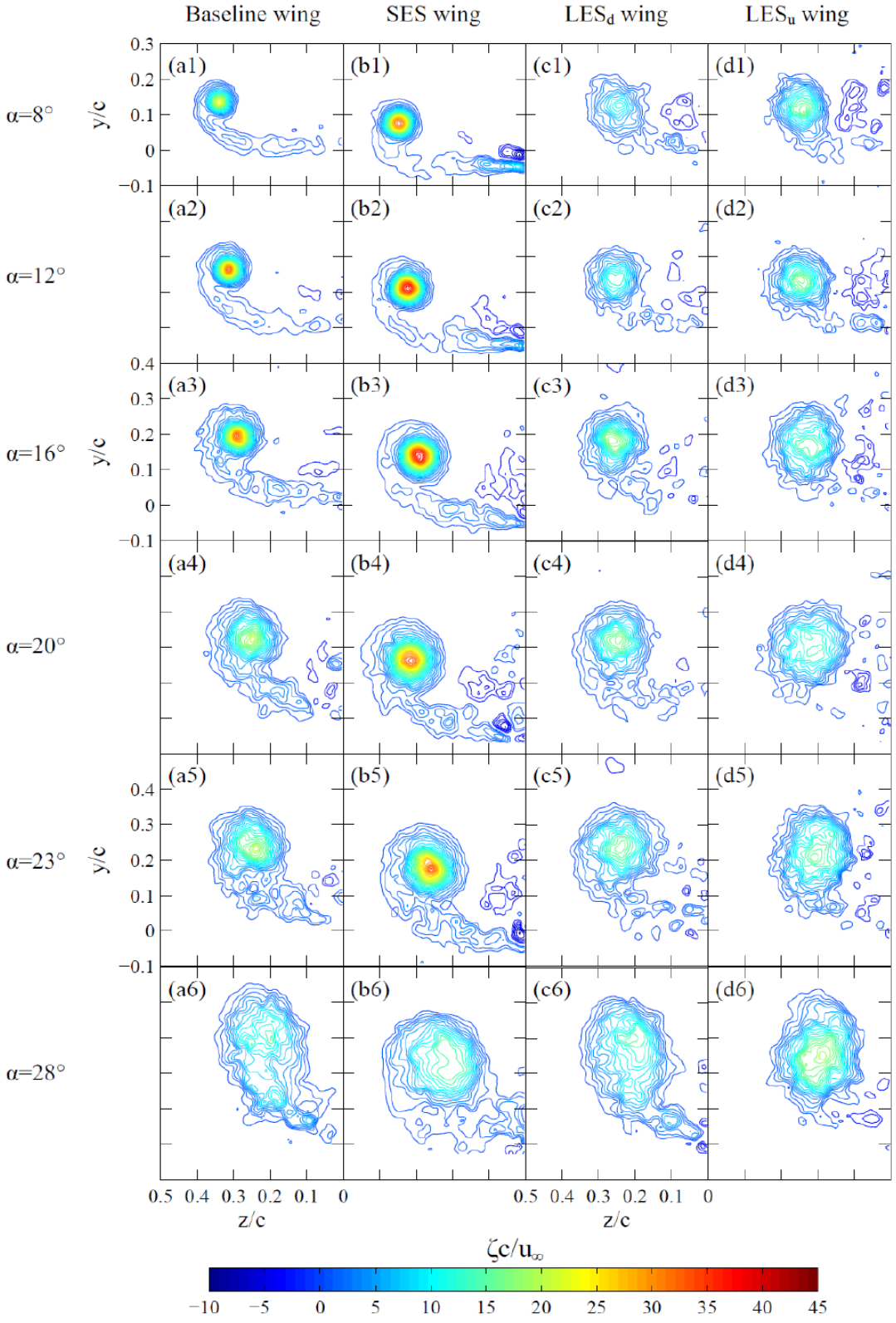

Figure 4.36 Normalized iso-vorticity contours at $x/c = 1.01$ for selected angles of attack.

CHAPTER 5

CONCLUSIONS

The vortex and aerodynamic characteristics of a reverse delta wing (RDW) were investigated by using particle image velocimetry (PIV) in conjunction with flow visualization and force balance measurements. The conclusions corresponding to Sections 4.1, 4.2 and 4.3 are discussed below.

5.1 Conclusions of findings on the 65°-sweep slender reverse delta wing

The following conclusions on a slender reverse delta wing were drawn. The reverse delta wing was found to have a delayed stall but a lower maximum lift compared to its regular delta wing counterpart. In contrast to the leading-edge vortex breakdown-induced stalling, the stalling mechanism of the reverse delta wing was found to be triggered by the breakdown of the unique multiple spanwise vortex filaments developed over its upper wing surface. The lower lift of the reverse delta wing was, however, overwhelmed by the lowered drag, leading to an improved lift-to-drag ratio compared to the regular delta wing of the same sweep angle. The particle-image-velocimetry flowfield measurements show that, in contrast to the outboard movement of the DW vortex, the RDW vortex (originated from the spanwise leading-edge vortex filament) always lay outside the wing and moved further inboard as it progressed downstream, which suggests that the RDW vortices have little relevance to the reverse delta wing lift generation. The higher the angle of attack the larger the inboard movement of the RDW vortex center was observed. The DW vortex was more concentrated and had a higher circulation and peak tangential velocity compared to the RDW vortex. The roll-up of the RDW vortex was, however, found to be completed for $x/c \geq 0.7$, leading to an invariant total circulation, while the DW vortex attained axisymmetry only for $x/c \geq 1.5$. The total lift coefficient computed, based on the total circulation and the distance between the RDW vortices, via Kutta-Joukowski theorem agrees well with the force balance data. Finally, the RDW vortex was found to remain concentrated and axisymmetric for $\alpha \leq 16°$ and became diffused for $16° < \alpha \leq 23°$. For $\alpha > 22°$, the RDW vortex resembled a circulation-like flow with small patches of vorticity.

5.2 Conclusions of the findings on the 50°-sweep non-slender reverse delta wing aerodynamics and vortex flow characteristics

The vortex flow structure and lift generation of a 50°-sweep non-slender reverse delta wing were investigated at Re = 11,000. There existed a large similarity in the aerodynamic and vortex flow characteristics between the non-slender and slender delta wings. Regardless of the slenderness, the reverse delta wing (RDW) always had a delayed stall but a lower maximum lift compared to its regular delta wing counterpart. In contrast to the leading-edge vortex breakdown-induced stalling of the regular delta wing, the stalling mechanism of reverse delta wing was again found to be triggered by the disruption of the multiple spanwise vortex filaments developed over its upper wing surface. The upper surface of the non-slender reverse delta wing therefore acts like a wake generator. Additionally, the RDW vortex was always located outside the wing and moved further inboard as it progressed downstream, which suggests that the RDW vortices have little relevance to the reverse delta wing lift generation. The RDW vortex center was found to move inboard with increasing angle of attack. The vortex generated by the non-slender reverse delta wing was, however, less concentrated and had a lower circulation and peak tangential velocity compared to its slender counterpart. The roll-up of the RDW65 vortex completed earlier. The strength of the RDW50 vortex was lower than the RDW65. In addition, the 50°-sweep non-slender was also found to become disorganized at lower angle of attack.

5.3 Conclusions of the findings on passive reverse delta wing control

The following conclusions were drawn for a reverse delta wing with the addition of passive Gurney flap-like strips, of different height and configurations. The addition of the side-edge strip (SES) caused a leftward shifting of the C_L–α curve, especially for the h = 3%c case, resembling the employment of a trailing-edge flap of a rectangular wing, and thereby led to a significant lift increase comparable to that of a regular delta wing. The lift increase overwhelmed the drag increase, rendering an improved lift-to-drag ratio compared to the baseline reverse delta wing. The SES wing-generated vortex remained similar to its baseline reverse delta wing counterpart but had a higher strength and peak vorticity and

tangential velocity. The larger the strip height is, the higher the SES-wing vortex strength and lift generation become. The SES-wing vortex was also found to remain concentrated up to $\alpha = 24°$ while the baseline RDW vortex stayed well-defined for $\alpha \leq 16°$. On the other hand, the employment of the leading-edge strip (LES) always led to a diffused RDW vortex and also a reduced (or an increased) lift for the pre-stall (or post-stall) α regime compared to the baseline wing. The downward LES-wing produced a lower vortex strength and lift compared to their upward counterpart. The LES_d also caused a large stall delay and maximum lift increment compared to the baseline wing. The larger the strip height the larger the stall delay and maximum lift increase was obtained. Finally, the application of leading-edge strips can provide a potential wingtip vortex suppression scheme while the side-edge strips can give an enhanced aerodynamic performance of the reverse delta wing.

CHAPTER 6

LIST OF CONTRIBUTIONS AND FUTURE WORK

The reverse delta wing planform has been extensively employed in the Lippisch-type wing-in-ground effect craft. Surprisingly, the aerodynamics and the vortex flowfield characteristics of the reverse delta wing, both slender and non-slender, were, however, not available in open archives. To improve our understanding of the behavior of the reverse delta wing, an experimental investigation utilizing particle image velocimetry, force balance, and flow visualization techniques in a free stream were conducted. The major first-hand findings or contributions are listed below.

(*a*) In contrast to the regular or conventional delta wing (which have been studied by researchers elsewhere), the reverse delta wing was found to have a delayed stall but also a lowered lift and drag compared to its regular delta wing counterpart.

(*b*) The upper surface of the reverse delta wing was characterized by the formation and growth of unique multiple spanwise vortex filaments.

(*c*) In contrast to the leading-edge vortex breakdown-induced stalling of the regular delta wing, the stalling mechanism of the reverse delta wing was found to be triggered by the breakdown of the multiple spanwise vortex filaments developed over its upper wing surface.

(*d*) The vortices generated by the reverse delta wing were found to be located outside the wing (in contrast to the inboard location of the leading-edge vortices), and were found to complete their rolling up at 70% chord location downstream from the leading edge of the reverse delta wing.

(*e*) In contrast to the significant lift contribution of the leading-edge vortices to the regular delta wing, the reverse-delta-wing vortices were found to be irrelevant to the lift generation of the reverse delta wing.

(*f*) The lift generation of the reverse delta wing was mainly from the pressure acting on its lower surface, while its upper surface acted as a wake generator.

(*g*) For the non-slender reverse wing, the aerodynamic loading, including the stalling mechanism and the vortex characteristics, were found to be similar to those of a slender reverse delta wing but had a reduced magnitude.

(*h*) The lift generation capability of the reverse delta wing could be enhanced via the use of Gurney flaplike strips, of different heights and configurations. The addition of side-edge strips not only caused a leftward shift of the lift curve, resembling a conventional trailing-edge flap, but also a large lift increment, which overwhelmed the corresponding drag increase and led to an improved lift-to-drag ratio compared to the clean baseline wing. The lift and drag coefficients were also found to increase with the strip height. The side-edge strip-equipped wing also produced a strengthened vortex compared to its baseline or clean wing counterpart.

(*j*) The passive lift control employed in the present study also shows that the leading-edge strips persistently produced a greatly diffused vortex flow and, therefore, offered a promising wingtip vortex control alternative. The downward leading-edge strip, in particular, was found to able to deliver a delayed stall and an increased maximum lift force compared to the baseline or clean wing. To further investigate the study of Lee and Su (2012), where a half RDW was used as a wingtip vortex control device, the LES_d can be added to it in order its effect and potential application. At the present, most of the wingtip vortex controls are have a swept back leading edge, such as on winglets or rake wingtips, however, a half RDW device can also be added without too much weight and span penalty. Furthermore, the angle of the HRDW relative to the main wing can also be changed in order to maximum its effectiveness.

It is believed that the present investigation not only advances our understanding of the reverse delta wing, but also lay the foundation for the study of the aerodynamics and vortex flowfield of a reverse delta wing in ground proximity. The present measurements would also serve as benchmark data for CFD validation. The near-future study involving

the effects of ground clearance and also the anhedral should allow us to significantly improve the performance as well as the design and development of the Lippisch-type wing-in-ground effect craft.

REFERENCES

Ahmed, M. R., and Sharma, S. D., 2005, "An investigation on the aerodynamics of a symmetric airfoil in ground effect," *Experimental Thermal and Fluid Science*, Vol. 29, No. 6, pp. 633-647.

Ahmed, M. R., Takasaki, T. and Kohama, Y., 2007, "Aerodynamics of a NACA 4412 airfoil in ground effect," *AIAA Journal*, Vol. 45, No. 1, pp. 37-47.

Alexander Lippisch, n.d., In *Wikipedia*. Retrieved April 10, 2017, from https://en.wikipedia.org/wiki/Alexander_Lippisch

Allan, et al., 2004, "Wind-tunnel interference effects on a 70 degree delta wing," *Aeronautical Journal*, Vol. 108, pp. 505-514.

Altaf, A., Omar, A. A., Asrar, W., and Jamaluddin, H. B. L., (2011) "Study of the reverse delta wing," *Journal of Aircraft*, Vol. 48, No. 1, pp. 277-286.

Arndt, R., n.d., "Lippisch aerodyne research." Retrieved April 10, 2017, from http://discaircraft.greyfalcon.us/LIPPISCHE%20AERODYNE%20RESEARCH.htm

Badarn, B., McCormick, S., and Gursul, I., 1998, "Control of leading-edge vortices with suction," *Journal of Aircraft*, Vol. 35, No. 1, pp. 163-165.

Benmeddour, A., Mebarki, Y., and X. Huang, X., 2009, "Computational investigation of the centerbody effects on the aerodynamics of delta wings," *RTO-AVT Rep 2009.84*.

Birch, D., and Lee, T., 2004, "The structure and induced drag of a tip vortex," *Journal of Aircraft,* Vol. 41, No. 5, pp. 1138-1145.

Caspian Sea Monster, n.d., In *Wikipedia*. Retrieved April 10, 2017, from https://en.wikipedia.org/wiki/Caspian_Sea_Monster

Cho, J., Han, C., Moon, Y, and Baek, J., 2001, "Aerodynamic analysis and design of an aero-leviatation electric vehicle," *AIAA-2001-2345*.

Cui, E., and Zhang, X., 2010, Chapter 18: Ground effect aerodynamics, Encyclopedia Aerospace Engineering, edited by Richard Blockley and Wei Shyy, John Wiley & Sons, Ltd.

Delery, J. M., 1994, "Aspects of vortex breakdown," *Progress in Aerospace Sciences*, Vol. 30, No. 1, pp. 1-59.

Deng, Q., and Gursul, I., 1996, "Effect of leading-edge flaps on vortices and vortex breakdown," *Journal of Aircraft*, Vol. 33, No. 6, pp. 1079-1086.

Devenport, et al., 1996, "The structure and development of a wing-tip vortex," *Journal of Fluid Mechanics*, Vol. 312, pp. 67-106.

Dogar, M., 2012, "An investigation of aerodynamics and flow characteristics of slender and non-slender delta wing," MS thesis, Department of Mechanical Engineering, McGill University, Montreal, Quebec, Canada.

Earnshaw, P. B., 1961, "An experimental investigation of the structure of a leading-edge vortex," *British Aeronautical Research Council, Reports and Memoranda 3281*.

Earnshaw, P., 1964, "Measurements of vortex-breakdown position at low speed on a series of sharp-edged symmetrical models," *BARC Reports & Memoranda No. 3424*.

Elsayed, O. A., Asrar, W., and Omar, A. A., 2008, "Reverse delta wing trailing vortex characteristics by particle image velocimetry," *3rd Internaltional Symposium on Advanced Fluid/Solid Science and Technology in Experimental Mechanics*, Tainan, Taiwan, 7-10 December.

Gerontakos, P., and Lee, T., 2008, "PIV study of flow around unsteady airfoil with dynamic trailing-edge flap deflection," *Experiments in Fluids*, Vol. 45, pp. 955-972.

Gerhardt, H. A., 1996, "Supersonic natural laminar flow wing," Northrop Grunman Corp., Los Angeles, Patent No. 5538201.

Green, S. I., 1995, Fluid Vortices, Kluwer Academic Publisher.

Gu, W., Robinson, O., and Rockwell, D., 1993, "Control of vortices on a delta wing by leading-edge injection," *AIAA Journal*, Vol. 31, No. 7, pp. 1177-1186.

Gursul, I., 2004, "Recent developments in delta wing aerodynamics," *Aeronautical Journal*, Vol. 108, No. 1087, pp. 437-452.

Gursul, I., 2005, "Review of unsteady vortex flows over slender delta wings," *Journal of Aircraft*, Vol. 45, No. 2, pp. 299.

Gursul, .I, Wang, Z., and Vardaki, E., 2007, "Review of flow control mechanisms of leading-edge vortices," *Progress in Aerospace Science,* Vol. 43, pp. 246-270.

Halloran, M., and O'Meara S., 1999, "Wing in ground effect craft review," Australia Aeronautical and Maritime Research Laboratory, *DSTO-GD-0201*.

Han, C., Cho, J., Moon, Y., and Song, Y., 2005, "Design of an aerolevitation electric vehicle for high-speed ground transportation system," *Journal of Aircraft*, Vol. 42, No.1, pp.93-104.

Helin, H. E., and Waltry, C. W., 1994, "Effects of trailing-edge jet entrainment on delta wing vortices," *AIAA Journal*, Vol. 32, No. 4, pp. 802-804.

Hoffmann, E. R., and Joubert, P.N., 1963, "Turbulent line vortices," *Journal of Fluid Mechanics*, Vol. 16, No. 3, pp. 395-411.

Honkan, A., and Andreopoulos, A., 1997, "Instantaneous three-dimensional vorticity measurements in vortical flow over a delta wing," *AIAA Journal*, Vol. 35, No. 10, pp. 1612-1620.

Huang, X. Z., Sun, Y. Z., and Hanff, E. S., 1997, "Further investigations of leading-edge vortex breakdown over delta wings," *AIAA-97-2263*.

Jobe, C. E., 2004, “Vortex breakdown location over 65 degrees delta wings empiricism and experiment,” *Aeronautical Journal*, Vol. 108, No. 7, pp. 475-482.

Johari, H., and Durgin, W. W., 1998, “Direct measurement of circulation using ultrasound,” *Experiments in Fluids*, Vol. 25, No. 5, pp. 445-454.

Kaplan, S. M., Altman, A., and Ol, M., 2007, “Wake vorticity measurements for low aspect ratio wings at low Reynolds number,” *Journal of Aircraft*, Vol. 44, No. 1, pp. 241-251.

Kocivar, B., 1977, Ram-wing X-114: floats, skims, and flies,” *Popular Science*, pp. 70-73.

Klute, S. M., Rediniostis, O. K., and Telionis, D. P., 1996, “Flow control over a maneuvering delta wing at high angles of attack,” *AIAA Journal*, Vol. 34, No. 4, pp. 662-668.

Kusonose, K., 1998, “Drag reduction based on a wake-integral method,” *AIAA-98-2723*.

Lambourne, N. C., and Bryer, D. W., 1961, “The bursting of leading edge vortices-Some observations and discussion of the phenomenon,” *American Research Council*, *RM 3282*, pp. 1-37.

Lee, G. -B., Shih, C., Tai, Y. -C., Tsao, T., Liu, C., Huang, A., and Ho, C. -M., 2000, “Robust vortex control of a delta wing by distributed micro electro mechanical-systems actuators,” *Journal of Aircraft*, Vol. 37, No. 4, pp. 697-706.

Lee, T., and Su, Y. Y., 2012, "Wingtip vortex control via the use of a reverse half-delta wing," *Experiments in Fluids,* Vol. 52, No. 6, pp. 1593-1609.

Lee, T., and Pereira, J., (2013) "Modification of static-wing tip vortex via a slender half-delta wing," *Journal of Fluids and Structures*, Vol. 43, pp. 1-14.

Lee, T., and Choi, S., 2015, “Wingtip vortex control via tip-mounted half-delta wings of different geometric configurations,” *ASME Journal of Fluids Engineering*, Vol. 137, pp. 1-9.

Lee, T., and Ko, L. S., 2016, "Experimental study of the vortex flow and aerodynamic characteristics of a reverse delta wing," *Journal of Aerospace Engineering*, Vol. 230, No. 6, pp. 1126-1138.

Lee, T., 2016, "Impact of Gurney flaplike strips on the aerodynamic and vortex flow characteristics of a reverse delta wing," *ASME Journal of Fluids Engineering*, Vol. 138, pp; 061104-1 to -9.

Liu, T., Makhmalbaf, M. M., Ramasamy, R., Kode, S. S., and Merati, P. P., 2015, "Skin friction fields and surface dye patterns on delta wings in water flows," *ASME Journal of Fluids Engineering*, Vol. 137, No. 7, pp. 202-214.

Lowson, M. V., and Riley, A. J., 1995, "Vortex breakdown control by delta wing geometry," *Journal of Aircraft*, Vol. 32, No. 4, pp. 832-838.

Luckring, J. M., 2004, "Reynolds number, compressibility, and leading-edge bluntness effects on delta-wing aerodynamics," 24th International Congress of the Aeronautical Sciences, Yokohama, Japan.

Marchman, J. F., 1981, "Aerodynamics of inverted leading-edge flaps on delta wings," *Journal of Aircraft*, Vol. 18, No. 12, pp. 1051-1056.

Maskell, E., 1973, "Progress towards a method for the measurement of the components of the drag of a wing of finite span," *RAE Technical Report 72232*.

Menke, M. and Gursul, I., 1997 "Unsteady nature of leading edge vortices," *Physics of Fluids*, Vol. 9, pp. 2960.

Menke, M., Yang, H., and Gursul, I., 1999, "Experiments on the unsteady nature of vortex breakdown over delta wings," *Experiments in Fluids*, Vol. 27, No. 3, pp. 262-272.

Mitchell, A. M. and Molton, P., 2002, "Vortical substructures in the shear layers forming leading-edge vortices," *AIAA Journal*, Vol. 40, No. 8, pp. 1689-1692.

Mitchell, A. M., Barberis, D., Molton, P., and Delery, J., 2002, "Control of leading-edge vortex breakdown by trailing-edge injection," *Journal of Aicraft*, Vol. 39, No. 2, pp. 221-226.

Mitchell, et al., 2006, "Analysis of delta-wing vortical substructures using detached-eddy simulation," *AIAA Journal*, Vol. 44, No. 5, pp. 964-972.

Miyaji, K., Fujiii, K., and Karashima, K., 1996, "Enhancement of the lateral leading-edge separation vortices by trailing-edge lateral blowing," *AIAA Journal*, Vol. 34, No. 9, pp. 1943-1945.

Moffat, R. J., 1988, "Describing the uncertainties in experimental results," *Experimental Thermal & Fluid Science*, Vol. 1, pp. 3-17.

Moore, N., Wilson, P. A. and Peters, A. J., 2002, "An investigation into wing in ground effect airfoil geometry." In *RTO SCI Symposium on Challenges in Dynamics, System Identification, Control and Handling Qualities for Land, Air, Sea and Space Vehicles*, Berlin, Germany, 13 - 15 May 2002.

Morton, S., Forsythe, J., Mitchell, A., and Hajek, D., 2002, "Detached-eddy simulations and Reynolds-averaged Navier-Stokes simulations of delta wing vortical flowfields," *ASME Journal of Fluids Engineering*, Vol. 24, No. 4, pp. 924-932.

Musaj, M., and Prince, S. A., 2008, "Numerical and experimental investigation of the aerodynamics of an unconventional W-leading edge reversed delta wing in ground effect," *26th International Congress of the Aeronautical Science (ICAS)*, 14-19 September, Alaska, USA.

Nelson, R. C., and Pelletier, A., 2003, "The unsteady aerodynamics of slender wings and aircraft undergoing large amplitude maneuvers," *Progress in Aerospace Science,* Vol. 39, pp. 185-248.

Nikolic, V., 2005, "Movable tip strakes and wing aerodynamics," *Journal of Aircraft*, Vol. 42, No. 6, pp. 1418-1426.

Norris, G., 1999, "Novel SST configuration revealed," *Fight International*, 5 Jan, p.4.

Ol, M. V., and Gharib, M., 2003, "Leading-edge vortex structure of nonslender delta wings at low Reynolds number," *AIAA Journal*, Vol. 41, No. 1, pp. 16-26.

Ollila, R. G., 1980, "Historical review of WIG vehicles," *Journal of Hydronautics*, Vol. 14, No. 3, pp. 65-76.

Panton, R. L., 1990, "Effects of a contoured apex on vortex breakdown," *Journal of Aircraft*, Vol. 27, No. 3, pp. 285-288.

Payne, et al., 1988, "Visualization and wake surveys of vortical flow over a delta-wing," *AIAA Journal*, Vol. 26, No. 2, pp. 137-143.

Payne, F. M., Ng, T. T., and Nelson, R. C., 1989, "Seven hole probe measurement of leading edge vortex flows," *Experiemnts in Fluids*, Vol. 7, pp. 1-8.

Pereira, J., 2011, "Experimental investigation of tip vortex control using a half delta shaped tip strake," Ph.D. thesis, Department of Mechanical Engineering, McGill University, Montreal, Quebec, Canada.

Phillips, W. R. C., 1981, "The turbulent trailing vortex during roll-up," *Journal of Fluid Mechanics*, Vol. 105, pp. 451-467.

Polhamus, E. C., 1971, "Predictions of vortex-lift characteristics by a leading-edge suction analogy," *Journal of Aircraft*, Vol. 8, No. 4, pp. 193-199.

Qu, Q., Lu, Z., Guo, H., Liu, P., and Agarwal, R. K., 2015, "Numerical investigation of the aerodynamics of a delta wing in ground effect," *Journal of Aircraft,* Vol. 52, No. 1, pp. 329-340.

Raffel, M., Willert, C. E., and Kompenhans, J., 1998, Particle image velocimetry. Berlin, Springer.

Rao, D. M., and Huffman, J. K., 1982, "Hinged strakes for enhanced maneuverability at high angles of attack," *Journal of Aircraft*, Vol. 19, No. 4, pp. 278-282.

Roberts, L. S., Finnis, M. V., and Knowles, K., 2016, "Characteristics of boundary-layer transition and Reynolds-number sensitivity of three-dimensional wings of varying complexity operating in ground effect," To appear in *ASME Journal of Fluids Engineering*.

Rozhdestvensky, K. V., 2006, "Wing-in-ground effect vehicles," *Progress in Aerospace Science*, Vol. 42, pp. 211-283.

Skow, A. M., and Erickson, G. E., 1982, "Modern fighter aircraft design for high-angle-of-attack maneuvering," *AGARD-LS-121*, pp. 4-1 to 4-59.

Soltani, M. R., and Bragg, M. B., 1990, "Measurements on an oscillating 70-degree delta wing in subsonic flow," *Journal of Aircraft*, Vol. 27, No. 3, pp. 211-217.

Tarantola, A., 2013, "This "Caspian Sea Monster" Was a Giant Soviet Spruce Goose." Retrieved April 10, 2017, from http://gizmodo.com/this-caspian-sea-monster-was-a-giant-soviet-spruce-go-1456423681

Thompson, D. H., 1975, "A water tunnel study of vortex breakdown over wings with highly swept leading edges," *Australian Defence Scientific Service, Note ARL/A 356*.

Tomaru, H., and Kohama, Y., 1990, "Experiments on wing in ground effect with fixed ground plates," *Proceedings of the 2nd JSME-KSME Fluids Eng. Conference*, Japan Society of Mechanical Engineers, Tokyo, pp.370-373.

Traub, L. W., 2000, "Aerodynamic characteristics of spanwise cambered delta wings," *Journal of Aircraft*, Vol. 37, No. 4, pp. 714-724.

Visser, K. D., and Nelson, R. C., 1993, "Measurements of circulation and vorticity in the leading-edge vortex of a delta-wing," *AIAA Journal*, Vol. 31, No. 1, pp. 104-111.

Wahls, R. A., Vess, R. J., and Moskovitz, C. A., 1986, "Experimental investigation of apex fence flaps on delta wings," *Journal of Aircraft*, Vol. 23, No. 10, pp.789-797.

Wang, J. J., Xu, Y., and Li, Y. C., 2002, "Experimental studies on the aerodynamic characteristics of a 70-degree delta wing with apex flap," *Experiments and Measurements in Fluid Mechanics*, Vol. 16, No. 2, pp. 52-56.

Wang, F. Y., Milanovic, I. M., Zaman, K. B., and Povinelli, L. A., 2005, "A quantitative comparison of delta wing vortices in the near-wake for incompressible and supersonic free streams," *ASME Journal of Fluids Engineering*, Vol. 127, No. 6, pp. 1071-1084.

Wang, H., Teo, C. J., Khoo, B. C., and Goh, C. J., 2013, "Computational aerodynamics and flight stability of wing-in-ground (WIG) craft," *Procedia Engineering*, Vol. 67, pp. 15-24.

Wang, J. J., Li, Y. C., and Choi, K. -S., 2008, "Gurney flap-Lift enhancement, mechanisms and applications," *Progress in Aerospace Science*, Vol. 44, pp. 22-47.

Wenger, C. W., and Devenport, W. J., 1999, "Seven-Hole Pressure Probe Calibration Method Utilizing Look-Up Error Tables," *AIAA Journal*, Vol. 37, No. 6, pp. 6-14.

Wentz, W. H., and Kohlman, D. L., 1971, "Vortex breakdown on slender sharp-edge wings," *Journal of Aircraft*, Vol. 8, No. 3, pp. 156-161.

Wing Ship Technology, n.d., "Wing Ship Technology." Retrieved April 10, 2017 from http://www.wingship.com

Wu, H., Miorini, R.L., Tan, D., and Katz, J., 2012, "Turbulence within the tip-leakage vortex of an axial waterjet pump," *AIAA Journal*, Vol. 50, No. 11, pp. 2574-2587.

Yun, L., Bliault, A., and Doo, J., 2010, WIG craft and Ekranoplan-Ground effect craft technology. Springer, New York.

Zerihan,J., and Zhang, X., 2000, "Aerodynamics of a single-element wing in ground effect," *Journal of Aircraft*, Vol.. 37, No. 6, pp. 1058-1064.

Zerihan, J., and Zhang, X., 2001, "Aerodynamics of Gurney flaps on a wing in ground effect," *AIAA Journal,* Vol. 39, No. 5, pp. 772-780.

Zhan, J.X., and Wang, J.J., 2004, "Experimental study on Gurney flap and apex flap on a delta wing," *Journal of Aircraft*, Vol. 41, No. 6, pp. 1379-1383.

Zhang, X., and Zerihan, J., 2003a, "Off-surface aerodynamic measurements of a wing in ground effect," *Journal of Aircraft*, Vol. 40, No. 4, pp. 716-725.

Zhang, X., and Zerihan, J., 2003b, "Aerodynamics of a double-element wing in ground effect," *AIAA Journal*, Vol. 45, No. 6, pp. 1007-1016.

APPENDIX

APPENDIX A

Details of particle-image-velocimetry flow measurement system

A1. Introduction

In the early 1900s, Ludwig Prandtl had utilized a manually powered water tunnel suspended with mica particles on the surface of water in order to study two-dimensional models such as cylinders, prisms and wings. Prandtl could vary parameters such as wing model, angle of attack, flow velocity and steady or unsteady flow. He was able to gain insight into the flow properties qualitatively. No quantitative data about flow field behavior could be achieved. Today, a century later, extracting quantitative information about the instantaneous flow field is easily achieved by the particle image velocimetry (PIV) technique. Particle image velocimetry is an experimental technique used to obtain the velocity flow field at a location by following tracer objects. It is a quantitative experimental technique that is made possible by carefully extracting the flow information utilizing visualization technique.

A typical PIV setup consists of several apparatus. The technique can be applied in both water and air flow facilities. Tracer particles, which can consist of small diameter beads or droplets of oil, are added into the flow. The particles are then illuminated two times within a known very short duration of time. The light scattered by the particles is then capture by a camera onto a single or multiple frames. The displacement of the particles between the two laser light pulses can be determined through the evaluation of the PIV recording. Finally, through specialized computer software, the images can be processed in order to obtain the instantaneous flow field of the flow of interest.

A2. Principle of operation

Figure A1 shows a schematic diagram of a classic setup for PIV experiments in a wind tunnel. Small tracer particles are added into the air. As the particles travel into the field of view, they are illuminated twice by a laser light sheet aligned to the region of interest. The delay between the two illuminations is determined by the flow velocity and magnification

at imaging. One assumption is that the tracer particles move with the local flow velocity between the two illuminations. A high quality camera finally captures the light scattered by the tracer particles via a high quality lens either on a single frame or on two separate frames. In the past, the images are then developed and scanned for further processing. Modern digital cameras can bypass this step and show the particle images directly on the computer screen.

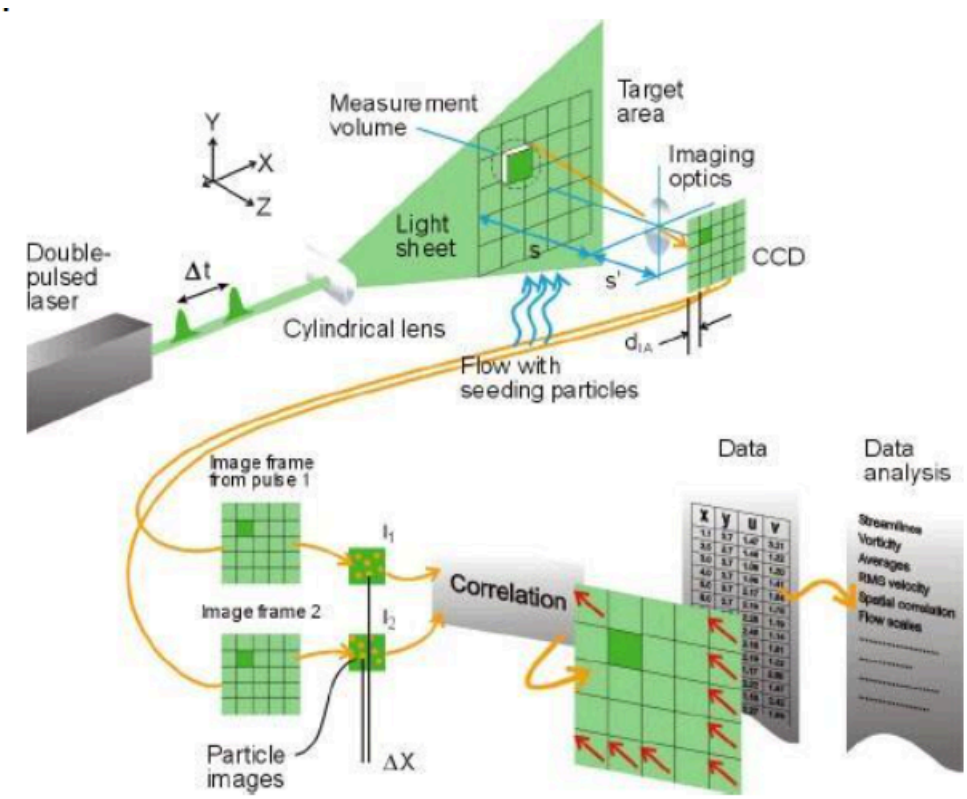

Figure A1 Overview of the particle image velocimetry flow chart (Dantec dynamics n.d.)

In order to analyze the PIV images, the digital image is subdivided into smaller areas called interrogation areas. In each interrogation area, the tracer particles are assumed to follow the flow field inside that area. Hence, each interrogation area is evaluated by comparing the two light sheet illuminations and a velocity vector flow field is obtained. This evaluation is done by means of statistical methods (auto- or cross-correlation).

In contrast to traditional sensor based measurement techniques used in wind tunnels such as seven-hole pressure probes and hot-wire probes, the particle image velocimetry has several distinct characteristics. First, PIV is a non-intrusive velocity measurement because it is an optical technique. This can be important in some experiments where the flow being measured can be easily disrupted by mechanical probe interference. Hence, high speed flow with shock waves or flow near the boundary layer close to be the wall can also be investigated. Second, the PIV technique measures velocity indirectly because it measures the velocity of the fluid elements by measuring tracer particles within the flow. This indirect measurement is similar to laser Doppler velocimetry. Third, the PIV technique is a whole field technique. It is able to record image of large parts of the flow field and be able to extract the velocity vectors out of it. Hence, this allows for the study of instantaneous velocity vector flow field of the area of interest and is unique to the PIV technique. This is opposed to probe based technique where only the mean flow field can be studied because the probe has to traverse point by point the entire area of interest.

Furthermore, the PIV technique has several constraints. The tracer particles used in the experiment need to faithfully follow the motion of the fluid elements as much as possible. Experimentally, small particles will follow the flow field better. In addition, an illumination source is required for this technique. For the same power light source, in order to capture the light scattered by the particles, bigger particles are easily to capture. However, this is in contradiction with the previous requirement where smaller particles follow the flow field better. Hence, a compromise has to be made usually. Moreover, the illumination laser light pulse has to be short enough in order to freeze the motion of the particles in the flow field. A pulse of too long duration will cause the particles to streak in the PIV image. The time delay between illuminations is just as important. It has to be set such that the distance travelled by the tracer particles during the pulse is short enough to avoid particles from going outside the light sheet thickness or outside the interrogation area. Figure A2 shows different image densities: low (Particle Tracking Velocimetry), medium (PIV), and high (Laser Speckle Velocimetry). The density of the tracer particles in the picture should be uniform and of medium density (PIV). Depending on the seeding device, the tracer particles will be entrained into different parts of the flow differently.

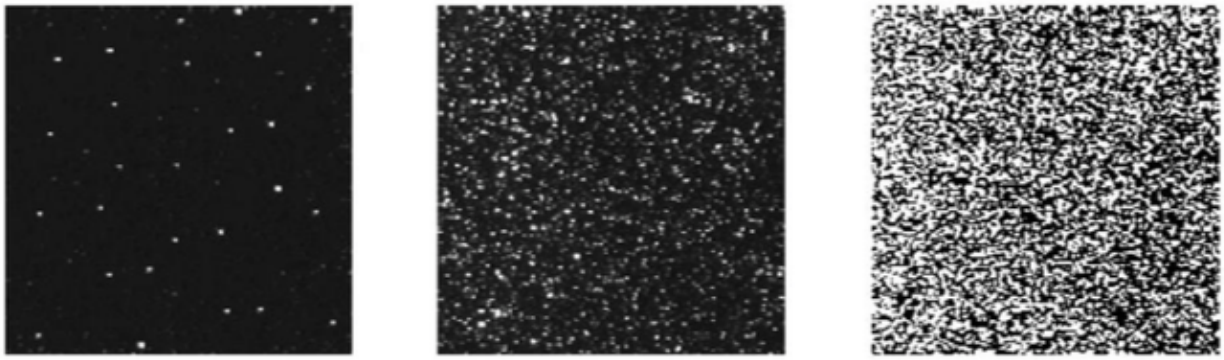

Figure A2 The three modes of particle image density: (a) low (PTV), (b) medium (PIV), and (c) high image density (Raffel et al. 1998).

A3. Elements of particle image velocimetry

A3.1 Seeding

Seeding the flow, or introducing tracer particles into the medium of interest, is essential in order to image the flow field. The size of the particles is dictated by the fact that the particles need to be small enough to follow the fluid and large enough to scatter enough light. Under typical application, PIV would require a higher seeding density than Laser Doppler Velocity (LDV). Figures A2(a)-(c) show different density of particles, low, medium, and high density. In the case of low image density, the images of individual particles can be detected and images corresponding to the same particle originating from different illuminations can be identified. Low image density requires tracking methods for evaluation and is commonly referred to as Particle Tracking Velocimetry (PTV). In medium density images, the images of individual particles can be detected as well. However, it is no longer possible to identify image pairs by visual inspection of the recording. This medium particle density is required to apply the standard statistical PIV evaluation techniques. In Figure A2(c), the high image density contains so many particles that it is no longer possible to detect individual images as they overlap in most cases and form speckles. This type of image is called Laser Speckle Velocimetry (LSV).

Seeding particles and their properties can easily be found in scientific publications. Seeding the flow can sometimes be very easy or does not have to be done at all, as natural seeding is sometimes enough. For liquid flow such as in this investigation, there are a number of particles to choose from (see Table A1).

Table A1 Seeding materials for liquid flows

Type	Material	Mean diameter in μm
Solid	Polystyrene	10-100
	Aluminum flakes	2-7
	Hollow glass spheres	10-1000
	Polyamid	5-20
	Granules for synthetic coatings	10-500
Liquid	Different oils	50-500
Gaseous	Oxygen bubbles	50-1000

Oxygen bubbles as tracer particles can be observed when the water tunnel is just turned on before adding any external tracer particles. The oxygen bubbles, albeit with an uncontrollable concentration, can be observed flowing down the test section. The seeding particles used in this investigation in the water tunnel PIV experiments were the Dantec PSP polyamid seeding particles, 20 μm in diameter. Another alternative considered was the Dantec S-HGS silver-coated hollow glass spheres. They have the most efficient light scattering ability but are rather heavy, with a density of 1.4 g/cm^3, and will settle over time. Because of the low speed of the experiment (0.12 m/s), the investigation required the nearly neutrally buoyant PSP particles with a density of 1.03 g/cm^3. The particles are not perfectly spherical like the S-HGS but are rather round with a refractive index of 1.5 as they are produced by polymerization processes. At a 20 μm mean particle size, the PSP size distribution is between 5 – 35 μm. This particular size, versus the available 5 and 50 μm particles, was chosen so that the particle size in the PIV image is bigger than 1 pixel size of the sensor. If the particle size is too small and cover less than 1 pixel in the image, it will lead to peak locking which severely limits the dynamic range and accuracy of the measurement.

One source of error is the influence of gravitational force if the densities of the fluid ρ and seeding particles ρ_p do not match. Even though this error can normally be neglected, the gravitationally induced velocity U_g can be derived from Stokes' drag law in order to introduce the particle's behavior under acceleration. Assuming spherical particles in a viscous fluid at low Reynolds number, we have:

$$U_g = d_p^2 \frac{(\rho_p - \rho)}{18\mu} g \tag{1}$$

where g is the acceleration due to gravity, μ is the dynamic viscosity of the fluid and d_p is the diameter of the particle. Furthermore, Equation (1) can further be applied to estimate the velocity lag of a particle in a continuously accelerating fluid:

$$U_s = U_p - U = d_p^2 \frac{(\rho_p - \rho)}{18\mu} a \tag{2}$$

where U_p is the tracer particle velocity. The step response of U_p normally follows an exponential law if ρ_p is much greater than ρ:

$$U_p(t) = U\left[1 - \exp\left(-\frac{t}{\tau_s}\right)\right] \tag{3}$$

where the relaxation time τ_s is expressed as:

$$\tau_s = d_p^2 \frac{\rho_p}{18\mu} \qquad \left(\simeq \frac{d^2}{\nu}\right) \tag{4}$$

The result of equation (3) is plotted in Figure A3 for where the time response of particles with different diameters is shown for a strong deceleration in an air flow. As the figure A3 shows, the smaller the particle, the faster the response time, with the d_p = 1 particle response being almost instantaneous.

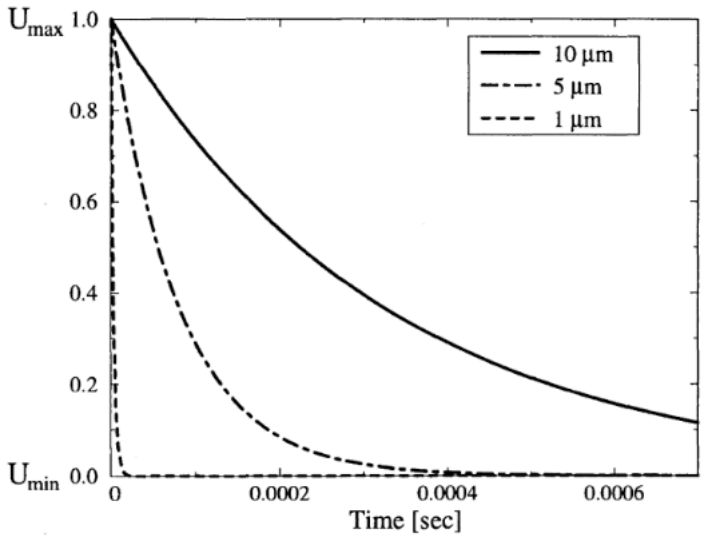

Figure A3 Time response of oil particles with different diameters in a decelerating air flow (Raffel et al. 1998).

A3.2 Light sources

The primary light sources in PIV are lasers. They are chosen because of their ability to emit monochromatic light with high energy density and can easily, through the use of optical elements, be converted into a thin light sheet. This light sheet is used to illuminate the tracer particles for image taking. Continuous wave (CW) lasers can be used, but pulsed lasers are better. Typical CW lasers are argon-ion lasers producing just a few watts of power, even lower power requirement experiments can use helium-neon lasers.

In this investigation, neodymium-doped yttrium aluminum garnet laser, or Continuum Surelite II Nd:YAG laser, was used. This is a pulsed laser with an energy output of 300 mJ at a wavelength of 532 nm. The pulse width is approximately between 4-6 ns with a repetition rate of 10Hz. This short duration of the laser pulse allows us to 'freeze' the tracer particles without motion blurring even though they could be traveling at a relatively high speed. For example, a particle moving at 100 m/s will only move 600 nm in 6 ns. For double exposure image taking, the effective rate of picture taking becomes 5 Hz. In order

to obtain the time delay between laser pulses, two identical laser heads are required to operate in tandem. Figure A4 is a schematic diagram of the Continuum Nd:YAG laser, showing the two laser heads that output two separated laser pulses at the same output location (water tunnel test section). Table A2 shows the specifications of the laser used in this experiment.

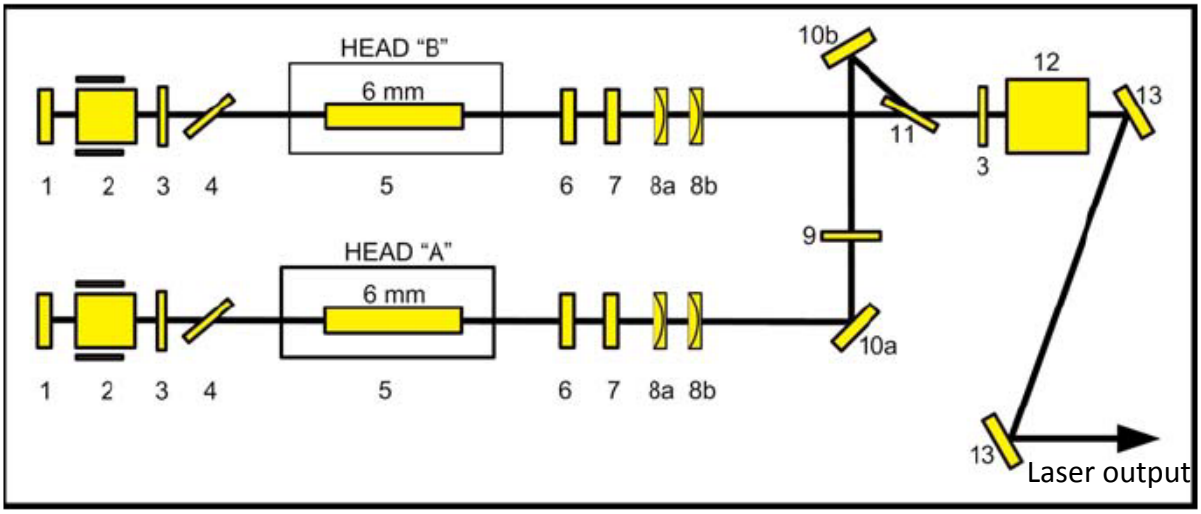

1. HR mirror
2. Pockel cell
3. λ/4 plate
4. Dielectric polarizer, 199-0116
5. Head
6. Gaussian mirror output coupler
7. Compensator
8. Shaping lenses
9. λ/2 plate
10. 45° mirror, 1064 nm
11. Polarizer, 199-0055
12. SHG (second harmonic generator) crystal
13. 45° mirror, 532 nm

Figure A4 Nd:YAG laser internal optical layout.

Table A2 Continuum Surelite II laser specifications

Repetition rate:	10 Hz	Beam pointing stability:	100 μrads
Energy at 532 nm:	300 mJ	Jitter:	±0.5 ns
Pulsewidth at 532 nm:	4 – 6 ns	Energy stability (532 nm):	±3.5%
Linewidth:	1.0 cm^{-1}	Power drift (532 nm):	±6%
Divergence:	0.6 mrads	Beam spatial profile :	0.95
Rod diameter:	7 mm	Service requirements:	Power 220/240V, 10A

Since the PIV image tracer particles contrast is directly proportional to the scatter light power, there are two ways to set the image intensity: changing particle size and increasing the laser power. Most often, it is more economical to choose particles with better light scattering properties than increasing the laser power. The light scattered by small particles is a function of the ratio of refractive index of the particle to that of the surrounding medium, the particles' size, their shape and orientation, and observation angle (Raffel et al. 1998). For spherical particles with diameters d_p, larger than the wavelength of the incident light λ, Mie's scattering theory can be characterized by the normalized diameter, q, defined by:

$$q = \frac{\pi d_p}{\lambda} \tag{5}$$

If q is larger than unity, approximately q local maxima appear in the angular distribution over the range from 0° to 180° (Raffel et al. 1998). In Figures A5(a)-(c), the normalized scattered intensity of different glass particle diameters in water according to Mie theory are shown for λ = 532nm:

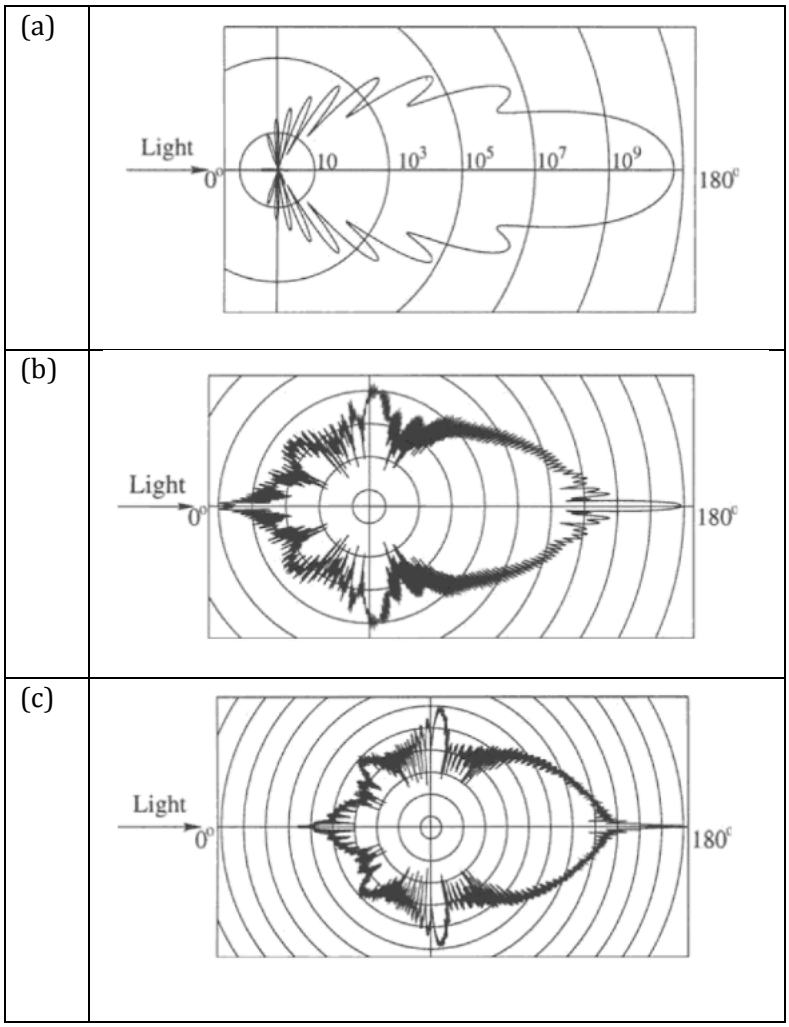

Figure A5 Light scattering by a (a) 1 μm, (b) 10 μm, and (c) 30 μm glass particle in water (Raffel et al. 1998).

The intensity scales are in logarithmic scale and are plotted so that the intensity for neighboring circles differs by a factor of 100. There is a clear tendency for the scattered light intensity to increase with increasing particle diameter size. One consequence is that particle images of high intensity do not always mean that the particle crossed the center of the measurement volume. Hence, the determination of the out-of-plane particle displacement by analyzing particle positions in a light sheet with known intensity profile by image intensity is typically not doable. Furthermore, since the refractive index of water is significantly higher than that of air, much larger particles have to be used for water flow

experiments compared to experiments in air. The above Mie scattering diagrams show that the light is not blocked by the small particles but spread in all directions. Hence, massive multi-scattering occurs when there is a large number of particles inside the light sheet. In heavily seeded flows, this considerably increases the intensity of individual particle images.

A3.3 Image capturing

In this investigation, the PIV images were captured by a TSI PowerView™ Plus Model 630159 charge-coupled-device (CCD) camera. The lens used is a Nikon 105 mm at f/5.6. This camera is designed to be used for PIV. Two modes of operations can be used with the camera: free-run mode for alignment and diagnostics of the system, and frame straddling mode which is actually used to do flow field measurements.

In free-run mode, the camera can capture instantaneous images or display a live continuous feed of the region of interest. However, there is no synchronization between the laser and the camera. This mode is used when we just want to view the images the camera and not worry about the laser timing yet.

The frame straddling mode is used to record each of the each two exposures on separate frames. Traditionally, both exposures have been recorded on a single frame, creating a double exposure image. However, this limitation of this technique is the directional ambiguity caused by having no reference for which particles were in the first and second pulse. Other techniques such as image shifting using a rotating mirror can be used to overcome this ambiguity but it increases experimental complexity. The time delay between laser pulses while using frame straddling with CCD camera is limited by the speed at which information from the first pulse can be transferred outside the CCD chip before taking the second image. Modern CCD camera can overcome this limitation by using more advanced technologies that allow a faster readout time between successive frames, down into the microsecond range. Figure A6 is a schematic diagram of the frame straddling mode timing.

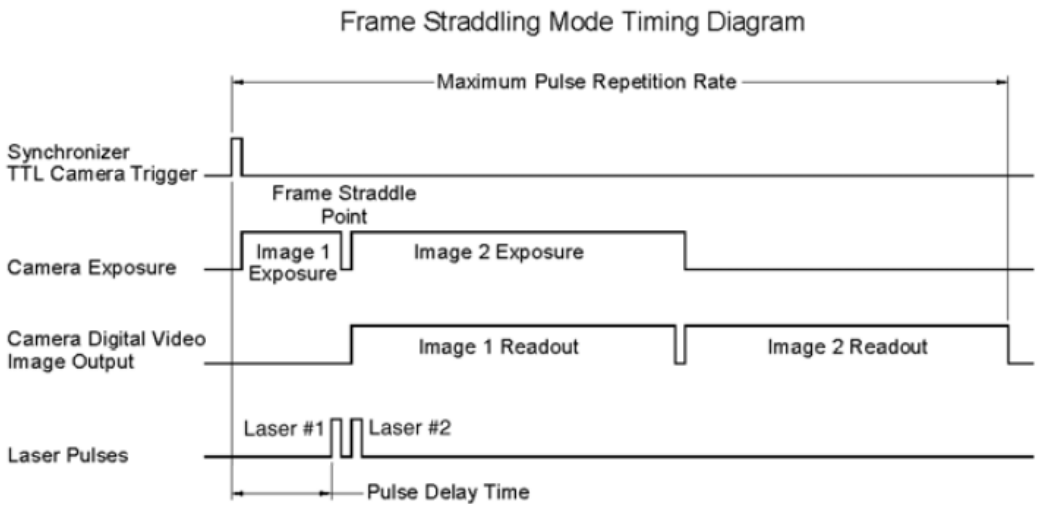

Figure A6 Sequence diagram of Model 630159 PowerView Plus 4MP Camera.

While PIV requires a laser light sheet of sufficient light intensity, if the intensity is too strong, it can damage the CCD array when the particles scatter the light into the camera. While using the Insight 3G software, if the particle reflections show up as pink in the picture, it means the intensity is too high and care must be taken to lower the intensity to prevent accidental dead pixels. Furthermore, even though the test models are painted black, it is still possible that the laser reflection off the laser model is too high. In this case, a special mixture made of rhodamine and Minwax polycrylic protective finish can be applied onto the surface of the model. This will turn the reflection off the model to an amber color instead of the 532 nm green and a special filter can be installed on the camera to allow only 532 nm green light to pass through.

The following table is specifications of the PowerView™ Plus 4MP camera:

Table A3 Specifications of the 630159 PowerView™ Plus 4MP camera

Image device:	Progressive Scan Interline CCD with microlens	Camera lens mount:	F-mount for Nikon lens with 14 mm extension ring
Light sensitive pixels:	4.19 million pixels, 2048 x 2048	CCD protective mask:	Integral protective mask for horizontal readout registers
Pixel size:	7.4 x 7.4 μm	Operation modes:	Free, triggered and frame straddling
Active area:	16.67 mm x 16.05 mm	Camera control:	RS-232 serial
Dynamic range:	12 bits (deliver up to 4096 gray levels)	Camera trigger input:	TTL high level at the rising edge
Min. frame straddling time for PIV capture:	200 ns	Power:	12 volt at 1 amp
Frame rate:	16 frames/second	Camera display:	LED display of camera operating status
CCD quantum efficiency:	53% at 532 nm	Camera output:	Camera link signal
Dark current:	< 0.5 nA/cm^2	Camera body size:	45 mm x 68 mm x 66 mm
Blooming suppression:	300X	Camera body weight:	0.8 kg
Operating temperature:	0° to 40°		

Furthermore, a number of parameters will influence the quality and properties of the picture taken by the CCD camera (Grant 1997). First, the spatial resolution is an important factor. As the seeding particles are circular in shape, if they are smaller than one pixel, the CCD sensor will not reproduce the image faithfully. Depending whether the particles fall inside the sensor pixel or on the vertex, a smaller than one pixel particle can show up as one or four pixels. Hence, it is important that, when choosing the particle size and light intensity, the particle size is at least three by three pixels. Only then will we obtain an image that is more realistically reproduced (Andor n.d.). Second, the depth of field of the camera lens is important in order to obtain a sharp image. It is the distance by which an object may be shifted before the image becomes out of focus. This distance depends on a number of factors such as lens focal length and the lens f-number. In order to get the best sharp and focused image, the particles inside the laser light sheet will need to fall into the depth of field. Third, the image size of the particle will depend on the particle diameter and

the lens magnification ratio. Finally, the recording medium chosen is dependent on the size of the flow field to be recorded and the required resolution. For example, in this investigation, the CCD camera resolution is 2048 x 2048, this means that a single image file will contain 4.2 million pixels. This will have an impact on the how fast the computer can handle and store the images on the host computer.

A3.4 Recording hardware

Finally, having a CCD camera would mean nothing without a data acquisition system to record the images. In this investigation, a HP workstation computer is used in conjunction with a Coreco Imaging 0 X64-CL frame grabber and a TSI 610035 synchronizer. The specifications of the synchronizer are listed in Table A4.

The role of the synchronizer is to make sure that all the timings are correct for the pulse width, pulse delay time, frame straddling and image taking. It controls the timings with high precisions together with the TSI Insight3G software. If necessary, the synchronizer can also accept an external trigger for when to acquire the PIV images. Although not used in this investigation, this feature can allow periodic flow fields to be studied by triggering the image acquisition at a specific phase in the cycle.

Table A4 Specifications of the TSI 610035 synchronizer

Pulse generation		**External trigger**	
Delay:	0 – 1000 s	Rate:	DC to 5 MHz
Pulsewidth:	10 ns to 1000 s	Threshold:	500 mV to 15 V
Resolution:	1 ns	Input range:	0 – 30 V
Time base:	100 Mhz, 25 PPM crystal oscillator	Trigger slope:	Rising or falling edge
RMS jitter:	< 400 ps	RMS jitter:	< 5 ns
		Insertion delay:	< 150 ns
Output		**Miscellaneous**	
Outputs:	TTL/CMOS, adjustable 2 – 20 V. 35 V optional	Communication to computer:	RS-232
Impedance:	50 Ohms	Operating voltage:	120/240 VAC, 50 – 60 Hz
Slew rate:	0.5 V/ns	Dimension	20.3 x 12 x 26.7 cm^3
Overshoot:	< 100 mV + 10% of pulse amplitude	Weight:	1.1 kg
Amplitude:	1 – 6 V into 50 Ohm load 2 – 12 V into high impendance load		

A3.5 Image processing

Although the PIV software, TSI Insight 3G, is responsible for analyzing the PIV images, it is still important to learn the theoretical details behind the analysis. PIV images can be processed by using one of the three correlation processes: autocorrelation, one-frame cross-correlation and two-frame cross-correlation. These correlation techniques differ in the image window areas for the first and second particle images. In autocorrelation, both the first and second image windows are on the same image window. For one-frame cross-correlation, the second image window is offset from the first image window on the same frame (TSI document). Finally, in 2-frame cross-correlation, image 1 and image 2 are on their own respective frame.

The above techniques have their advantages for some applications. When the particle motion and image shift together give less than ¼ of the interrogation spot image displacement in multiple exposure images, autocorrelation is used. One-frame cross-correlation is a multiple exposure technique used when the image shift displacement is

large relative to the particle motion displacement. High resolution measurements can be made by offsetting the second image window from the first by the mean particle image displacement distance. Two-frame cross-correlation measures the displacement of the particles as they moved between the exposures on two image frames. Each of these frames only has a single light pulse. By knowing the order of the first and second pulse image, the signal-to-noise ratio relative to the single frame technique is improved. Another advantage of the 2-frame cross-correlation technique is that reversed flow and zero displacement measurements can be made without image shifting.

In this investigation, the two-frame cross-correlation technique is used. The Nd:YAG laser pulses twice to give two separate image frames. Hence, the first laser pulse image is in frame 1 and second laser pulse image is in frame 2. The particle velocity can be obtained without directional ambiguity because the images are separated. A drawback of using two-frame cross-correlation is the slow effective image capture rate. As a rule of thumb, the particles must move less than ¼ of the interrogation spot in the time between the first and second laser pulses.

Cross-correlation is a statistical approach used to find the most likely displacement of a group of particles. First, frame A is broken into a grid of interrogation region. This group of particles inside the interrogation region forms a unique pattern that we can look for in frame B.

Frame A's interrogation region (spot A) is smaller than frame B's search area (spot B). A spot mask is created from frame A and is scanned across the search area of frame B to form a correlation map. This correlation map will have a peak relative to the location where the unique pattern of the spot mask is identified in frame B. By searching the entire search area of frame B using frame A, the correlation values for different locations of the spot mask can be represented on a correlation map. In the best case, there is only one distinct round peak in the correlation map. In real life, however, there will be several peaks in the correlation map and the one with the strongest intensity is chosen as the correct correlation. The displacement in X and Y are then obtained by the offset of the spot mask to the peak of the correlation map. Since the laser pulse time delay Δt was set by the user and

is known, a single velocity vector for the spot mask of frame A can be calculated by dividing the displacement by Δt. This above process is repeated for each of the interrogation region in frame A, resulting in a two-dimensional velocity flow field for the imaged window.

Furthermore, the results obtained by cross-correlation represent the instantaneous flow field at that instant of time. In order to study the mean flow field, similar to what a seven-hole pressure probe would output, an ensemble average (EA) result is needed. This is performed by taking a number of PIV images at the same location and taking an average of the results. The mean flow field properties can depend on the number of PIV images used to ensemble average. In this investigation, the PIV images were ensemble averaged over 60 images in order to represent the mean flow field of the region of interest. The effect of the PIV image number on the ensemble average has been investigated and found to be insensitive to the number of images at 60 images.

In the remaining section, a mathematical background of cross-correlation is presented. It is assumed that a constant displacement D is applied to all the particles inside the interrogation volume, so that the particle locations during the second exposure at time $t' = t + \Delta t$ are given by:

$$X_i' = X_i + D = \begin{pmatrix} X_i + D_X \\ Y_i + D_Y \\ Z + D_Z \end{pmatrix} \tag{6}$$

We can also assume that the particle image displacement are given by

$$d = \begin{pmatrix} MD_x \\ MD_Y \end{pmatrix} \tag{7}$$

where M is defined as the magnification ratio. The above equation is a simplification of the perspective projection and is only valid for particles located in the vicinity of the optical axis. The image intensity field for the time of the second exposure can be defined as:

$$I'(x, \Gamma) = \sum_{j=1}^{N} V_0' \left(X_j + D\right) \tau\left(x - x_j - d\right) \tag{8}$$

where $V_0'(X)$ defines the interrogation volume during the second exposure. Under identical light sheet and windowing characteristics conditions, the cross-correlation function of the two interrogation areas can be written as:

$$R_{II}(s,\Gamma,D) = \frac{1}{a_I}\sum_{i,j} V_0(X_i)V_0(X_j+D)\int_{a_I}\tau(x-x_i)\tau\big(x-x_j+s-d\big)dx \tag{9}$$

where s is the separation vector in the correlation plane. The expression can be further written as (Raffel et al. 1998):

$$R_{II}(s,\Gamma,D) = \sum_{i,j} V_0(X_i)V_0(X_j+D)\,R_\tau\big(x_i-x_j+s-d\big) \tag{10}$$

By distinguishing the $i \neq j$ terms which represent the correlation of different randomly distributed particles (noise) and the $i = j$ terms, which contain the displacement information we want, we further obtain:

$$R_{II}(s,\Gamma,D) = \sum_{i\neq j} V_0(X_i)V_0(X_j+D)\,R_\tau\big(x_i-x_j+s-d\big) + R_\tau(s-d)\sum_{i=1}^{N} V_0(X_i)V_0(X_j+D) \tag{11}$$

and after decomposing the correlation into three parts:

$$R_{II}(s,\Gamma,D) = R_C(s,\Gamma,D) + R_F(s,\Gamma,D) + R_D(s,\Gamma,D) \tag{12}$$

where $R_D(s,\Gamma,D)$ represent the component of the cross-correlation function that corresponds to the correlation of images of particles obtained from the first exposure with images of identical particles obtained from the second exposure ($i = j$ terms):

$$R_D(s,\Gamma,D) = R_\tau(s-d)\sum_{i=1}^{N} V_0(X_i)V_0(X_j+D) \tag{13}$$

Therefore, for a given distribution of particles inside the flow, the displacement correlation peak reaches a maximum for $s = d$. The location of this maximum yields the average in-plane displacement, and as a result, the U and V velocity component inside the flow.

A5. PIV parameters

A5.1 PIV image calibration

In order to convert the pixel units to the physical units relevant to our flow field, we need to perform a spatial calibration. In order to do so, we must first make sure that the light sheet is aligned properly at the desired location. The camera will have to see the light sheet at an appropriate zoom and the lens will have to be focused at the plane. Next, we place a ruler in the field of view, coinciding with the laser light sheet. A picture of the ruler is now taken with the PIV camera. We make sure the ruler is focused in the picture. Using the Insight3G software, create a new spatial calibration and enter a known distance on the ruler. Click on the extremity of the distance on the ruler and the software will now calculate the spatial calibration. In this investigation, the spatial calibration was calculated to be 45.15 μm/pixel and a magnification ratio of 6.10.

A5.2 Optimizing Δt and laser light sheet thickness

Selecting Δt, or the time delay between frame A and B is critical. In order to do so, we must follow some rules-of-thumb. The rule of thumb is that the displacement must be less than 25% of our intended interrogation region. However, in this investigation, a more important parameter exists: out-of-plane particle motion. In most applications, the tracer particles mostly travel in the plane of the laser light sheet. However, in the current study, the particles are traveling normal to the plane of the laser light sheet. Hence, in order for the particles to be visible in both frame A and B (so they have not traveled out of plane), the light sheet thickness is also important. The light sheet thickness was chosen to be 0.001143 m (0.045") and the time it took for the particle to travel 25% of the thickness was, based on a freestream velocity of 0.12 m/s, found to be 2381 μs. This allow the particles to travel and stay inside the laser light sheet perpendicularly, and also allowed motion in the plane of the laser light sheet.

A6. PIV rules of thumb

Furthermore, the following are a few rules-of-thumb for autocorrelation PIV analysis as suggested by the TSI PIV manual:

1. Interrogation spot size should be small enough so that one vector describes the flow within that spot.
2. There should be more than ten particle image pairs per interrogation spot.
3. Maximum in plane displacements should be less than ¼ of the interrogation spot size.
4. Maximum out of plane displacement should be less than ¼ of the light sheet thickness.
5. Minimum in-plane displacement should be two particle-image diameters.
6. Exposure must be large enough to clearly show the particles.

A7. References

Andor, n.d., "CCD Spatial Resolution," Retrieved April 10, 2017 from http://www.andor.com/learning-academy/ccd-spatial-resolution-understanding-spatial-resolution

Dantec dynamics, n.d., "Measurement Principles of PIV," Retrieved April 10, 2017 from http://www.dantecdynamics.com/measurement-principles-of-piv

Grant, I., 1997, "Particle image velocimetry: a review," *Proceedings of the Institution of Mechanical Engineers*, Vol. 211, Part C, pp. 55-76.

Raffel, M., Willert, C. E., and Kompenhans, J., 1998, Particle image velocimetry. Berlin, Springer.